New spintronic components based on antiferromagnetic materials

Théophile Chirac

université PARIS-SACLAY

NNT : 2019SACLS482

Thèse de doctorat

New spintronic components based on antiferromagnetic materials

Thèse de doctorat de l'Université Paris-Saclay
préparée à l'université Paris-Sud

École doctorale n°564 École Doctorale Physique en Île-de-France (EDPIF)
Spécialité de doctorat : Physique

Thèse présentée et soutenue à Gif-sur-Yvette, le 17/12/2019, par

THÉOPHILE CHIRAC

Composition du Jury :

Alexandra Mougin Directrice de recherche, Laboratoire de Physique des Solides, Université Paris-Sud, CNRS UMR 8502, 91405 Orsay Cedex, France	Président
Vincent Baltz Directeur de recherche, SPINTEC, URA CNRS/CEA 2512, CEA-Grenoble, 38054 Grenoble Cedex 9, France	Rapporteur
Manfred Fiebig Professor, Department of Materials, Laboratory for Multifunctional Ferroic Materials, ETH Zürich, Vladimir-Prelog-Weg 4, Zürich, CH-8093, Switzerland	Rapporteur
Laurent Ranno Maître de conférences, Institut Néel et Université Joseph Fourier, 38042 Grenoble, France	Examinateur
Pascal Ruello Professeur, Institut des Molécules et Matérieux du Mans, UMR CNRS 6283 et Université du Mans, Av O.Messiaen, 72085 Le Mans, France	Examinateur
André Thiaville Directeur de recherche, Laboratoire de Physique des Solides, Université Paris-Sud, CNRS UMR 8502, 91405 Orsay Cedex, France	Examinateur
Michel Viret Directeur de recherche, Service de Physique de l'Etat Condensé, CEA Saclay, DSM/IRAMIS/SPEC, URA CNRS 2464, 91191 Gif sur Yvette, France	Directeur de thèse
Jean-Yves Chauleau Chercheur, Service de Physique de l'Etat Condensé, CEA Saclay, DSM/IRAMIS/SPEC, URA CNRS 2464, 91191 Gif sur Yvette, France	Invité

Preface

This PhD thesis work started on November 15th 2016 and was carried out over three years, at Laboratoire de Nanomagnétisme et Oxydes (LNO), Service de Physique de l'État Condensé (SPEC), CEA Saclay, under the supervision of Michel Viret and in close interraction with Jean-Yves Chauleau. Most of the work presented here would not have been possible without their precious help, visions and discussions.

Paris, November 4th, 2019

Théophile CHIRAC

Acknowledgment

I would like to address my most sincere gratitude to the members of the jury, who showed their interest in the work I have achieved, and with whom I shared a very interesting discussion, in the limits of my knowledge, during the defence of the work I had the opportunity to present.

I would also like to thank the main actors, without whom I would not have been able to explore that deep into the physics: Michel Viret, my PhD supervisor, who was always reachable and available for discussions despite his responsibilities, and who has, in addition to his great understanding and passion for physics, the valuable capacity of explaining phenomena simply. Jean-Yves Chauleau, who truly was a second supervisor of heart, and good companion in our dark times of confusion, every time the physics or the experiments would challenge us. His passion, humility and rigor are valuable and inspirational. Jean-Baptiste Moussy, Grégoire de Loubens, collaborators in Thalès (Stéphane Fusil, Vincent Garcia, Cécile Carrétéro), in LPS (Raphaël Veil), Montpellier (Vincent Jacques, Aurore Finco, Angela Haykal), Le Mans (Vincent Juvé, Pascal Ruello, Gwenaëlle Vaudel), Tours (Pascal Thibaudeau), Albuquerque (Julien Tranchida), ...who, more than being good and talented coworkers, were contributors to the daily good atmosphere in our scientific discussions.

Because no experimental physics can be done on scientific discussion only, it would be unfair not to thank the following persons for their great help behind the scene during these three years of PhD: Gregory Cannies and Gerald Le Goff for their amazing work in manufacturing assets for the experiment, Dominique, Vincent, Pascal, Jean-Claude from the workshop, and their dedication every time a little help was needed on the daily troubles. Corinne, Nadine and Anne for their patience and their help with the administration and formations.

Many thanks to the LNO, to everyone in the corridors and to the lunch company: PP, Matthieu, Philippe, Aurélia, Cyril, Yannick, Sasha, Geneviève, Nadine, Thomas, Patrice, François, Preden, Aurélie, Myriam, Hélène, Antoine, Hervé, Claude, Pierre, Élodie ...
Thanks, greetings and good wishes to current and former PhD students, postdocs, apprentices and young employees who took part in my everyday company: Vincent, Julien, Chloé, Manon, François-Damien, Nathanaël, Kakoli, Vishal, Bartolo, Sebastian, Philip, Andrin, Reina, Anaëlle, Xavier, Fawaz, Amal, Sylvio, Jacob, Eswara, Anas, Paul, Titiksha, Fernanda, Maëlle, Matthieu, Anil, Ambroise, Gerbod, Ludovic, Adel, Philip, Mathieu, Ramon, Ryhei, Mathieu, Maïkane, Nahuel,...

Finally, I would like to address a very special thank you to my family and all my friends for the underlying long run moral support.

From the bottom of my heart *thank you*, and sorry to everyone that I have forgotten to mention here.

T.C.

Contents

Notations

Conventions

$scalar$, $\boldsymbol{vector}$, $\underline{\boldsymbol{2D-tensor}}$, $\underline{\underline{\boldsymbol{3D-tensor}}}$, $\underline{\underline{\underline{\boldsymbol{4D-tensor}}}}$, ...

$\hat{\boldsymbol{v}}$ unitary vector along vector $\boldsymbol{v}$.

$[1\bar{1}0]$ is the *axis* meeting the points $x=0, y=0, z=0$ and $x=1, y=-1, z=0$ in cartesian coordinate.

$(1\bar{1}0)$ is the *plane* perpendicular to the $[1\bar{1}0]$ axis.

$\langle 1\bar{1}0\rangle$ is the ensemble of all axes equivalent to $[1\bar{1}0]$ in our [111] revolution axis geometry, namely $[1\bar{1}0]$, $[01\bar{1}]$,$[\bar{1}01]$, $[\bar{1}10]$, $[0\bar{1}1]$ and $[10\bar{1}]$.

$\{1\bar{1}0\}$ are all the planes equivalent to the $(1\bar{1}0)$ plane, i.e. perpendicular to $\langle 1\bar{1}0\rangle$.

Acronyms

AFM Antiferromagnetic

AFM Atomic Force Microscope

BFO $BiFeO_3$

DC Direct Current

DSO $DyScO_3$

FE Ferroelectric

FM Ferromagnet

HM Heavy Metal

IREE Inverse Rashba-Edelstein Effect

ISHE Inverse Spin Hall Effect

MBE Molecular Beam Epitaxy

MOKE Magneto-Optic Kerr Effect

OPA Optical Parametric Amplifyer

PFM Piezoelectric Force Microscopy

SHE Spin Hall Effect

SHG Second harmonic generation

SRO $SrRuO_3$

STO $SrTiO_3$

RXES Resonant soft-Xray Elastic Scattering

TRMOKE Time-Resolved Magneto-Optic Kerr Effect

TRSHG Time-Resolved Second Harmonic Generation

Constants

$\hbar$ Reduced Planck constant

c Speed of light in vacuum

ε_0 Vacuum permittivity

μ_0 Magnetic permeability of free space

Variables

$\mathscr{H}$ Hamiltonian

$\boldsymbol{E}$ Electric field

$\boldsymbol{B}$ Magnetic B-field = Magnetic induction = Magnetic flux density

$\boldsymbol{H}$ Magnetic H-field = Magnetic field intensity = Magnetic field strength = Magnetizing field

$\boldsymbol{D}$ Dielectric field

$\boldsymbol{P}$ Electric Polarization

$\boldsymbol{M}$ Magnetization

$\boldsymbol{\mu}$ Magnetic moment

$\boldsymbol{s}$ classical spin vector

$\hat{\boldsymbol{s}}$ unitary classical spin

$\boldsymbol{L}$ Orbital moment

$\mathbf{L}$ Néel vector

$\underline{\boldsymbol{Q}}$ Electric Quadrupole

μ magnetic permeability

ε electric permittivity

χ electric susceptibility

$\frac{\partial X}{\partial Y}$ partial derivative of X with respect to Y

$\mathbf{t}$ time

ϕ Phase

Introduction

The past decades were marked by an exponential use of digital technologies, especially since the discovery of the transistor, which enabled the possibility for miniaturization and thus the realization of versatile portable electronics. The technological breakthrough was induced by material science via the understanding of the behavior of charge carriers in semiconductors. Nowadays, digital technologies are omnipresent in all the sectors of the societies of the developed countries, and increasingly growing in developing countries. We experience theirs benefits daily, and the needs for more speed, more data storage is constantly growing. The current achievements have made possible the manufacturing of devices for manipulation and storage of a never stopping flow of information, leading to gigantic volumes of data, accessible anytime anywhere all over the planet. Recent fields of computer science, *big data* and *deep learning* are based on the availability of huge volumes of data, and still more is to expect to reach one day the computing power of a human brain. The pressure on the electronics industry is therefore huge to develop and release every year a new component for data storage or data processing that would be faster, smaller or more robust than the previous ones. Following Moore's law, people expect a doubling of computing power capacity every two years, all in the size of a device that could fit in their pocket. Yet, as the miniaturization race goes on, scientists are facing challenges to reduce further the sizes of electronics components. Today's electronics happens at a scale of tens of nanometers. This mesoscopic scale, only a few orders of magnitude over the size of the atoms, require a good knowledge of solid state physics to predict, understand and use the effects of collective behaviors of physical entities of intrinsic quantum nature.

A good candidate for the future of electronics could be the approach proposed in the field of spintronics. The idea, already illustrated in magnetic hard disk drives is to use magnetism as the support of information. Magnetism provides natural non-volatile multi-state memories with rich and controllable dynamics in close link with the electronics, and good compatibility with the current CMOS-based technology. Among magnetically ordered materials, antiferromagnets are promising candidates for the future of spintronics. Their internal antiparallel atomic spins arrangement protect them from parasitic signals, at the same time as enabling a very fast dynamical operation. Yet, antiferromagnetic spintronics is a very recent field, which has only emerged less than a decade ago. It is subject to active research given the many advantages they offer.

In this thesis, we study the possibility of realizing active antiferromagnets-based components for spintronics, using two approaches: experimental and numerical simulations. The two main challenges for having functional components is being able to *read* antiferromagnetic information, and to *modify* it. These are the challenges this

thesis is aiming to address.

This thesis is divided into four chapters:

In the first chapter, an introduction to the concepts of spintronics and antiferromagnets is presented, to introduce the tools and the notions on which this thesis is based.

In the second chapter, we introduce two antiferromagnets: NiO (prototypical) and $BiFeO_3$ (multiferroic), on which a theoretical study based on atomistic simulations is carried out. Firstly, magnetization dynamics on NiO unveils the possibility of switching a simple antiferromagnetic domain using spin currents. A second static study looks at the formation of antiferromagnetic chiral structures at multiferroic domain walls in $BiFeO_3$.

In the third chapter, the experimental observation of antiferromagnetic textures is achieved in $BiFeO_3$ using an imaging technique based on second harmonic generation (SHG). We then analyze the picosecond response of $BiFeO_3$ under optical stimuli using time-resolved SHG imaging.

In the fourth chapter, we characterize terahertz emitters based on the ultrafast demagnetization of a ferromagnetic layer, with the help of four different techniques, each probing a different timescale. These emitters can generate picosecond electrical bursts or spin currents which can be used to excite the $BiFeO_3$ sample measured in the third chapter. The first measurements with this technique are presented here.

Chapter 1

General Concepts for Antiferromagnetic Spintronics

1.1 An Overview of Spintronics

1.1.1 Introduction

As electronics endlessly keeps on miniaturizing to follow Moore's predictions, and improving computing speed to match the needs of our society's massive data technologies, memory bit sizes and computing units are steadily scaling down towards the atomic scale. The electronics industry is facing more and more technological challenges intrinsic to the very nature of the physical processes at stake. Spintronics is a fellow paradigm to electronics motivated by the ambition to help it face these new challenges. The basic idea is to consider using magnetism, and the spin of the electron rather than its charge. Most often nowadays, the digital information is processed and stored via voltages, but magnetization is also a good vector of information, as this is illustrated in magnetic cards and magnetic hard disk drives. We will see in the course of this introductory chapter that spintronics offers room and opportunities for research and developments to improve today's technology, especially by the use of antiferromagnets as active elements.

First, we will define the basic concepts of spintronics which will lead to the statement that information can travel, be stored and processed via magnetism. We will then define antiferromagnetism and its basic properties to finally see that antiferromagnets can be of huge interest in the frame of spintronics.

1.1.2 Magnetization

This subsection will set the frame of our physics but has no claim to be a physics lecture on magnetism. It will rather introduce our notations and the key concepts that will be useful to be familiar with for the rest of the thesis.

Spin

The *spin* is a quantum mechanical form of angular momentum intrinsic to particles, that emerges from the Dirac equation (a relativistic version of the more famous Shrödinger's equation). It has the conservation properties of an angular momentum, but exhibits quantum mechanical behaviors such as quantization, and state superposition. Particles with spin S_z along a quantization axis $\hat{\boldsymbol{z}}$ carry a magnetic moment $\boldsymbol{\mu}_s$. The proportionality coefficient between them is called the *gyromagnetic ratio* γ.

$$\boldsymbol{\mu}_s = \gamma S_z \hat{\boldsymbol{z}} \tag{1.1}$$

In the classical limit, and especially in solids with a large number of particles, $S_z\hat{\boldsymbol{z}}$ and $\boldsymbol{\mu}_s$ behave like classical vectors, rather than quantum eigenstates. In this thesis, we will often deal with the classical approximation of the spins that we will note $\boldsymbol{s}$.

Magnetization

In solids, all the atomic magnetic moments sum up. Often, they average to zero, but in magnetic materials, a net magnetic moment $\boldsymbol{\mu}$ emerges. The magnetic moment per volume unit ($\mathcal{V}$) is called the *magnetization* and is noted $\boldsymbol{M}$. The magnetization and magnetic moments are linked via the relations:

$$\boldsymbol{M} = \frac{\mathrm{d}\boldsymbol{\mu}}{\mathrm{d}\mathcal{V}} \tag{1.2a}$$

$$\boldsymbol{\mu} = \iiint \boldsymbol{M}\mathrm{d}\mathcal{V} \tag{1.2b}$$

$\boldsymbol{M}$ is expressed in A/m and $\boldsymbol{\mu}$ in $A.m^2$. As a generality in magnetic materials, the local magnetic moments self arrange in *(Weiss) domains*, and the magnetization is not uniform. The magnetization contributes to the total *magnetic flux density* $\boldsymbol{B}$ via the relation:

$$\boldsymbol{B} = \mu_0 (\boldsymbol{M} + \boldsymbol{H}) \tag{1.3}$$

$\boldsymbol{H}$ is the *magnetizing field*. When no distinction needs to be done, $\boldsymbol{B}$ and $\boldsymbol{H}$ can indifferently be designed by the generic denomination "magnetic field". In this thesis, we use Si units [1], $\boldsymbol{B}$ is expressed in T, the *magnetic permeability* μ_0 in H/m, $\boldsymbol{M}$ and $\boldsymbol{H}$ in A/m.

[1] Contrary to the recommendations from the International Bureau of Weights and Measures, some authors still use the CGS units, and historical papers may use them. For information only, we recall that in CGS units:

$$\boldsymbol{B}[Gauss] = 4\pi \boldsymbol{M}[emu] + \boldsymbol{H}[Oe] \tag{1.4}$$

With $1\,Gauss = 1\times10^{-4}$T, and $1\,Oe = \frac{1}{4\pi}\times10^{3}\,A/m$.

Magnetic energy

In a magnetic field, a magnetic moment has a magnetic energy, which is lower when aligned parallel to the field:

$$\mathscr{H}_{\text{magn}} = -\boldsymbol{\mu} \cdot \boldsymbol{B} \tag{1.5}$$

When the magnetic field is static and produced externally, we call it a *Zeeman field*, and the associated magnetic energy is called the *Zeeman energy*.

Magnetic precession

Because of the angular momentum conservation, magnetic moments do not simply align with the magnetic field. They experience a torque τ which make them precess:

$$\boldsymbol{\tau} = \boldsymbol{\mu} \times \boldsymbol{B} \tag{1.6}$$

Through other processes, the angular momentum can be transfered to the material (damping) and eventually cause alignment to minimize the magnetic energy. The equation of precession that we will present in details in chapter 2 leads to a resonant frequency which is called *ferromagnetic resonnance*.

Magnetic anisotropy

In magnetic materials, the prefered direction of the magnetic moments at rest is generally not isotropic in direction and commonly sets preferably along an *easy axis*, a set of easy axes, or an *easy plane*. It is mostly due to the crystalline structure of the material and the bounding between orbitals of atoms carrying spins, or simply to the shape of the magnetic object, wich maximizes the long distance magnetic dipole alignments for certain directions. In the first case, we talk about *magnetocrystalline anisotropy*, in the second case, about *shape anisotropy*.

Magnetic anisotropy can also have origins from *exchange anisotropy* or induced anisotropies due to stress, magnetic annealing, plastic deformation or irradiation [2], but they will not be considered in the frame of this thesis, or can be considered as included in our definition of magnetocrystalline anisotropy.

Magnetization as a data storage support

The magnetization in magnetic materials undergoes a hysteretic behavior when subject to an external magnetic field: the magnetization tends to align with the external field and remains when the external field is removed. The hysteretic behavior is significantly affected by the magnetic anisotropy, and is not isotropic (Figure 1.1). When the coercitive field is strong along the easy axis, materials are called *hard* magnetic materials, and they are called *soft* magnetic material when the coercitive is weak. When the dependence is linear, with no hysteresis, they are called *paramagnetic*. In this thesis, the term “magnetic material” will most often exclude paramagnetic materials.

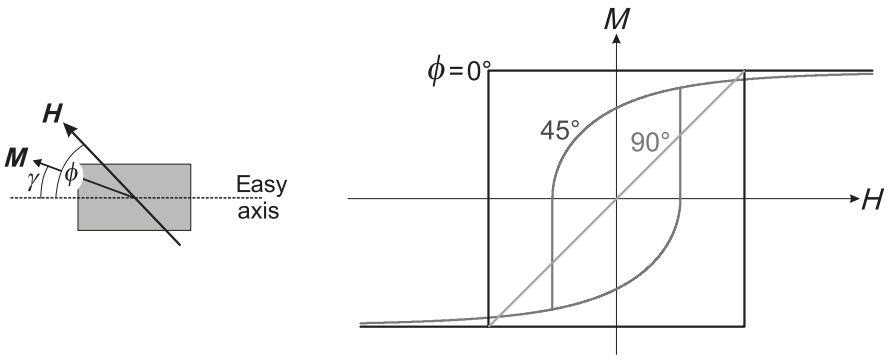

Figure 1.1: Hysteretic behavior of the magnetization. The remanent magnetization offers two stable states for memory supports. Figure adapted from [3].

The hysteretic behaviour of magnetic materials provides two stable states suitable for memory devices. A binary information can be stored using an magnetizing field, and the information remains stable until the next writing. This basic principle is largelly used nowadays in all sort of static memory supports: magnetic cards, metro tickets, hard disk drive memories, etc... Their serious competitors nowadays are *solid-state* memories (SSD and flash technology) based on semiconductor technology, but the magnetic technology is not at its last breath yet since the first magnetoresistive random-access memory devices are set to industrial production and are predicted to supplant the semiconductors (static RAM, dynamic RAM and Flash all at once) in terms of non-volatility and endurance, with relatively high read and write speeds [4].

1.1.3 The notion of spintronics

Today's hard disk drives have magnetic domain sizes in the order of 200×20nm. Research tries to find ways to increase the magnetic data storage density, but also to increase the writing speed, the stability, and limit the power consumption of these devices. For this, one must study the collective behavior of spins in matter. By analogy with the *electronics*, this field of study is called *spintronics*, and aims at making the spin carry the information similarly to how the charge does in electronics. The combination of spintronics and electronics can give the future of electronic devices the best of both worlds. Today, the magnetic hard disk drive is the most popular spintronics device, but much more is to expect. Among others, researchers study domain wall motion, magnetic bubbles formation and stabilization, magneto-optical effects, magnetostriction, magnetic wave propagation, magnetic materials, couplings and interplay between magnetic layers, and so on. Spintronics is a wide field which can hardly be reviewed in a single chapter, so we will simply focus on the fundamental concepts that will be useful for this thesis, in the forthcoming sections.

1.1.4 Spin interactions

A fundamental question concerns how the individual spins interact with matter to create mesoscopic magnetic moments, and how we can interact with them.

The main contributor to magnetism are the spins of the valence electrons of the atoms. Because of Hund's rules, spins from the core tend to pair up antiparallel, causing no global magnetic moment, while only lone electrons from the outer shells can contribute to the magnetism. The spins of the electrons interact with the matter in various complex ways through the valence orbitals. We focus here on the two key interactions that give rise to most of the spintronics phenomena: the *exchange interaction* and the *spin-orbit interraction*.

Localized spins

Exchange interaction Two atomic orbitals interact via a Coulomb integral (repulsion between electrons), an overlap integral (causing repulsion at short distance), and exchange integral for which the spin is at stake. In a first approximation, the exchange integral between atoms i and j can be expressed by a constant that we call J_{ij}, and the exchange interraction described by the following Heisenberg Hamiltonian [5]:

$$\mathcal{H}_{exch\|} = \sum_{i,j} J_{ij} \boldsymbol{s}_i \cdot \boldsymbol{s}_j \tag{1.7}$$

The sign of J_{ij} will tell if the spins of the two atoms tend to align parallel or antiparallel[2]. If the alignment is parallel, the material will be ferromagnetic, if the alignment is antiparallel, it will be either antiferromagnetic or ferrimagnetic. If the exchange contribution is negligible, the material can also be non-magnetic. More details on the exchange interaction will be given in section 1.2.

Spin-orbit interaction The spins also interact with their near environment via the *spin-orbit interaction* (also called *spin-orbit coupling*). This is a purely relativistic effect, which is simple to understand within a classical picture: in the reference frame of the orbiting electron, the electric field of the atom core is orbiting and produces a magnetic field, which interracts with the spin via the magnetic energy $-\boldsymbol{\mu} \cdot \boldsymbol{B}$. More realistically, what the the electrons see is the electric field from the whole crystal field, screened by other electrons. The magnetic field experienced in the rest frame of the electron is related to its orbital momentum $\boldsymbol{L}$, and the Hamiltonian for the spin orbit coupling reads :

$$\mathcal{H}_{SO} = V_{SO} \boldsymbol{L} \cdot \boldsymbol{s} \tag{1.8}$$

Where V_{SO} contains contributions from the Larmor interaction and Thomas relativistic effects. An internal symmetry breaking is required so that this interaction does not average to zero. The spin-orbit interraction is often the main contribution to the *magneto-crystalline anisotropy* [2][3] [3][4]. The spin-orbit interaction not only applies to bound electrons, but also to free electrons. This gives rise to valuable conversion effects (the Spin Hall Effect and the Edelstein effect), which will be developped in detail in chapter 4.

[2] In the conventional definition of the Heisenberg Hamiltonian for ferromagnets, authors write $-J_{ij}$ instead, to keep J_{ij} positive, but in the context of this thesis, the minus sign will be considered included in J_{ij}.

[3] p204

[4] p209

Non-localized spins

Spins are not necessarily localized, especially in metals. In this case, it is convenient to have a look at the density of states. Mainly because of exchange, two opposite spin polarities give two different densities of state. A simple model for this is the *Stoner model*, which gives different energy densities for spins up or down (Figure 1.2). Electrons fill up the lower energy levels up till the Fermi energy. The disbalanced amount of spin up electrons comparatively to spin down electrons give rise to ferromagnetism, and spin-dependent transport properties.

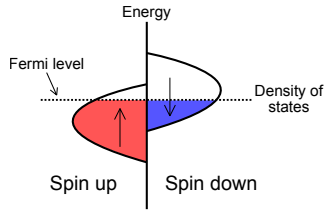

Figure 1.2: Stoner model. From [6].

1.1.5 Spin currents

Definitions

Spin Polarization When an electrical current passes through a magnetic metal, the carriers experience scattering and their spins tend to align in agreement with the available states, which can be spin-split. This explains why a charge current passing through a magnetic material becomes spin polarized.

Spin currents By analogy to the electrical current, one can count the net number of spins up respective to the number of spins down transfered through a device per time units. They are called *spin currents*. In a more general picture, a spin current does not necessarily require a motion of charge carriers.

Spin waves and magnons Spin currents can also be transported via *spin waves*. Spin waves can appear even in insulator materials for which the electrons are bound to their atoms. A local perturbation of a magnetic moment acts at neighboring range via the dipolar or exchange interactions and can influence its closest neighbors. The magnetic perturbation can propagate without charge transport, and carry a spin current. The quantized particles associated to the magnetic wave are called *magnons*. Spin waves are interresting on an applicative perspective because they enable the propagation of magnetic information through insulators. Charge transport in metals causes Joule effect which is responsible for heating and power loss. Spintronics in insulators could lower our energy consumption since pure spin waves (without motion of charge carriers) theoretically produce no Joule heating. Moreover, in metals, spin waves are damped rapidly [7]; spin lifetimes can be longer in insulators. Good magnetically ordered insulators such as yttrium iron garnet (YIG) have shown to propagate spin waves at comparatively large distance (attenuation length: 25µm in YIG) [8, 9].

Free spins By analogy to the free electrons in metals, we will also occasionally talk about *"free spins"*. They are the virtual carriers of the spin current, indifferently from spin polarized charge currents or spin waves; they are not necessarily attached to charge carriers. Contrary to magnons, they do not necessarily imply that they behave in a coherent way, they can scatter, recombine and so on.

Generation of a spin current

To generate a spin current in a material, several approaches are possible. The first approach which has already been discussed consists in spin polarizing the charge carriers of a charge current, for example by passing through a metallic ferromagnet, or as it naturally occurs in the spin-Seebeck effect (an analogous to the Seebeck effect). Another approach consists simply in injecting a spin current from an adjascent layer. The spin currents carry angular momentum, which must be conserved, therefore a spin current can be transmitted to another material without vanishing, if both the material and the interface allow it. A third method consists in generating spin waves, for example by using the ferromagnetic resonance of magnetic materials: a radiated magnetic field produced by an electromagnet is absorbed by the material near its resonance, which can be collected into another material via an interface. Light excitations can also generate magnon modes from inelastic scattering. Coupled orders such as magnetostriction or magneto-electric couplings can also generate propagative magnetic excitations. Finally, we will mention a last method taking advantage of the spin orbit coupling: conversion effects such as spin Hall effect and Rashba-Edelstein effect, which create a spin current transversally to the charge current (details in section 4.1). They are kindred to the first approach since they require the transport of electrons, but the particularity concerning the orthogonality between the charge and spin currents is worth to be mentioned.

Effects of spin currents and spintronics applications

Spin transfer torque A spin current carries a magnetic angular momentum, which can be transfered to its local environment. The local magnetization $\boldsymbol{M}$ experiences a torque [10]:

$$\tau = \frac{2\Delta}{\hbar}\delta\boldsymbol{s} \times \boldsymbol{M} \tag{1.9}$$

Where Δ is an exchange parameter and $\delta\boldsymbol{s}$ the local nonequilibrium spin density. This *spin transfer torque* (STT) could be used for example, to flip a magnetic state to write a bit of information. This will be illustrated in chapter 2.

Anisotropic Magneto-Resistance (AMR) A material can experience a change of electric resistance depending on its magnetization. This effect is called the Anisotropic Magneto-Resistance (AMR), and is one of the many approaches to spintronics reading teachniques.

1.1.6 Examples of applied spintronics

Giant Magneto-Resistance (GMR) The difference of resistance from AMR is enhanced when two adjacent magnetic layers have the same orientation of magnetization or not. This effect, discovered independently in 1988 by Nobel laureates Albert Fert[11] and Peter Grünberg[12], is called the Giant Magneto Resistance (GMR). It is nowadays widely used for its sensitivity in magnetic hard disk drives for reading a memory state. This is also the central brick component of the new magnetoresistive random-access memories (MRAM). A visual picture for the GMR is

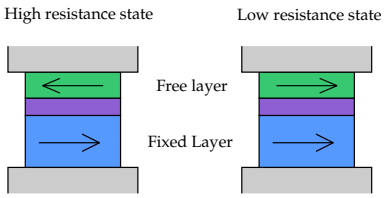

Figure 1.3: GMR concept. When the magnetizations of the two layers are alligned, the electrical resistance is lower than when they are not.

that when a charge current flows through the magnetic staking, the electrons first align their spin to the first magnetic layer, and then have to re-orient in the second layer. If the orientation is the same, they undergo less scattering than if the second magnetic layer has a different orientation.

For making a GMR sensor (a *'spin valve'*), in principle a soft layer which aligns to the external field is stacked on top of a hard magnetic layer (the reference). Usually, a non-magnetic metal is used in between as a spacer, and an antiferromagnetic material is used to pin the hard layer to prevent its alignment to the external field. The voltage of this structure when a currents flows through it gives us the relative orientation of the external field to the hard layer. GMR sensors are a perfect illustration on how a spintronic device can be engineered.

Since the discovery of the GMR effect, the spintronics research community has experienced a significant emulation which has lead to the discovery of other similar effects: tunnel magnetoresistance (TMR), colossal magnetoresistance (CMR), extraordinary magnetoresistance (EMR)...

Memories, magnetic bubbles, skyrmions and domain walls Magnetic data storage has not always been about writing static domains on a magnetic material. Bubble memory technology [13] was promising in the 1980's. Magnetic bubbles were moved along tracks with the application of a magnetic field, without the need for mechanical moving parts. It was finally supplanted by Flash RAM memories in the same decades, because of their better performances. Nowadays the research on the magnetic bubbles continues since new topological objects, protected magnetic solitons called *skyrmions* have been discovered and could be used as the smallest possible movable magnetic domain with a relatively good stability. Skyrmions could be manipulated with ultra low currents, making them competitive for future memory devices [14, 15]. A similar conceptual design called racetrack memory uses magnetic domain walls that can be moved along tracks to store information. This technology, along with others based on the dynamics of domain walls has promizing performances [16].

1.1.7 Conclusion on ferromagnetic spintronics

In this brief overview on spintronics, we have seen that the magnetic degree of freedom induced by the spin of the electrons could be used complementary to their charges, for electronic-like purposes. Through a limited number of examples, we showed that spintronics was already present in our day-to-day life and that this insight already offered open gates for active research, with promising perspectives.

In the next section, we will introduce the notion of antiferromagnetism, and see that antiferromagnetic materials are very promising candidates for future spintronics components.

1.2 Antiferromagnetism

1.2.1 Definition

Antiferromagnetism is defined as the natural tendency in some materials for neighboring spins to align antiparallel. They were first described by Louis Néel as early as 1932 [17, 18], and an experiment confirmed their existence in 1938 [19]. From a mathematical point of view, the Heisenberg Hamiltonian (already introduced in the previous section) can define such a system:

$$\mathscr{H}_{exch\parallel} = \sum_{i,j} J_{ij}\, \boldsymbol{s}_i \cdot \boldsymbol{s}_j \tag{1.10}$$

where J_{ij} is the interatomic exchange interaction between the j^{th} and the i^{th} spin sites and $\boldsymbol{s}_n$ is the unit vector representing the direction of the local magnetic moment on the n^{th} site. The scalar product in the expression tends to align parallel or antiparallel the magnetic moments, depending on the sign of the exchange prefactor J_{ij}. J_{ij} can have a complex expression, and depends in particular on the nature of the atoms at stake as well as the distance separating them. This model is particularly suited for materials in which the electrons that carry the spin are localized, like in ionic solids. In metals where the electrons are delocalized, like pure iron, cobalt or nickel, the *Stoner model* should be used to describe their ferromagnetic nature. This thesis focuses on oxides where the localization criterion applies.

When J_{ij} is negative, like in ferromagnets, spins tend to align to minimize their energies. The combined stray fields over the whole sample causes the macroscopic magnetization we experience in magnets. But when J_{ij} is positive, like in ferrimagnets or antiferromagnets, the spins tend to align antiparallel to minimize their energy. This arrangement results in the screening of the stray field of one sublattice over the other. When an atom is more magnetic than its neighbor, the competition in unbalanced and a macroscopic magnetization leaks, we speak about ferrimagnets. On the contrary, in the case of perfect balance of the sublattices, no net magnetization emerges and the material is known to be an antiferromagnet.

These phases are heavily dependent on the composition of the material, and its temperature. Above a certain temperature, the magnetic order is lost and the material enters a paramagnetic phase. Such a transitional temperature is called *Curie temperature* T_C in the case of ferro- and ferri-magnets, and *Néel temperature* T_N in the case of antiferromagnets.

Likewise, additional external and internal interactions can compete with the antiferromagnetic alignment.

$$\mathcal{H} = \mathcal{H}_{exch} + \mathcal{H}_Z + \mathcal{H}_{anisotropy} + \mathcal{H}_{other} \tag{1.11}$$

In this example, the total Hamiltonian contains a Zeeman term due to an external field, and an anisotropy term due to the internal arrangement of the crystalline structure. In most cases nonetheless, the exchange interaction is stronger than the anisotropy interactions by several orders of magnitude [20, 21], and one needs to apply typically between 1 and 50 Tesla for flopping the magnetic moments via the Zeeman interaction [10, 22, 23, 24]. Under T_N, antiferromagnetism is a robust state.

1.2.2 Ferromagnetism versus antiferromagnetism

The ferromagnetic or antiferromagnetic coupling is determined by the sign of J_{ij} in the exchange interraction (equation (1.10)). There is in general no easy way to assess the value of J_{ij}, and it has to be computed by ab initio calculations adjusted on experimental data. The value of J_{ij} depends both on the elements at stake and on the distance to these elements in the crystal.

Bethe-Slater model

For some elements (Mn, Ni, Co, Fe,... and more), the dependence of J_{ij} with respect to the interatomic distance can be modeled by a *Bethe-Slater curve* of the form [25]:

$$J_{ij}(r_{ij}) = 4a\left(\frac{r_{ij}}{d}\right)^2\left(1 - b\left(\frac{r_{ij}}{d}\right)^2\right)e^{-\left(\frac{r_{ij}}{d}\right)^2} \tag{1.12}$$

Where a,b and d are parameters to adjust according to the material, and r_{ij} is the distance between atom i and atom j. This model shows that for a given material, J_{ij} can take both positive or negative values depending on the distance seperating the neighbors.

Superexchange mechanism

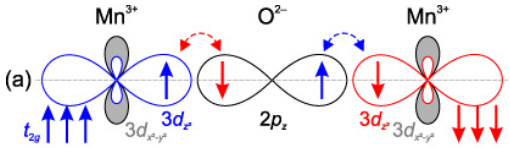

Figure 1.4: Superexchange between half-filled $3d_{z^2}$ orbitals of Mn^{3+} and $2p_z$ orbitals of O^{2-}, leading to an antiferromagnetic coupling at 180° in MnO. Adapted from [26].

Nonetheless, a good rule of thumb to predict antiferromagnetism can be used in oxides, thanks to the so-called *superexchange mechanism*. When two atoms X,Y (especially transition metals) with half-filled orbitals are separated

at 180° by an oxygen atom O, p orbitals associated to the oxygen site favor an anti-alignment of the spins from each side of the oxygen [27] (Figure 1.4). This mechanism explains why so many oxides carrying magnetism are either antiferromagnetic of ferrimagnetic.

TABLE II. Sign of the interaction.

	If internal coupling favors spin of added electron	and exchange coupling of p-electron and other atom is	then coupling is
1	parallel	ferromagnetic	antiferromagnetic
2	parallel	antiferromagnetic	ferromagnetic
3	antiparallel	ferromagnetic	ferromagnetic
4	antiparallel	antiferromagnetic	antiferromagnetic

(a) The sign of the superexchange interraction depends on the filling of the electrons orbitals of each of the two atoms. From [28]

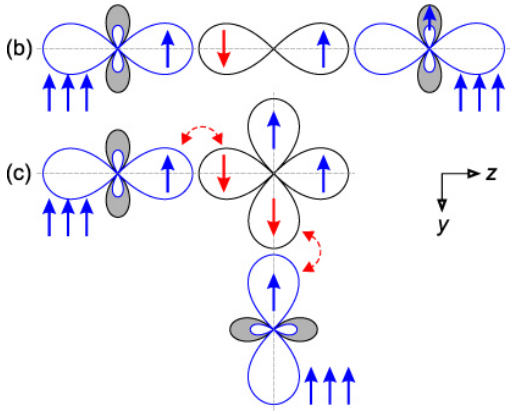

Ferromagnetic superexchange in MnO. Adapted from [26].

Figure 1.5: Other cases of superexchange

The case described above gives the strongest superexchange interaction, but in some cases, superexchange can also favor ferromagnetism (Figure 1.5a). For example, when the orbitals of the X atom are filled, they are favorable to a ferromagnetic allignment of the electron brought by the oxygen. Likewise, oxygen's unfilled p_z orbitals favor ferromagnetism with the other ion's $d_{x^2-y^2}$ unfilled orbitals (Figure 1.5b). Finally, let us mention that when the angle of the X—O—Y bound is not at 180°, the $d_{x^2-y^2}$ orbital of the oxygen favors a weak ferromagnetic superexchange too (Figure 1.5c). The complete description of all cases of superexchange with their respective weights is a bit tedious, but for our concerns, the first interaction that we decribed —and which couples ions at 180° antiferromagentically— is the strongest [28, 27, 26].

Asymmetric Exchange and Dzyaloshinskii-Moriya interaction

More generally, in the case where spins do not allign parallel, we can decompose the exchange interaction into a parallel component and an asymmetric component.

$$\mathcal{H}_{exch} = \sum_{i,j} J_{ij} \left(\boldsymbol{s}_i \cdot \boldsymbol{s}_j \right) + J_{ij\perp} \left(\boldsymbol{s}_i \times \boldsymbol{s}_j \right) \tag{1.13}$$

The second term is commonly referred as Dzyaloshinskii-Moriya interaction (DMI). Asymmetric effects can cause DMI. For example, a spin charged interface, a defect or an intrinsic symmetry breaking in the crystal.

If the value of the Dzyaloshinskii-Moriya interaction is constant on each site, a cycloidal or helical spin texture can form. If the sign alternates from one site to the next, we get a canted antiferromagnet, with a small uncompensated magnetization.

Types of antiferromagnetic arrangements

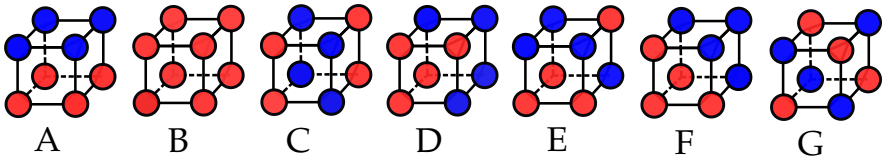

Figure 1.6: Crystallographic magnetic types. Adapted from [29, 30]. The colors correspond to the directions of the spins (up or down along the quantization axis).

Depending on the composition of the crystal, several types of arrangement are possible, with the standard labels shown in Figure 1.6. The A-type has antiferromagnetism along only one axis, leading to an antiferromagnetic stacking of ferromagnetic planes along a crystallographic axis. The B-type structure is the standard ferromagnetic arrangement, with no antiferromagnetism. The C-type structure has antiferromagnetism along two crystallographic axes, leading to a stacking of ferromagnetic planes along the small diagonal. The G-type corresponds to an antiferromagnetic coulping in all three crystallographic directions, leading to a stacking of ferromagnetic planes along the big diagonal.

1.2.3 The Néel vector

The antiparallel allignments of the moment defines two cohabiting ferromagnetic sublattices of opposite direction. Collinear antiferromagnets have no net magnetic moment at mesoscopic scale. To describe the orientation of the magnetic ordering in antiferromagnets, we define the *Néel vector* **L** by subtracting the magnetization of a sublattice ($\boldsymbol{M}_1$) by the magnetization of the other sublattice ($\boldsymbol{M}_2$):

$$\mathbf{L} = \boldsymbol{M}_1 - \boldsymbol{M}_2 \tag{1.14}$$

The numbering of the sublattices is arbitrary. The difference between **L** and $-\mathbf{L}$ is just a matter of convention. When describing the dynamics of the antiferromagnets, **L** appears to be a very convenient quantity. For example, in memory devices, the orientation of **L** could store the bits of information.

1.3 Antiferromagnetic Spintronics

1.3.1 Advantages of antiferromagnets for spintronics

For long, antiferromagnetic materials have been considered as a physical curiosity without possible applications [31]. Their industrial use began when they were discovered to have the capacity of pinning ferromagnetic domains in thin films, making them interesting materials for spintronic devices such as GMR-based sensors.

Even though nowadays antiferromagnets are mainly used as passive layers for pinning ferromagnets, they recently gained interest as potentially interesting active materials in devices such as non-volatile memories [32] or

nano THz oscillators [33, 34] and emitters [35]. Indeed, they could provide us with

- higher storage density,
- robustness against perturbative magnetic fields,
- ultrafast THz dynamics,
- compatibility with insulator spintronics,
- abundance of materials.

Higher storage density: Since antiferromagnets do not produce stray field, the presence of a domain of one type do not destabilize a neighboring domain of another type. Only exchange energy at the domain wall is at stake, no long-range dipolar interaction, and thus limited cross-talks between domains.

Robustness against perturbative magnetic fields: External fields induce Zeeman energy $\mathscr{H}_Z = -\sum_i \boldsymbol{B}\cdot\boldsymbol{s_i}$, and influence ferromagnetic moments to align along them. In the case of antiferromagnets, a sublattice that would align along the field would force the other sublattice to align antiparallel to the field and then gain as much energy as the first sublattice has lost. Alignment to the external field is therefore not so interesting as far as the fields involved cannot compete with exchange or anisotropy energies. That is why in such systems, the *spin-flop field* is often in the range of tens of Tesla [21, 23]. For such strong fields, spins flop into the plane perpendicular to the external field, with a small out-of-plane angle that produce a small uncompensated magnetic moment aligned to the external field. The flop transition is usually quite sharp around the spin-flop field. Below that field, antiferromagnets are quite insensitive to external magnetic perturbations.

Ultrafast THz dynamics For antiferromagnets, one precessing sublattice has to do so in the exchange field of the second. Hence, the magnetic resonance is reported to be in the THz range for NiO and $BiFeO_3$ [20, 36, 34, 35]. As potential applications, this resonance could be used to make terahertz nano-oscillators or transistors for high-speed electronics [33, 37, 34]. Using spin torques, a domain switch at picosecond time scale is predicted, which could provide extremely fast writable memories [1]. Experimental picosecond writing speed in an antiferromagnet-based design have recently been achieved [38].

Compatible with insulator spintronics Like in ferro- and ferrimagnets, in antiferromagnets spin waves can propagate without the need for motion of carriers. Propagation of spin currents through insulating antiferromagnetic oxides has been demonstrated [39, 40]. Since many oxides are both antiferromagnetic and insulating, it opens the gates to a wide range of new materials for spintronics.

Abundant Although among the pure elements of the periodic table, only chromium is antiferromagnetic at ambiant temperature [41], antiferromagnets are very common among transition metal compounds of oxygen or sulfur [31]. Many oxides can indeed favor antiferromagnetic ordering through the *superexchange mechanism* with their

oxygen atoms (see section 1.2.2). In fact, while ferromagnets are mostly metals, antiferromagents can be insulators, metals, semi-metals, semiconductors or even superconductors. They are permitted in all magnetic symmetry groups [42].

Their abundance make them particularly interesting from a material engineering perspective, since a given spintronic effect could be tunned or enhanced by the proper choice of alloys. In research and high-tech industry, people know how to grow epitaxial layers of all sort of oxides, at the interface of which strong effects can arise (spin valves, Rashba-Edelstein effect, etc.).

1.3.2 Antiferromagnetic specificities

As mentioned earlier, antiferromagnets are predicted to offer better performance than ferromagnets in memory applications. Because of their internal magnetic ordering, many of the spintronic effects mentioned earlier have their antiferromagnetic equivalent.

Antiferromagnets in a static magnetic field

When no magnetic field is applied, **L** tends to allign along its easy axis, since each of its two sublattices are favorable to this alignment, regardless of the direction. If a magnetic field is applied perpendicular to the axis of anisotropy of the antiferromagnet, the two sublattices cant slightly towards the field so that a net magnetization appears and aligns with the field. When the magnetic field is applied parallel to the anisotropy axis, no change of orientation is observed until the Zeeman field beats the anisotropy field and a *spin-flop* is observed. **L** aligns perpendicularly to the field and a canting creates the magnetization required to compensate the gain of anisotropy energy and exchange energy by reducing the Zeeman energy. This is known as the spin-flop transition [10].

Spin currents in antiferromagnets

Because of their intrinsinc magnetic ordering, antiferromagnets can host spin currents despite their lack of magnetization. In particular, magnons can travel thanks of the strong exchange between neigbouring atoms, regardless of their antiparallel directions [39]. It was demonstrated that spin currents can travel over more than tens of micrometers in antiferromagnets [40], which is sufficient to imagine nano-devices using them.

AMR

The anisotropic magneto-resistance is also present in antiferromagnets and can be used to read the orientation of **L** [32].

Dynamics, Resonances, Larmor Precession and LLG equation

The dynamics equations of precession apply to each of the two sublattices, coupled by the exchange interraction. The coupled system gives rich behaviour for **L**, and described modes of precessions for an antiferromagnetic reson-

nance [33, 43, 44, 45, 46, 47]. More details will be given in chapter 2.

STT

The spin transfer torque transmits the magnetic angular momentum of the spin current into a net magnetic moment to the antiferromagnetic lattice via each of the two sublattices [10].

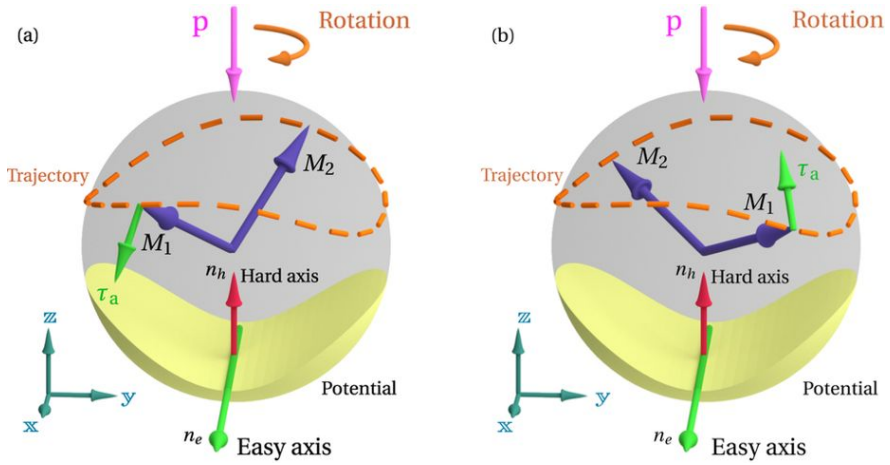

Figure 1.7: Antiferromagnetic precession under the action of a spin transfer torque. A magnetic moment $-\boldsymbol{p}$ transfered perpendicularly to the easy axis induces a torque which makes the moments of the two sublattices ($\boldsymbol{M_1}$ and $\boldsymbol{M_2}$) precess. The anisotropy field produces an extra torque τ_a which modifies the dynamics. From [34].

Interrestingly, the net magnetization can create a canting, and therefore a exchange field which can trigger large precessions [33, 48, 45, 49, 34]. Details about this dynamics will be given in chapter 2. [43, 44, 45, 46, 47]

1.3.3 Antiferromagnetic spintronics proofs of concept

Nowadays many antiferromagnetic spintronics devices are under study [10], and listing them would lead us too far. To illustrate this thesis, we will focus only on two illustrative cases. The first one is a realization of an antiferromagnetic memory, and the second one is a predictive ultrafast antiferromagnetic domain switch.

Antiferromagnetic based memory device

A proof of concept of an antiferromagnetic memory has been realized by Reference [32]. The antiferromagnet is CuMnAs, and a reproducible memory switch can be done by applying an electrical current (Figure 1.8). In this crystal, applying a current generating a staggered internal field, resulting in a spin-orbit torque whose sign alternates with the periodicity of the antiferromagnetic lattice. A current of 10^6A/cm^2 is sufficient to induce a switch. The memory bits can be written by applying the current in a direction or its perpendicular. They are then read with another set of electrodes by measuring the resistance, which changes according to the memory state due to the AMR effect.

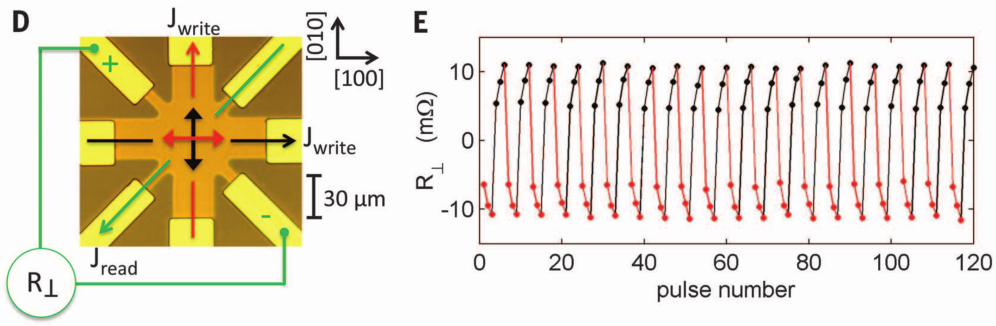

Figure 1.8: Antiferromagnetic memory device by [32].

Ultrafast antiferromagnetic switch

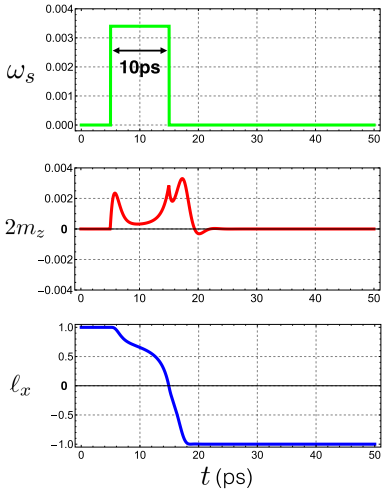

Figure 1.9: Picosecond switch in NiO induced by STT. From [33]. **Top:** Duration of the STT equivalent to a charge density of $6-7\times10^7$A/cm^2 along z during 10ps. **Middle:** Time evolution of the magnetization along z. **Bottom:** Time evolution of the Neel vector along x.

Not only are memories based on antiferromagnets possible, they could be extreamely fast. As an illustration, Reference [33] predicts a possible switch of the Néel vector under 15ps in NiO (Figure 1.9). The Néel vector is supposed initially aligned along its easy axis x. A STT equivalent to a charge density of $6-7\times10^7$A/cm^2 is applied along the hard axis z during 10ps and results in the 180° rotation of the Néel vector in the z plane, in less than 15ps.

1.4 Conclusion

In this chapter, we have seen that the field of spintronics has numerous tools for manipulating (antiferro-)magnetic domains and spin currents, which can be used jointly with electronics for devices designs. Antiferromagnetic based spintronics would bring a consequent set of advantages, in particular concerning memory devices and nano-oscillators.

Antiferromagnetic spintronics is a rather recent field of research, so many fundamental behaviors are yet to be

explored before active antiferromagnetic devices can be deployed at the industrial scale. In particular, the dynamics of antiferromagnets for domain switches is theoretized but not experimentally mastered in its full extent, mainly because antiferromagnetism is a subtle order which challenges the conventional magnetometry techniques.

In the next chapters, we will address these challenges by studying antiferromagnets both from a simulation side, and from and experimental approach. We will focus on the dynamical aspect of antiferromagnetism.

Chapter 2

Atomistic Spin Simulation of Antiferromagnetic Systems

2.1 State of the Art and Motivations for a Dynamic Model

Several approaches are possible to simulate the behavior of antiferromagnets. Minimization of the energy and Monte Carlo simulations are often used [50], but very few large scale dynamical solvers are used because of the difficulty they have to deal with a nanoscale amount of particles. Yet, dynamical models have the advantage of predicting in real space the evolution of magnetic structures under stimuli. In the perspective of improving the current data storage devices, micromagnetic solvers are extensively used for ferromagnets. They can predict the formation and the motion under stimulus of domain walls, magnetic bubbles or skyrmions in a data channel. The stimuli can be magnetic fields, electric currents as well as laser pulses. They are used either for studying in detail the dynamics of an experimental observation or to theoretically predict a behavior in a particular geometry. For instance, it is observed that skyrmion trajectory is not straight, and that domain walls can experience merging or pinning in non-rectilinear channels. Dynamic solvers can also be used for studying the dynamics of the oscillation of magnetic vortices. They are of particular interest in microwave signal-processing applications and could even constitute elemental bricks for building artificial neural networks. Dynamical micromagnetic solvers are therefore well established (Mumax3 [51] and OOMMF [52] for example), and are scalable to all kinds of problems. With antiferromagnets, two main issues arise:

- antiferromagnets have opposite direction of spin for each neighbouring site, making the micromagnetic approximation unrealizable (scalability problem);
- antiferromagnets present negligible long-range stray fields.

The second point is an advantage, because it allows us to neglect the dipolar interaction at long range, which is one of the big challenges in micromagnetic simulations. On the contrary, the first point is a major challenge because the fact that each atom carries an opposite moment prevents us from averaging on a mesoscopic area; we need to

deal with individual atoms. This can be computationally costly, even for nanoscale devices, and could lead to the need of advanced quantum treatment. A discussion on this point is carried out in section 2.2.3.

In the mean time, dynamic studies are starting to be a hot topic in antiferromagnetic spintronics. Reference [53] set the basis for antiferromagnetic dynamics. Since then, it has been predicted that spin torques could act constructively on both sublattices and act at THz speed. [34, 33]. As an illustration, with a simple model, Reference [1] predicted that a 10ps pulse could trigger a 180° antiferromagnetic domain switch in NiO in less that 15ps. This exciting prediction would benefit from being pushed forward, namely, by considering in details the actual feasibility of this switch in real conditions with available pulses. Besides, it was pointed out by Reference [34] that the anisotropy profile of the antiferromagnet plays an important role in the acceleration dynamics. The physical values of anisotropy of NiO are well known and building a full anisotropy model can be done [20, 54].

Spintronics related works focus on the creation and manipulation of protected magnetic structures for data storage, while theoretical and dynamical studies predict a very fast response in antiferromagnets. Dynamical solvers represent the best option to conciliate both, and study the ultrafast response of the antiferromagnetic structures in real space. To dynamically simulate antiferromagnets in real space, a common approach is to use micromagnetic simulation on each of the two sublattices, but the exchange interaction needs a special treatment, and the dipolar field must be subtracted before moving the spins. Another natural approach is to deal directly with individual spins, without micromagnetic approximation, based on the theory of Reference [53]. Often, these studies are analytical or limited to a restricted number of spins. In fact, antiferromagnetic dynamics is mostly modeled using a set of two spins, assuming the repetition of the set in a domain. But under some conditions, notably Dzyaloshinskii-Moriya interaction, incommensurate orders can appear. For example, a cycloid of period 64nm is observed in $BiFeO_3$ [55] because of the magnetoelectric coupling. The magnetic ordering of $BiFeO_3$ in an anharmonic cycloidal structure with spin density wave has been simulated [56], and its parameters are well known. Most simulations on $BiFeO_3$ concern its static structure — which is sufficiently rich for having led to hundreds of publications —, but rarely the motion of its domains motion for example.

In this chapter, we first describe the dynamic model we use for our simulations. Then, we present two separate studies: the first one concerns the dynamics in NiO, for which we envision the possibility of a spin torque driven domain switch via an ultrashort laser excitation, based on a realistic model for the magnetic anisotropy. We characterize the requirements for the pulse to induce a switch and confront it to available technology. The second study is static. It focuses on the multiferroic $BiFeO_3$, and in particular on the effects of its magnetoelectric interactions on the possibility to create multiferroic structures (e.g. for data storage). It sets the stage for possible future dynamical studies.

2.2 LLG Model and Range

2.2.1 Landau Lifshitz Gilbert (LLG) equation

When a magnetic moment $\boldsymbol{\mu}$ is in the presence of a magnetic field $\boldsymbol{B}$, it experiences a torque $\boldsymbol{\mu} \times \boldsymbol{B}$ which leads to a precession around the $\boldsymbol{B}$ field. This is the *Larmor precession*. Without additional torque, the magnetic moment precesses with angular velocity $\boldsymbol{\omega}_{Larmor} = -\gamma \boldsymbol{B}$, known as *Larmor frequency*, where γ is defined as the *gyromagnetic ratio* which links the magnetic moment to the angular momentum ($\boldsymbol{\mu} = -\gamma \mathbf{L}$). In physical systems, damping effects cause the precession to eventually spiral down towards the direction of $\boldsymbol{B}$. The same behavior holds for micromagnetic domains in solids. Each localized moment $\boldsymbol{\mu}$ follows the Landau-Lifshitz Gilbert equation:

$$\frac{\mathrm{d}\boldsymbol{\mu}}{\mathrm{d}t} = \gamma \mu_0 \boldsymbol{H}_\Sigma \times \boldsymbol{\mu} - \alpha_s \frac{\mathrm{d}\boldsymbol{\mu}}{\mathrm{d}t} \times \boldsymbol{\mu} \tag{2.1}$$

In accordance with Larmor precession, the first term traduces the torque exerted by $\boldsymbol{H}_\Sigma$, the sum of all the local magnetic fields (γ is the gyromagnetic ratio and μ_0 the vacuum permeability). The second term is a transverse damping term introduced in this form by Gilbert to account for losses that eventually leads to the alignment of the magnetic moment $\boldsymbol{\mu}$ with the field. In the micromagnetic approximation, we consider $\boldsymbol{\mu} = \mu_s \hat{\boldsymbol{s}}$ with $\hat{\boldsymbol{s}}$ unitary and μ_s constant. For antiferromagnets, this is true at the atomic scale. We can then normalize by μ_s and define $\alpha = \alpha_s \mu_s$:

$$\frac{\mathrm{d}\hat{\boldsymbol{s}}}{\mathrm{d}t} = \boldsymbol{\omega}_\Sigma \times \hat{\boldsymbol{s}} - \alpha \frac{\mathrm{d}\hat{\boldsymbol{s}}}{\mathrm{d}t} \times \hat{\boldsymbol{s}} \tag{2.2}$$

Under this form, α is a dimensionless constant intrinsic to the material (and the material's quality). In solids, the origins of losses are various: the angular momentum can be transfered to the lattice via spin-orbit coupling, to induction electrons (in metals), to defects, to magnon sinks,... Typically, $1 \times 10^{-5} \leq \alpha \leq 1$. Mathematically, the damping term under this form introduces an unpleasant coupling between the right hand side and the left hand side via the differential term. By replacing the differential element in the damping term by the right hand side of the equation, and using basic geometry on unit vectors, equation (2.2) can be rewritten in the equivalent resolved form:

$$\frac{\mathrm{d}\hat{\boldsymbol{s}}}{\mathrm{d}t} = \boldsymbol{\omega}_{eff} \times \hat{\boldsymbol{s}} \tag{2.3}$$

$$\boldsymbol{\omega}_{eff} = \frac{1}{1+\alpha^2} \left(\boldsymbol{\omega}_\Sigma - \alpha \boldsymbol{\omega}_\Sigma \times \hat{\boldsymbol{s}} \right) \tag{2.4}$$

We are set back to a simple precession equation about an effective damped field $\boldsymbol{\omega}_{eff} / \left(\gamma \mu_0\right)$. The variable $\boldsymbol{\omega}_\Sigma = \gamma \mu_0 \boldsymbol{H}_\Sigma$ accounts for all the contributions to the precession.

In this thesis, we will apply this equation of motion for each moment carrier in antiferromagnets. The validity of this approach is discussed in section 2.2.3. Typically, we will consider a magnetic atom subject to the Zeeman

field, the exchange field, the anisotropy field, the Dzyaloshinskii-Moriya interaction and a spin transfer torque:

$$\boldsymbol{\omega_\Sigma} = \boldsymbol{\omega_{Ze}} + \boldsymbol{\omega_E} + \boldsymbol{\omega_K} + \boldsymbol{\omega_D} + \hat{\boldsymbol{s}} \times \boldsymbol{\omega_\tau} \tag{2.5}$$

Zeeman field

The Zeeman contribution is the most natural one: an external magnetic field $\boldsymbol{H}_{external}$ forces a magnetic moment to precess around it. If any external magnetic field is applied, we simply have:

$$\boldsymbol{\omega_{Ze}} = \left(\mu_0 \gamma\right) \boldsymbol{H}_{external} \tag{2.6}$$

Exchange field

The exchange field is a simplification of the influence exchange orbitals from the surrounding atoms have on a given spin. Rather than dealing with overlap integrals, it is a fair approximation to see the exchange as a local magnetic field. The exchange field $\boldsymbol{\omega_E} / \left(\mu_0 \gamma\right)$ is computed using the Heisenberg model on the surrounding neighbors (typically, first only or first and second neighbors).

$$\boldsymbol{\omega_E} = \sum_j J_{n_j} \hat{\boldsymbol{s}}_{n_j} \tag{2.7}$$

J_{n_j} stands for the exchange value with the neighbor n_j, whose spin is noted $\hat{\boldsymbol{s}}_{n_j}$.

Anisotropy field

Anisotropy can in general be separated into two types: *shape anisotropy* and *magneto-crystalline anisotropy*. The shape anisotropy is only really present in ferro- or ferri-magnetic materials because its origin comes from the stray field. When a magnetic object has a large dimension in one direction, spins will tend to align in this direction because they will feel the field at long range of the other atoms. In the case of antiferromagnets, because the stray field in negligible, no shape anisotropy is to be considered. Nonetheless, an anisotropy can arise at very small dimensions, in thin films for example due to interfacial interactions with the substrate. In that case, we can talk about *surface anisotropy*. Likewise, the magneto-crystalline anisotropy can be strong in magnetically ordered solids, even antiferromagnets. In crystals, due to the spatial arrangement of the neighboring atoms, orbitals overlap more or less with certain neighbors, and can favor a bonding over an other, resulting in a preferential direction for the spins. Often, one axis is beneficial or not for the spin alignment. We call it uniaxial anisotropy. Sometimes, all the cubic axes are favorable (or not), this is the cubic anisotropy. Uniaxial, cubic, or more exotic anisotropies are contained in $\boldsymbol{\omega_K}$.

- An uniaxial anisotropy reads

$$\boldsymbol{\omega_{K_{1u}}} = K_{1u} \left(\hat{\boldsymbol{s}} \cdot \boldsymbol{a}\right) \tag{2.8}$$

where $\boldsymbol{a}$ is the anisotropy axis direction. The axis can be easy (favorable for the spins to align along) or hard,

depending on the sign of K_{1u}. The latter case favors a spin alignment in the easy plane perpendicular to the axis.

- A cubic anisotropy can read:

$$\boldsymbol{\omega}_{\boldsymbol{K_c}} = K_c \begin{pmatrix} \alpha(\beta^2+\gamma^2) \\ \beta(\alpha^2+\gamma^2) \\ \gamma(\beta^2+\alpha^2) \end{pmatrix} + K_d \begin{pmatrix} \alpha(\beta^2\gamma^2) \\ \beta(\alpha^2\gamma^2) \\ \gamma(\beta^2\alpha^2) \end{pmatrix} \tag{2.9}$$

where α, β and γ are the spin components along the cubic axis. Depending on the signs of K_c and K_d, the spins may favor an orientation along the cubic axes or not, along the cubic planes or not. K_d is generally taken as a higher order correction of K_c. Cubic anisotropy expressions can adapt to the distortions of the crystal.

Dzyaloshinskii-Moriya interaction

As presented in section 1.2.2, an antisymmetric exchange can exist. It is possible to express it in a field form. If we note $\boldsymbol{D}$ the vector pointing perpendicular to the canting induced by Dzyaloshinskii-Moriya interaction, with a norm equal to the amplitude of the canting in units of frequency, we have:

$$\boldsymbol{\omega}_{\boldsymbol{D}} = \sum_i s_j \times \boldsymbol{D} \tag{2.10}$$

Spin Transfer Torques

Spin transfer torques can be of various origins, and can be entered in $\boldsymbol{\omega}_{\boldsymbol{\tau}}$. In general, when a spin current is transfered to an antiferromagnet, conservation of the angular momentum produces a canting of the spins in the lattice. This canting is detrimental to the exchange interaction. Consequently, a precession around the exchange field occurs [48]. Everything happens as if a torque was produced by a spin transfer. In ferromagnets, a spin transfer tilts all the spins in the same direction without drastic canting.

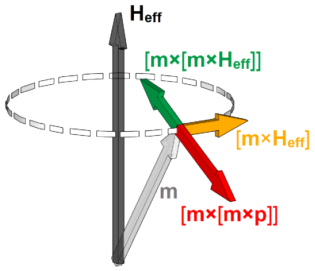

Figure 2.1: Field-like torques and damping-like torques. From [57]. Field-like torque (yellow) are responsible for the precession. Positive damping (green) reduces the angle to the field and negative damping (red) increases it.

Spin torques can be separated into two types: a *field-like* torque, parallel to the precession and a *damping-like* torque, perpendicular to it (Figure 2.1) [58]. The field-like torque acts like an external Zeeman field and can induce precession in ferromagnets. The damping-like torque can act as a 'positive damping' and maintain magnetic

oscillations. They can be written [10, 58]:

$$\boldsymbol{\tau} = \tau_{\parallel} \underbrace{\hat{\boldsymbol{s}} \times \left(\boldsymbol{p} \times \hat{\boldsymbol{s}}\right)}_{\text{Damping-like}} + \tau_{\perp} \underbrace{\hat{\boldsymbol{s}} \times \boldsymbol{p}}_{\text{Field-like}} \tag{2.11}$$

Where $\boldsymbol{p}$ is a vector related to the symmetry of the system, and $\tau_{\parallel}$, $\tau_{\perp}$ the projected contributions of the torque. In the rest or our studies, we mostly use the damping-like STT, which acts constructively on both sublattices while the field-like torque has often little effect on antiferromagnets, due to their antiparallel alignment (field-like torques are inefficient when aligned with **L**, and mostly hindered by the anisotropy field otherwise).

Suppose we inject a spin current density $\boldsymbol{j_s}$ perpendicular to the interface of a thin film of surface S and thickness l of a material with lattice parameter a. The current is transfered to an amount of spins N in the material of surface S, with an efficiency G (the spin transparency at the interface). Per cell unit, $S = a^2$. If the film is sufficiently thin, all unit cells in the depth receive approximately the same amount of current, that they share into N_l spins per unit of surface. In this case, $N_l \simeq= \frac{a}{l n_s}$, with n_s the number of magnetic spin per unit cell. Per unit cell, the damping-like spin transfer torque will be:

$$\boldsymbol{\omega_\tau} = GN\boldsymbol{j_s} \tag{2.12}$$

$$= GN_l S\boldsymbol{j_s} \tag{2.13}$$

$$\simeq G\frac{a}{l n_s}a^2\boldsymbol{j_s} \tag{2.14}$$

$$\simeq G\frac{a^3}{l n_s}\boldsymbol{j_s} \tag{2.15}$$

We illustrate a practical case in section 2.3.

2.2.2 Code implementation

Now that the equation of motion has a simple form, it can be discretized and solved numerically for each time step. Let's start with a simple approach of numerical resolutions, and suppose we have the following differential equation:

$$\frac{\mathrm{d}\boldsymbol{x}}{\mathrm{d}t}(t) = f(\boldsymbol{x}, t) \tag{2.16}$$

Let us suppose that we know our system at a time t, and we would like to deduce its state at time $t + \Delta t$. We can approach this forthcoming state $\boldsymbol{x}(t + \Delta t)$ with a Taylor expansion:

$$\boldsymbol{x}(t + \Delta t) = \boldsymbol{x}(t) + \Delta t\frac{\mathrm{d}\boldsymbol{x}}{\mathrm{d}t}(t) + \mathcal{O}(\Delta t^2) \tag{2.17}$$

Using the equation of motion 2.16, we get:

$$\boldsymbol{x}(t+\Delta t) = \boldsymbol{x}(t) + \Delta t\, f(\boldsymbol{x}, t) + \mathcal{O}(\Delta t^2) \tag{2.18}$$

The right hand side depends only on state values at t. Therefore, the time evolution of $\boldsymbol{x}$ can be easily approached, step by step, by an iterative algorithm. Note that at each time step Δt, an error in $\mathcal{O}(\Delta t^2)$ is accumulating. If not done carefully, the computation can diverge from the real trajectory. A way to avoid this is to ensure an energy conservation law at each time step, and that Δt is small enough. In LAMMPS, a similar symplectic integration is done at each timestep up to $\mathcal{O}(\Delta t^3)$ precision [59]:

$$\boldsymbol{s}_{t+\Delta t} = \frac{\boldsymbol{s}_t + \Delta t\left(\boldsymbol{\omega}_{eff} \times \boldsymbol{s}_t\right) + \frac{1}{4}(\Delta t)^2\left(2\left(\boldsymbol{\omega}_{eff} \cdot \boldsymbol{s}_t\right)\boldsymbol{\omega}_{eff} - \boldsymbol{\omega}_{eff}^2 \boldsymbol{s}_t\right)}{1 + \frac{1}{4}(\Delta t)^2 \boldsymbol{\omega}_{eff}^2} + \mathcal{O}(\Delta t^3) \tag{2.19}$$

The LLG equation at first order can be recognized in the first two terms. The rest and the prefactor guarantee a certain stability by making sure the norm of $\boldsymbol{s}$ is preserved over time [59, 60]. For optimal results, the time-step must be chosen much smaller than the inverse of the frequency $\boldsymbol{\omega}_{eff}$. In our case, the exchange energy being orders of magnitude larger than the other energies involved, we need in particular $\Delta t \ll \frac{2\pi}{|\boldsymbol{\omega}_E|}$.

This is the basic core of our dynamic solver. For more details, refer to Reference [59]. We see that with this approach, the evolution of a system can be followed along its trajectory from initial time to final time. This is of particular interest in our case for studying the dynamics underlying a domain switch, domain wall motions, soliton propagations, relaxation to equilibrium after an excitation,... and so on.

2.2.3 Range of validity: Quantum equivalent

Since we deal with individual spins, we need to be careful of their quantum nature before converting them to classical magnetic moments. The first question that can arise concerns the norm of the spins. Spin $\frac{1}{2}$ particles have a norm for their spin equal to $S = \frac{\sqrt{3}}{2}\hbar$, and a projection $S_z = \pm\frac{1}{2}\hbar$ along an quantization z axis. Which value is it reasonable to take for their magnetic moment? Secondly, does the LLG equation 2.2 still hold at such atomic scale? As for the first question, the answer is that one should take the projected value, since this is always the value we measure in real experiments. For iron atoms, the norm of the spin in our simulations will be $\pm\frac{5}{2}\hbar$, for nickel, $\pm\frac{3}{2}\hbar$. The validity of the LLG equation (2.2) for individual atoms is a quite established basis among theoreticians [53, 48, 1]. As a justification, the LLG equation seen from a quantum point of view, based on quantum Larmor precession is developed in Appendix B for the curious reader, and gives also justification to the first question.

2.3 Simulation of an Antiferromagnetic Domain Switch in NiO

In this section, we will present some predictions of domain switching in NiO based on the presented computation method, on a code initially developed by CEA Le Ripault [61, 25, 62, 63], that I helped debugging. The goal is to quantify the spin current necessary to induce an antiferromagnetic domain switch by spin transfer torque (STT) in a NiO crystal. Such a switch has been attempted experimentally using spin injection via electric currents [64],

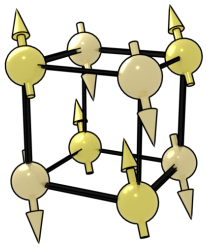

Figure 2.2: In a G-type antiferromagnetic crystal, atoms couple antiferromagnetically to all their main axis neighbours, forming a stacking of ferromagnetic sheets in the ⟨111⟩ directions.

while theoretical predictions and experimental excitation reveals an ultrafast dynamics in NiO excited optically [65, 66, 67].

In this section, we first present the crystallography of NiO, including its magnetic anisotropy to justify the model we use, and its dynamic response to small perturbations. Then we present the mechanism of STT for inducing a switch. Finally, we present our predictions concerning the necessary spin pulse to reversibly switching in NiO, and we discuss its feasibility.

2.3.1 Crystallographic model of NiO

Among the common oxides presenting antiferromagnetism, NiO is a typical case. At room temperature, it crystallizes in a NaCl structure. Ni^{2+} ions carry the strongest magnetic moment. Due to superexchange with oxygens, Ni^{2+} is antiferromagnetic of G type, meaning it has a type II fcc structure with ferromagnetic sheets of spins in (111) planes antiferromagnetically stacked along the ⟨111⟩ directions [20] (See Figure 2.2). Its Néel temperature is 525K, which is the highest among the transition metal monoxides [68].

As we can see from its NaCl structure (Figure 2.3), Ni^{2+} ions share 180° oxygen superexchange only to their second neighbors, while their first neighboring Ni^{2+} share only 90° oxygen superexchange. As 180° oxygen superexchange strongly favors antiferromagnetism, while 90° oxygen superexchange is weakly ferromagnetic, second neighbors are always carrying antiferromagnetically coupled spins, while first neighbors can be either parallel or antiparallel, so that the ferromagnetic layers are stacked along [111]. All in all, the oxygens are generating four G-type antiferromagnetic sublattices inside the NiO crystal. For the sake of clarity, we will focus on only one of the four equivalent sublattices in the rest of this thesis, and assume that the three other sublattices behave so that the [111] ferromagnetic stacking is always respected.

NiO is magnetostrictive. Its cubic lattice is slightly deformed along the [111] diagonal, thus becoming trigonal. This leads to a strong planar magnetic anisotropy in the (111) easy plane [69, 70]. In this easy (111) plane, three magnetic axes at 120° from one another are favored: $\pm[11\bar{2}]$, $\pm[\bar{2}11]$ and $\pm[1\bar{2}1]$, with an anisotropy strength $\simeq 20$ times weaker ($\hbar K_{hard} = 100 \pm 10 \mu eV$ and $\hbar K_{easy} = 5 \pm 4 \mu eV$) [20, 71, 70]. In between, separated by 30°, $\pm[1\bar{1}0]$, $\pm[01\bar{1}]$ and $\pm[\bar{1}01]$ are the hard axes of the (111) easy plane. These values have been confirmed by observation of beating patterns in time-resolved second harmonic generation experiments [72, 73].

A mathematical way to model this anisotropy is to superimpose a cubic anisotropy K_c with a hard axis anisotropy

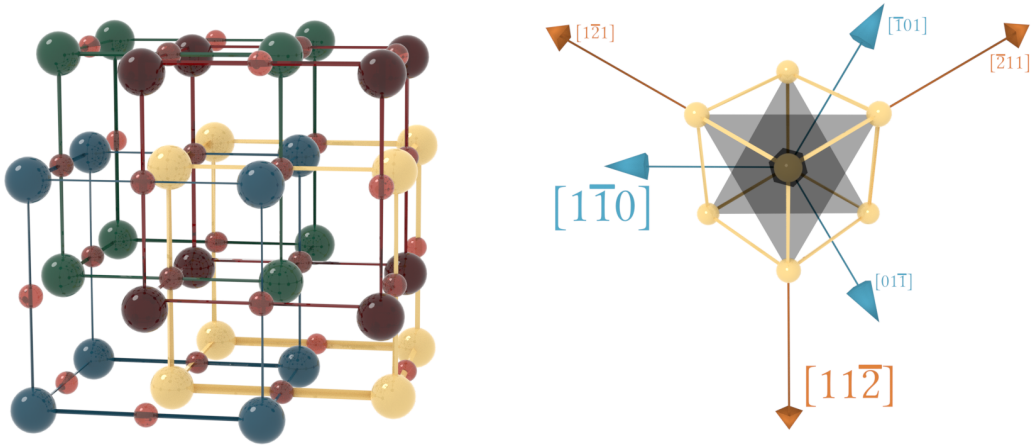

Figure 2.3: **Left:** NiO crystalline structure reveals 4 similar Ni^{2+} sublattices coupled by 90° oxygen superexchange. **Right:** Easy and hard axes in the (111) plane.

K_{1u} along the long diagonal, reflecting the geometrical contraction which naturally occurs in this direction. In units of frequency, it reads:

$$\boldsymbol{\omega_K} = K_{1u}\,(\hat{\boldsymbol{s}}\cdot\boldsymbol{a})\,\boldsymbol{a} + K_c \begin{pmatrix} \hat{s}_{100}(\hat{s}^2_{010}+\hat{s}^2_{001}) \\ \hat{s}_{010}(\hat{s}^2_{100}+\hat{s}^2_{001}) \\ \hat{s}_{001}(\hat{s}^2_{010}+\hat{s}^2_{100}) \end{pmatrix} \tag{2.20}$$

So that, introducing the Landé g-factor, the gyromagnetic ratio γ, the Bohr magneton μ_B and the reduced Planck constant $\hbar$, the energy of anisotropy per electronic spin is:

$$E_K = -\frac{g\mu_B}{\gamma}\,\hat{\boldsymbol{s}}\cdot\boldsymbol{\omega_K} = -\hbar\left(K_{1u}\,(\boldsymbol{s}\cdot\boldsymbol{a})^2 + 2K_c\left(\hat{s}^2_{100}\hat{s}^2_{010}+\hat{s}^2_{010}\hat{s}^2_{001}+\hat{s}^2_{001}\hat{s}^2_{100}\right)\right) \tag{2.21}$$

With this model, the spins do not lie in exactly in the (111) plane, but for ratios sufficiently high of $\frac{K_{1u}}{K_c}$, the out-of-plane angle is very small. Reference [70] also reports a slight out-of-(111) plane equilibrium position.

2.3.2 Dynamical parameters for NiO

Starting from our crystallographic model, we need to find the good parameter values to reproduce accurate dynamics.

Exchange and anisotropy values for NiO have been measured by neutron diffraction [20]. Besides, antiferromagnetic resonance measurements have shown a clear resonance at 1THz [35, 74], confirmed by measurements done by members of our group (Figure 2.4), corresponding to the hard axis anisotropy. Additionnaly, a moderate resonance around 0.2THz is reported by some authors, and corresponds to the in-plane anisotropy [54, 75, 1, 76]. As noted in pagenote 19 of [1], the observed frequency can vary of tens of gigahertz depending on the value of the Gilbert damping α (generally ranking between 0.005 and 0.01). For an axial anisotropy ω_a, the observed frequency is $\sqrt{2\omega_a\omega_E - \alpha^2\omega_E^2}$. For our study, we set it at 0.2THz, and $\alpha = 0.005$.

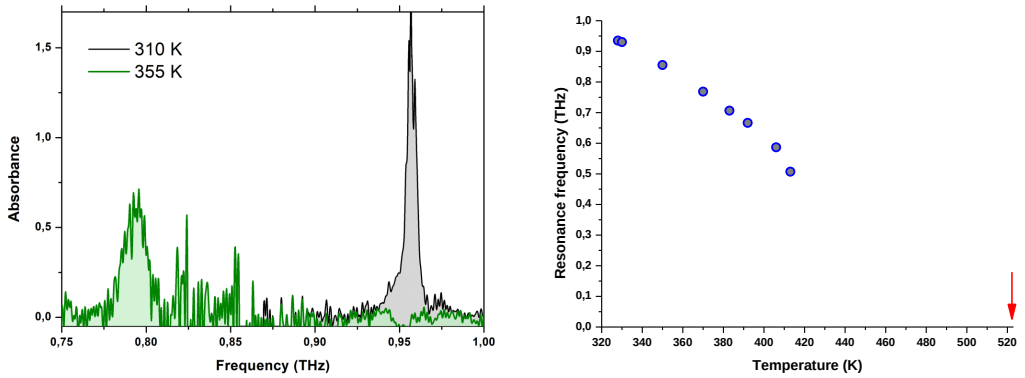

Figure 2.4: Evolution of the antiferromagnetic resonnance in NiO with respect to the temperature. From absorbtion measurements on NiO bulk at synchrotron SOLEIL. A resonnance at 1THz at ambiant temerature is clearly visible, which drifts and broadens towards lower frequencies for higher temperatures, well before the Néel temperature (red arrow).

Starting from our model presented in equation (2.5), we define the interaction fields as follows:

Zeeman field No Zeeman field is applied. $\boldsymbol{\omega_{Ze}}$ is set to zero.

Exchange field The exchange field $\boldsymbol{\omega_E}/\left(\mu_0\gamma\right)$ is computed using Heisenberg model on the first six neighbors of the superexchange lattice (nnn), with $J_{\text{nnn}} = -19\text{meV}/(2\pi\hbar) = -4.6\text{THz}$, so that $6J_{\text{nnn}} = -27.4\text{THz}$. [20, 1, 54, 34].

$$\boldsymbol{\omega_E} = \sum_{j=1}^{6} J_{\text{nnn}} \hat{\mathbf{s}}_{\text{nnn}_j} \tag{2.22}$$

Anisotropy field Our model of anisotropy for NiO is given in equation 2.20. To find the parameters in accordance to the resonances, we started from a near equilibrium state, let it relax and measured the period of the oscillations. α was taken equal to 2.1×10^{-4} to match reference [35]. With this method, K_c could be adjusted so that an out-of plane motion gives a peak at 1THz in frequency, while K_{1u} was simultaneously adjusted so that the in-plane motion had a mode around 0.2THz (Figure 2.5).

We find $\hbar K_{1u} = -8 \times 10^{-5} eV$ and $\hbar K_c = -2 \times 10^{-5} eV$. The equivalent energies when projected on hard [111] and easy $[11\bar{2}]$ axes are $-9.33 \times 10^{-5} eV$ and $-1.0 \times 10^{-5} eV$ respectively, which is consistent with the values of $-9.72 \times 10^{-5} eV$ and $0.5 \times 10^{-5} eV$ measured by References [20, 77]. With these values, the equilibrium directions are close to the $\langle 11\bar{2} \rangle$ directions, with a slight out-of-(111)plane component of about 4° (Figure 2.5).

Spin torque Let $\boldsymbol{\omega_\tau}$ be the damping-like spin transfer torque, G the spin transparency at the interface, a the lattice constant and n_s the number of magnetic atoms per unit cell. From a spin current $\boldsymbol{j_s}$ injected at the interface of a

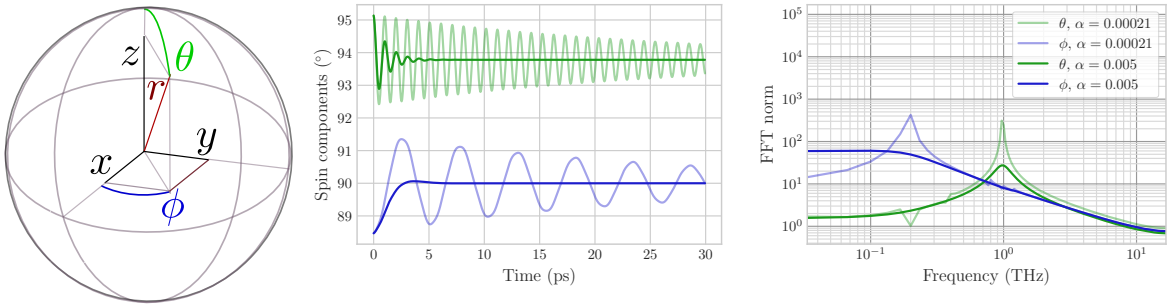

Figure 2.5: Spin relaxation and resonnances in NiO. **Left:** Coordinate system in the anisotropy basis. $x = [1\bar{1}0]$, $y = [11\bar{2}]$, $z = [111]$. **Middle:** Temporal evolution of the spin angle during the relaxation for two values of α. **Right:** FFT of the corresponding time evolutions. A higher α smoothes the resonnance.

thin film of thickness l, as explained in section 2.2.1, we can expect:

$$\boldsymbol{\omega_\tau} \simeq \frac{G}{l}\frac{a^3}{n_s}\boldsymbol{j_s} \tag{2.23}$$

Where $\boldsymbol{\omega_\tau}$ has the dimension of a frequency and $\boldsymbol{j_s}$ is expressed in $electron.s^{-1}.m^{-2}$. For a thin layer of fcc NiO, we take:

$$a = 4.177\text{Å} \qquad n_s = 4 \tag{2.24}$$

$$l = 5nm \qquad G = 0.1\ electron^{-1} \tag{2.25}$$

In all this chapter, simulated frequencies ω_τ will be converted into spin currents using these values with equation (2.23).

Now that our model is set, we will present in the next parts how a spin current can trigger an ultrafast switch of antiferromagnetic domain orientation in NiO.

2.3.3 Mechanism used for switching

Depending on the orientation and strength of the STT with respect to the anisotropies and spin directions, different behaviors can occur.

For illustrative purposes, in this section let us focus on two spins $(\boldsymbol{s_1}, \boldsymbol{s_2})$ antiferromagnetically coupled with an exchange energy $\omega_E\hbar = 6 \times J_{nnn}\hbar = 27.4\text{THz}(2\pi\hbar)$, in a simple easy axis anisotropy of energy $\omega_a\hbar = 1\text{GHz}(2\pi\hbar)$ (instead of the full anisotropy model), and with damping $\alpha = 0.005$. Let us initialize our state with a small canting of the the spins in a given direction perpendicular to their easy axis, and let us monitor their dynamics while they relax to their equilibrium position. The net magnetization of the system produces an initial torque via the exchange interaction that drives the dynamics (Figure 2.6), until the damping annihilates completely the extra magnetic moment. With our parameters, we find that above a canting of about 1.5°, the initial extra energy given to the system is sufficient to overcome the anisotropy and make the two spins swap orientations.

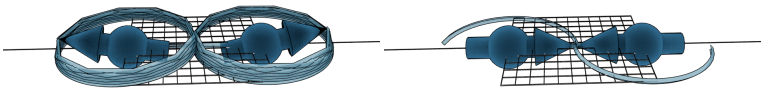

Figure 2.6: A small canting triggers precession around the net magnetization axis. **Left:** initial canting of 25° with its induced precession. **Right:** initial canting of 1.5° resulting in an orientation swap.

A similar situation can be triggered by the effect of a spin current injected into the antiferromagnet in virtue of equation (2.5). Indeed, it has been shown by Reference [1] that when a STT is applied perpendicularly to the easy axis, the equation of precession can be compared to that of a rigid damped pendulum subject to gravity and a driving force, where the STT plays the role of the driving force, the anisotropy that of the gravity and α the fluid damping. When the STT is too weak, the torque is quickly compensated by damping and the spins find an equilibrium position along their effective field, off from the easy anisotropy axis with an angle given by the magnitude of the STT. When this magnitude overcomes a certain threshold (3.4GHz or $9.3 \times 10^{30} electrons.m^{-2}.s^{-1}$ in this case), auto-oscillation around the STT direction can occur [1] (Figure 2.7).

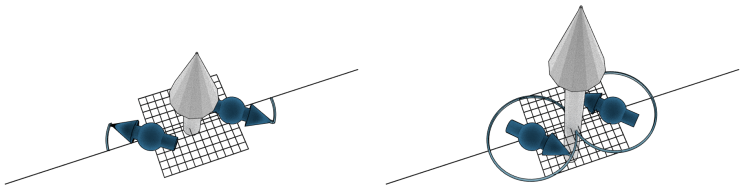

Figure 2.7: STT along the anisotropy axis.**Left:** At low STT orthogonal to the easy axis, **L** reorients in another equilibrium direction. **Right:** For STT strong enough to beat the anisotropy, **L** precesses around the STT axis.

Interestingly, the situation is quite different when the STT is applied along the easy axis (Figure 2.8). In this case, no change in direction is observed until a certain threshold. When the exact balance relative to the damping is achieved, a small auto-oscillation of roughly 0.1° about the easy axis is observed. In this situation, the two sublattices precess with a slightly different angle as angular momentum pumped into the system unbalances the magnetization. The ratio between the two sublattice angles is predicted to be $\frac{\theta_1}{\theta_2} = \left(1 + \sqrt{\frac{\omega_a}{\omega_E}}\right)^2$ [78]. This corresponds to generating circularly polarized magnons with a specific orientation. As reported by [33, 79], auto-oscillations can be stabilized by a feedback mechanism happening at the interface with a normal metal. When the STT gets stronger, the antiferromagnetic vector (**L**) flips into the perpendicular plane and the auto-oscillation occurs around the magnetization (***M***). The situation resembles the spin-flop state under high magnetic field with precession around the field direction.

Following these observations, canting along [111] seems the most efficient direction for a change of orientation in the case of NiO with its full anisotropy form (equation 2.20, Figure 2.3), as it makes the spins precess in their easy plane. On the contrary, an in-plane STT significantly strong could induce an elliptical precession for which it seems

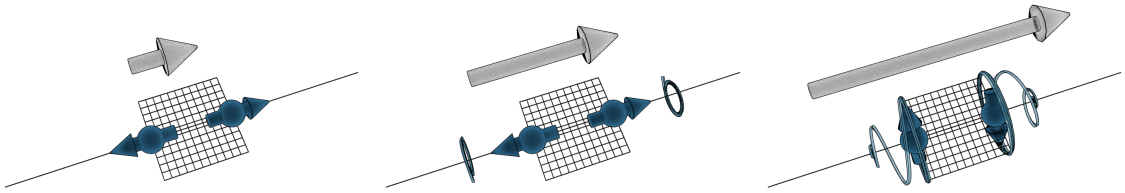

Figure 2.8: STT along the anisotropy axis. **Left:** At very low values of STT along the easy axis, the spins remain aligned. **Middle:** For a given value of STT applied along the easy axis, a small auto-oscillation around a circle of tenths of degrees can occur (0.089° with our parameters). To make them visible, the trajectory circles are scaled up by 250 here). More details in Ref. [33]. **Right:** For strong STT applied along the easy axis, precession occurs at 90 degrees around the STT axis.

hard — though not impossible — to initiate a change of rest axis.

2.3.4 Dynamical switch in NiO

Motivations

The dynamics we just presented is in the THz range as typical resonance frequencies are in $\sqrt{\omega_E \omega_a}$ when $\omega_E >> \omega_a$ (general case: $\sqrt{\omega_a(2\omega_E + \omega_a)}$ [53, 80]), which is at least two orders of magnitude faster than for ferromagnets. Therefore, several interesting applications can be envisioned from this dynamical behavior, including building a magnetic oscillator in the THz or a fast-switching memory. We will concentrate here on the latter as a fine-tuned SST pulse could be used for sub-picosecond switching of an antiferromagnetic domain from one stable position to another. Such memories would also be insensitive to external magnetic fields and compatible with spintronics and oxide technologies. Incidentally, NiO is a charge transfer insulator compatible with spin 'insulatronic' materials reducing Joule heating. In a context of energy saving devices, one can indeed be interested in the minimal energy required to switch a memory bit.

For details of making a memory element with NiO, we recall that there are three easy axes in the (111) plane, so in principle 6 different equilibrium magnetic configurations . If the sense of **L** cannot be easily probed, this reduces to three the number of states that can be probed e.g. by Spin Hall Magneto-Resistance. Considering spin current injection, there are several possible ways and two of these will be considered here. The first consists in depositing a Pt stripe on NiO in which current pulses can be passed. By virtue of the Spin Hall effect, a transverse spin current is generated producing a non equilibrium spin population in the adjacent material. A proof of concept has been realized by Reference [64]. The other envisioned possibility is even more optimal as it relies on ultra-fast demagnetization of a ferromagnetic layer by an intense laser pulse. This produces the fastest and strongest spin pulses available so far [35, 81] with the extra functionality of setting easily the spin directions with a magnetic field controlling the direction of the ferromagnetic layer's magnetization.

Therefore, we focus on two interesting STT directions:

- [111], requiring the lowest STT amplitude;
- the one leading to the fastest antiferromagnetic switch.

Minimal value for the pulse

For evaluating the minimal amount of STT needed to initiate a switch, we consider gate pulses, where we can change the intensity and the duration of the pulse. In the full anisotropy model of NiO, it is clear that a STT of low value has more impact when along [111], because the spin can rotate in their easy plane. The threshold for switching is directly linked to the anisotropy. The lowest STT amplitude is obtained when the spin trajectories remain in the easy plane. This corresponds to a spin current pointing along the [111] direction.

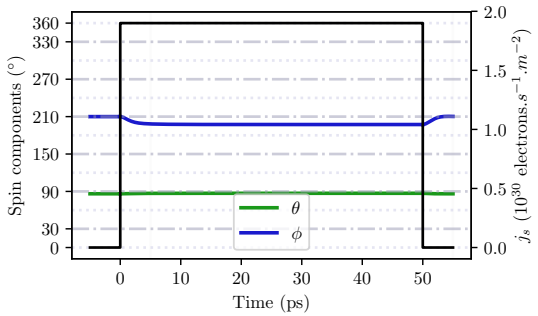

Figure 2.9: STT just above threshold. A STT of 1.9×10^{30}electrons.m^{-2}.s^{-1} (black curve) is above the threshold value to initiate a switch, but a pulse duration of 50ps is still not sufficient to achieve the switch (the blue curve goes back to its initial dashed line, and not to the next one). The higher the STT, the faster the switch.

According to our damped pendulum model and similarly to the case in Figure 2.7, when the value of the STT is too low, the switch cannot occur, no matter the duration of it. There is a threshold value close to 1.9×10^{30}electrons.m^{-2}.s^{-1} (see Figure 2.9), for which the equilibrium angle is close to a in-plane hard axis. A slightly higher value of STT moves the equilibrium angle to the other side of the hard axis, where the potential energy decreases to the next easy axis, and the auto-oscillation can begin.

This is the case studied analytically by Reference [1] albeit in a simple uniaxial model for the in-plane anisotropy. The threshold STT they obtain is close to 3.4GHz ($9.3 \times 10^{30} electrons.m^{-2}.s^{-1}$) whereas it falls down to 1.9×10^{30} electrons.m^{-2}.s^{-1} with our more realistic anisotropy model.

Amount of transfered spins

Above the threshold value, it is always possible to compensate a low value of STT by a longer duration, and maintain the rotation until the desired angle is reached. Once this barrier is passed, as soon as the pulse stops, the system will relax back into one of its equilibrium positions. This in turn depends on how much above the threshold the system has been driven by spin torque as well as its natural timescale and damping. At zero damping the system would oscillate and never find an equilibrium position whereas a large damping would lead to a fast return to the closest equilibrium position. For realistic α (0.005 in our case) all the in-plane equilibrium angles can be attained providing a suitable spin pulse strength and duration. The shorter the pulse duration the stronger SST strength is required, as shown on Figure 2.10.

For a given system, to a first approximation, the final switching angle depends only on the number of injected

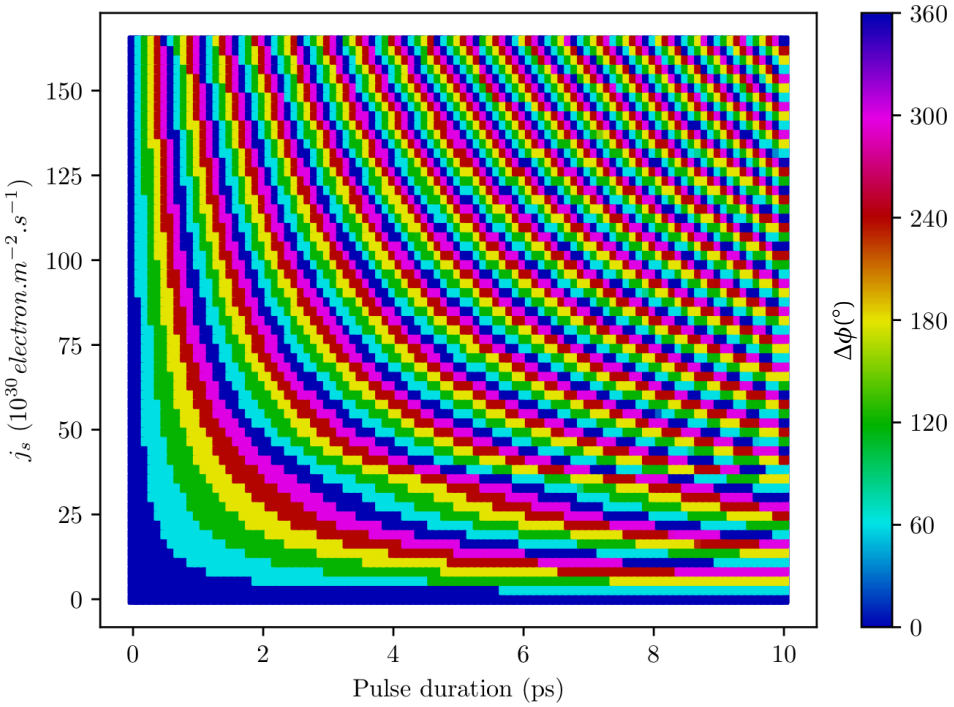

Figure 2.10: Phase diagram in spin current. Change of equilibrium angle (in degrees in the (111) plane) after a pulse along [111], for different pulses strenghts and durations. Values for $\alpha = 0.05$.

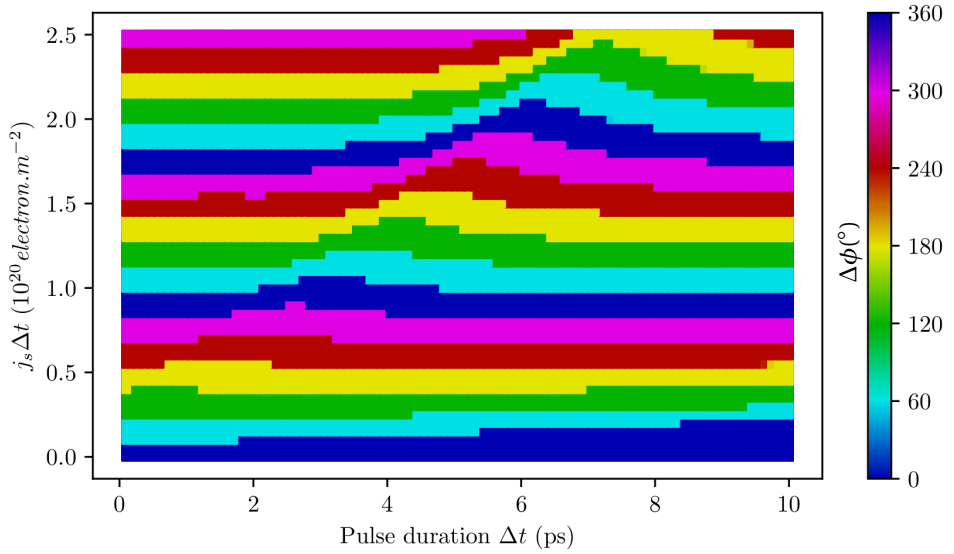

Figure 2.11: Phase diagram in total number of spins. To a first approximation, a constant number of injected spin $j_s\Delta t$ gives approximately a constant switching angle, with only little dependance on the duration. Nonetheless, a noticeable area of lower efficiency is to be avoided. Values for $\alpha = 0.05$.

spin, as shown on Figure 2.11. That's why above the threshold it is always possible to compensate the strength by a longer duration, and that even ultrashort pulses trigger a switch, provided the strength of the spin current is large enough. Nonetheless, dynamical effects cannot be completely ignored. Figure 2.11 does not display constant lines, and show a noticeable area for which the spin injection is less efficient. This effect is purely dynamical and largely

depends on the value of α. For a power-efficient device, this area should be avoided. The diagram also shows that the minimal number of spin for a switch is 0.1×10^{20} *electron*m^{-2}, and that they must be transfered in a time shorter than 1.7ps to operate before α has time to brake.

Switching time

Interestingly, even if the pulse is ultrashort, the spins will take a few picoseconds to relax. Figure 2.10 and 2.11 do not show the time it takes for the spins to reach their equilibrium position. In practice, the equilibrium position was measured at $t = 50$ps for each and every point of the phase diagram, to ensure the equilibrium position was reached.

In the practical case of a memory device, it can be crucial to know the time it takes for a bit to be written before being able to read it. So far, we only studied the final position of **L**, but not the time it takes to reach it.

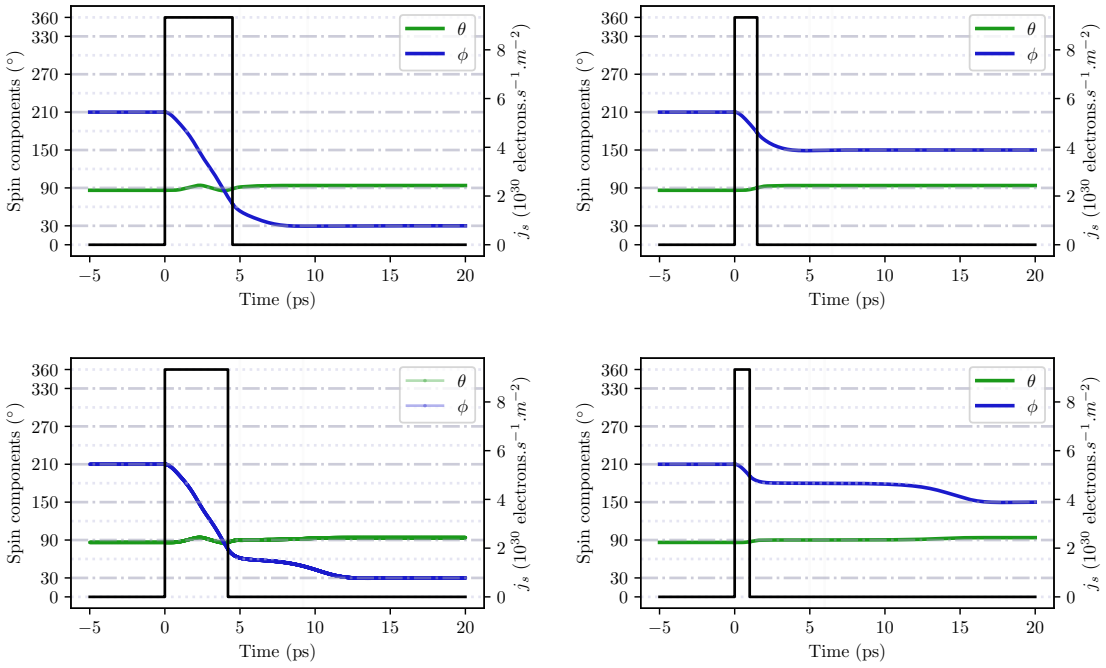

Figure 2.12: NiO switches with a STT of 9.3×10^{30}electrons.$m^{-2}.s^{-1}$ along [111]. Black curves show the switching on and off of the STT. A duration of $4.5ps$ gives a 180° switch, whereas a $1.5ps$ pulse is enough to trigger a 60° switch. For the same final result, the durations of the pulses can be reduced to $4.2ps$ and $1ps$ respectively, but at a cost of a longer relaxation time.

As a point of comparison with Reference [1], let us consider a STT of 3.4GHz ($j_s = 9.3 \times 10^{30}$ electrons.$m^{-2}.s^{-1}$), and watch the impact of its duration on the switching time. A minimal switch corresponds to a 60° rotation. A 180° rotation is also considered to compare our values with Reference [1]. The minimal pulse duration for a 60° rotation with this value of STT is 1ps. This is enough to bring **L** at the edge of a hard in-plane axis. When the pulse stops, **L** will relax to the closest easy axis, but if **L** is dropped too close to the local maximum of energy, its angular speed will be very slow, similar to a marble that loses kinetic energy when reaching the top of a hill. With no extra momentum,

it can take several picoseconds for **L** to reach its equilibrium position, as illustrated on Figure 2.12. When the pulse duration is extended to 1.5ps, **L** reaches its final position faster because it is brought much closer. A pulse even longer would give overshoot.

Depending on the value of α, **L** can oscillate or not before reaching its equilibrium. For the bit to be written as fast as possible, a large or critical damping is preferable. When no control on the damping is possible, the duration of the pulse must be tuned according to the needs. If a short relaxation to equilibrium is paramount, extending the duration of the pulse must be considered. On the contrary, and probably closer to the needs of the hard drive industry, if we are limited in power, or if we are interested in writing as many bits as possible as fast as possible, the pulse duration can be shortened, even though the equilibrium state will be reached only several picosecond later. It is probably not a problem to wait 50ps before reading the bit we have just written, since current hard drives process at nanosecond time-scale, but in other applications such as signal conversion in telecommunications, it could be a limitation.

Realistic pulse

The previous results settle the amount of spin injection needed for a switch, but we also saw that the dynamics could play an important role. Since the required energies are rather high relative to the available technology, we decided to confront our theoretical model to the reality, and see whether a realistic pulse created by the available technology could trigger a switch. For that, we designed the shape of spin current pulses based on the spin currents that can be generated at the interface Fe/Ru or Fe/Au when excited by a femtosecond laser [81]. Using the same conversion formula (2.23) as usual, we could simulate the trajectories displayed in Figure 2.13. The STT was applied in the [111] direction.

The shape inspired from Fe/Ru manages to realize a 60° switch, without overshoot, in approximately 2ps. On the contrary, the pulse inspired from Fe/Ru fails for one simple reason: its integral is too small. Its positive part is compensated by its negative part.

The results are rather positive: a switch seems possible with the available technology, but it is clear from the trajectories that we only barely touch the surface of the switching possibilities. The shapes we used are only examples of what one can expect with cutting-edge technology, but it is not excluded that a good device design gives better spin currents, therefore better switching possibilities. The spin current shapes we used are intrinsic to the bilayers under consideration, it is difficult to predict what the shape of a spin current generated by Fe/NiO would be. Material and growth engineering would be valuable for having as much spin current conversion as possible, and create reliable and tunable switches.

2.3.5 Out-of-plane switch

Previously, we have determined the minimal pulse needed to realize a switch. The torque needed to be in the [111] direction to trigger a rotation in the easy plane. Now, we are interested in the other directions. The dynamics being in $\sim \sqrt{\omega_E \omega_K}$, we could expect a faster switch making use of the hard anisotropy, provided we supply a pulse strong

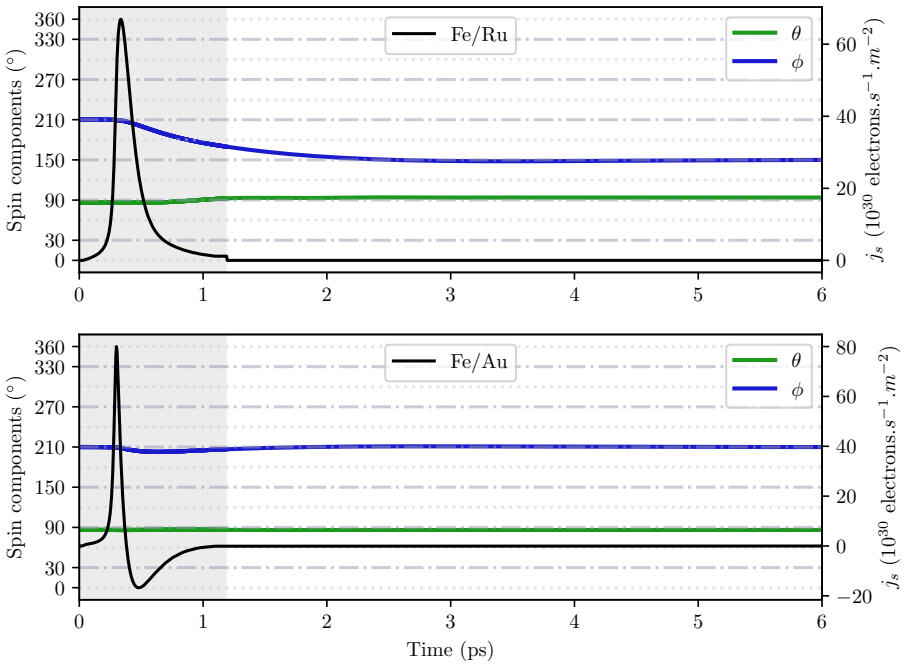

Figure 2.13: Switching (or not) after excitations inspired from [81].

enough. The idea is to use a very strong switch to send **L** out of the plane, and profit of the strong anisotropy to relax quickly to an equilibrium position.

As shown on Figure 2.15, the in-plane directions are not as interesting as it seems. They require much higher spin current to initiate a switch. For the same current in the [111] direction, all the equilibrium positions can be reached, and in a shorter time since the extra spin current is converted into momentum instead of potential anisotropy energy.

Moreover, the initial idea to take advantage of the out-of-plane anisotropy for relaxing fast does not work with our α. The parameter we need to act on for a switch is ϕ, and ϕ's dynamics is monitored by the in-plane anisotropy. The out-of plane anisotropy is orthogonal and cannot act on ϕ. Still, a very strong SST can accelerate the dynamics during the pulse, but the damping limits the relaxation to a minimum of 1ps. Several directions and strength have been tested, and this time limit seem incompressible.

As for the realistic pulse shape, it is clear from this analysis that a STT in a direction different than [111] would give poorer results.

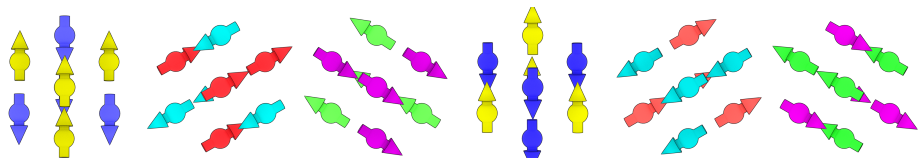

Figure 2.14: Colors used for the equilibrium positions

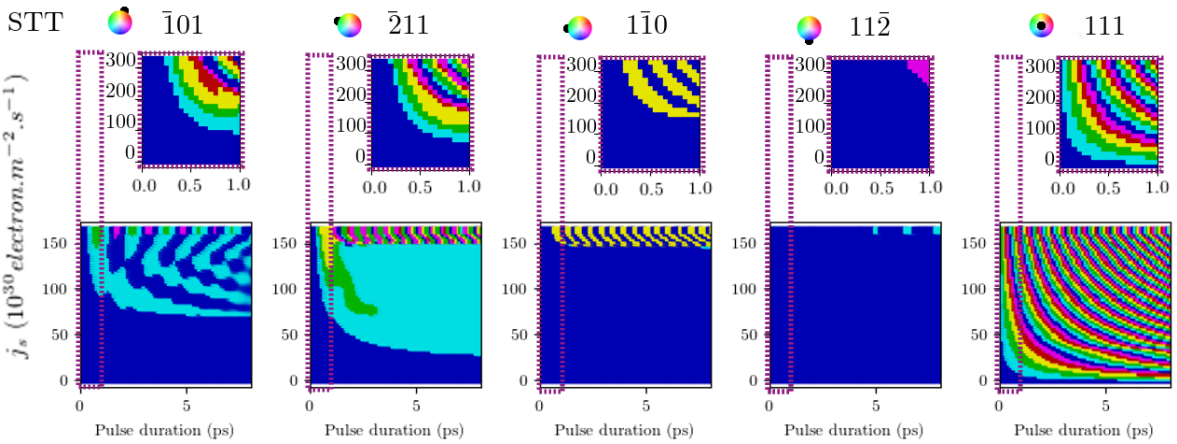

Figure 2.15: Switches for gate pulses in the main inplane directions. Insets: zoom for subpicosecond switches.

2.3.6 Conclusion on NiO

In this part, we have found a realistic model for the anisotropy in NiO. We have used it to simulate a switch induced by a spin transfer torque for possible memory device applications. We have shown that the most important parameter is the amount of spin to inject, and that a maximum efficiency is reached for a spin current in the [111] direction. We have shown that dynamical effects could lower the efficiency of the STT, and we have found the minimal possible pulse for a switch. We have positive results for switching using a realistic pulse. This theoretical study paves a promising route for ultrafast spintronic devices based on NiO.

2.4 $BiFeO_3$ Simulation

In this section, our attention moves to $BiFeO_3$— the most prototypical multiferroic at ambiant temperature —, because it has, in addition to its antiferromagnetic order, a strong magneto-electric coupling with a large electrical polarization. This is of huge interest since it enables a certain control over the antiferromagnetic structures, as illustrated in this section 2.4, as well as in chapter 3.

2.4.1 Multiferroics and Motivations

Since antiferromagnets have their spins aligned antiparallel, the Zeeman field has very weak influence as the two sublattices compete for torque and alignment. Moving an antiferromagnetic domain is generally not an easy task. One possible approach can be to take advantage of a coupling in a material to see or excite their magnetic ordering [82]. For example, some materials called multiferroics, can have both a magnetic ordering as well as a mechanical or electrical ordering. Sometimes their orderings are coupled together and one could use one to see or excite the other.

Such materials are quite rare. In fact, while magnetic ordering requires partially filled d-shells, most technologically important ferroelectrics are perovskites ABO_3 for which a displaced metallic cation B hybridizes its empty

$3d$ shell with the $2p$ of the surrounding oxygens [83]. Perovskites are crystal structures of type ABX_3, where A and B atoms have cubic arrangements nested half a primitive cell apart, and B is surrounded by octahedral formation of X, as shown on Figure 2.16. This competition on the filling of the d shells results in a very limited number of multiferroic materials [84]. Most of the time, their ordering temperatures are below room temperature.

Coincidently, bismuth ferrite ($BiFeO_3$), the most famous and prototypical multiferroic at room temperature is a perovskite both ferroelectric and antiferromagnetic, which makes it well suited for our study. Moreover, it has a strong magnetoelectric coupling between its two orders. Since it has for long been labeled as 'the only known multiferroic material at room temperature' , the huge emulation around this revolutionary material lead to a gigantic set of publications and thus, $BiFeO_3$ remains by far the most largely explored multiferroic material.

What makes it particularly interesting in our case is that $BiFeO_3$ is the only multiferroic at room temperatures which exhibits a magnetoelectric coupling between its polarization and its antiferromagnetic order. As stated earlier, antiferromagnetism is usually very hard to control, and this magneto-electrical coupling can be a precious help as a controller. We decided to simulate the magnetically ordering of this material to investigate the possible formation of promising antiferromagnetic structures for spintronics. The simulator we used leaves possible for future studies the investigation of the dynamical behavior of these structures.

2.4.2 $BiFeO_3$ crystal and primitive cell

Between temperatures of $1203K$ and $1100K$, $BiFeO_3$ in its $\beta-$phase has a perovskite crystalline structure, where the iron ions are surrounded by a cube of bismuth ions and a octahedral cage of oxygen (Figure 2.16).

Under $T_C = 1100K$, $BiFeO_3$ enters its $\alpha-$phase[85], in which the cubic structure elongates along the [111] direction, making it slightly rhombohedral, with an angle $\alpha = 89.47°$ in the acute corners. Since the difference is only $0.53°$ away from the cubic phase, we speak of a *pseudocubic* phase. This angle will be neglected in the rest of this thesis for greater simplicity. More importantly, Fe^{3+} ions shift by 41pm along the big diagonal [111] and the octahedral oxygen cages undergo both a rotation of $\pm 13.8°$ around the same [111] diagonal, alternatively from one iron site to the other, as well as a shift of 54pm with respect to their original position, i.e. 13pm from the iron ions (Figure 2.17)[86]. The relative displacement of iron and bismuth ions relative to oxygen ions shifts the barycenter of the charge in the [111] direction, causing a polarization $\boldsymbol{P_e}$ and a large ferroelectricity ($|\boldsymbol{P_e}| \simeq 100\mu C/cm^3$ [87]). The 8 directions $\langle 111 \rangle$ are possible for $\boldsymbol{P_e}$, leading to eight possible ferroelectric domains in a virgin $BiFeO_3$.

Under $T_N = 653K$, the spins coming from the d orbitals of the iron ions order antiferromagnetically. Just like for NiO, the antiferromagnetic coupling is enhanced by the superexchange with the median oxygen atoms, and we get G-type antiferromagnetism. [88] This distortion results in a symmetry breaking of the Fe^{3+} environment causing a magnetoelectric and a Dzyaloshinskii-Moriya interactions

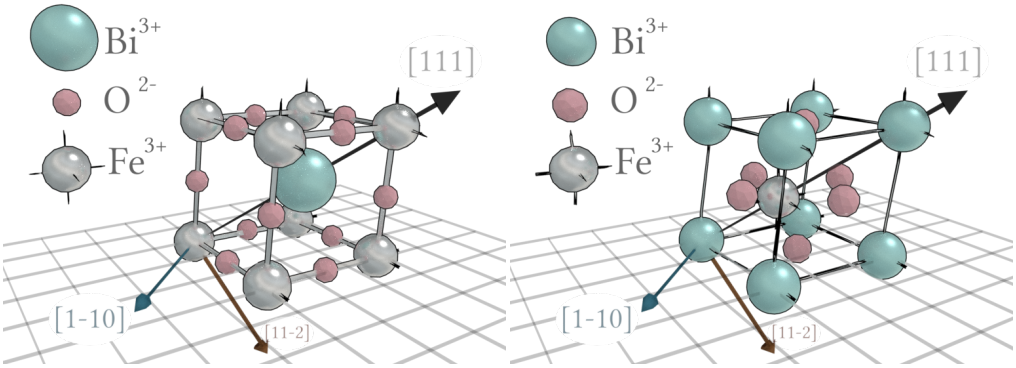

Figure 2.16: $BiFeO_3$ has a perovskite composition.

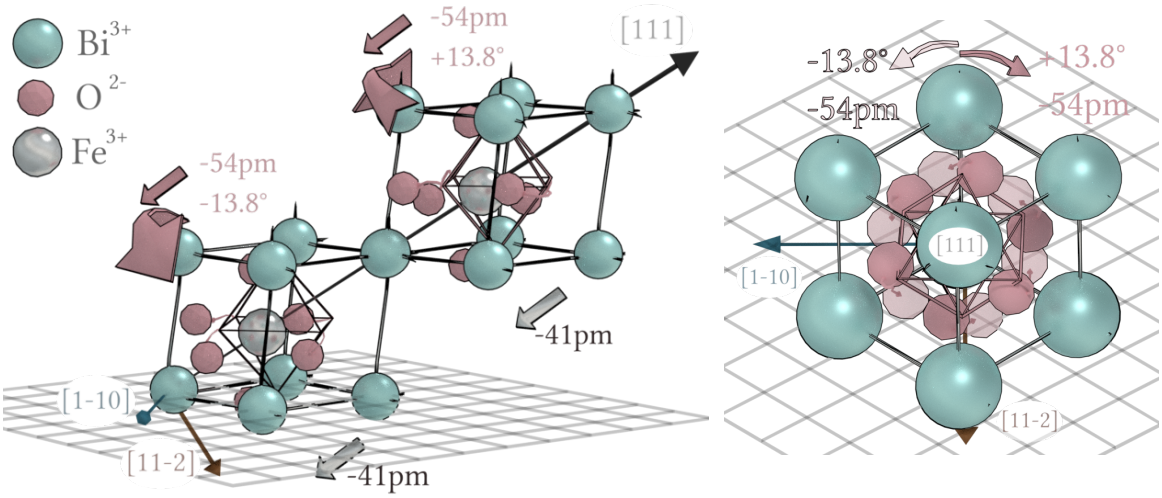

Figure 2.17: $\alpha-BiFeO_3$ full primitive cell including the 0.53° distortion of the cubes, the tilts along 111 and the alternative ±13.8° rotation of the oxygen cages around 111.

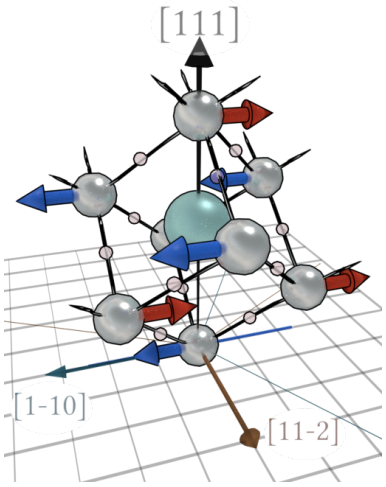

Figure 2.18: G type antiferromagnetic perovskite, with spin aligned along $\pm[1\bar{1}0]$

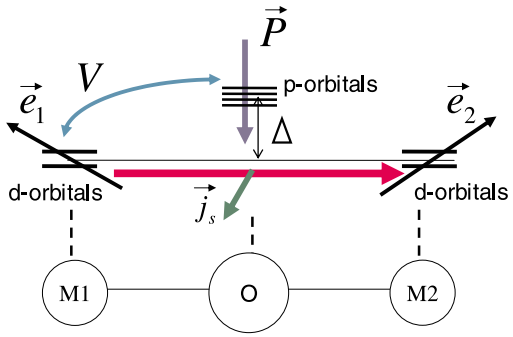

Figure 2.19: Origin of the magneto-electric coupling. From[89]. Electrons hopping between p-orbital of O and d-orbitals of M_1/M_2 with different spin orientation ($\boldsymbol{e_1}$,$\boldsymbol{e_2}$) leads to a spin current $\boldsymbol{j_s} \propto \boldsymbol{e_1} \times \boldsymbol{e_2}$ and an electrical polarization $\boldsymbol{P} \propto \boldsymbol{r_{12}} \times \boldsymbol{j_s}$.

2.4.3 Magnetoelectric Interaction, type I cycloid

Magnetoelectric interaction and DMI in $BiFeO_3$

Let us first remind our reader that $BiFeO_3$ is subject to exchange interaction, with antiferromagnetic coupling to the first neighbor (G-type antiferromagnet):

$$\mathcal{H}_E = \sum_{i,j} J_{ij} \hat{\boldsymbol{s}}_i \cdot \hat{\boldsymbol{s}}_j \tag{2.26}$$

In addition, due to the [111] elongation, a small uniaxial magnetic anisotropy exists along this direction:

$$\mathcal{H}_a = K_p \sum_i (\hat{\boldsymbol{s}}_i \cdot \boldsymbol{P_e})^2 \tag{2.27}$$

More importantly, because the oxygen cages are shifted 13pm away from the iron atom, $d-$orbitals of the iron atoms experience an asymmetric superexchange, wich cants the spins in average, in the direction of $\boldsymbol{P_e}$. Due to hoping between the $d-$orbitals of Fe and $p-$orbitals of O (Figure 2.19), a magneto-electric coupling carried by $\boldsymbol{P_e}$ arises [89]. This leads to the formation of an antiferromagnetic cycloid. Since the direction of the Dzyaloshinskii-Moriya interaction is systematically the same as the one of $\boldsymbol{P_e}$, we call it a magnetoelectric interaction. The contribution to the Hamiltonian can be written:

$$\mathcal{H}_{ME} = \sum_{ij} \left(\boldsymbol{r_{ij}} \times \boldsymbol{P_e}\right) \cdot \left(\hat{\boldsymbol{s}}_i \times \hat{\boldsymbol{s}}_j\right) \tag{2.28}$$

where $\boldsymbol{r_{ij}} = \frac{\boldsymbol{r_i} - \boldsymbol{r_j}}{||\boldsymbol{r_i} - \boldsymbol{r_j}||}$ is the unit vector between sites i and j, on which magnetic moments have unitary directions $\hat{\boldsymbol{s}}_i$ and $\hat{\boldsymbol{s}}_j$ respectively. $\boldsymbol{P_e}$ is the local ferroelectric polarization.

Secondly, because the oxygen cages are alternatively rotated from one site to the other, an average asymmetric superexchange causes another Dzyaloshinskii-Moriya interaction, perpendicular to the first one, which alternates sign from one atomic layer perpendicular to $\boldsymbol{P_e}$ to the other. This second Dzyaloshinskii-Moriya interaction $\boldsymbol{D'}$

averages in one of the $\langle 11\bar{2} \rangle$ directions. We write:

$$\mathcal{H}_{D'} = \sum_{ij} (-1)^{n_{ij}} \left(\boldsymbol{r_{ij}} \times \boldsymbol{D'} \right) \cdot \left(\hat{\boldsymbol{s}}_i \times \hat{\boldsymbol{s}}_j \right) \tag{2.29}$$

With the same notations as before for $i, \hat{\boldsymbol{s}}_{\boldsymbol{i}}, \boldsymbol{r_i}$ and where the $(-1)^{n_{ij}}$ prefactor accounts for the alternation of sign from one (111) atomic layer to the next.

The competition of exchange and magnetoelectric interactions results in the formation of a cycloidal state propagating along the $[1\bar{1}0]$ direction [55, 87, 90, 91, 92] Figure 2.29 shows that this cycloidal state can be favored, modified or destroyed according to the strain from the substrate. A good understanding of the competitions between the energies at stake is crucial for a prediction of the formation of antiferromagnetic structures. The influence of each term will be developed in the coming sections, thanks to our simulations in bulk and in thin layers.

$BiFeO_3$ crystal and its spin interactions according to the presented model can be simulated with the LAMMPS software, using the package 'manybody' and the new package 'spin' (which I contributed to debug) [59].

In the rest of the chapter, only static studies will be carried out on $BiFeO_3$, but LAMMPS has the same simulating approach as the software we presented previously ([59]), so dynamics studies are also possible. One big advantage of LAMMPS is that it benefits from parallelization computing, making it suitable for simulation of relatively large structures.

Type I cycloid

As a starting point, let us take only the leading terms into account, namely the exchange and the magnetoelectric interactions (equations (2.26) and (2.28)).

$$\mathcal{H}_E + \mathcal{H}_{ME} \tag{2.30}$$

The parameters we use are taken from Reference [22]:

- $J_1 = -4.5meV$
- $J_2 = -0.2meV$
- $\boldsymbol{P_e} = 0.107meV$ along **[111]**

Let us start from an initial crystal of $400 \times 4 \times 12 = 19200$ atoms (2240.2Å deep in the $[1\bar{1}0]$ direction, 19.5Å wide in the $[11\bar{2}]$ direction and 27.53Å high along [111]). The lattice parameter is $a = 3.96$Å, and we ensure that the $BiFeO_3$ crystal structure is respected. We define periodic boundary conditions for $[11\bar{2}]$ and [111], and voluntarily let the $[1\bar{1}0]$ axis free of neighbors at its boundaries. The simulation converges to the formation of a cycloid along $[1\bar{1}0]$, turning around $[11\bar{2}]$ (Figure 2.20), in agreement with the observations reported in the litterature [55].

To make sure the obtained cycloidal state corresponds to a global minimum of energy, and not a local one, we[1] have run a computation of the total energy per atom for different cycloidal periods. Compared to the previous simulation, dimensions along $[11\bar{2}]$ and [111] are left unchanged and periodic, but this time we let the number of

[1] Many of the simulations concerning the single cycloid have been run with the help of Ruyhei Kohno, intern that I trained on the simulations.

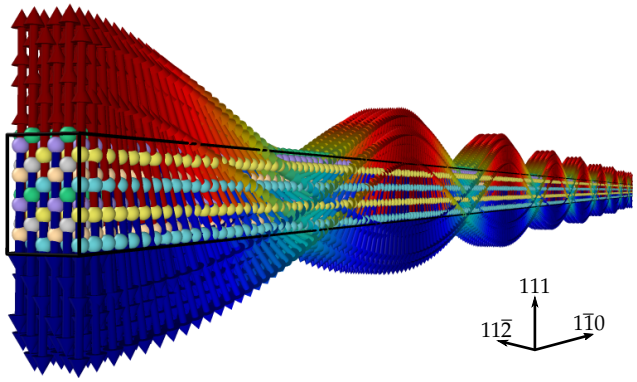

Figure 2.20: Antiferromagnetic cycloidal equilibrium state in $BiFeO_3$. Simulation with LAMMPS. Colored arrows represent the orientation of the spins, colored dots represent the different layers of $Fe_3{}^+$ ions stacking along [111]. The period is 64nm long.

atoms along [1$\bar{1}$0] vary from 10 to 400, ensuring that the periodic boundary conditions are met for all periods in this direction too. We initialize the state to a cycloid of the corresponding period, and let LAMMPS compute the energy per atom, without letting it relax the state. This is equivalent to a computation of the energy par atom for different cycloidal periods in a bulk crystal. The result of the computation is shown on Figure 2.21. The minimum is close to 64nm, which is again consistent with the previous convergence and the values found in the literature.

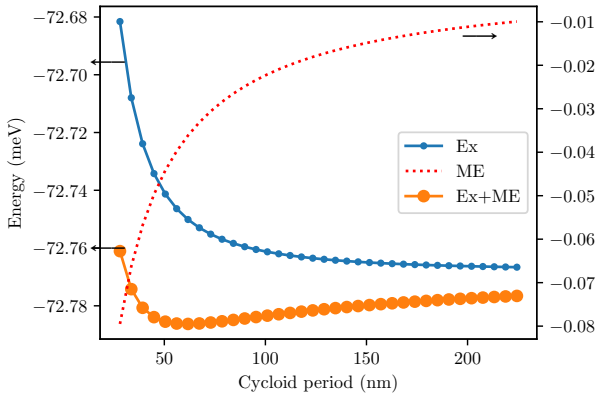

Figure 2.21: Energy of a cycloid with respect to its period. Exchange (Ex) and magnetoelectric (ME) contributions are ploted separately. The minimum of total energy is at 64nm.

If we now multiply by 10 the magnetoelectric coefficient, and run the simulation again, we observe that a cycloid of period 6.4nm forms. This is consistent with the theoretical evolution of the cycloidal period proportional to the ratio $\mathscr{H}_{ME}/\mathscr{H}_E$ [93].

Influence of the anisotropy on the cycloid

Because of the small anisotropy, the cycloid is slightly deformed, and loses harmonicity. This effect has only very little incidence on the magnetic configuration because the anisotropy energy is much weaker than the magneto-electric energy ($3.3\mu eV << 107meV$) In fact, it was measured that the anisotropy is very weak [94], and it can be

neglected for the rest of our study.

In thin films, the anisotropy can be enhanced. If along [111], the cycloid will progressively lose harmonicity to maximize allignment in this direction, until it flops for a value big enough. Along another axis, the anisotropy will bend the cycloid.

Influence of the alternating DMI on the cycloid

Let us go back to the initial cycloidal chain for now and add the additional alternate Dzyaloshinskii-Moriya interaction contribution to evaluate its influence on the cycloid:

$$\mathcal{H}_E + \mathcal{H}_{ME} + \mathcal{H}_{D'} \tag{2.31}$$

The parameters we use are taken from Reference [22].

- $J_1 = -4.5meV$
- $J_2 = -0.2meV$
- $\boldsymbol{P_e} = 0.107meV$ along **[111]**
- $\boldsymbol{D'} = 0.054meV$ along $(-1)^n$**[11$\bar{2}$]**

The $(-1)^n$ stands for the alternation of sign from one (111) layer to the next. The origin of sign is purely arbitrary, and depends fully on the rotation of the oxygen on the original cell (Figure 2.17). The implementation of this additional DMI is not straightforward and requires some care regarding the affectation of the atoms in the simulation. In particular, we need to know the direction of the cycloid propagation prior to the definition of $\boldsymbol{D'}$, which needs to be along [11$\bar{2}$] *relative to* the defined [1$\bar{1}$0] $\boldsymbol{q}$-direction of the cycloid. Other approaches defining more $\boldsymbol{D'}$ directions —globally or relative to the local oxygen positions— were envisioned, but brings with them an unnecessary too high level of complexity.

After adding the additional Dzyaloshinskii-Moriya interaction, which alternates from one (111) layer to the next, and letting the simulation converge, we observe a perturbation from the perfect cycloidal state causing a static wiggling — a spin density wave — perpendicular to the direction of propagation (Figure 2.22)[95].

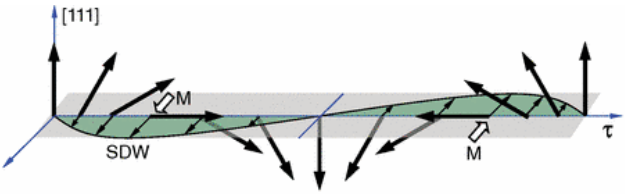

Figure 2.22: From [95]. The alternating DMI causes a static wiggling of the cycloid, which results in a net magnetization (M) orthogonal to the cycloid direction (τ): the Spin Density Wave (SDW).

For a pure cycloidal state, the barycenter of the spins is perfectly anti-aligned, and therefore, no stray field is visible at long range. In the case of the wiggled cycloid with the spin density wave, a small perpendicular canting of $\sim 1°$ appears and causes magnetic flux to escape. The local magnetization due to this canting has been measured to be $0.06\mu_B$/Fe by Reference[95].

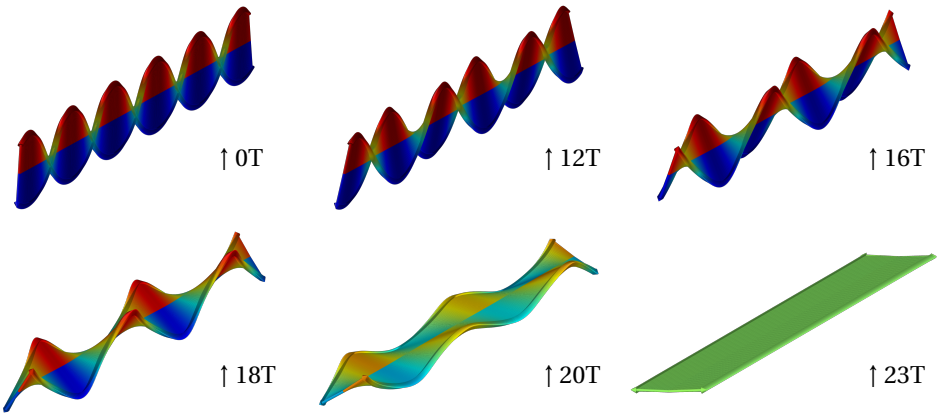

Figure 2.23: Deformation of the cycloid in $BiFeO_3$ under a [111] magnetic field, until the flop at 23T.

Strong magnetic fields can flop the cycloid and force a non-collinear antiferromagnetic state, where the small canting aligns with the external field. Flopping fields can be very high for antiferromagnets, and are predicted to be near 20T for $BiFeO_3$ [22].

Our simulations could reproduce the flop at 23T for a field in the [111] direction (Figure 2.23), and we could observe the equilibrium states at intermediate fields. Our analysis reveals that the small alternating DMI helps opening the cycloid smoothly until a relatively brutal flop near 23T.

Discussion and perspectives with regard to the magnetic simulation of $BiFeO_3$

We showed in this section that the antiferromagnetic cycloidal state of $BiFeO_3$ could be simulated. We detailed the influence of each term in the Hamiltonian on the cycloid. We did it in real space and with a dynamic algorithm. We have all the ingredients to run more complex simulations, close to real systems. The next section will deal with thin films simulations.

2.4.4 Thin layer simulations

2D bubbles structures

Since for large values of magnetoelectric exchange, the simulation is significantly faster, and that we showed in section 2.4.3 that it simply scales down the cycloidal period accordingly, we decided to run the simulations with a large number of atoms with a value of magnetoelectric multiplied by 10, and scale the qualitative conclusion we draw taking this factor into account.

As an illustration of relatively large scale simulation, we let converge a 2D surface with periodic boundary conditions from a random antiferromagnetic configuration. We observe that generally, the structures try to form large cycloidal domains, but since we only imposed $\boldsymbol{P_e}$, the 3 perpendicular $\langle 1\bar{1}0\rangle$ directions of propagation for the cycloid are possible. As a result, it is common to observe the formation of domain walls and antiferromagnetic bubbles (Figure 2.24).

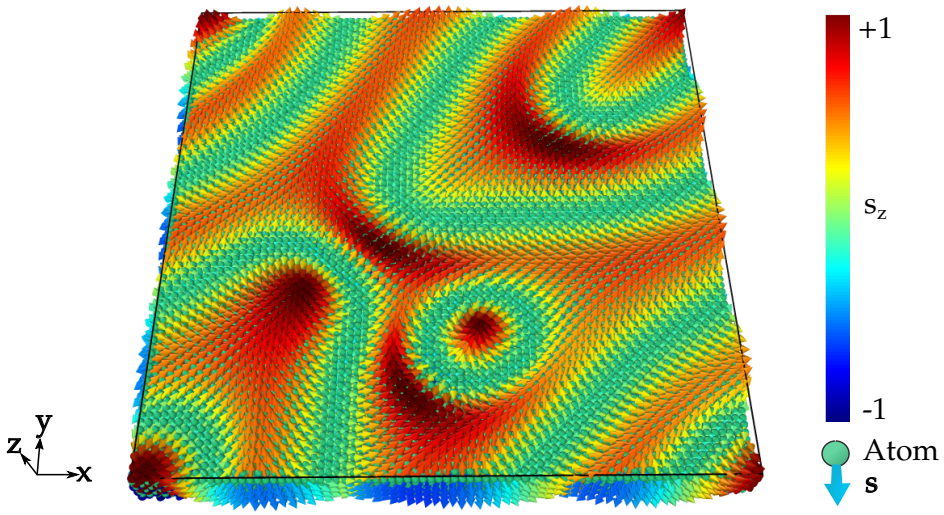

Figure 2.24: Formation of 2D antiferromagnetic bubbles. A possible convergence from random state. ($80 \times 80 \times 6$ particles in [100], [010], [001] frame, magnetoelectric $\times 10$).

These bubble states are not a ground state, but are rather metastable states. Such structures could be used in memory devices, for storing information, for example. Magnetic structures are often considered for storing magnetic bits, and in particular skyrmions, which are bubbles equivalents with topological protection, providing better stability for storage. It is not proven that the structures we observe here are topologically protected or not, but they seem to present a certain stability, which is a promising result.

2.4.5 Thin layer striped samples: Geometry and motivations

The $[1\bar{1}0]$ direction in which the cycloid develops is called $\boldsymbol{q}$. In $BiFeO_3$ bulk, there are 3 possible $\boldsymbol{q}$ directions at 120° form one another. So far, only single-$\boldsymbol{q}$ phases have been observed, but considering the degeneracy of the three directions, a multi-$\boldsymbol{q}$ phase is theoretically possible. A multi-$\boldsymbol{q}$ state including all three possible $\boldsymbol{q}$ would favor the formation of antiferromagnetic *'skyrmion crystals'*, an array of antiferromagnetic skyrmions[96].

Skyrmions are magnetic solitons, they are topologically protected, and can be moved with spin currents. They are of vivid interest both theoretically and practically because they could provide a way to move bits of magnetic information safely and with minimal energy. Ferromagnetic skyrmions naturally drift sideways when moved forward, because of their magnetic topology (an effect equivalent to the Magnus effect in fluid dynamics)[97]. Antiferromagnetic skyrmions would not suffer from this effect because the two sublattices push the drift in opposite directions, which results in a straight propagation[98]

Antiferromagnetic skyrmions have not been observed yet, so their discovery is a great physical challenge which could trigger a vivid emulation. Forcing a multi-$\boldsymbol{q}$ phase in $BiFeO_3$ could help create antiferromagnetic skyrmions. As a first step, we are interested in seeing what happens at a junction of two $\boldsymbol{q}$-domains, and if possible magnetic bubbles could form. To that aim, a sample of $BiFeO_3$ has been grown on $DyScO_3$ (DSO) by pulsed laser deposition (PLD) by Stephane Fusil and Vincent Garcia at UMPhy CNRS Thalès. When grown on a [110] DSO substrate, ferro-

electric domains arrange in stripes, as seen by piezoresponse force microscopy (PFM) (Figure 2.25). For details, a short description of the PFM is given in section 3.2.1.

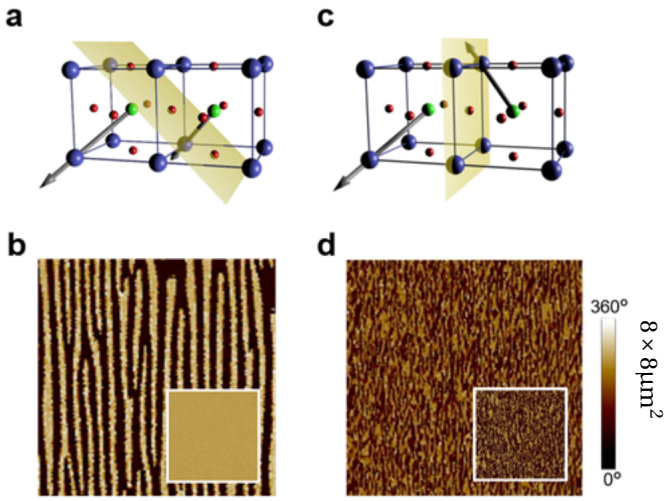

Figure 2.25: Phase PFM images of the striped $BiFeO_3$ samples. (a) Sketch and (b) PFM image of 71° ferroelectric domains. (c) Sketch and (d) PFM image of 109° ferroelectric domains. As grown, in-plane component. Inset: out-of plane component.

Let us suppose we have two ferroelectric domains, that we name A and B. At a domain wall, depending on the two diagonals the polarizations $\boldsymbol{P_{e}}_A$ and $\boldsymbol{P_{e}}_B$ choose among the 8×8 possible one in the cube, we can distinguish three types of domain wall. They are defined by the angle between $\boldsymbol{P_{e}}_A$ and $\boldsymbol{P_{e}}_B$:

- domains at 71°
- domains at 109°
- domains at 180°

With the suitable parameters, it is possible to grow by Pulsed Laser Deposition (PLD) thin films with repetitive patterns of domain walls of the 71° or 109° types. In this chapter we focus exclusively on the samples of the 71° type, because the stripes are of better quality (Figure 2.25). Under these conditions, they naturally form stripes of width 230nm. Annealing can confirm this tendency. These striped structures are interesting because they force stitching of two different $\boldsymbol{q}$-domains. Hopefully some antiferromagnetic bubbles could appear at the domain walls.

A revealed chirality... Circular dichroism measurements of these samples at synchrotron SOLEIL by Resonant soft X-ray Elastic Scattering (RXES) (Figure 2.28a) reveals the presence of a chiral pattern in the sample at the oxygen edge. Chirality commonly emerges from magnetic structures, but in this case, since oxygen carry no magnetic moment, these measurements suggest that they are of pure ferroelectric origin (roughness have been discarded), and with the same periodicity as the domain walls. This suggests a rotation of $\boldsymbol{P_e}$ at domain walls, with the same chirality from domain A to B as from domain B to A. This result is uncanny because from A to B, a rotation of $\boldsymbol{P_e}$ of only 71° is needed, while from B to A, to keep the same chirality, a rotation of $71+71+71°$ is needed (Figure 2.28c, upper insets).

To unveil the mystery on these samples, a simulation is a great help, if not necessary.

In the next section, we compute the magnetic texture generated by the inferred configuration of $\boldsymbol{P_e}$, and confront the result to magnetic imaging measurements. These show a good consistency and permit to visualize the multiferroic configuration.

2.4.6 Simulations of the thin layer striped samples

To understand what the configuration at the domain walls is, we need to simulate our sample, with the two kinds of domain walls, where $\boldsymbol{P_e}$ rotates by 71° in one direction, and one where it rotates by $71+71+71°$. If the simulation confirms what we observe, it can give us some insight on the magnetic structures.

Simulated geometry For a significant gain of speed in the simulations, the magneto-electric term is multiplied by ten compared to its real value. As a consequence, the cycloid period converges faster and is ten times smaller. Consequently, we scale down all the real geometry of the sample by a factor of ten. This, in turn reduces our number of simulated particles and speeds up the simulation. The geometrical results, as well as the resulting magnetic fields must be corrected by the appropriate factor.

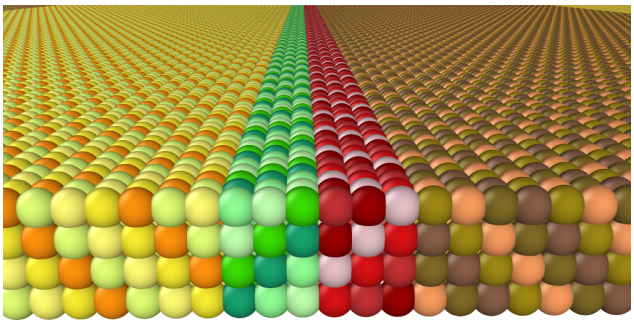

Figure 2.26: Detail of the stacking of the iron sheets along the [111], [11$\bar{1}$], [1$\bar{1}\bar{1}$] and [1$\bar{1}$1] directions (respectively yellow, green, red and brown), necessary for accounting for the alternating sign of the Dzyaloshinskii-Moriya interaction. Each nuance of color represents a ferromagnetic familly. Periodic boundary conditions in z are respected.

Our geometry presents 4 stripes of 230nm/10 each, enclosed in periodic boundary conditions in x (width) and z (thickness). The y direction, along the stripes, is let free to let the cycloid relax in its natural period (Figure 2.28c, upper part). In the striped domains, $\boldsymbol{P_e}$ are defined along [111] and [1$\bar{1}$1] respectively. To ensure chirality of $\boldsymbol{P_e}$, we reserve a 6 atom width ($\sim$ 23nm/10) region on even domain walls to rotate $\boldsymbol{P_e}$ in directions [11$\bar{1}$] and [1$\bar{1}\bar{1}$] (Figure2.26). Odd domain walls are left without buffer region.

Role of the alternating DMI For simplicity, we first run a simulation without the alternating DMI term $\boldsymbol{D'}$ (2.29). The result was a magnetic vector $\boldsymbol{M}$ with no component along z, and no stray magnetic field on the stripes, only some present at the domain walls. A perfect regular cycloid does not produce stray field.

The addition of the alternating DMI term $\boldsymbol{D'}$ is crucial for comparing our results to the stray field imaging. For that, we defined the stacking of iron layers along the $\langle 111 \rangle$ directions, as shown on Figure 2.26.

When all the terms are taken into account, the magnetic $\boldsymbol{M}$ and Néel $\mathbf{L}$ vectors result in the maps given in Figure 2.27, on which it is clear that an incommensurate alternation of sign, matching the cycloidal period is present in the stripes. Especially, the z components are non zero. $\boldsymbol{M}$ and $\mathbf{L}$ are particularly strong at the domain walls.

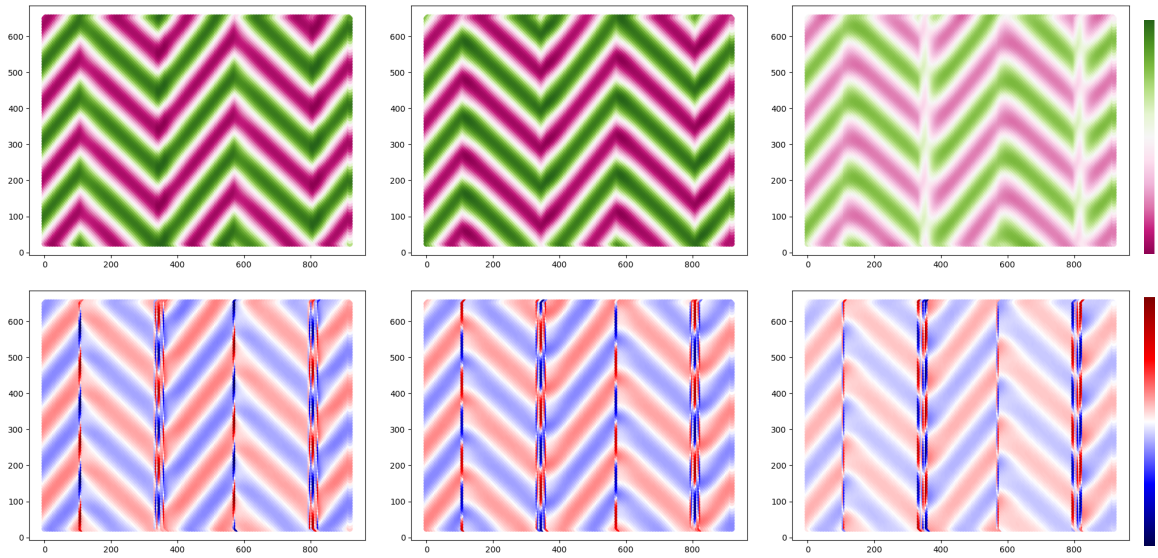

Figure 2.27: Maps of L_x, L_y L_z and M_x, M_y, M_z issued from our simulations. Without alternating DMI, $\boldsymbol{M}$ would be blank.

Confirmation of the magnetic structures by measurement of the magnetic stray field by NV-center magnetometry. Aurore Finco, Angela Haykal et Vincent Jacques at Laboratoire Charles Coulomb, Université de Montpellier - CNRS have measured the magnetic stray field generated by such stripped samples using NV-center magnetometry. A NV-center consists in a pair Nitrogen-vacancy replacing two neighboring carbons in a diamond crystal. A NV-center has a fluorescence ray which depends on the local magnetic field. The measurement of this fluorescence can be used for non-invasive local probing of magnetic field. Commonly, on a NV-center magnetometer the NV-center is placed at the tip of an cantilever hovering over the surface of the sample, similarly to an Atomic Force Microscope (*AFM*). Generally the support of the sample moves while the NV-center remains fixed, so that a laser can excite the fluorescence, measured optically.

From the maps of $\boldsymbol{M}$ and $\mathbf{L}$ (or the individual spin directions), it is possible to extract the stray field that a NV-center would see, via a dipolar field computation. The result is displayed on Figure 2.28d. The real measurement (Figure 2.28b) and the simulation (2.28d) display similar patterns. An inversion in the image can be noticed and is explained by the fact that the orientation of $\boldsymbol{P_e}$ is inverted in our simulation compared to the one of the sample. In both cases, it reveals structures at the boundary, with an enhanced magnetic stray field every second stripe only. Without the rotation at $71+71+71°$ of $\boldsymbol{P_e}$ at these domain walls, such an enhancement is not observed. On some domain walls, our $\boldsymbol{M}$ maps show that $\boldsymbol{M}$ seems to jump from red to blue. This is in fact not surprising and purely related to the direction in which the first octahedron of oxygen will chose to turn (the 'origin of the $(-1)^n$' mentioned earlier). It is not particularly clear how the oxygen arrange in reality at a domain wall, and such brutal

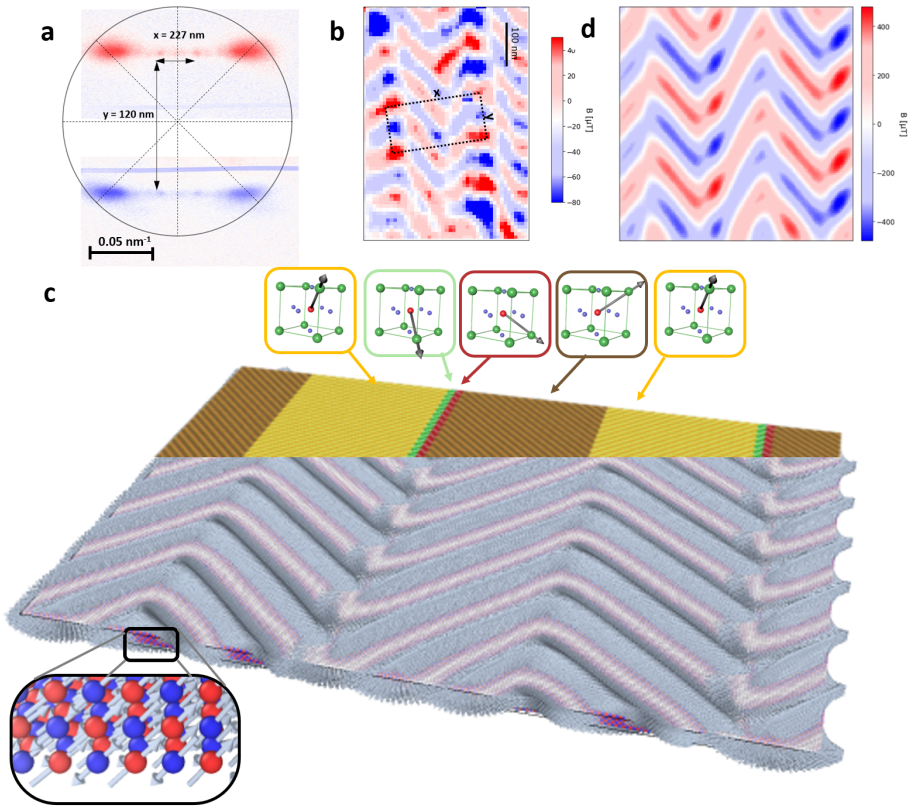

Figure 2.28: Simulation of a 71° striped $BiFeO_3$ sample. (a) Chirality as observed in the RXES diffraction pattern at the non-magnetic OK edge. (b) Magnetic stray field seen by NV-center magnetometry (Courtesy LCC Montpellier). (c) Geometry of our atomistic simulation. Ferroelectric chirality is forced at domain walls (upper side). Spins relax into chevron patterns (lower side), with complex stitching structures. (d) Stray field issued from our simulations, calculated from 2.27. The real system exhibits similar patterns.

changes of the stray field at domain walls have been measured by NV center magnetometry (Figure 2.28).

Conclusion

Our simulation could recreate magnetic structures similar to the ones observed by NV-magnetometry, based on the only assumption that the ferroelectric polarization should rotate with the same chirality at both domain walls. This result is consistent with the chirality of $\boldsymbol{P_e}$ deduced from the RXES measurements. This simulation helped us to understand the origin of the magnetic stray field, and some magnetic stitching arrangements at the domain walls. The identical chirality of $\boldsymbol{P_e}$ on both domain wall is an explanation fully compatible with all the measurements carried out.

2.4.7 Flopped state

As shown on Figure 2.29, when grown on $SrTiO_3$ (STO), which has a slightly smaller lattice constant (3.89Å, compared to 3.96Å for $BiFeO_3$), $BiFeO_3$'s cycloidal state is too constrained to exist and is destroyed. In the next chapter, we will see that in a given ferroelectric domains of a 100nm thick $BiFeO_3$ grown on (100)STO, antiferromagnetic

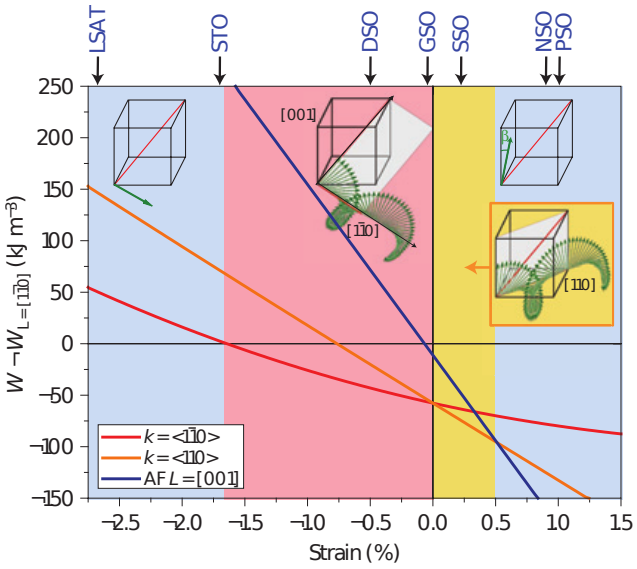

Figure 2.29: Magnetic phase diagram of strained $BiFeO_3$ films, from [90].

domains organize naturally with a typical size of 0.5µm. Under compressive strain, the antiferromagnetic vector **L** aligns along one of the $\langle 1\bar{1}0\rangle$ directions, in the (111) plane of the ferroelectricity (Figure 2.30).

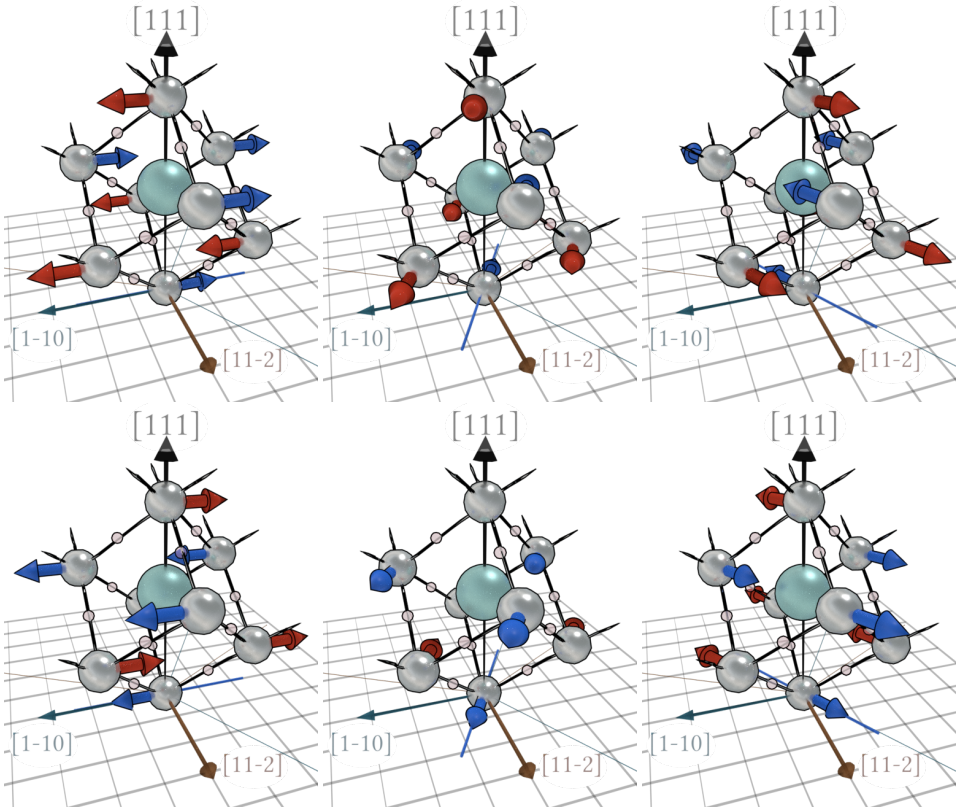

Figure 2.30: Six possible antiferromagnetic orientations of spins in $BiFeO_3$ under compressive strain ≤ 1.75%. Easy axes are $\langle 1\bar{1}0\rangle$, at 60° from one another in the (111) plane.

Since we can experimentally probe the static spin states and the dynamic behavior of such a sample, a simulation could be welcome to backup our findings. Now that the LAMMPS software correctly reproduces the behavior of the cycloids in $BiFeO_3$ and that the proper coefficients have been found to reproduce the flops of the cycloid, it will be possible to simulate the observed spin states by inducing an anisotropy flop induced by the substrate. Some steps have been made in this direction, but did not come to an end before the end of this PhD. The advances are nonetheless positive: our simulations have proven their success in the understanding of static 2D multiferroic structures, and could be as well a great help for the following works on a flopped state sample, especially with respect to the dynamical aspect that we explore in section 3.3.

2.5 Conclusion on the Simulations

In this chapter, we presented an atomistic dynamical simulation well suited for studying the antiferromagnetic states in crystals, in particular NiO and $BiFeO_3$. We illustrated how a switch could be triggered in NiO with a realistic anisotropy model, via spin transfer torques, and quantified extensively the associated dynamics, by spotting the important thresholds on the parameters. We also showed that the same computational approach could simulate the behavior of a multiferroic material with magnetoelectric coupling of the level of complexity of $BiFeO_3$. The simulation has proven been central to the understanding of chiral structures in thin films.

The next chapters deal with the same concerns (probing, exciting, switching and generating antiferromagnetic structures) from an experimental approach.

Chapter 3

Experimental Study of Ultrafast Dynamics in a Magneto-Electric Antiferromagnet

3.1 Imaging by Second Harmonic Generation (SHG)

3.1.1 Motivations: optical measurement of antiferromagnets

Since antiferromagnets present no net magnetization, conventionnal magnetometry measurements cannot probe their state. An exception to this rule is when dealing with canted antiferromgnets, for which a magnetic moment is present, or when a temporary magnetization can be induced by coherent dynamics of spins [42]. Except from these, the methods for measuring antiferromagnetic states are comparatively rare.

Neutron diffraction is a method of choice for bulk crystals of antiferromagnets, but are rarely used for thin layers because the intensity is in general very low. It is however feasible to get some useful information in thin films, but usually at the price of long counting times. Similar information can be obtained with synchrotron beams with signals orders of magnitude more intense (but often harder to quantify). Regarding optical laboratory techniques, probing antiferromagnets remains challenging. The magnetic texture at the surfaces of antiferromagnets are more commonly observed using *spin polarized scanning tunneling microscopy*. The first measurement for which the antiferromagnet was measured as an active element was done by Reference [99], where they showed that a tunnel junction based on the antiferromagnet IrMn exhibits a strong spin-valve-like behavior. Moreover, if the antiferromagnet is metallic, it can be measured with anisotropic magneto-resistance. This technique is one of the most promising for integration in devices, as it was historically used in the proof of concept of Reference [32]. On the other hand, antiferromagnetic insulators cannot be directly probed electrically. The 'spin-Hall Magneto-Resistance' (SMR) can nevertheless be used when a heavy metal is deposited on the AF. The spin-dependent transparency of the interface in these bilayers adds a small resistive contribution that depends on the AF vector orientation from the current lines. The technique has been applied to global measurements of the AF direction, but it gives no mi-

croscopic details and suffers from a very low efficiency. For electrical measurements to be possible, they should be coupled somehow to a metallic layer, which limits their compatibility with the 'insulatronics' and the low heat loss advantages they promise.

The other limitation of electrical measurements concerns the response time. The shortest signals experimentalists can get electrically are barely below the picosecond, while optical signals can reach femtosecond speed. We have seen that the dynamics of the antiferromagnets are in the picosecond range. Only measurements involving shorter phenomena can probe their dynamics with sufficient resolution. For reaching the sub-picosecond dynamical regime, because the electronics in the terahertz regime is still under developmental, and higher frequencies are not available, one has no choice but using optical methods. Several of them are usable to probe the antiferromagnetic order (Magnetic Linear Dichroism in the visible (MLD) for crystals; Magnetic birefringeance; Xrays Magnetic Linear[1] Dichroism (XMLD) with Photo-Emission Electron Microscopy (PEEM); SHG) [42], and even conventional magnetometry could measure the dynamical changes in spin ordering via the temporary magnetization induced by the stimulation. [100, 42]

The second motivation for the use of optical techniques is that they have shown relativelly good efficiency in manipulating the antiferromagnetic order [101, 102, 103, 104], whereas static magnetic fields needed for achieving the same goal are comparatively extremely high ($1-50$ Tesla). Many of the optical methods compatible with time resolution use synchrotron radiation. Synchrotrons are versatile facilities, which can probe the matter in many various ways, but their accessibility is limited. Other methods, such as SHG, can use table top lasers. The time resolution can be obtained using femtosecond lasers, which have benefited from huge developments over the past decades and are now reasonably affordable for optical laboratories.

In this thesis work, the experimental measurements use second harmonic generation, an optical method suitable for probing symmetry breakings in crystals. The SHG technique is possible with Ti:Sapphire femtosecond lasers, which make it convenient, compatible with time-resolved measurements and and easily adaptable.

3.1.2 State of the art of the SHG applied to antiferromagnets

Second Harmonic Generation is a phenomenon that typically occurs in crystals that break time-space inversion symmetry. Light traveling through or reflected by such crystals can exit partially converted into light of double frequency. In fact, two photons can combine and re-emit another photon whose frequency is the sum of those of the two (Figure 3.1).

Second Harmonic generation has proven to be a powerful tool for probing electric and magnetic structures [106]. Because the second harmonic can be generated by various and very subtle effects, it was shown suitable for imaging centrosymmetric or non-centrosymmetric structures, with or without centrosymmetric magnetic order. For each of the four possible cases, a different measuring procedure must be used, as detailed in Reference [106]. In particular, antiferromagnetism was observed using this technique on non-centrosymmetric Cr_2O_3 [107, 108] (Figure 3.2) and even on centrosymmetric NiO [109] (Figure 3.2) A step further was achieved on multiferroic $YMnO_3$

[1] Xray Magnetic *Circular* Dichroism with PEEM does not work for probing the antiferromagnetic order.

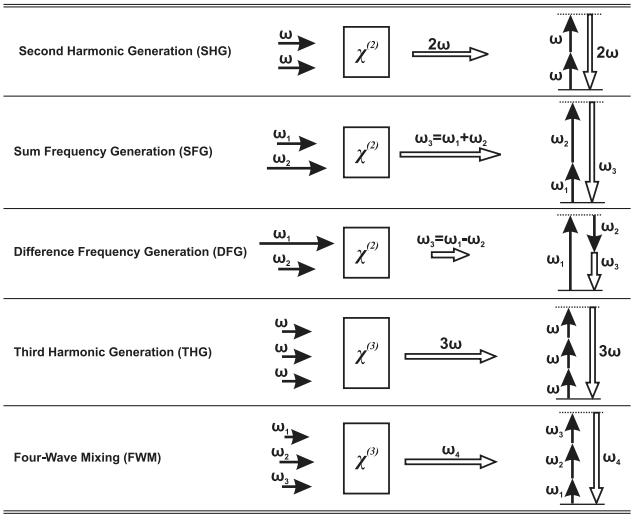

Figure 3.1: Non linear optical phenomena, from [105].

[110], by decoupling the ferroelectric and antiferromagnetic contributions (Figure 3.2).

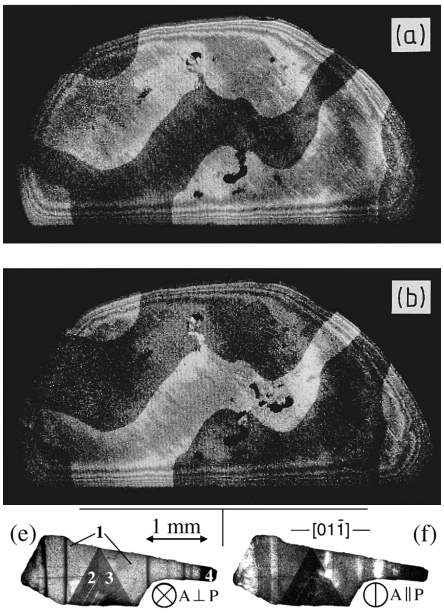

(a) and **(b)**: Cr_2O_3 seen in SHG imagery by Reference [107] for (a) right and (b) left circular polarized light. **(e)** and **(f)**: NiO seen in SHG imagery by Reference [109] with parallel or perpendicular orientations of the polarizer and analyzer.

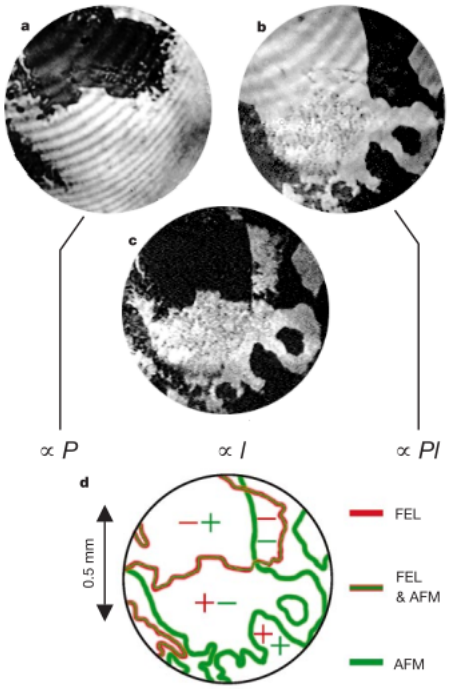

$YMnO_3$ seen in SHG imagery by Reference [110] after interfering with the adequate reference beams to distinguish the different multiferroic domains.

Figure 3.2: SHG imaging of the antiferromagnets Cr_2O_3,NiO and $YMnO_3$.

Several second harmonic generation measurements were done on $BiFeO_3$, notably the extraction of its susceptibility coefficients [111, 112]. SHG imaging of $BiFeO_3$ was used by Reference [113] to observe the change of the antiferromagnetic texture under several stimuli (heat, change of ferroelectric polarization, voltage and light). A

modification of the antiferromagnetic texture was reported, but not controlled. One of the objectives of this PhD work was to acheive a control of antiferromagnetic domains, spatially or dynamically.

3.1.3 Theory of the second harmonic generation

Harmonic generation

An incident electromagnetic wave $\{\boldsymbol{E},\boldsymbol{B}\}$ acts on a crystal as a small perturbation on the electron positions due to Lorentz forces (Figure 3.3). The shift from the rest position creates a small local oscillating electric dipole $\boldsymbol{P}$ in the

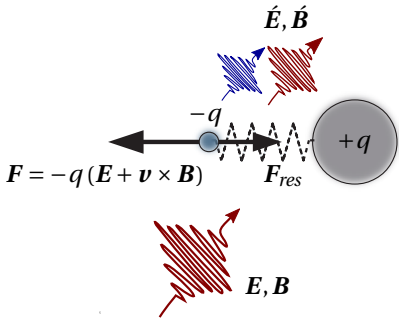

Figure 3.3: Spring model of the second harmonic generation [105].

material, and as one knows, an accelerated charge acts as a source of light. Likewise, a local rotation of the charges causes a magnetic dipole $\boldsymbol{M}$ which, when varying in time, also contributes to the light emission. Electric dipole and magnetic moments are only the first terms of the expansion, and the actual time-varying electromagnetic distribution can always be decomposed into a *multipole expansion*, which re-emits light $\{\acute{\boldsymbol{E}},\acute{\boldsymbol{B}}\}$ when accelerated, according to the same logic.

Following Maxwell's equations, the mathematical formula reads [105]:

$$\boxed{\nabla^2\acute{\boldsymbol{E}}-\mu\varepsilon_0\frac{\partial^2\acute{\boldsymbol{E}}}{\partial t^2}=\mu\frac{\partial^2\boldsymbol{P}}{\partial t^2}}+\mu\nabla_\times\frac{\partial\boldsymbol{M}}{\partial t}-\mu\nabla\frac{\partial^2\underline{\boldsymbol{Q}}}{\partial t^2}+\ldots \tag{3.1}$$

where the source terms on the right hand side are the multipole expansion approaching the variation in the geometry of the charge and magnetic distributions. We define an electric dipole $\boldsymbol{P}$, a magnetic dipole $\boldsymbol{M}$, an electric quadrupolar term $\underline{\boldsymbol{Q}}$... the expansion could go on, but the two later contributions are already in general such small corrections compared to the one due to electric dipole when dealing with atoms, that they are largely neglected when $\boldsymbol{P}$ exists, and so will they in the rest of this thesis. Each of these source terms are generated by the incident

electromagnetic field $\{\boldsymbol{E}, \boldsymbol{B}\}$ and can be expanded as such:

$$\boxed{P_i} = \boxed{\chi^{ee}_{ij} E_j} + \chi^{em}_{ij} B_j + \boxed{\chi^{eee}_{ijk} E_j E_k} + \chi^{eem}_{ijk} E_j B_k + \chi^{emm}_{ijk} B_j B_k + \dots \tag{3.2a}$$

$$M_i = \chi^{me}_{ij} E_j + \chi^{mm}_{ij} B_j + \chi^{mee}_{ijk} E_j E_k + \chi^{mem}_{ijk} E_j B_k + \chi^{mmm}_{ijk} B_j B_k + \dots \tag{3.2b}$$

$$Q_{ij} = \underbrace{\chi^{qe}_{ijk} E_k + \chi^{qm}_{ijk} B_k}_{\text{Linear optics}} + \underbrace{\chi^{qee}_{ijkl} E_k E_l + \chi^{qem}_{ijkl} E_k B_l + \chi^{qmm}_{ijkl} B_k B_l + \dots}_{\text{Non-linear optics}} \tag{3.2c}$$

Superscripts label the electric or magnetic parts of the susceptibility tensors χ and subscripts refer to space components, for which we used the Einstein summation convention. Physically, it can be easily understood with a simple non-linear spring model (Figure 3.3), neglecting the Lorentz's term $\boldsymbol{v} \times \boldsymbol{B}$ for the sake of clarity. At first order, the electrons follow the electric field in their harmonic potential well and the electric dipole they induce by oscillating is linear with the incident electric field $\boldsymbol{E}$. But any anharmonicity in the potential well of the electrons can generate quadratic or higher order terms, and therefore higher harmonics in the light they re-emit (Figure 3.4). In that picture, the different χ coefficients are directly linked to the anharmonicities of the local potential. In particular, *even orders in the development will give non-symmetric contributions to the potentials, and thus will be linked to the broken symmetries in the crystal.* This statement is central in the second harmonic generation imaging techniques.

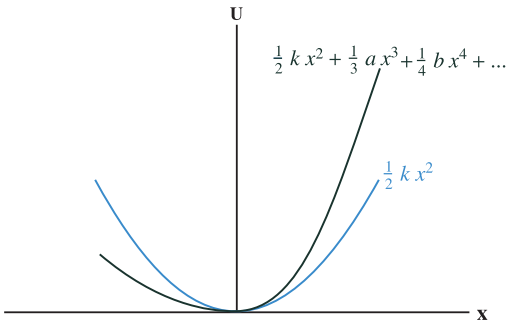

Figure 3.4: Non-symmetric potential well and its Taylor expansion.

In the upper expansion of the source terms, $\boldsymbol{B}$ terms are weaker by a factor $1/c$ compared to those in $\boldsymbol{E}$, and are totally obscured by terms in $\boldsymbol{E}$ if allowed by the crystal symmetries. In that case, we can reasonably keep only the boxed terms in equation (3.2a) [2].

If we keep only the leading electric terms of the dipolar contribution in the source terms, we get the simpler Taylor expansion:

$$\boldsymbol{P} = \boldsymbol{P}_0 + \underline{\boldsymbol{\chi}^{ee}} \boldsymbol{E} + \underline{\underline{\boldsymbol{\chi}^{eee}}} \boldsymbol{E}\boldsymbol{E} + \underline{\underline{\underline{\boldsymbol{\chi}^{eeee}}}} \boldsymbol{E}\boldsymbol{E}\boldsymbol{E} + \cdots \tag{3.3}$$

[2] This thesis work will apply second harmonic generation techniques on $BiFeO_3$, which is in the first approximation in the $3m$ symmetry point group (space group $R3c$), and is even in m if we take into account the magnetism, therefore allowing nonzero terms in $\underline{\boldsymbol{\chi}^{ee}}$ and $\underline{\underline{\boldsymbol{\chi}^{eee}}}$ which justifies this simplification. A sanity check based on crystal symmetries should always be done before transposing the exposed results to other materials. In particular, NiO is centrosymmetric and therefore $\underline{\underline{\boldsymbol{\chi}^{eee}}}$ is not allowed for this crystal. We also would like to recall that $\underline{\underline{\underline{\boldsymbol{\chi}^{eeee}}}}$ is of odd order, and is therefore always allowed, even in centrosymmetric crystals.

Or, more explicitly:

$$\boldsymbol{P}(t) = \boldsymbol{P}_0(t) + \varepsilon_0 \left(\underline{\boldsymbol{\chi}^{(1)}} \boldsymbol{E}(t) + \underline{\underline{\boldsymbol{\chi}^{(2)}}} : [\boldsymbol{E}(t) \otimes \boldsymbol{E}(t)] + \underline{\underline{\underline{\boldsymbol{\chi}^{(3)}}}} \vdots [\boldsymbol{E}(t) \otimes \boldsymbol{E}(t) \otimes \boldsymbol{E}(t)] + \cdots \right) \tag{3.4a}$$

$$\stackrel{\text{def}}{=} \boldsymbol{P}^{(0)} + \boldsymbol{P}^{(1)} + \boldsymbol{P}^{(2)} + \boldsymbol{P}^{(3)} + \cdots \tag{3.4b}$$

$$= \sum_k \boldsymbol{P}^{(k)} \tag{3.4c}$$

where $\otimes$ denotes the *tensor product*, : and $\vdots$ the double dot products. χ are *electric susceptibility* tensors, with their superscripts marking the order they refer to in the Taylor series. One must add 1 to this number to get the tensor rank. For instance, $\underline{\boldsymbol{\chi}^{(1)}}$ is a 2D matrix, and $\underline{\underline{\boldsymbol{\chi}^{(2)}}}$ is a third rank tensor. As it will be illustrated later in section 3.1.4, the even order susceptibilities are related to the fact that the material is non-centrosymmetric due to its internal broken symmetries.

The tensor products in the expansion are responsible for the generation of harmonics. Let us suppose a monochromatic incident light $E\cos(\omega t)$ excites the sample. $[\boldsymbol{E}(t) \otimes \boldsymbol{E}(t)]$ will generate terms in $\cos(\omega t)\cos(\omega t) = \frac{1+\cos(2\omega t)}{2}$, that is, light at different frequencies.

Second harmonic terms

Because of the linearity of equation (3.1), any harmonic from $\boldsymbol{P}$ will create the same corresponding harmonic for the re-emitted field $\boldsymbol{E}$. But because of the non-linearities in equation (3.4a), a monochromatic incident field $\boldsymbol{E}^{(\omega)}$ will create several harmonics for $\boldsymbol{P}$, hence a polychromatic emitted light.

$$\boldsymbol{P} = \sum_N \boldsymbol{P}^{[N\omega]} \tag{3.5a}$$

$$= \sum_k \sum_{N \leq k} \boldsymbol{P}^{(k)[N\omega]} \tag{3.5b}$$

In our notation, the superscript between brackets refers to the frequency dependence, while the superscript between parenthesis refers to the order in the expansion (3.4b).

High harmonic terms get contributions from all higher tensor ranks, and because of trigonometric multiplication rules, harmonic $N\omega$ can only be generated by orders higher or equal to N in the expansion (we always have $N \leq k$). In particular, it is easy to see in the expansion (3.4a) that $\boldsymbol{P}^{(0)}$ contributes to the zeroth harmonic, $\boldsymbol{P}^{(1)}$ contributes to the first harmonic and, using the trigonometric composition formula $\cos(\omega t)\cos(\omega t) = \frac{1+\cos(2\omega t)}{2}$ that $\boldsymbol{P}^{(2)}$, as a product of two iso-periodic time dependent terms, contributes to the zeroth and the second harmonics.

$$\boldsymbol{P}^{(2)} = \varepsilon_0 \underline{\underline{\boldsymbol{\chi}_{\boldsymbol{e}}^{(2)}}} : \left(\boldsymbol{E}^{[\omega]} \otimes \boldsymbol{E}^{[\omega]} \right) \tag{3.6}$$

$$= \boldsymbol{P}^{(2)[0\omega]} + \boldsymbol{P}^{(2)[2\omega]} \tag{3.7}$$

The second harmonic generation appears in the second term $\boldsymbol{P}^{(2)[2\omega]}$, and the continuous term $\boldsymbol{P}^{(2)[0\omega]}$ is an *optical rectification* term. On a quantum scheme, this corresponds to a two-photons absorption process: two photons are absorbed by the crystal on a virtual state which instantly and coherently remit a photon of the sum of the two frequencies (Figure 3.5). This process can be extended to the case of two different incident frequencies ω_1 and ω_2, which can re-emit photons at $\omega_1+\omega_2$ (*Sum Frequency Generation*) and $|\omega_1-\omega_2|$ (*Difference Frequency Generation*) (Figure 3.1).

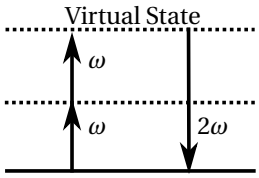

Figure 3.5: Two photons absorption model.

Higher even order tensor ranks also contribute to the second harmonic generation, but often to a weaker extent, since $\underline{\underline{\underline{\underline{\boldsymbol{\chi}^{(4)}}}}}$ and higher have generally much smaller[3] terms than $\underline{\underline{\underline{\boldsymbol{\chi}^{(2)}}}}$. In some cases, $\underline{\underline{\underline{\underline{\boldsymbol{\chi}^{(3)}}}}}$ and odd orders can also generate terms assimilated to second harmonic. Indeed, $\underline{\underline{\underline{\underline{\boldsymbol{\chi}^{(3)}}}}} : [\boldsymbol{E}(t)\otimes\boldsymbol{E}(t)\otimes\boldsymbol{E}(t)]$ normally only generates terms in ωt and $3\omega t$, but if another light at slow frequency Ω is present, light of frequency $2\omega\pm\Omega$ can be generated and assimilated to second harmonic, provided $\Omega << \omega$.

If the crystal has space-time inversion centrosymmetry, necessarily $\underline{\underline{\underline{\boldsymbol{\chi}^{(2)}}}}$ and all other even order terms are reduced to zero. Contributions from $\underline{\underline{\underline{\underline{\boldsymbol{\chi}^{(3)}}}}}$ may start to be dominant . Likewise, all the other tensors we neglected in equations 3.2a can start to play a non-negligible part.

If we sum all the electric dipolar contributions to the second harmonic, we get:

$$\boldsymbol{P}^{[2\omega]} = \underbrace{\boldsymbol{P}^{(1)[2\omega]}}_{=0} + \boldsymbol{P}^{(2)[2\omega]} + \underbrace{\boldsymbol{P}^{(\geq 3)[2\omega]}}_{weak} \tag{3.8a}$$

$$= \boldsymbol{P}^{(2)[2\omega]} + \left(\boldsymbol{P}^{(\geq 3)[2\omega]}\right) \tag{3.8b}$$

$$= \boldsymbol{P}^{(2)} - \boldsymbol{P}^{(2)[0\omega]} + \left(\boldsymbol{P}^{(\geq 3)[2\omega]}\right) \tag{3.8c}$$

$$\underbrace{\boldsymbol{P}^{[2\omega]}}_{Total\ SHG} = \underbrace{\varepsilon_0 \underline{\underline{\underline{\boldsymbol{\chi}^{(2)}}}}\boldsymbol{E}\boldsymbol{E}}_{Second\ Order} - \underbrace{\boldsymbol{P}^{(2)[0\omega]}}_{DC} + \underbrace{\left(\boldsymbol{P}^{(\geq 3)[2\omega]}\right)}_{Higher\ Orders} \tag{3.8d}$$

The term $\boldsymbol{P}^{(2)[0\omega]}$ is a constant ('DC') electric dipole when the laser excitation frequency ω is of infinite duration. In the case of a pulse, for which the envelope can be considered sufficiently slow with respect to the frequency ω, the "DC" electric dipole will also be time-dependent and follow a variation related to the one of the envelope. The acceleration of this electric dipolar variation emits light too. The phenomenon is called *optical rectification*. For example, for a femtosecond pulse on $BiFeO_3$, the optical rectification gives a reemission in the THz range [36].

[3] Counter-examples can certainly be found, depending on the inner crystal structure, but let's take it as a general rule, as such crystal must be very rare.

Isolating the second harmonic light with optical filters means keeping only the second harmonic terms in the linear equation (3.1). We get:

$$\nabla^2 \acute{\boldsymbol{E}}^{[2\omega]} - \mu\varepsilon_0 \frac{\partial^2 \acute{\boldsymbol{E}}^{[2\omega]}}{\partial t^2} \simeq \mu \frac{\partial^2 \boldsymbol{P}^{[2\omega]}}{\partial t^2} \tag{3.9a}$$

$$\simeq \mu \underbrace{\frac{\partial^2 \boldsymbol{P}^{(2)}}{\partial t^2}}_{\textit{Second Order}} - \mu \underbrace{\frac{\partial^2 \boldsymbol{P}^{(2)^{[0\omega]}}}{\partial t^2}}_{\textit{Opt. Rect.}} + \underbrace{\left(\mu \frac{\partial^2 \boldsymbol{P}^{(\geq 3)\,[2\omega]}}{\partial t^2}\right)}_{\textit{Higher Orders}} \tag{3.9b}$$

Except when explicitly stated, the higher order terms in the expansion will be neglected in the rest of this thesis. The optical rectification $\boldsymbol{P}^{(2)^{[0\omega]}}$ has a much slower time variation comparatively to the one of $\boldsymbol{P}^{[2\omega]}$, so its acceleration will be much lower, and we can approximate $\frac{\partial^2 \boldsymbol{P}^{[2\omega]}}{\partial t^2} \simeq \frac{\partial^2 \boldsymbol{P}^{(2)}}{\partial t^2}$. To sum up, the second harmonic of the re-emitted light $\acute{\boldsymbol{E}}^{[2\omega]}$ is proportional to the acceleration of $\boldsymbol{P}^{[2\omega]}$, whose main contribution accounts for the one of $\boldsymbol{P}^{(2)}$ and will therefore mostly give us informations about $\underline{\underline{\boldsymbol{\chi}^{(2)}}}$, directly linked to the crystal symmetry. This is how the second harmonic generation is related to the crystal symmetries and can be used as a probing technique.

3.1.4 Using second harmonic generation to probe crystal structure

From an experimentalist point of view, one can shine a monochromatic light on a given crystal and use optical filters to only keep the generated second harmonic. As mentionned previously and detailed in this section, the light collected will be at first order directly linked to $\underline{\underline{\boldsymbol{\chi}_{\boldsymbol{e}}^{(2)}}}$, whose non-zero terms give precious informations about the crystal symmetry.

Let us focus on the second order term:

$$\boldsymbol{P}_i^{(2)} = \sum_{ijk} \chi_{ijk}^{(2)} E_j E_k \tag{3.10}$$

Since $E_j E_k = E_k E_j$ for every k and j, we have $\chi_{ikj}^{(2)} = \chi_{ijk}^{(2)}$ and the three-dimensional tensor $\underline{\underline{\boldsymbol{\chi}^{(2)}}}$ can be represented

in a contracted form according to the following process [105]:

$$\underline{\underline{\boldsymbol{\chi}^{(2)}}} = \begin{array}{|ccc|} \hline \chi_{311} & \chi_{312} & \chi_{313} \\ \chi_{321} & \chi_{322} & \chi_{323} \\ \chi_{331} & \chi_{332} & \chi_{333} \\ \hline \end{array} \begin{array}{|ccc|} \hline \chi_{211} & \chi_{212} & \chi_{213} \\ \chi_{221} & \chi_{222} & \chi_{223} \\ \chi_{231} & \chi_{232} & \chi_{233} \\ \hline \end{array} \begin{array}{|ccc|} \hline \chi_{111} & \chi_{112} & \chi_{113} \\ \chi_{121} & \chi_{122} & \chi_{123} \\ \chi_{131} & \chi_{132} & \chi_{133} \\ \hline \end{array} \tag{3.11a}$$

$$= \begin{array}{|ccc|} \hline \chi_{311} & \chi_{312} & \chi_{313} \\ \chi_{321} & \chi_{322} & \chi_{323} \\ \chi_{331} & \chi_{332} & \chi_{333} \\ \hline \end{array} \begin{array}{|ccc|} \hline \chi_{211} & \chi_{212} & \chi_{213} \\ \chi_{221} & \chi_{222} & \chi_{223} \\ \chi_{231} & \chi_{223} & \chi_{233} \\ \hline \end{array} \begin{array}{|ccc|} \hline \chi_{111} & \chi_{112} & \chi_{113} \\ \chi_{112} & \chi_{122} & \chi_{123} \\ \chi_{113} & \chi_{123} & \chi_{133} \\ \hline \end{array} \tag{3.11b}$$

$$= \begin{bmatrix} \chi_{111} & \chi_{122} & \chi_{133} & \chi_{123} & \chi_{113} & \chi_{112} \\ \chi_{211} & \chi_{222} & \chi_{233} & \chi_{223} & \chi_{213} & \chi_{212} \\ \chi_{311} & \chi_{322} & \chi_{333} & \chi_{323} & \chi_{313} & \chi_{312} \end{bmatrix} \tag{3.11c}$$

$$\overset{\text{def}}{=} \begin{bmatrix} \chi_{11} & \chi_{12} & \chi_{13} & \chi_{14} & \chi_{15} & \chi_{16} \\ \chi_{21} & \chi_{22} & \chi_{23} & \chi_{24} & \chi_{25} & \chi_{26} \\ \chi_{31} & \chi_{32} & \chi_{33} & \chi_{34} & \chi_{35} & \chi_{36} \end{bmatrix} \tag{3.11d}$$

The two last representations imply that the product $\boldsymbol{E} \otimes \boldsymbol{E}$ is written $\begin{bmatrix} E_1^2 \\ E_2^2 \\ E_3^2 \\ 2E_2E_3 \\ 2E_1E_3 \\ 2E_1E_2 \end{bmatrix}$, so that the tensor relation (3.10) is respected:

$$\boldsymbol{P}^{(2)} = \begin{bmatrix} \chi_{11} & \chi_{12} & \chi_{13} & \chi_{14} & \chi_{15} & \chi_{16} \\ \chi_{21} & \chi_{22} & \chi_{23} & \chi_{24} & \chi_{25} & \chi_{26} \\ \chi_{31} & \chi_{32} & \chi_{33} & \chi_{34} & \chi_{35} & \chi_{36} \end{bmatrix} \begin{bmatrix} E_1^2 \\ E_2^2 \\ E_3^2 \\ 2E_2E_3 \\ 2E_1E_3 \\ 2E_1E_2 \end{bmatrix} \tag{3.12}$$

According to Neumann's theorem, the χ components are directly related to the symmetry of the lattice. For

example, for a tetragonal 4mm crystal (like $PbZrTiO_3$ or $BaTiO_3$), $\chi_{31} = \chi_{32} = \chi_{24} = \chi_{15}$ and all the other terms except χ_{33} are zero. For a fully symmetric crystal (cubic m4m), all the terms are null. Every symmetry breaking in the lattice creates a contribution in χ, accounting for the fact that the symmetry of the potential well of the electrons is broken, and thus acts on $\boldsymbol{P}$. The stronger the breaking, the more it weights in χ.

The potential well of the electrons can be non-centrosymmetric either because of broken spatial symmetries in the electron environment, or because of symmetry breaking concerning the magnetization and electric currents. In the later case case we traditionally say that the time-reversal symmetry is broken. The susceptibility tensors are linear, thus contributions simply add up:

$$\underline{\underline{\boldsymbol{\chi}_e^{(2)}}} = \underline{\underline{\boldsymbol{\chi}_e^{(2)(i)}}} + \underline{\underline{\boldsymbol{\chi}_e^{(2)(c)}}} \tag{3.13}$$

$\underline{\underline{\boldsymbol{\chi}_e^{(2)(i)}}}$ is called the time-*invariant* part of the tensor, and $\underline{\underline{\boldsymbol{\chi}_e^{(2)(c)}}}$ is its time-*covariant* part [106][114][4].

Mathematically, using the complex notation $e^{i\omega t}$, a simple time-reversal operator $\widehat{T}$ would be the conjugation operator [114][5] [115][6].

$$\widehat{T}\underline{\underline{\boldsymbol{\chi}}} = \underline{\underline{\boldsymbol{\chi}}}^* \tag{3.14}$$

In this simple scheme, $\underline{\underline{\boldsymbol{\chi}_e^{(2)(i)}}}$ to be invariant under $\widehat{T}$ needs to be real, while $\underline{\underline{\boldsymbol{\chi}_e^{(2)(c)}}}$ to change sign under time reversal symmetry needs to be pure imaginary. This is a simple scheme and near resonnance, both suceptibilty tensors are actually complex since absorbtion phenomena occur. Some authors argue that in the context of nonlinear optics, the *time-reversal* symmetry is strictly speaking not a good symmetry because the light propagation should be reversed as well, and the term *spin-reversal* symmetry should be prefered [116]. Nonetheless, far from resonnance, this subtelty can be neglected, we will assume orthogonality of $\underline{\underline{\boldsymbol{\chi}_e^{(2)(i)}}}$ and $\underline{\underline{\boldsymbol{\chi}_e^{(2)(c)}}}$ in the complex plane later in this thesis, and keep the *time-reversal* terminology.

3.1.5 Tensor rotation from crystal frame to laboratory frame

Let us consider a crystal with $3m$ point group symmetry. The symmetries of the crystal annihilate some components in the expression of the susceptibility tensor, when expressed in its own frame. Handbooks such as Reference [114] express all possible permitted terms for all possible symmetry point groups. For $3m$ symmetry, defining our basis with the third coordinate along the highest symmetry axis ([111] with symmetry 3) and the second coordinate along the second highest symmetry axis ([11$\bar{2}$] with symmetry $\bar{2}$) [114][7], we get:

$$\underline{\underline{\boldsymbol{\chi}^{(2)}}} = \begin{bmatrix} \chi_{11} & -\chi_{11} & 0 & 0 & \chi_{31} & 0 \\ 0 & 0 & 0 & \chi_{31} & 0 & -\chi_{11} \\ \chi_{31} & \chi_{31} & \chi_{33} & 0 & 0 & 0 \end{bmatrix} \tag{3.15}$$

Therefore, for the electric field of the light expressed in the crystal frame, the second harmonic generation will

[4] p102
[5] p74-83
[6] p141-144
[7] p57

simply be:

$$\boldsymbol{P}^{(2)} = \begin{bmatrix} \chi_{11} & -\chi_{11} & 0 & 0 & \chi_{31} & 0 \\ 0 & 0 & 0 & \chi_{31} & 0 & -\chi_{11} \\ \chi_{31} & \chi_{31} & \chi_{33} & 0 & 0 & 0 \end{bmatrix} \begin{bmatrix} E_1^2 \\ E_2^2 \\ E_3^2 \\ 2E_2E_3 \\ 2E_1E_3 \\ 2E_1E_2 \end{bmatrix} \tag{3.16a}$$

$$= \begin{bmatrix} \chi_{11}\left(E_1^2 - E_2^2\right) + \chi_{31}2E_1E_3 \\ \chi_{31}2E_2E_3 - \chi_{11}2E_1E_2 \\ \chi_{31}\left(E_1^2 + E_2^2\right) + \chi_{33}E_3^2 \end{bmatrix} \tag{3.16b}$$

Nonetheless, it is not always handy to express the light in the crystal frame. In the case of polycrystals or in the context of domain writing (where domains natural frame are subject to change), it is much more natural to express the tensors in the laboratory frame. For that, we need to operate a rotation on the susceptibility tensor to express it in the laboratory frame, for each possible domain orientation. Let's call $\underline{\boldsymbol{R}}$ the rotation matrix that moves the basis vectors of the crystal frame to those of the laboratory frame, the tensor expressed in the laboratory frame is:

$$\chi_{ijk}^{[lab\ frame]} = \sum_{l,m,n} R_{il}R_{jm}R_{kn}\chi_{lmn}^{[crystal\ frame]} \tag{3.17}$$

Note that several rotations like this can be achieved successively to reach the lab frame.

3.1.6 Probing electric fields by second harmonic generation

When a static electric field $\boldsymbol{E}^{[0]}$ is present additionally to the incoming light $\boldsymbol{E}^{\{\omega\}}$, the second order susceptibility tensor will generate light at 0, ω, 2ω via all the combinations of $\{i,j\}$ in $\underline{\underline{\boldsymbol{\chi}}}^{(2)}\boldsymbol{E}^i\boldsymbol{E}^j$. Likewise, the third order susceptibility tensor $\underline{\underline{\underline{\boldsymbol{\chi}}}}^{(3)}$ will generate light at 0, ω, 2ω and 3ω via $\underline{\underline{\underline{\boldsymbol{\chi}}}}^{(3)}\boldsymbol{E}^i\boldsymbol{E}^j\boldsymbol{E}^k$. We see that the third order susceptibility generates second harmonic. In particular, the term producing 2ω light is $\underline{\underline{\underline{\boldsymbol{\chi}}}}^{(3)}\boldsymbol{E}^\omega\boldsymbol{E}^\omega\boldsymbol{E}^0$ and is "proportional" to the static electric field $\boldsymbol{E}^{[0]}$. This can be used to probe electric fields. $\underline{\underline{\underline{\boldsymbol{\chi}}}}^{(3)}$ is always allowed by symmetry, so it can even be a leading term in centrosymmetric crystals.

With the same logic, an electric field $\boldsymbol{E}^{[\Omega]}$ at frequency Ω will produce light at $|2\omega \pm \Omega|$ (among others) via the third order susceptibility tensor. If the variation is slow enough ($\Omega << \omega$), these frequencies will be seen as second harmonic terms ($|2\omega \pm \Omega| \simeq 2\omega$). This technique is used for measuring terahertz fields [117].

3.1.7 Experimental setup for SHG microscopy

Our experimental setup (Figure 3.6) uses Laser pulses emitted from amplified Ti-Sapphire LIBRA form Coherent whose energy (wavelength) can be continuously adjusted by Optical Parametric Amplification (OPA) from $0.47eV$ to $2.34eV$ ($2600nm$ to $530nm$). The linearly polarized light exiting the laser system is optimized by a Glan polarizer and its direction of polarization can be rotated using a $\lambda/2$ waveplate. A set of long-pass optical density filter (FGL780S) and interference filter (FELH0750) ensures that no second harmonic light is shone on the sample. After the sample, an interference short-pass filter (FESH0750) immediately suppresses the first harmonic before the light is collected in an objective lens ($\times 50$ N.A. = 0.7) for a wide-field imaging of the sample. Finally, an analyzer in vertical position and two optical density filters (BG39 and GG380) meant to filter out the fundamental and third harmonic lights from the optical path are inserted just before a Peltier cooled CCD camera ($-50°C$). The references of the main filters are listed in appendix F.

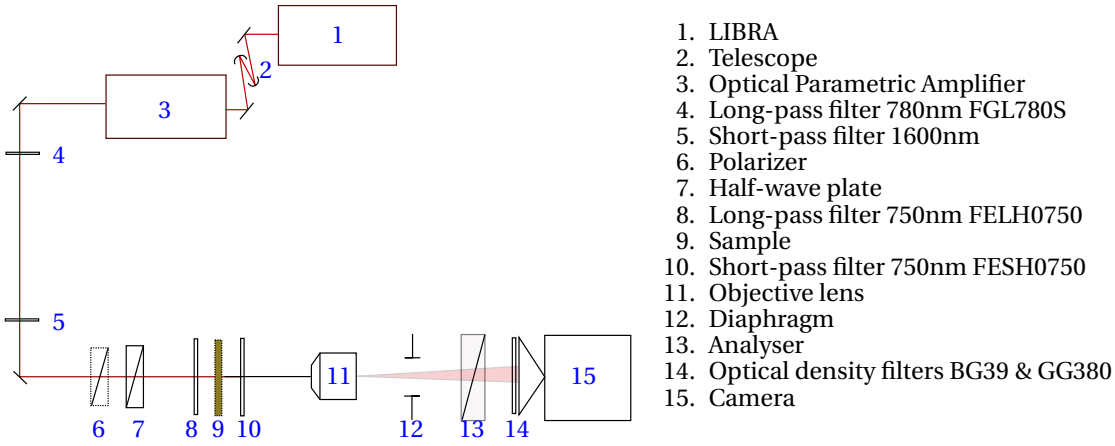

Figure 3.6: Experimental setup for SHG microscopy.

The laser, after passing through the optical parametric amplifier can deliver up to 120µJ during 100fs on the sample, for a repetition rate of 1kHz. The duration is too short and the repetition too large to induce an increase of temperature larger than 10K in the sample. Moreover, the second harmonic signal is proportional to the square of the amplitude of the electric field, that is why short duration high amplitude pulses are well suited.

3.1.8 Application: imaging of a piezoelectric

Though presenting no magnetic ordering, we would like to illustrate this SHG microscopy technique on a sample of $PbZrTiO_3$ (PZT). Indeed, it is one of the most piezoelectric materials, thus its crystal structure can be tunned by simple application of a voltage. This was a preliminary study that we carried out aside from our antiferromagnetic concerns, to assess its feasibility, but it also constitutes a good introduction to the technique.

Description of the sample

An epitaxial thin film of PZT grown on (001)$SrTiO_3$ by Pulsed Laser Deposition (PLD) was provided by Sylvia Matzen from Center for Nanoscience and Nanotechnology (C2N) UMR CNRS. It was delivered to us with interdigited electrical contacts of Pt on it, deposited by lithography (Figure 3.7a).

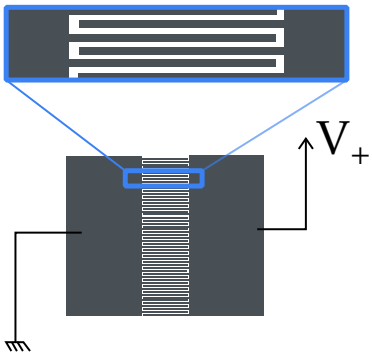

(a) Sketch of the Pt electrodes deposited on PZT.

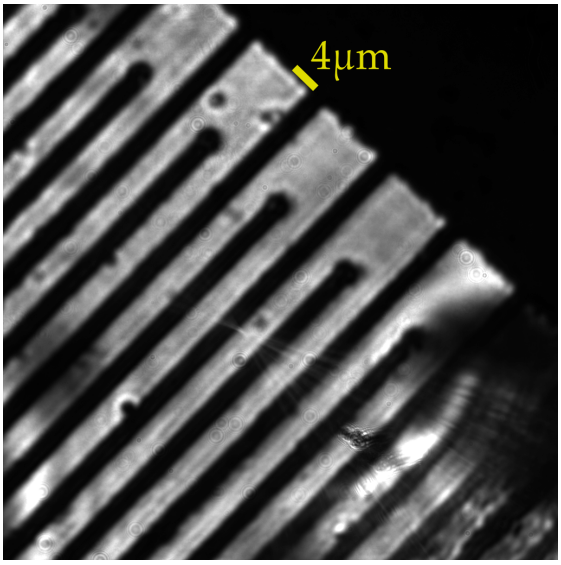

(b) Interdigit structures on PZT seen by optical microscope (first harmonic). Electrodes (in black) and spaces interdigits (in grey) are both 4µm wide.

Figure 3.7: Interdigit structures on PZT.

Experimental setup

We used micro-bounding to connect the electrodes to a generator able to deliver a voltage between −100V and 100V.The optical setup is detailed in section 3.1.7 (Figure 3.6). The laser excitation works at 900nm. Using optical filters, only the second harmonic signal is observed and recorded on the camera thanks to an objective lens. A set of polarizer/analyzer enable us to analyze the SHG response for different polarizations.

Visualization in SHG

A voltage up till ±60V was applied on the digits. Close to zero voltage, very little second harmonic signal is visible. The second harmonic signal had started to appear for ±30V and got more and more intense as the voltage got higher (Figure 3.9). Pictures for a voltage of 50V are displayed on Figure 3.8. The SHG intensity highly depends on the incident polarization of the light. We observe many irregularities in the picture, which resemble ferroelectric domains of size 1µm. They can be differentiated from their intensity angular dependence with respect to the incident polarization (Figure3.8).

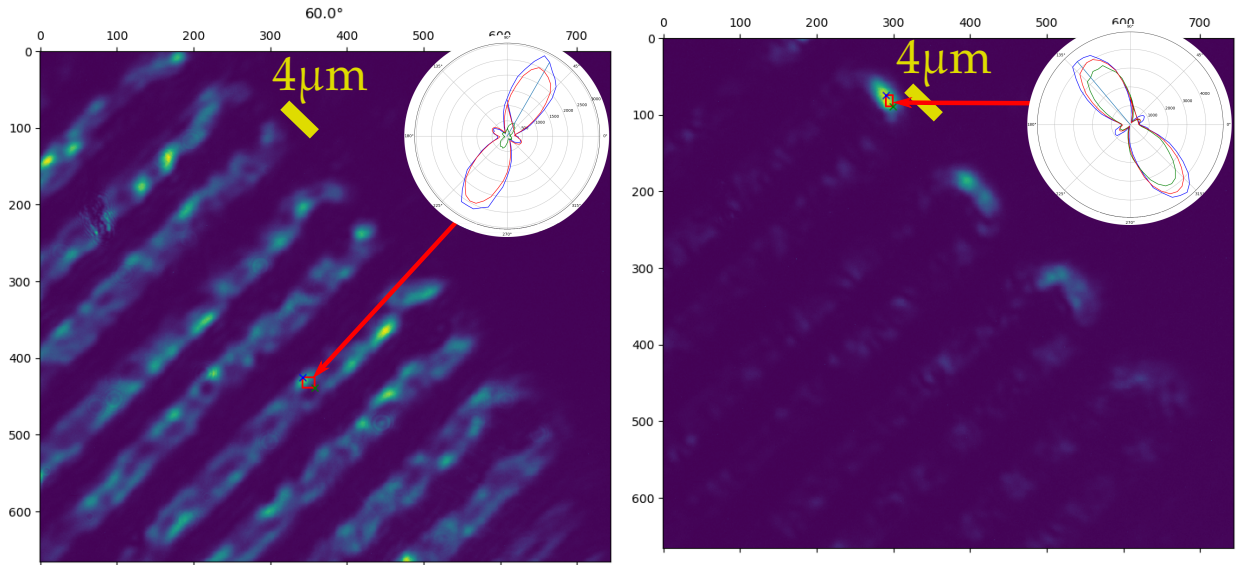

(a) 60° (b) 120°

Figure 3.8: SHG pictures of PZT for two different light polarization. 50V are applied. The analyzer is vertical (0°). Insets: angular intensity profiles at marked spot.

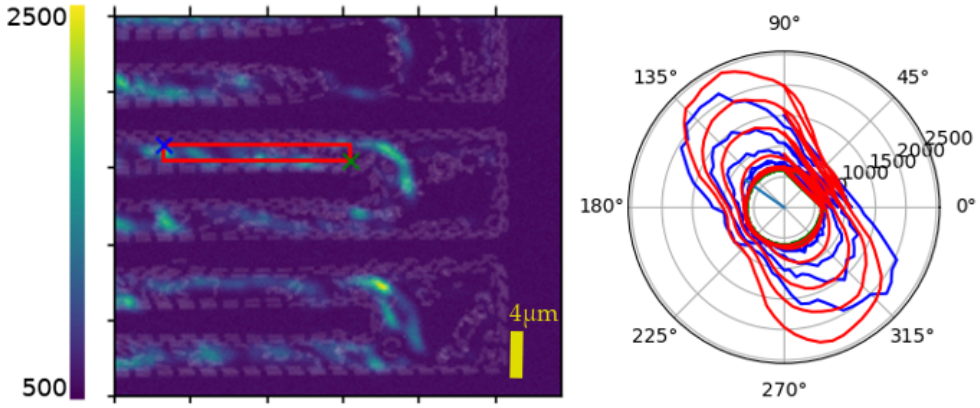

Figure 3.9: SHG imaging of the PZT sample. **Left:** Second harmonic image of the PZT sample for polarizer angle at 145° under 60V. Grey lines are added to show the contour of the digits seen in linear imaging. **Right:** Angular intensity profiles for different voltages ranging from 0V to 60V every 10V. Blue: pixel spotted by ×. Red: average over the area delimited by the red rectangle. A higher voltage increases the SHG signal.

Interpretation

The SHG signal can be produced by interfaces, crystal symmetry breakings and by the electric field itself. We observe that the signal is strong along the edges, because interfaces break symmetry, and produce SHG. It is also stronger closer to the electrodes as it is where the electric field is more intense. To interpret the shape of the angular profiles, we could study the crystal's inner symmetries. Here, the domain sizes seem to be at the edge of, or below the limit of our resolution of 0.5µm, hence too small for a detailed analysis. Nonetheless, the orientation of the lobes in the angular profiles, when comparing along digits versus at the tips of digits, is consistent with the symmetry of the electrical field we applied. On the images at light polarizations 120° and 60°, the contrast is striking.

Before reaching 30V, the domains were too small to be seen. SHG is a coherent phenomenon which can interfere destructively when to many domain randomly arranged are in the same area.

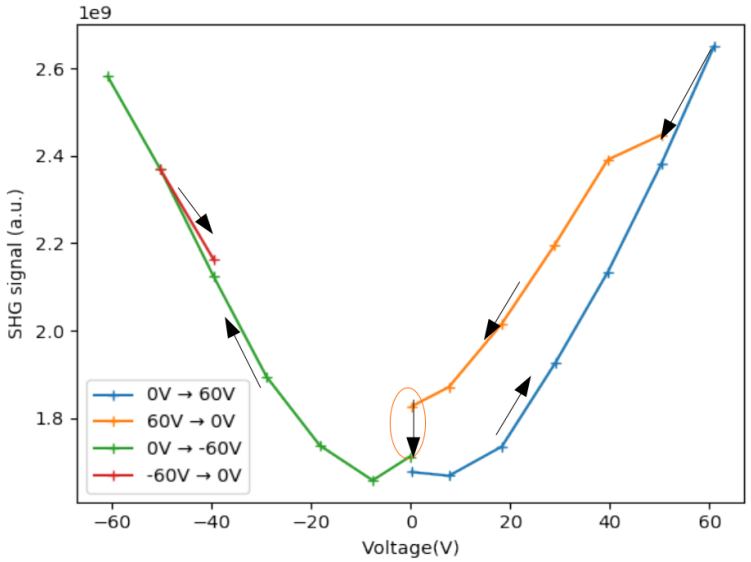

Figure 3.10: Hysteresis of SHG on PZT. The SHG signal is averaged on the image for all angles of polarization, and plotted with respect to the voltage between the interdigited contacts. The measurements stopped after −40V due to a sudden electrical damage on the sample.

The SHG signal starts to appear for 30V and gets more intense with the voltage. We measured up till 60V and went back to 0V. An hysteretic behavior was observed in the SHG intensity (Figure 3.10) and the patterns did not disappear when the voltage was set back to 0V. The sample was then disconnected and the cycle was done for negative voltages, but the sample got damaged during the process. Parasitic charges during the disconnection and swapping of the the contact could explain the discontinuity observed at 0V. The hysteresis behavior shows that the ferroelectric domains contribute to the SHG signal.

These measurements should be seen as a preliminary study. A more advanced analysis could for example reveal rich information about the electric field and the orientation of the ferroelectric domains. As it, they already give a good taste of how SHG imagery works. For the presented sample, the typical size of the domains is too small for our optical resolution, and a near field SHG setup would be more adapted.

Conclusions on PZT

The visualization of an epitaxial thin layer of PZT whose polarization can be controlled using Pt electrodes illustrates the fact that SHG can be used as a microscopy technique for probing the electric order. We observed that the SHG signal could be enhanced by increasing the symmetry breakings.

3.1.9 Other susceptibilities

When not allowed by symmetry, $\underline{\underline{\chi}}^{(2)}$ can be strictly equal to zero and other susceptibilities in equation (3.2a) can play a non negligible role. For example, for centrosymmetric crystals, all the polar tensors of odd rank (*i.e.* of even order in the Taylor expansion) are null [114]. Nonetheles, even though NiO is a centrosymmetric crystal, it still generates second harmonic via χ^{mee}, χ^{eem}, χ^{mmm} and can be observed experimentally [109]. In the cited experiment, the main second harmonic signal is generated by χ^{eem}, whose response is enhanced by taking advantage of a resonant conversion of the photons.

3.1.10 Conclusion on the SHG microscopy

A doubling of the frequency of the light occurs at locations where the time-space centrosymmetry is broken. In the centrosymmetric case, second harmonic can also be generated by higher orders in the non-linear expansion, and are related to the crystaline structure. In both cases, this second harmonic generation provides a powerful tool for probing subtle orders in crystal, like antiferromagnetism. In our full field setup, we use near infrared light giving SHG signals in the visible. Hence, our spatial resolution cannot be better than about 400nm.

In the next section, we will apply this technique on an epitaxial $BiFeO_3$ thin film.

3.2 Imaging of the Magneto-Electric Antiferromagnet $BiFeO_3$

3.2.1 Preparation of the sample

The material chosen for this study is the prototypical multiferroic bismuth ferrite $BiFeO_3$, that we introduced in the chapter 2. 110nm of $BiFeO_3$ are grown on a [100] substrate of $SrTiO_3$ (STO) by Pulsed Laser Deposition (PLD) by Cécile Carrétero at UMPhy CNRS Thalès, with 14nm of $SrRuO_3$ (SRO) between the substrate and the $BiFeO_3$ to ensure a ground voltage and enabling the visualization and manipulation of the ferroelectric domains of $BiFeO_3$ with Piezoresponse Force Microscopy (PFM).

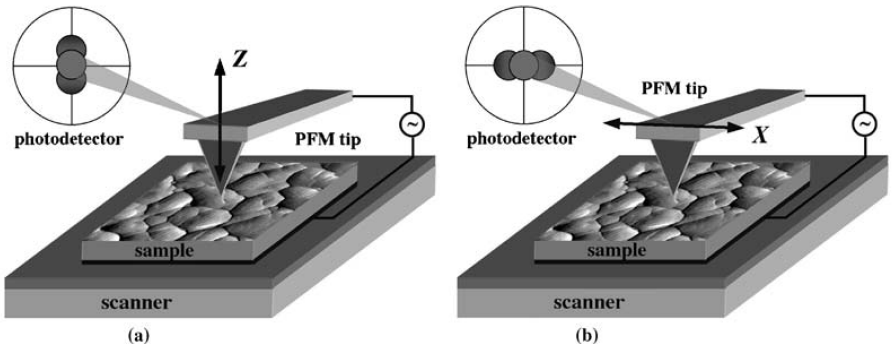

Figure 3.11: Piezoresponse Force Microscopy (PFM). From [118]. The tip at the apex of a cantilever can measure the local electric field, or write ferroelectric domains by applying a voltage. A laser measures accurately the bending, buckling, torsion or deflexion of the cantilever. (a) out-of-plane and (b) in-plane detections.

As sketched on Figure 3.11, a PFM is a near-field technique allowing the imaging of ferroelectric domains. It is composed of a metalic tip at the appex of a cantilever, whose deflexion can be accurately measured thanks to a pointing laser. A voltage can be applied to the metallic tip for writing ferroelectric patterns at the surface of the sample. Generally, the cantilever is in a forced oscillating regime. The measurements we collect from the photodiode can provide the amplitude and the phase of the signal. All presented PFM measurements (both reading and writing) were done by Stéphane Fusil at UMPhy CNRS Thalès. The roughness of the sample when writing is displayed on Figure 3.13.

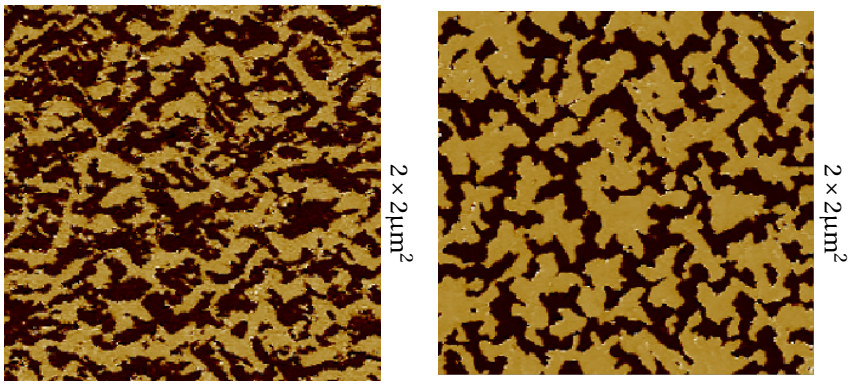

(a) In-plane (b) Out-of-plane

Figure 3.12: PFM amplitude of the as grown $BiFeO_3$ sample. It is composed of ferroelectric domains of various sizes, with a caracteristic length of 0.1µm. Both pictures are measured on the same region of the sample. Courtesy S.Fusil (UMPhy CNRS Thales).

Since the observed ferroelectric domains have a characteristic size of ≃ 100nm (Figure 3.12), and that our optical resolution (limited both by the objective lens, and by the wavelength of the laser) is of about 0.5µm, we need to write bigger ferroelectric domains. Several square patterns of few μm^2 of ferroelectric monodomains were written (Figure 3.14) using the following parameters: $V_{DC} = +15V$/SRO, $V_{AC} = 1V$.

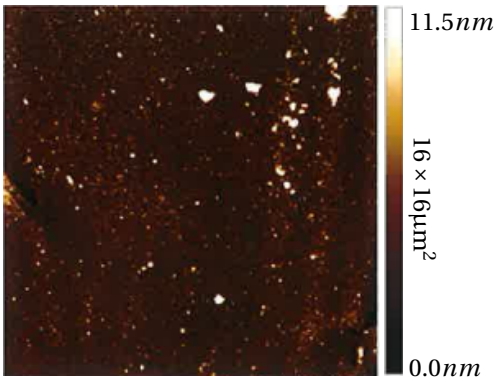

Figure 3.13: $BiFeO_3$ sample Roughness PFM height map of $16x16\mu m^2$ of the $BiFeO_3$ sample in the region of the ferroelectric patterns.

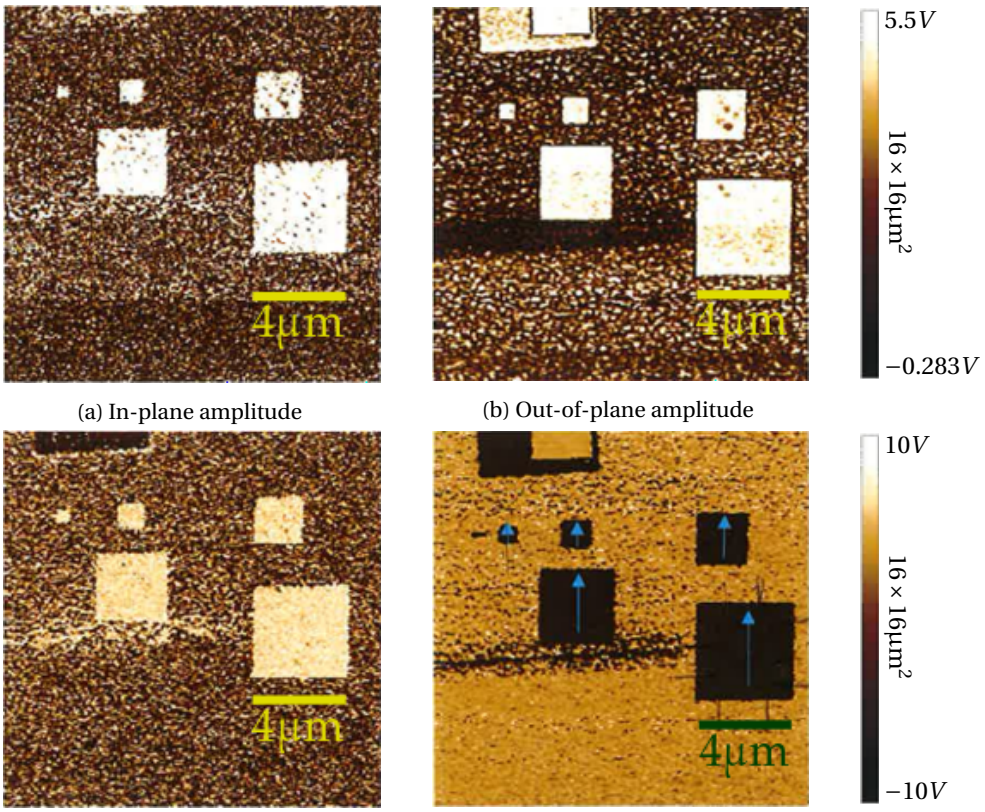

(a) In-plane amplitude (b) Out-of-plane amplitude

(c) In-plane phase (d) Out-of-plane phase

Figure 3.14: Ferroelectric patterns in $BiFeO_3$ seen by PFM. Reading $V_{AC} = 2V$.
The in-plane direction of the polarization in the monodomains is indicated by the blue arrows. The widths of the squares are respectivelly 0.5µm, 1µm, 2µm, 3µm and 4µm. Courtesy S.Fusil (UMPhy CNRS Thalès).

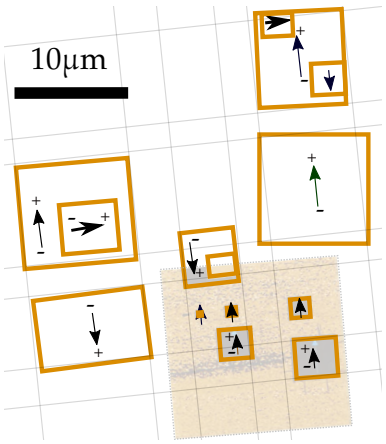

Figure 3.15: Orientation of the ferroelectricity in the patterns written with the PFM. The out-of plane component is not represented.

First harmonic signal

No pattern were found using a white light source with linear optics on our setup. The sample looks uniformly transparent to visible light.

3.2.2 Experimental Setup for the Second Harmonic Signal

The experimental setup is the one presented on Figure 3.6. When properly adjusted, an exposure time of 1s can be enough to see the ferroelectric patterns. For quantitative measurements, our exposure times are typically 30 – 60s. When needed, several pictures can be taken for averaging. A uniform background and readout noise of about 550 ± 100 photons counts is present on every picture.

3.2.3 Experimental Observations of the Second Harmonic Signal

When we filter out the first harmonic, and only observe the second harmonic emitted light, the ferroelectric squares are clearly visible for all incident polarization, but with variable intensities (Figure 3.16).

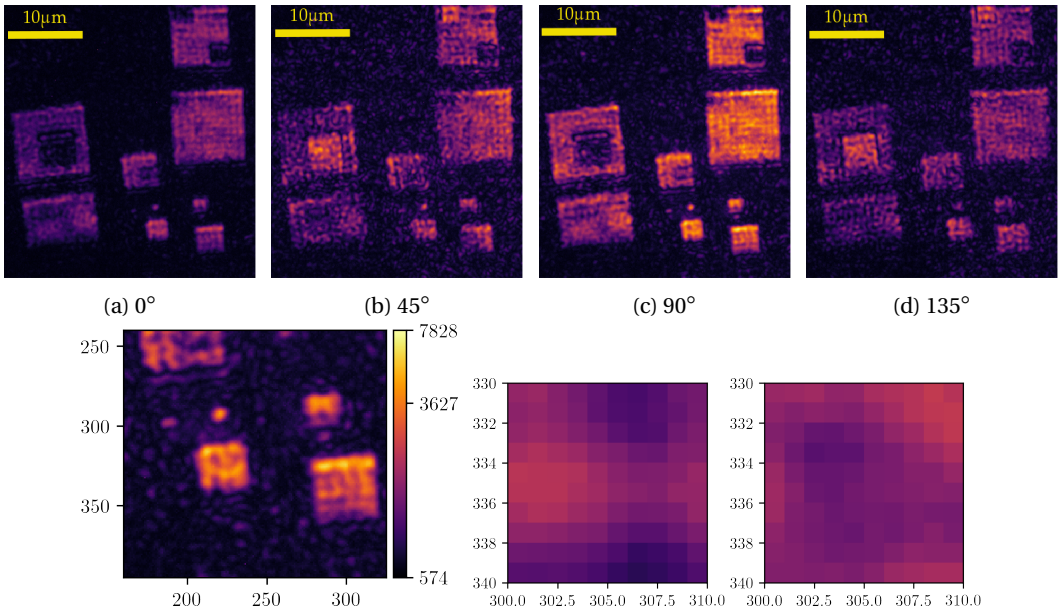

(a) 0° (b) 45° (c) 90° (d) 135°

(e) 90° - detail (f) 45° - Pixel size detail (g) 135° - Pixel size detail

Figure 3.16: Second harmonic intensities for different incident light polarization angles.

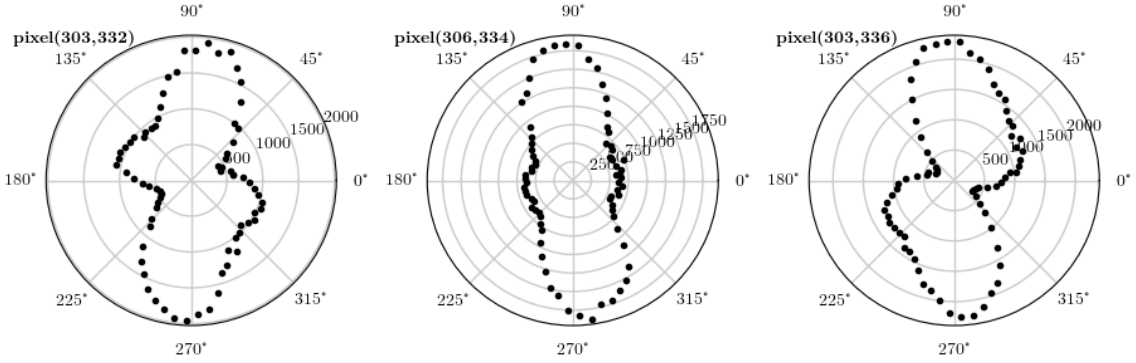

(a) 'blue' type (b) 'white' type (c) 'red' type

Figure 3.17: Angular profiles from three typical pixels.

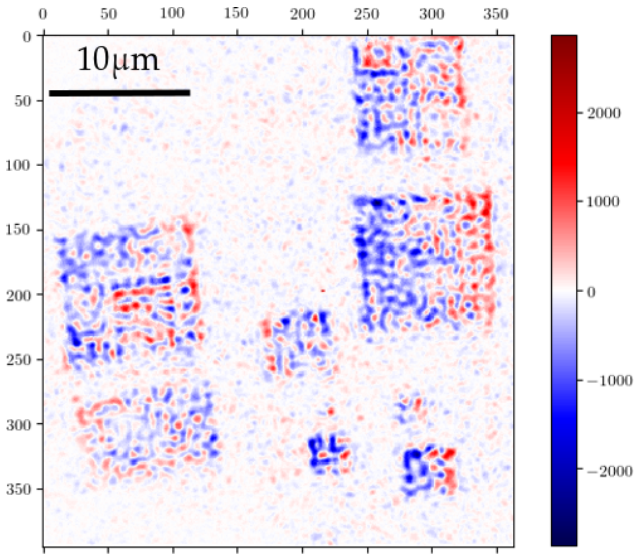

Figure 3.18: Difference 45° – 135°

Inside the squares, grains are visible, whose texture and shape take different aspects for different incident polarizations. When we plot the angular profile of a given pixel inside a ferroelectric domain, three possibilities occur: either the profile is symmetric with respect to the vertical and horizontal axes (Figure 3.17b), or an asymmetry is present, with a higher intensity when the polarization is at 45°(±180°) (Figure 3.17c), or the asymmetry is present with a higher intensity at 135°(±180°) polarization (Figure 3.17a). If we assign the colors *white, blue and red* to these three types of pixels respectively, we get an asymmetry map, similar to the one presented on Figure 3.18. This map was simply obtained by subtracting the image at 135° from the one at 45°, and assigning a symmetric tricolor colormap.

3.2.4 Interpretation of the second harmonic generation signal

Since an asymmetry is present in the second harmonic signal, it seems thats a certain symmetry is broken differently in the crystal for these three regions. The asymmetric textures observed are inside a single ferroelectric domain, and do not correspond to the roughness of the sample. The natural guess is that they correspond to the antiferromagnetic domains. We confirm that in the next section. The repartition of these asymmetric regions seems to organize in domains of size approximately 0.5µm, except for the pixels of symmetric type ('white'), which are localized at the separation of two asymmetric phases rather than forming comparable domains on its own.

Outside the ferroelectric patterns, the SHG intensity is comparatively very low, and the angular profiles of the pixels can have various shapes, due to the complex combination of several multiferroic domains. The SHG is a coherent phenomenon and can interact destructively in such regions.

In the next section, we show with a more in-depth analysis of the $BiFeO_3$ crystal that the presence of antiferromagnetic domains in the ferroelectric domain can explain our observations.

3.2.5 Analysis of the second harmonic generation signal

Susceptibility Tensor Symmetries

The complete crystalline structure of $BiFeO_3$ was developed in section 2.4.2.

Here our sample is $SrTiO_3(100)/SrRuO_3(14nm)/BiFeO_3(100nm)$. We are in the pseudo-cubic approximation, with a pure G-type antiferromagnetic state where the cycloid does not form because of the compressive strain of the $SrTiO_3$ substrate [90]. We base our symmetry analysis on the lattices represented on Figure 2.30. A measurement of the susceptibility coefficients of $BiFeO_3$ has been achieved by [112].

We can distinguish the components in $\underline{\underline{\boldsymbol{\chi}_e^{(2)}}}$ that are covariant with a change of sign in time, and mark them with a superscript (c), from the components that are invariant to time reversal, and mark them with a superscript (i).

$$\underline{\underline{\boldsymbol{\chi}_e^{(2)}}} = \underline{\underline{\boldsymbol{\chi}_e^{(2)(c)}}} + \underline{\underline{\boldsymbol{\chi}_e^{(2)(i)}}} \tag{3.18}$$

The spatial (time-invariant) part of the crystal (when the magnetism is disregarded, and accounting mainly for ferroelectricity) has $3m$ point group symmetry, with main symmetry axis [111]. Using Birss' notation, in the crystal frame[114]:

$$\underline{\underline{\boldsymbol{\chi}^{(2)(i)}}} = \begin{bmatrix} \chi_{11}^{(i)} & -\chi_{11}^{(i)} & 0 & 0 & \chi_{31}^{(i)} & 0 \\ 0 & 0 & 0 & \chi_{31}^{(i)} & 0 & -\chi_{11}^{(i)} \\ \chi_{31}^{(i)} & \chi_{31}^{(i)} & \chi_{33}^{(i)} & 0 & 0 & 0 \end{bmatrix} \tag{3.19}$$

Now, if we take the magnetic structure into account, the antiferromagnetic vectors in the (111) plane kill the 3-fold symmetry. The Point group is m. In the crystal frame:

$$\underline{\underline{\boldsymbol{\chi}^{(2)(c)}}} = \begin{bmatrix} \chi_{11}^{(c)} & \chi_{12}^{(c)} & \chi_{13}^{(c)} & 0 & \chi_{31}^{(c)} & 0 \\ 0 & 0 & 0 & \chi_{32}^{(c)} & 0 & \chi_{12}^{(c)} \\ \chi_{31}^{(c)} & \chi_{32}^{(c)} & \chi_{33}^{(c)} & 0 & \chi_{13}^{(c)} & 0 \end{bmatrix} \tag{3.20}$$

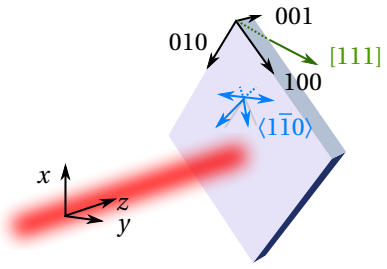

Figure 3.19: Orientation of the crystal axes in the laboratory frame.

Susceptibility Tensor in the Laboratory Frame

For practical reasons related to our polarizers, we define ϕ the rotation angle of the light polarization around $-z$, with its origin taken vertically (along x, see Figure 3.19). The incident linearly polarized electric field at angle ϕ in the in the laboratory frame is:

$$\boldsymbol{E} = \begin{bmatrix} E_x \cos(\phi) \\ -E_y \sin(\phi) \\ 0 \end{bmatrix} \tag{3.21}$$

So, in the laboratory frame, in contracted form, we have:

$$\boldsymbol{E} \otimes \boldsymbol{E} = \begin{bmatrix} E_x^2 \cos^2(\phi) \\ E_y^2 \sin^2(\phi) \\ 0 \\ 0 \\ 0 \\ -2E_x E_y \cos(\phi) \sin(\phi) \end{bmatrix} \tag{3.22}$$

$\underline{\underline{\chi}}$ has to be expressed in the laboratory frame. As explained in section 3.1.5, one needs to rotate the basis of the tensor to match with the one of the laboratory frame.

With our second harmonic generation microscopy technique, we start from a multi-domain material. Each domain can be seen as a small crystal with its own point group symmetries. Two identical domains with different orientations will give two different second harmonic generation responses since in their respective frame, the light has a different incident angle. Now, let's move back to the laboratory frame, the generated second harmonic collected in one direction will be different for the two domains. This is how a microscope can distinguish two different domains, and SHG microscopy can be achieved. A step further consists in analyzing the second harmonic generated by each domain in details to deduce the orientation of the order parameter in the sample, thus the multi-domain texture.

In the (111) plane, the antiferromagnetic vector **L** aligns along the 6 possible $\langle 1\bar{1}0 \rangle$ directions. Since the unit cell is recovered by a one-cell translation after the inversion symmetry operation (spins go from one $\langle 1\bar{1}0 \rangle$ axis to its opposite, and a one-cell translation recovers the original state), we are left with only three susceptibility tensor directions related to the **L**-symmetry, instead of six.

Considering we have three different possible antiferromagnetic orientations, we actually have 3 different bases to rotate. Based on Figure 3.19, the rotations matrices we are looking for are:

- one rotation around z to bring $\langle 1\bar{1}0\rangle$ along y (three different ones for the three possible magnetic domains);

$$\underline{\boldsymbol{R_{z+}}} = \begin{bmatrix} -\frac{1}{2} & -\frac{\sqrt{3}}{2} & 0 \\ \frac{\sqrt{3}}{2} & -\frac{1}{2} & 0 \\ 0 & 0 & 1 \end{bmatrix}, \underline{\boldsymbol{R_{z-}}} = \begin{bmatrix} -\frac{1}{2} & \frac{\sqrt{3}}{2} & 0 \\ -\frac{\sqrt{3}}{2} & -\frac{1}{2} & 0 \\ 0 & 0 & 1 \end{bmatrix}, \underline{\boldsymbol{R_{z0}}} = \begin{bmatrix} 1 & 0 & 0 \\ 0 & 1 & 0 \\ 0 & 0 & 1 \end{bmatrix} \tag{3.23}$$

- a second rotation around y to bring [111] along z.

$$\underline{\boldsymbol{R_y}} = \begin{bmatrix} \frac{\sqrt{3}}{3} & 0 & -\frac{\sqrt{6}}{3} \\ 0 & 1 & 0 \\ \frac{\sqrt{6}}{3} & 0 & \frac{\sqrt{3}}{3} \end{bmatrix} \tag{3.24}$$

Notice that for domain 3, the first rotation is the identity matrix since $\pm[1\bar{1}0]$ are already along y. Only the rotation around y is necessary, while for domains 1 and 2, a preliminary rotation of $\pm 60°$ around z must be achieved additionally.

After computation based on relation (3.17), we get expressions of the form:

$$\underline{\underline{\boldsymbol{\chi}^{(\mathbf{2})(\boldsymbol{i})}}}_{\text{Lab Frame}} = \begin{bmatrix} a^{(i)} & b^{(i)} & c^{(i)} & 0 & d^{(i)} & 0 \\ 0 & 0 & 0 & e^{(i)} & 0 & b^{(i)} \\ d^{(i)} & e^{(i)} & f^{(i)} & 0 & c^{(i)} & 0 \end{bmatrix} \tag{3.25a}$$

$$\underline{\underline{\boldsymbol{\chi}_{\mathbf{0}}^{(\mathbf{2})(\boldsymbol{c})}}}_{\text{Lab Frame}} = \begin{bmatrix} a^{(c)} & b^{(c)} & c^{(c)} & 0 & d^{(c)} & 0 \\ 0 & 0 & 0 & e^{(c)} & 0 & b^{(c)} \\ d^{(c)} & e^{(c)} & f^{(c)} & 0 & c^{(c)} & 0 \end{bmatrix} \tag{3.25b}$$

$$\underline{\underline{\boldsymbol{\chi}_{+}^{(\mathbf{2})(\boldsymbol{c})}}}_{\text{Lab Frame}} = \begin{bmatrix} a_+^{(c)} & b_+^{(c)} & c_+^{(c)} & +i_+^{(c)} & f_+^{(c)} & +k_+^{(c)} \\ +d_+^{(c)} & +e_+^{(c)} & +h_+^{(c)} & j_+^{(c)} & +l_+^{(c)} & b_+^{(c)} \\ f_+^{(c)} & j_+^{(c)} & t_+^{(c)} & +h_+^{(c)} & c_+^{(c)} & +l_+^{(c)} \end{bmatrix} \tag{3.25c}$$

$$\underline{\underline{\boldsymbol{\chi}_{-}^{(\mathbf{2})(\boldsymbol{c})}}}_{\text{Lab Frame}} = \begin{bmatrix} a_+^{(c)} & b_+^{(c)} & c_+^{(c)} & -i_+^{(c)} & f_+^{(c)} & -k_+^{(c)} \\ -d_+^{(c)} & -e_+^{(c)} & -h_+^{(c)} & j_+^{(c)} & -l_+^{(c)} & b_+^{(c)} \\ f_+^{(c)} & j_+^{(c)} & t_+^{(c)} & -h_+^{(c)} & c_+^{(c)} & -l_+^{(c)} \end{bmatrix} \tag{3.25d}$$

The exact expression of the coefficients of the four susceptibility tensors in the laboratory frame are expressed in appendix C. All we need to know for the following analysis, is that they form a linear combination of the χ coefficients, and that their relative signs are, in a more visual way:

$$\underline{\underline{\boldsymbol{\chi}_{\mathbf{0}}^{(\boldsymbol{i})}}} = \begin{bmatrix} & & & 0 & & 0 \\ 0 & 0 & 0 & & 0 & \\ & & & 0 & & 0 \end{bmatrix} \tag{3.26a}$$

$$\underline{\underline{\boldsymbol{\chi}_{\mathbf{0}}^{(c)}}} = \begin{bmatrix} & & & 0 & & 0 \\ 0 & 0 & 0 & & 0 & \\ & & & 0 & & 0 \end{bmatrix} \tag{3.26b}$$

$$\underline{\underline{\boldsymbol{\chi}_{\pm}^{(c)}}} = \begin{bmatrix} & & & \pm & & \pm \\ \pm & \pm & \pm & & \pm & \\ & & & \pm & & \pm \end{bmatrix} \tag{3.26c}$$

Now that they are expressed in the laboratory frame, we can compose with (3.22) to get $\boldsymbol{P}^{(2)}$. For each component of $\boldsymbol{P}$, we get linear combination of $\cos^2\phi$, $\sin^2\phi$ and $\cos\phi\sin\phi$ that we can factorize into the following form thanks to the relation $\sin^2 = 1 - cos^2$.

$$\underset{\pm}{\boldsymbol{P}_0} = \underset{\pm}{\boldsymbol{A}_0}\cos^2\phi + \underset{\pm}{\boldsymbol{B}_0}\cos\phi\sin\phi + \underset{\pm}{\boldsymbol{C}_0} \tag{3.27}$$

(We grouped the three corresponding equations for $\boldsymbol{P}_0$, $\boldsymbol{P}_+$, $\boldsymbol{P}_-$ into one with this notation.)

Using the remarkable symmetries of (3.26), we get the following simplifications along x (vertical) :

$$P_{0,x}^{(i)} = A_x^{(i)}\cos^2\phi + C_x^{(i)} \tag{3.28a}$$

$$P_{0,x}^{(c)} = A_{x0}\cos^2\phi + C_{x0} \tag{3.28b}$$

$$P_{\pm,x}^{(c)} = A_x\cos^2\phi \pm B_x\cos\phi\sin\phi + C_x \tag{3.28c}$$

... and along y (horizontal):

$$P_{0,y}^{(i)} = B_y^{(i)}\cos\phi\sin\phi \tag{3.29a}$$

$$P_{0,y}^{(c)} = B_{y0}\cos\phi\sin\phi \tag{3.29b}$$

$$P_{\pm,y}^{(c)} = \pm A_x\cos^2\phi + B_x\cos\phi\sin\phi \pm C_x \tag{3.29c}$$

Here we can already state two major remarks:

- The polarization induced by time-invariant symmetry breakings (ferroelectricity) has the same form as the polarization induced by the time-covariant symmetry breaking of type 0 (antiferromagnetic domain 3). They will be indistinguishable.
- On the contrary, the other two antiferromagnetic domains (1 and 2) can easily be taken apart from the rest and differ from one another only by a sign in their dependence on ϕ.

Intensity collected

The intensity collected on the camera is:

$$I(t) \propto \left\| \acute{\boldsymbol{E}}(\boldsymbol{r}_{cam}, t) \right\|^2 \tag{3.30}$$

Ultimately, each pixel from the camera gives us a count of photons proportional to $\int_{exposure} I(t)\mathrm{d}t$.

A particular [8] solution of the d'Alembert equation (framed part of equation (3.1)) is:

$$\acute{\boldsymbol{E}}(\boldsymbol{r},t) = \frac{1}{4\pi}\iiint \frac{1}{||\boldsymbol{r}-\boldsymbol{r'}||}\frac{\partial^2 \boldsymbol{P}}{\partial t^2}\left(\boldsymbol{r'}, t-\frac{||\boldsymbol{r}-\boldsymbol{r'}||}{c}\right)\mathrm{d}\boldsymbol{r'} \tag{3.31}$$

We commonly say that the electric field varies as $\frac{\partial^2 \boldsymbol{P}}{\partial t^2}$ at *retarded time*, for the light travels at finite speed. Now, considering we will collect the light in a objective lens for collimation and that the delay at which the light is collected in the camera is of no particular interest, we can simply state that the intensity collected in the camera will be proportional to the square of the acceleration of $\boldsymbol{P}$.

$$I \propto \left\| \frac{\partial^2 \iiint \boldsymbol{P}}{\partial t^2} \right\|^2 \tag{3.32}$$

$$\propto \left\| \frac{\partial^2}{\partial t^2} \iiint \left(\boldsymbol{P}^{(i)} + \boldsymbol{P}^{(c)}_{\substack{0\\\pm}} \right) \right\|^2 \tag{3.33}$$

For each pixel ($\simeq$ 90nm in our setup), the integral sums over the region under focus. Considering our resolution of 0.5µm comparable to the minimum size of the antiferromagnetic domains, we can assume a rough uniformity for a given pixel, and drop the integral sign for commodity. Dropping the integral symbol means neglecting the *speckle*, which is really not visible in our experiment.

Let us now insert an analyzer with direction $\boldsymbol{v_A}$ in the z plane before collecting the light, and improve the readability of our equations by using the double dot notation as for the double time derivative:

$$I \propto \left| \left(\ddot{\boldsymbol{P}}^{(i)} + \ddot{\boldsymbol{P}}^{(c)}_{\substack{0\\\pm}} \right) \cdot \boldsymbol{v_A} \right|^2 \tag{3.34}$$

We can distribute to clearly separate the contributions:

$$I \propto \left| \ddot{\boldsymbol{P}}^{(i)} \cdot \boldsymbol{v_A} \right|^2 + \left| \ddot{\boldsymbol{P}}^{(c)}_{\substack{0\\\pm}} \cdot \boldsymbol{v_A} \right|^2 + 2\,\mathrm{Re}\left(\left(\ddot{\boldsymbol{P}}^{(i)} \cdot \boldsymbol{v_A} \right) \left(\ddot{\boldsymbol{P}}^{(c)}_{\substack{0\\\pm}} \cdot \boldsymbol{v_A} \right)^* \right) \tag{3.35}$$

Let us now recall that $\ddot{\boldsymbol{P}}^{(i)}$ is proportionnal to $\underline{\underline{\boldsymbol{\chi}^{(i)}_{\mathbf{0}}}}$ while $\ddot{\boldsymbol{P}}^{(c)}_{\substack{0\\\pm}}$ is proportionnal to $\underline{\underline{\boldsymbol{\chi}^{(c)}_{\substack{\mathbf{0}\\\pm}}}}$. We operate at 800−950nm, in the optical gap of $BiFeO_3$ reported to be near 460nm ($2.7eV$ [119, 120]), far from the resonance at least for the first harmonic. As briefly discussed in section 3.1.4, the far-resonance condition assures that the two susceptibility tensors are orthogonal to one another in the complex plane. As a consequence, the interference term vanishes, and we are left with:

$$I \propto \left| \ddot{\boldsymbol{P}}^{(i)} \cdot \boldsymbol{v_A} \right|^2 + \left| \ddot{\boldsymbol{P}}^{(c)}_{\substack{0\\\pm}} \cdot \boldsymbol{v_A} \right|^2 \tag{3.36}$$

[8] We mean by this that we can write a generic solution of (3.1) under the form $\acute{\boldsymbol{E}}(\boldsymbol{r},t) + \boldsymbol{f}(\boldsymbol{r}+\mathbf{1}ct) + \boldsymbol{g}(\boldsymbol{r}-\mathbf{1}ct)$, where $\boldsymbol{f}$ and $\boldsymbol{g}$ are functions solution to the homogeneous equation, only determined by initial and boundary conditions. Their influence are completely irrelevant in our context, and they are set to $\mathbf{0}$ in our study.

In equation (3.27), the coefficients $\underset{\pm}{\boldsymbol{A_0}}$, $\underset{\pm}{\boldsymbol{B_0}}$ and $\underset{\pm}{\boldsymbol{C_0}}$ depend on time via $\boldsymbol{E}$, but not on the linear polarization ϕ, which is kept constant during a measurement. we have:

$$\underset{\pm}{\ddot{\boldsymbol{P}}_0} = \underset{\pm}{\ddot{\boldsymbol{A}}_0}\cos^2\phi + \underset{\pm}{\ddot{\boldsymbol{B}}_0}\cos\phi\sin\phi + \underset{\pm}{\ddot{\boldsymbol{C}}_0} \tag{3.37}$$

Likewise, $\underset{\pm}{\ddot{\boldsymbol{A}}_0}$, $\underset{\pm}{\ddot{\boldsymbol{B}}_0}$ and $\underset{\pm}{\ddot{\boldsymbol{C}}_0}$ follow the time variation of $\boldsymbol{E}$, but do not depend on ϕ. Now, supposing the resolution of our objective lens is so that one pixel sees a region composed of domains 1,2 and 3 in proportions λ_-, λ_+ and λ_0 respectively. The captured intensity will be:

$$I \propto \left|\left(\ddot{\boldsymbol{A}}^{(i)}\cos^2\phi + \ddot{\boldsymbol{B}}^{(i)}\cos\phi\sin\phi + \ddot{\boldsymbol{C}}^{(i)}\right)\cdot\boldsymbol{v_A}\right|^2 + \left|\sum_{\substack{0\\\pm}}\lambda_{\underset{\pm}{0}}\left(\left(\underset{\pm}{\ddot{\boldsymbol{A}}_0}\cos^2\phi + \underset{\pm}{\ddot{\boldsymbol{B}}_0}\cos\phi\sin\phi + \underset{\pm}{\ddot{\boldsymbol{C}}_0}\right)\right)\cdot\boldsymbol{v_A}\right|^2 \tag{3.38}$$

After distribution of the terms, we can rename our variables to match the following pattern:

$$I \propto \left|A\cos^2\phi + B\cos\phi\sin\phi + C\right|^2 + \left|\sum_{\substack{0\\\pm}}\lambda_{\underset{\pm}{0}}\left(\underset{\pm}{a_0}\cos^2\phi + \underset{\pm}{b_0}\cos\phi\sin\phi + \underset{\pm}{c_0}\right)\right|^2 \tag{3.39}$$

with $a_+ = a_-$, $c_+ = c_-$ and $b_+ = -b_-$.

The absolute value can be distributed, making an interference term appear:

$$I \propto \left|A\cos^2\phi + B\cos\phi\sin\phi + C\right|^2 + \sum_{\substack{0\\\pm}}\lambda_{\underset{\pm}{0}}^2\left|\underset{\pm}{a_0}\cos^2\phi + \underset{\pm}{b_0}\cos\phi\sin\phi + \underset{\pm}{c_0}\right|^2 + \textit{Interference Term} \tag{3.40}$$

The interference term can play a role in the intensity, since SHG is a coherent phenomenon, especially close to domain walls. We discuss about them after the analysis.

Shape of the lobes

Now that we have the expression of the expected intensity, it is time to link it with our data from the angular measurements (Figure 3.17). For this, we need to analyse the expressions of the form $A\cos^2\phi + B\cos\phi\sin\phi + C$ issued from (3.28c) and present in our expression of I (Equation (3.40)).

Let us first consider the following property:

☞*Property:* Generic expression $P = A\cos^2(\phi) + B\cos(\phi)\sin(\phi) + C$ (like in Equations (3.28c)) is an equation of a conic section, that we can rearrange into

$$P = \alpha \cos^2(\phi + \phi_0) + \gamma \tag{3.41}$$

under the following transformation:

$$\alpha = \sqrt{A^2 + B^2} \tag{3.42a}$$

$$\phi_0 = \mp\frac{1}{2}\arctan\left(\frac{B}{A}\right) \tag{3.42b}$$

$$\gamma = C - \sqrt{A^2 + B^2}\sin^2\left(\frac{1}{2}\arctan\left(\frac{B}{A}\right)\right) \tag{3.42c}$$

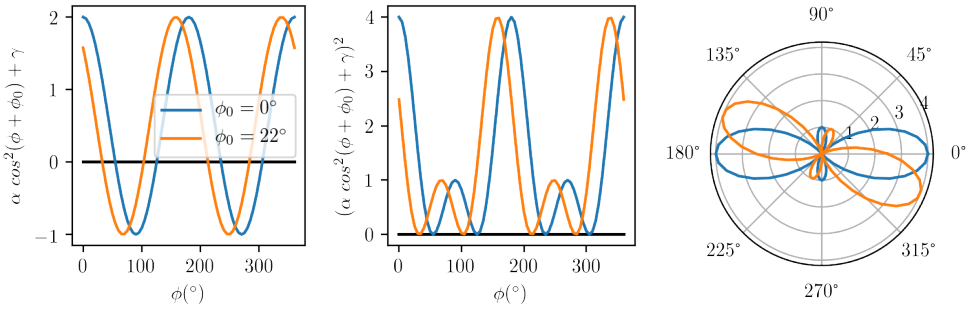

(a) $\alpha\ cos^2(\phi+\phi_0)+\gamma$ (b) $(\alpha\ cos^2(\phi+\phi_0)+\gamma)^2$ (c) $(\alpha\ cos^2(\phi+\phi_0)+\gamma)^2$

Figure 3.20: Shape of the lobes for $-|\alpha| < \gamma < 0$. The ratio $\frac{\alpha}{\gamma}$ determines the relative shape of the major and minor lobes, while ϕ_0 determines the inclination.

Applied to (3.28c), we get for the vertical x-axis:

$$\boldsymbol{P}_x^{(i)} = A\cos^2\phi + C \tag{3.43a}$$

$$\boldsymbol{P}_{+,x}^{(c)} = \alpha\cos^2(\phi + \phi_L) + \gamma \tag{3.43b}$$

$$\boldsymbol{P}_{-,x}^{(c)} = \alpha\cos^2(\phi - \phi_L) + \gamma \tag{3.43c}$$

$$\boldsymbol{P}_{0,x}^{(c)} = \alpha_0\cos^2(\phi) + \gamma_0 \tag{3.43d}$$

A correspondence in the shape of the lobes between the two writtings for remarkable angles are displayed Figure 3.21. Written under this from, it is easier to spot the maxima on the angular plots. The relative amplitudes between α and γ play an important role in the shapes, but for our concerns, $-|\alpha| < \gamma < 0$ and the corresponding generic shapes are sketched on Figure 3.20.

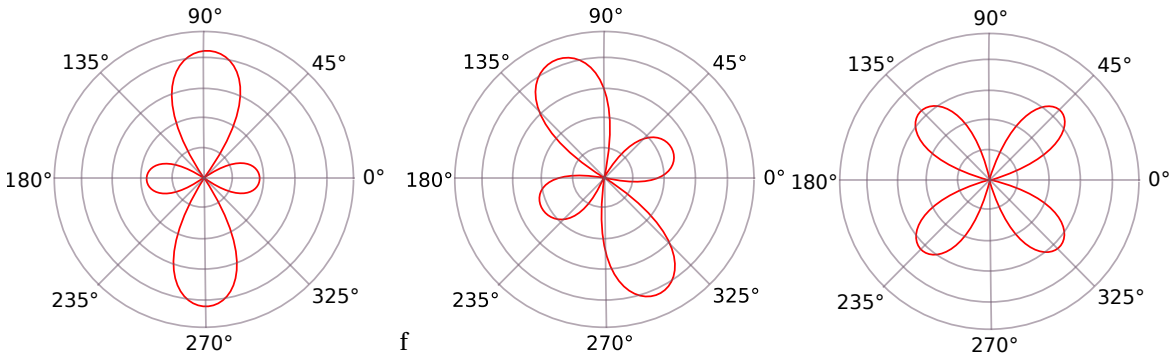

(a) $\frac{\left|A\cos^2\phi+C\right|^2}{\left|\alpha\cos^2(\phi+90°)+\gamma\right|^2}$ (b) $\frac{\left|A\cos^2\phi+B\cos\phi\sin\phi+C\right|^2}{\left|\alpha\cos^2(\phi+112°)+\gamma\right|^2}$ (c) $\frac{\left|B\cos\phi\sin\phi\right|^2}{\left|\alpha\cos^2(\phi+45°)\right|^2}$

Figure 3.21: Angular plot of the form $\left|A\cos^2\phi+B\cos\phi\sin\phi+C\right|^2$ and corresponding ϕ_0 angles.

Fit of the data

$$I_+ = \left(A\cos^2\phi + C\right)^2 + \left(\alpha\cos^2\left(\phi+\phi_L\right)+\gamma\right)^2 \tag{3.44a}$$

$$I_- = \left(A\cos^2\phi + C\right)^2 + \left(\alpha\cos^2\left(\phi-\phi_L\right)+\gamma\right)^2 \tag{3.44b}$$

$$I_0 = \left(A\cos^2\phi + C\right)^2 + \left(\alpha_0\cos^2\left(\phi\right)+\gamma_0\right)^2 \tag{3.44c}$$

The last equation (3.44c) can be factorized to the following form:

$$I_0 = \left(A_0\cos^2\phi + C_0\right)^2 + D_0 \tag{3.45}$$

With our geometry, it is not possible to distinguish the domain '0′ SHG from the ferroelectricity SHG, using the shape of the lobes only. The pictures at $\phi = 90°$ and $0°$ where we expect uniform ferroelectricity display some granularity, which do not superimpose with the white 'symmetric' domains in texture $45° - 135°$ (Figure 3.16 and 3.18). In fact, it is more probable that the ferroelectricity of the sample is altered by some charged particles on the surface. All in all, separating the contribution from s-domains '0' and ferroelectricity is a difficult problem.

We chose to fit the angular plot of each pixels with the following function:

$$I \propto \underbrace{\left(A\cos^2\left(\phi+\phi_\varepsilon\right)+C\right)^2 + D}_{\textit{Ferroelectric+Antiferromagnetic '0'}} + \lambda\underbrace{\left(\alpha\cos^2\left(\phi+\phi_L\right)+\gamma\right)^2}_{\textit{Antiferromagnetic '+'}} + (1-\lambda)\underbrace{\left(\alpha\cos^2\left(\phi-\phi_L\right)+\gamma\right)^2}_{\textit{Antiferromagnetic '−'}} \tag{3.46}$$

With $\frac{\gamma}{\alpha} \simeq -0.35$, measured at 45° and 135° on the pixels at center of domains presenting the most asymmetry. $\phi_L = 45°$ and ϕ_ε is a variable which allows the ferroelectricity not to be perfectly vertical, as the granularity at 90° and the angular plots at the edges of ferroelectric patterns suggest. λ will give us the proportion of domain '+' over domain '-'. Domain '0' is indistinguishable from ferroelectricity in our geometry, but can still be fitted by a value of λ close to 0.5 if present. Any interference term is neglected.

The success of the fit on our data for the three different families of pixels 'red', 'white' and 'blue' is shown on

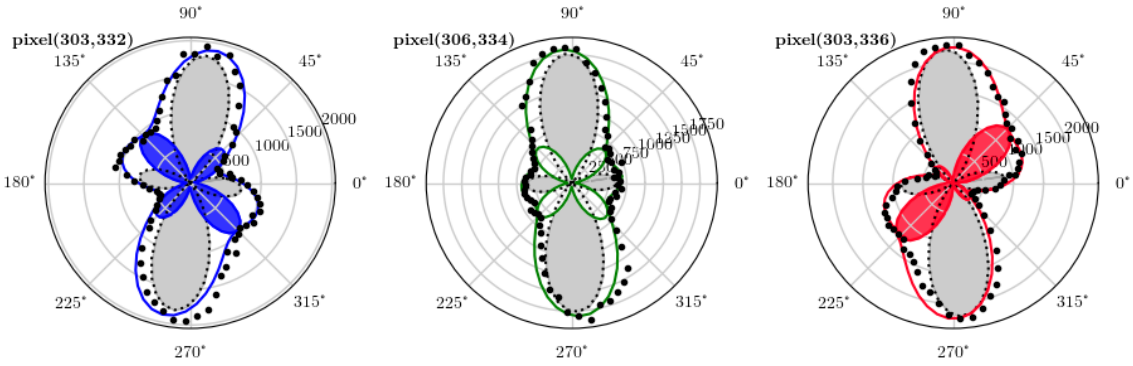

Figure 3.22: Fit of the three types of angular profiles.

Figure 3.22.

3.2.6 Extraction of the physical maps

The curve fitting procedure can be automated for each pixel of the images, even though it is worth mentioning that the fit is valid only for domains in which $\boldsymbol{P_e}$ is vertical. ϕ_ε can be seen as a small perturbation.

From the fitted data, we can extract the maps of:

- A, which gives us the ferroelectricity-related SHG amplitude (Figure 3.23a);
- ϕ_ε, which gives us the in-plane angle of the internal electric field (Figure 3.23b);
- λ, which gives us the antiferromagnetic orientation (Figure 3.25).

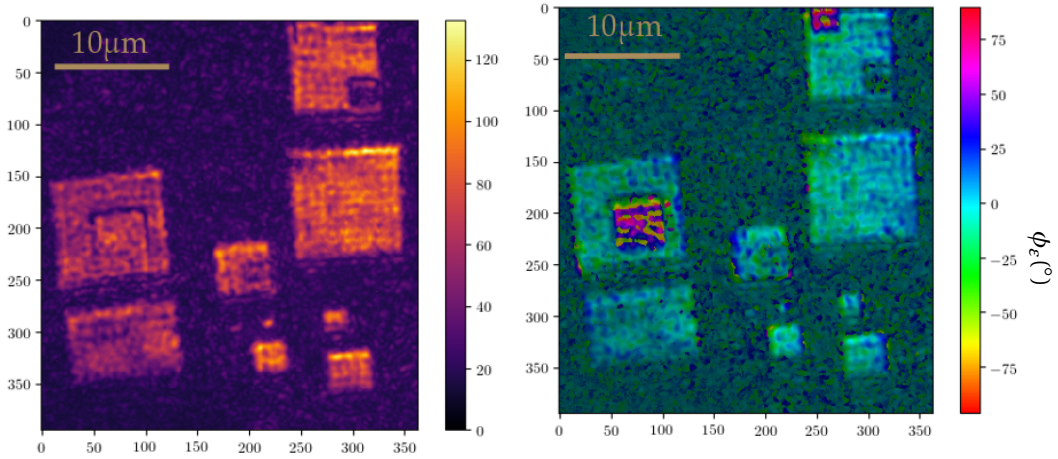

(a) Ferroelectric amplitude map (A).

(b) Ferroelectric orientation (ϕ_ε: hue) × Ferroelectricity amplitude (A: lightness)

Figure 3.23: Supplementary maps extracted from the fit.

Ferroelectric amplitude map

The ferroelectricity is not uniform in a monodomain, probably due to some charge on the surface acting on $\boldsymbol{P_e}$.

It looks very similar to maps at 90° or 0°, because most patterns were designed with vertical in-plane ferroelectricity. 90° (horizontal) polarization is the angle at which the ferroelectricity generates the most vertically polarized second harmonic.

Ferroelectric orientation map

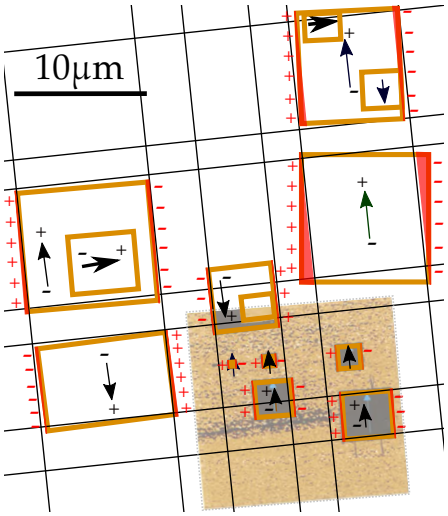

Figure 3.24: Explaination of the ferroelectric orientation. The orientation of $\boldsymbol{P_e}$ is caused by a charge accumulations at the edges of the pattern due to the missalignment of the squares with respect to the diagonals of the crystal axis (black lines).

According to the fit algorithm, the main lobe is not exactly at 90°, but more at $90° + \phi_\varepsilon$. Figure 3.23b show that in a domain, ϕ_ε can reach 20° at the edges of a domain. We think that this is because the squares are not drawn perfectly along the crystal axes, favoring a charge accumulation on the edges, influencing the internal electric field (Figure 3.24).

Antiferromagnetism Map

As developed in the previous sections, the asymmetry in the angular plot gives us the antiferromagnetism. The antiferromagnetic map we get from the fitting parameter λ is very similar to the assymetry between 45° and 135° of Figure 3.18. It confirms the position of the antiferromagnetic domains '+' (in blue), '-' (in red), and the absence of '0' domains (the white is distributed as domain walls and does not resemble the topography of domains).

It is worth mentioning that the the extraction of λ from the fit (Figure 3.25) provides a refinement over the raw asymmetry that is plotted on Figure 3.18. The main difference resides in a correction related to ϕ_ε. When not corrected, a small contribution from the big lobe of $\boldsymbol{P_e}$ can appear at 45° and at 135°. The fit separates the antiferromagnetic lobes from the ferroelectric lobes and therefore eliminate this bias. This, in particular, explains why most of our domains look very 'blue' on the left and 'red' on the right on the asymmetry map $45° - 135°$ (Figure 3.18), while this is mostly corrected on the fit parameter map Figure 3.25.

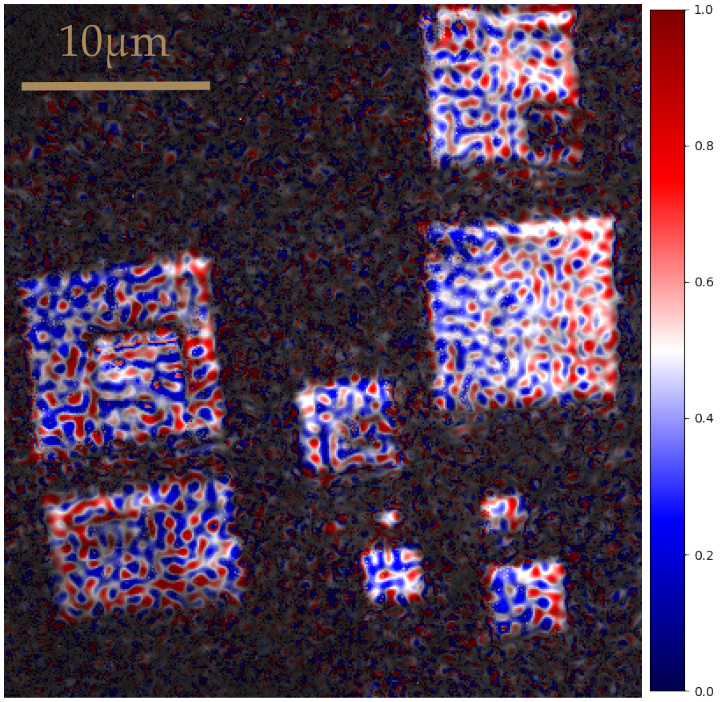

Figure 3.25: Antiferomagnetic domains map. λ (hue) and A (lightness) shows where the antiferromagnetic domains lie in the ferroelectric domains.

The biggest square on the middle right of our pictures still presents this red/blue distribution, possibly because of the strong rotation of $\boldsymbol{P_e}$ on the edges, and a possible influence on $\mathbf{L}$ due to magneto-electric couplings.

We consider that we have never found a pure antiferromagnetic domain of type '0', because the locations where these angles give a symmetric signal look much more like domain walls between domain '+' and domain '-' than actual domains. We can infer from these observations that the thin layer strain is favorable to domains '+' and '-', and not favorable for domain '0' [113]. Indeed, in domain '0', $\mathbf{L}$ is along $\pm[1\bar{1}0]$, in the plane of the sample, while domains '+' (along $\pm[01\bar{1}]$) and domains '-' (along $\pm[\bar{1}01]$) are degenerate with a $\mathbf{L}$ out-of plane. Domains '0' could simply be too high in energy to form. Our sample seems therefore mostly separated in two types of antiferromagnetic domains only.

3.2.7 Limitations

The fit we presented is well suited for domains for which (the z projection of) $\boldsymbol{P_e}$ is vertical. It is possible to adapt a similar method for $\boldsymbol{P_e}$ horizontal, or one could simply turn the analyser in horizontal position. We predict the given maps to be very similar to the one we already get on the present maps, though it needs to be checked.

In our model, we neglected the interference terms between domains. They could in fact play a role, and could possibly be useful to distinguish two neighboring domains at 180° from one another. They could patially explain the changes of intensity we observe in the 45° and 135° maps but should not change much the assymmetry patterns, so the role they play in our analysis for distinguishing the two antiferromagnetic domains would be only perturbative,

even though they needed to be mentioned. They could also partially explain the non uniformity we observe in the ferroelectric map.

3.2.8 Conclusions on static Measurements on $BiFeO_3$

In this section, several points have been made, which will be useful to keep in mind for the rest of the chapter:

• We managed to visualize antiferromagnetic domains in a BFO sample using SHG microscopy. Our spatial resolution reaches 0.5µm.

• The antiferromagnetic domain recognition method is based on an asymmetry in the angular profiles. Antiferromagnetic domains are mostly of two degenerate types only (blue and red), the third possible *s*-domain seems higher in energy. Antiferromagnetic patterns are mostly recognizable on a simple difference map between light polarization angles 45° and 135°.

• An analysis more in depth and a fit of the angular profiles led us to confirm our thoughts about the antiferromagnetic domains distribution, and gave us additional information on the ferroelectricity and the internal electric field. Ferroelectricity is influenced by the edges of our patterns, and even more when misaligned with respect to the crystal axes.

• The change in ferroelectricity seems to influence the distribution of our antiferromagnetic texture, which is likely to be a consequence of the magnetoelectric coupling.

In the next section, we attempt to optically excite the structures and use the present analysis to monitor the time-resolved multiferroic dynamics.

3.3 Time-resolved dynamics in $BiFeO_3$

Now that we have presented a method to optically measure antiferromagnetic textures, we would like to explore their dynamics, and especially probe whether the terahertz regime expected by the natural AF dynamics can be observed or not.

In this section, we will present the optical *pump-probe* technique for time-resolved measurements. We will first present the method of the measurement of ultrafast demagnetization of thin magnetic layer, and then move on to the time resolved SHG measurement of our multiferroic patterns.

3.3.1 Ultrafast excitation of the multiferroic order

It has been shown in the past that the antiferromagnetic patterns of our sample of $BiFeO_3$ could change under different stimuli, and especially femtosecond light pulses [113]. The change under this optical excitation can be time-resolved by proceeding to an upgrade of the setup, which we present in this section. It is worth mentionning that picosecond demagnetization of antiferromagnets NiO, Cr_2O_3 and $Pr_{1-x}Ca_xMnO_3$ have already been measured in SHG [103]. Even on ferromagnets, laser-induced ultrafast demagnetization occurs in the picosecond, and can have non-thermal origin [121, 122]. More details on that are given in section 4.2.1.

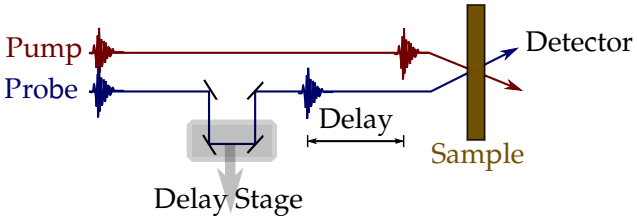

Figure 3.26: Delay Stage. The delay between the pump and the probe can be adjusted by a dealy stage, which consists in two mirrors on a rail. By probing several delays, one can reconstruct the temporal evolution triggered by the pump.

Ultrafast ferroelectric dynamics in $BiFeO_3$ have been observed [123], and can lead to a THz emission [36, 124]. Here we would like to extract signs of a similar dynamics from the antiferromagnetic part.

3.3.2 Ultrafast measurement technique

There are two types of ultrafast measurements. The first kind is called a *single-shot* measurement: a process is triggered, and as the system responds, measurement instruments register all the evolution as fast as they can. Unfortunately, when the response time of the phenomenon reaches nanosecond timescales, the time-response of the instruments (particularly the electronics) starts to be too slow for registering the evolution at a sufficiently good resolution. To tackle this, we commonly use measurement techniques of the second kind: *stroboscopic measurements*. In this frame, a phenomenon is repeated and the measurement averages over the repetition at a fixed delay time after the excitation. Averaging will give only the repeatability part of the phenomenon and will average to zero the stochastic contributions.

In our study, we use the stroboscopic approach. This is commonly referred as *pump-probe* techniques, because it involves the use of a pump channel to excite the system, and a probe channel to measure its reaction at a tunable time after the pump has excited the sample. For this technique to work, we need a system that can be reset to its initial state before another pump stimulus is achieved. If this repeatability condition is achieved, the probe signal can be averaged over many repetitions of the stimulus for a given delay, and the delay can be changed at will to reconstruct the full dynamics of the system after the excitation.

Optically, changing the delay is quite simple to achieve: on either the pump or the probe channel, collimated light can be deviated to a delay stage composed of mirrors on a mechanical platform. When the platform is moved, the optical path gets shorter or longer, and thus, the delay between the two channels is changed accordingly. The precision on the delay depends on the mechanical precision of the delay stage ($\leq 1\mu m$) and the alignment of the beam along the rails must be done carefully. Since the light travels twice the distance (way and back) on the stage, for a $1\mu m$ precision, the maximum delay precision is $\delta t = 2\mu m/c \simeq 6.7fs$, which, in our case is below the time resolution we can expect from our 100fs pulses.

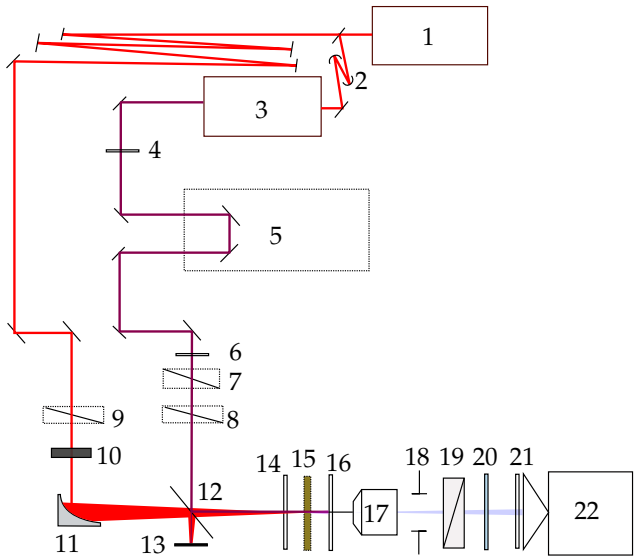

1. LIBRA
2. Telescope
3. Optical Parametric Amplifier
4. Long-pass filter 780nm FEGL780S
5. Delay stage
6. Short-pass filter 1600nm
7. Polarizer
8. Half-wave plate
9. Half-wave plate
10. Attenuator
11. Parabolic mirror
12. Bean splitter
13. Absorber (Teflon)
14. Long-pass filter 750nm FELH0750
15. Sample
16. Short-pass filter 750nm FESH0750
17. Objective lens
18. Diaphragm
19. Analyser
20. Narrow bandwidth pass filter 450nm
21. Optical density filters BG39 & GG380
22. Camera

Figure 3.27: Experimental setup for Time-Resolved Second Harmonic Generation (TRSHG) imagery.

3.3.3 Experimental setup for time-resolved SHG imaging

The experimental setup is sketched on Figure 3.27. We use a femtosecond laser, with pulse width 90fs, at $\omega' =$ 800nm wavelength, with a repetition rate of 1kHz. The average power can reach 3.5W, for a spot of Gaussian shape with diameter of 1cm. Thanks to a beam splitter, the laser is split into a pump line and a probe line. The OPA is on the probe line so that we can change its wavelength to $\omega =$ 900nm. A parabollic mirror focuses the pump on the sample up to 50mJ/cm^2. The spot diameter of the probe measures approximately 50µm on the sample. Because we need to keep the pump focused on a localized area during the delay sweep and that the delay stage could introduce a drift, the delay stage is set on the probe line to ensure an optimal stability of the pump. The probe is a collimated 1cm diameter gaussian spot, for which the stability of the delay stage is sufficient.

Attenuators can reduce the fluence of the pump on the sample. We typically work at 0.25mJ/cm^2 (low fluence) or 50mJ/cm^2 (high fluence). If not mentioned otherwise, the pump is linearly polarized horizontally (90°).

3.3.4 Influence of the setup geometry on the signal

The transmission of the beam splitter (element 12 on Figure 3.27) depends significantly on the incident polarization. A vertically (0° in the lab frame) polarized light is reflected to 60% while a horizontally (90°) polarized light in reflected a 40% only. This behavior introduces a bias in our angular profiles that we need to correct. We measured the (first harmonic) reflectivity response in Figure 3.28, thanks to a photo-diode.

Since the second harmonic intensity is proportional to the square of the first harmonic intensity, all our data are corrected by dividing our second harmonic signal by the square of the intensity response from the beam splitter at the corresponding angle.

The beam splitter can also introduce a small change in polarization (angle and ellipticity).

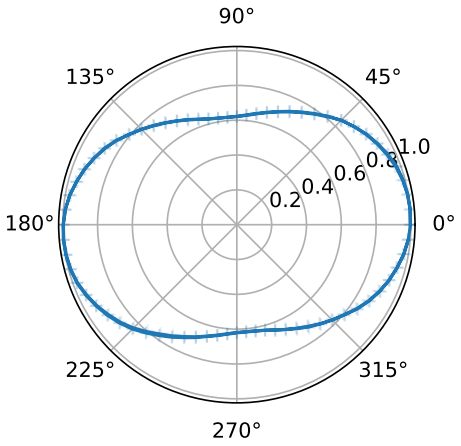

Figure 3.28: Beam-splitter reflectivity response with respect to incident polarization .

3.3.5 Influence of the pump on the signal

Adding a pump on the measurement setup triggers several phenomena that need to be considered. In this section, the pump is not focused on the sample (The parabolic mirror 11 on Figure 3.27 is replaced by a regular mirror), and is at relatively low power: 0.25mJ/cm^2 on the sample.

Sum Frequency Generation

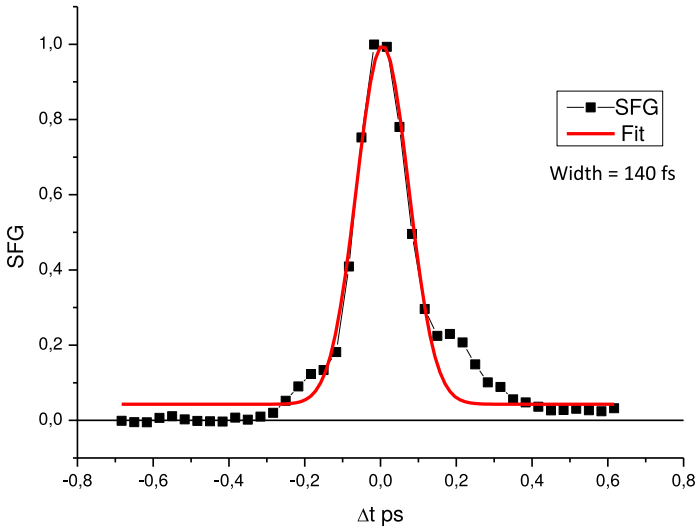

Figure 3.29: Origin of delays measured by Sum Frequency Generation (SFG). The half-size width is measured by a squared gaussian fit.

The first purely optical phenomenon that appears, is the Sum Frequency Generation, along with the Difference Frequency Generation. As partially discussed in section 3.1.3 with Figure 3.5, in nonlinear optics, two photons can mix, even if they are not of the same frequency, and even if the intermediate state is virtual. This process is immediate and coherent. Let's call ω' the frequency of the pump and ω the frequency of the probe. If the two

pulses reach the crystal *at the same time*, the mixing occurs and produces photons at $\omega' + \omega$, as well as photons at $|\omega' - \omega|$. In our case, the sum frequency generation between light at 800nm and 900nm produces light at 424nm (and the difference frequency generation produces light at 7200nm, which is filtered out). A change in intensity is clearly visible when this occurs, and it can be used for finding the origins of delays t_0 on the delay stage (Figure 3.29).

Once the origin of delays is found, a narrow band-gap filter (FBH450-10) centered around 450nm is added after the sample, to only keep the SHG of the probe (900nm/2), and filter out all the contributions from the pump in the signal (SHG, SFG and DFG). The only pure optical remaining contribution that we cannot filter is the loss of the ω photons that were converted into $\omega' \pm \omega$ instead of 2ω, but they should play for a minor part.

Optical rectification

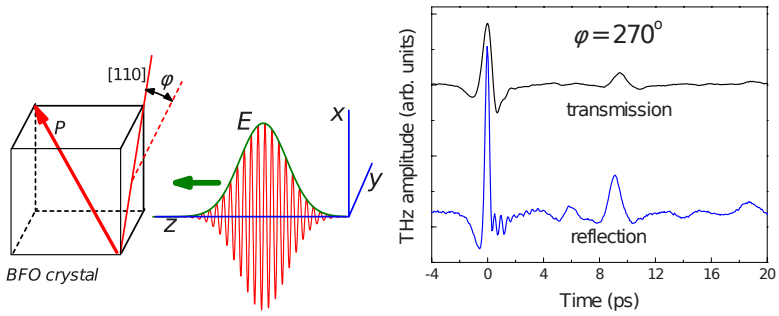

Figure 3.30: THz emission in $BiFeO_3$ via optical rectification. From [36].

As seen in section 3.1.3, optical rectification is inevitably produced in the second order non-linear process leading to second harmonic generation, according to the simple trigonometric formula:

$$\cos(\omega' t)\cos(\omega' t) = \underbrace{\frac{1}{2}}_{\text{optical rectification}} + \underbrace{\frac{\cos(2\omega' t)}{2}}_{\text{SHG}} \tag{3.47}$$

In the case of light of infinite duration, a DC term is produced, but in the case of light pulses, a slow variation related to the finite time duration of the pulse is generated. As shown by [36], a 100fs pulse on $BiFeO_3$ is rectified to generate a pulse with a heavy spectral weight in the terahertz (Figure 3.30). We can see this optical rectification as an additional perturbation of the electric polarization of the crystal $\boldsymbol{P_e}(t) = \boldsymbol{P_e} + \boldsymbol{p_e}(t)$ (Figure 3.31). Let's call Ω' the relatively slow frequency at which the optical rectification from the pump occurs. Since $\Omega' \simeq 1$THz [36] is close to the antiferromagnetic resonance, and that there is a strong magnetoelectric coupling in $BiFeO_3$, we can expect the perturbation to affect the antiferromagnetic domains.

On the probe side, this perturbation will change the symmetries of the electron potential well, and therefore the second order susceptibility $\underline{\underline{\boldsymbol{\chi}^{(2)}}}$.

$$\boldsymbol{P} = \underline{\underline{\boldsymbol{\chi}^{(2)}}}\left(\Omega' t\right) \boldsymbol{E}_{\omega t} \boldsymbol{E}_{\omega t} \tag{3.48}$$

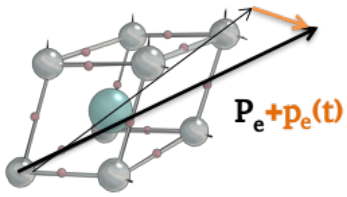

Figure 3.31: An additionnal electric polarization varying at low frequency can temporarly change the symmetries in the crystal.

3.3.6 Time-Resolved Measurement of the Optical Rectification

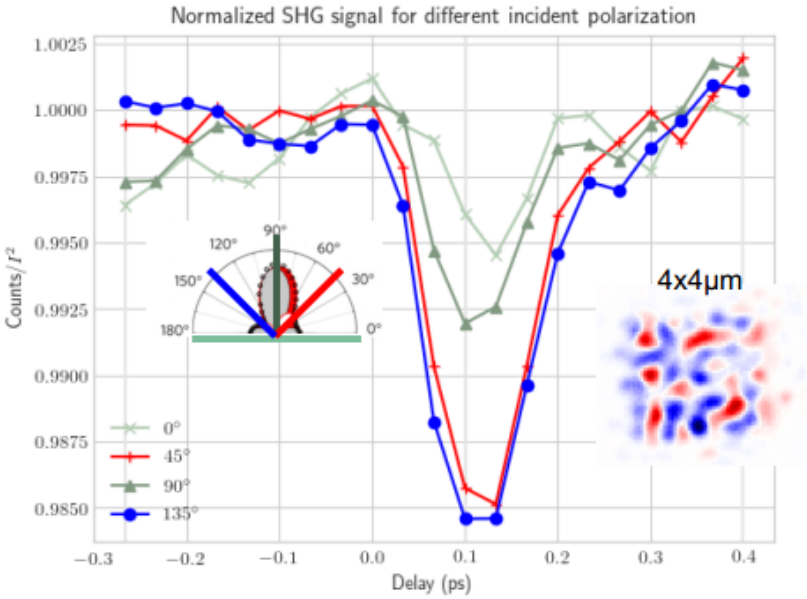

Figure 3.32: Time evolution of the SHG signal at probe angles 0, 45, 135 and 90°, averaged over a $4x4\mu m^2$ ferroelectric domain (inset), for a pump excitation of $0.25mJ/cm^2$.

Observations of the optical rectification and interpretation For a first approach, we work at low fluence ($0.25mJ/cm^2$) to observe the optical rectification due to the pump without perturbing $\boldsymbol{P_e}$ too much. We monitor the change of SHG intensity averaged on the $4 \times 4\mu m^2$ ferroelectric square, for the four main light polarization angles 0°, 90°, 45° and 135° (Figure 3.32). The change of SHG intensity is of 1.5%, and there is no significant change of the antiferromagnetic texture. We attribute the drop to the optical rectification, following the envelope of the pump pulse. After 300fs, the signal starts to be flat again (not displayed here), and no oscillation or dynamics that could originate from $\boldsymbol{P}$ (or $\mathbf{L}$) is clearly visible.

The pronounced intensity change for the angles 45° and 135° should not be attributed to an antiferromagnetic contribution too hastily. It could as well be explained by the optical rectification $\boldsymbol{p_e}(\Omega' t)$, for two main reasons. First reason, the expression of $\underline{\underline{\boldsymbol{\chi}^{(i)}}}$ changes, and could start influencing the angles 45° and 135°. Second reason,

$\underline{\underline{\boldsymbol{\chi}^{(c)}}}$ could also be changed by $\boldsymbol{p_e}$ (not only $\mathbf{L}$).

Order parameter dependence on $\chi^{(2)}$ The perturbation in the symmetry induced by the laser pulse will inevitably change the second harmonic signal through $\underline{\underline{\boldsymbol{\chi}^{(2)}}}$. To quantify the dependance of the suceptibility on the order parameters, a generalized Ginzburg-Landau approach can be done [125]. In principle, we analyze the symmetry of the paraelectric phase and ensure continuity at the ferroelectric transition by multiplying by the order parameter, and then proceed to the same logic with the magnetic ordering. The procedure is detailed in Appendix D. In short, for the second order suceptibility $\boldsymbol{P} = \left(\underline{\underline{\boldsymbol{\chi}^{(i)}}} + \underline{\underline{\boldsymbol{\chi}^{(c)}}}\right)\boldsymbol{EE}$, we have the following proportionality relations:

$$\underline{\underline{\boldsymbol{\chi}^{(i)}}} \propto \boldsymbol{P_e} \tag{3.49a}$$

$$\underline{\underline{\boldsymbol{\chi}^{(c)}}} \propto \boldsymbol{P_e}.\mathbf{L} \tag{3.49b}$$

If we follow a perturbative approach, in the case of a small perturbation of $\boldsymbol{p_e}(t)$ on $\boldsymbol{P_e}$ and $\boldsymbol{l}(t)$ on $\mathbf{L}$,

$$\underline{\underline{\boldsymbol{\chi}^{(i)}}} \propto \boldsymbol{P_e} + \boldsymbol{p_e}(t) \tag{3.50a}$$

$$\underline{\underline{\boldsymbol{\chi}^{(c)}}} \propto \left(\boldsymbol{P_e} + \boldsymbol{p_e}(t)\right).(\mathbf{L} + \boldsymbol{l}(t)) \tag{3.50b}$$

In other words, a change in SHG at angles 45° 135°, which would be due to $\underline{\underline{\boldsymbol{\chi}^{(c)}}}$ can be triggered by a change of $\boldsymbol{P_e}$, and not necessarily of $\mathbf{L}$.

3.3.7 Time-Resolved Dynamics by Second Harmonic Imaging (TR-SHG)

We have seen that our setup can measure subpicosecond phenomena, but so far, the effects were quite weak and could possibly be attributed to the optical rectification alone. In this section, the fluence is increased by a factor of 200, meaning that 50mJ/cm^2 are focused on a circular 50µm diameter spot on the sample.

Stability of the patterns and stroboscopy

Under high fluence, the change of SHG intensity due to the pumping is clearly visible on the pictures at 90°, and on the asymmetry maps 45° − 135° (Figure 3.33).

We also observe that, while the contrast and the intensity of the asymmetry maps changes over time, only very little variation from red to blue, or from blue to red is observed. It is especially true after the pulse, at $t \geq 0.3$ps, when the maps are almost identical to those preceding $t = 0$ps, except maybe on very small localized regions. The same goes for the pictures at 90°. In fact, at delays longer than 0.27ps, all the pictures seem identical and extremely similar the the ones at negative times. This means that we are meeting the reseting conditions necessary for the stroboscopic measurement to work, and that the system looks already reset to some extent after only 0.27ps.

At negative times, the system is considered at rest, since the last pump pulse happened nearly 1ms earlier. Our static SHG analysis is valid, and the asymmetry map corresponds to antiferromagnetic patters at these times. On

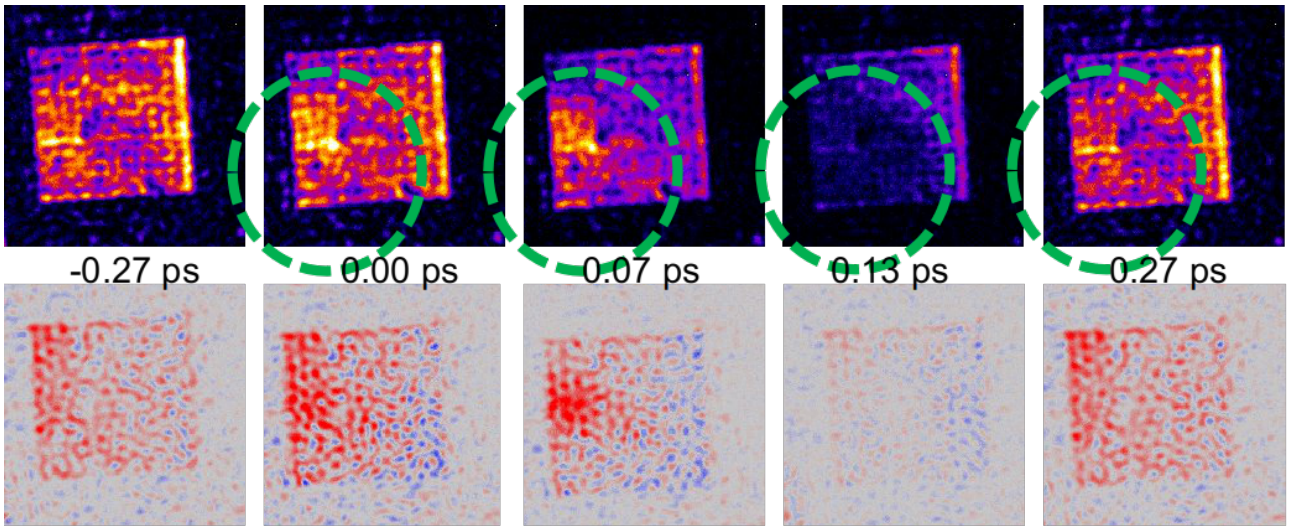

Figure 3.33: SHG pictures for different delays on a $10 \times 10 \mu m^2$ ferroelectric domain. Before the pulse, at the peak, in the middle, in the dip and after the pulse. Top: $\phi = 90°$. Bottom: $45 - 135°$. After a marked change in the area where the pump has its maximum of intensity (circled area), patterns recover their original textures in 0.27ps.

the contrary, during the excitation, the asymmetry could be caused by other phenomena ($\boldsymbol{P_e}$ changing or optical rectification), and it is not safe to say that the asymmetry maps are still a good representation of the location of the antiferromagnetic domains. For times after 0.27ps, the images being identical as before the pulse, the analysis seems valid again and since the measurement is stroboscopic, we can say that we do not observe cases where a red (blue) domain turns into a blue one (red one) during the pulse, and returns to its original red (blue) state before the next pulse, in a repeatable fashion.

Time evolution at $0°$ and $90°$

Under high fluence, the SHG signal in ferroelectric domains at 90° and 0° changes by up to 40% (Figure 3.34). The shape of the time evolution is also modified by the presence of an early peak before the dip, which was not present at low fluence.

To understand why the signal is not flat at negative times, we must recall that our origin of delay is taken on the peak of the Sum Frequency Generation (SFG) signal, which corresponds to the overlap of the maximum amplitude of the pump with the maximum of amplitude of the probe. The pump, being 100fs wide, starts hitting the sample approximately 50fs before. The probe has also a temporal width, of about 90fs, and starts probing the signal induced by the pump, at delays before the pump should start hitting the sample. In other words, the SHG signal we observe is convoluted by the temporal shape of both the pump and the probe. The dynamics we observe is at the edge of our temporal resolution, and faster than the picosecond.

Some effects induced by the pump last for longer timescales, but are of lower amplitude. For example, the map formed by the ratio $90°/0°$ has an evolution slower by a factor 2 compared to each polarization angle taken individually. This ratio is meant to represent roughly the balance between the big and the small ferroelectric lobes. A decrease of the ratio means a rounder angular shape. It can be noticed that after 0.27ps, an offset of nearly -5%

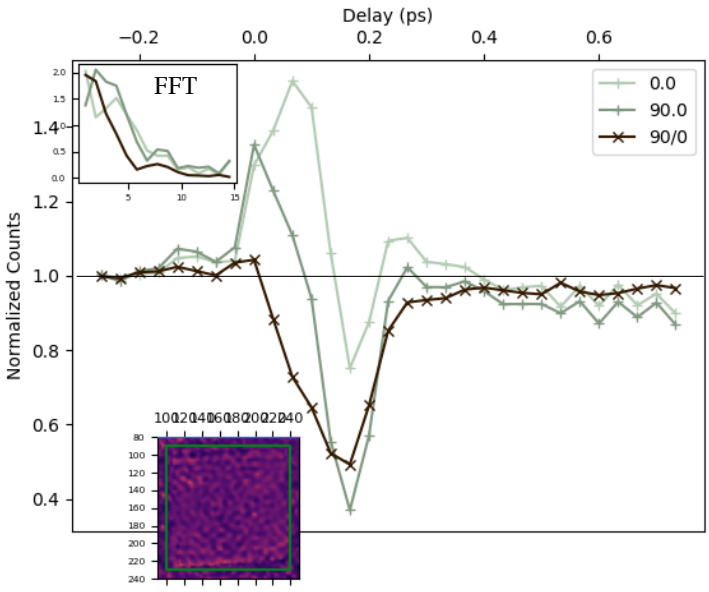

Figure 3.34: Time evolution of the SHG signal averaged over a $10 \times 10 \mu m^2$ ferroelectric domain (bottom inset), for probe polarized light at 0° and 90°, and horizontal pump (90°). Each signal is normalized by its value at negative times. The ratio 90/0 shows that a slight distorstion of 5% of the main lobe remains for times larger than 4ps. The FFT (top inset) shows that the relative distorsion happens at half the speed of those of the two angles independently.

remains, and we could measure that it lasts and looks flat to all appearances for at least 1ns. Nonetheless, the offset has to vanish somehow between 1ns and 1ms, to recover the SHG values at negative times. This timescale is out of reach for the current setup. The physical origin of this phenomenon is still unknown, but could probably be attributed to interractions within the crystallographic lattice, given the timescale. For example, a femtosecond pulse in $BiFeO_3$ can induce an inhomogeneous strain which decays at the nanosecond timescale [126].

Transmission of the substrate

In all our experiments, to approach the $BiFeO_3$ layer of our sample as close as possible to the objective lens, the laser hits the sample from the back. We need to make sure that the dip in the time-resolved SHG intensity is not simply due to a temporary change of transmission from the substrate, which would cause a drop of laser intensity. A time-resolved measurements of the transmission of the substrate alone have been done (Figure 3.35a). For that, the transmission is measured in first harmonic with a photodiode. For this measurement, even though the origin of times was remeasured by sum frequency generation as explained in section 3.29, the delay can be slightly shifted of $100 fs$ compared to the SHG measurement because several months have past in between. We indeed observe a transmission drop, and it can be seen on Figure 3.35a that the STO substrate plus the SRO layer indeed accounts for 7% among the 10% transmission drop from the full sample. A 7% drop of laser intensity will correspond to a 13.51% drop of SHG signal, which is not sufficient to explain the drop of 50% that we observed on the SHG signal. Moreover, the shape of the curves are sufficiently different to discard a full transmission-related scenario.

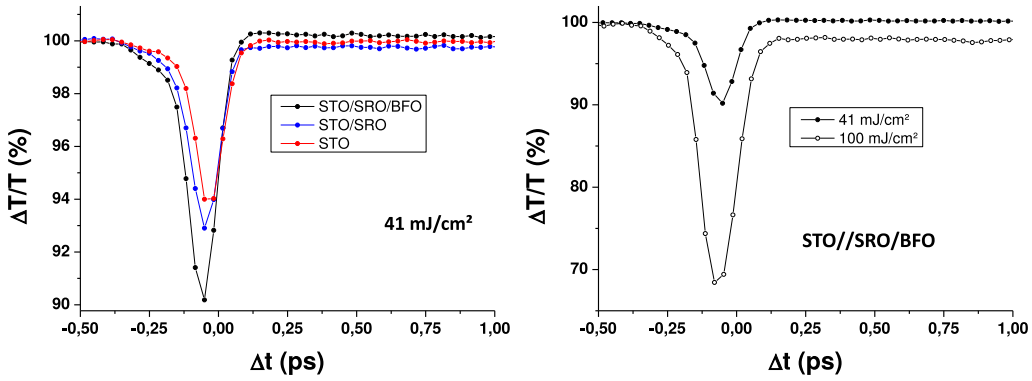

(a) Normalized time-resolved relative transmission measurements at 42mJ/cm^2 of our sample of $BiFeO_3$ compared to equivalents of its substrates.

(b) Normalized time-resolved transmission of the BFO sample for two different fluences: 41mJ/cm^2 and 100mJ/cm^2.

Figure 3.35: Time-resolved transmission measurements.

The transmission of the $BiFeO_3$ sample has also been measured for two different powers (Figure 3.35b). At very high fluence (100mJ/cm^2, *i.e.* twice as intense as the one we used in time-resolved SHG), a 30% transmission drop is observed, which would correspond to a 51% drop in the SHG signal.

We can see on Figures 3.35a and 3.35b that the transmission has not returned to its original state after 0.2ps, for the STO/SRO and for the STO/SRO/$BiFeO_3$ samples. This offset looks similar to the one we observed in our time-resolved SHG measurements, and could be part of the explanation. Nonetheless, it does not explain why the offset appears on the ratio 90°/0°, instead of being isotope. It seems more pronounced in the presence of $BiFeO_3$, and Figure 3.35b shows that the effect depends on the incident power. Our hypothesis on the effect happening in the $BiFeO_3$ lattice cannot be totally explained just by the change of transmission.

Distortion of the lobes

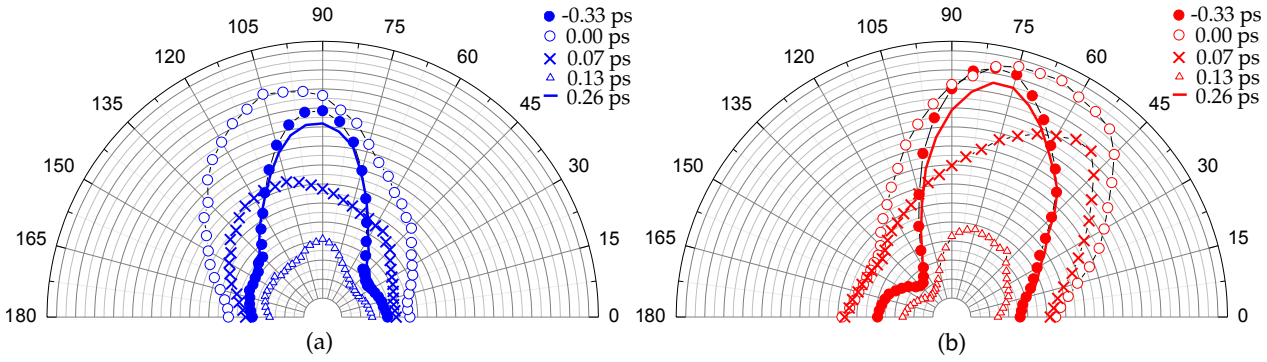

Figure 3.36: Time-evolution of the angular dependances. (a) Average over the blue domains. (b) Average over the red domains. The shape of the angular dependance changes over time and cannot be fitted by the previous method for times strictly between −0.33ps and 0.26ps.

Since we did not observe any domain switch between negatives times and times after 0.27ps, we can safely and easily isolate the red population from the blue population and compare their dynamics. As showed on Figure

3.36, an average of the angular response has been made over each domain population. The figure shows that the general shape of the angular profile changes completely on a window of 0.5ps, and cannot be fitted by the lobes we presented in section 3.2.6.

A tendency from the red domains to have their angular response temporary enhanced in the 135° direction is clear. Conversely, the blue domains have their blue asymmetry enhanced. In both cases, it is not just a scaling, the global angular shape is actually deformed, but if we consider that the SHG contribution at 90° is proportional to $\boldsymbol{P_e}$ and that the one at ±45° is proportional to $\boldsymbol{P_e}\cdot\mathbf{L}$ (Appendix D), this deformation can simply be explained by a deformation of the angular response of $\boldsymbol{P_e}$, without the need for $\mathbf{L}$ to change at all. A finer study on the angular changes of $\boldsymbol{P_e}$ (supposing it should preserve a certain mirror symmetry for example) should be done to be able to separate the antiferromagnetic from the ferroelectric contributions. The problem is that during the pulse, a SHG contribution from the electric field of the optical rectification of the pump can also superimpose and deform the angular profile in an asymmetric way.

Dependence on the pump polarization angle

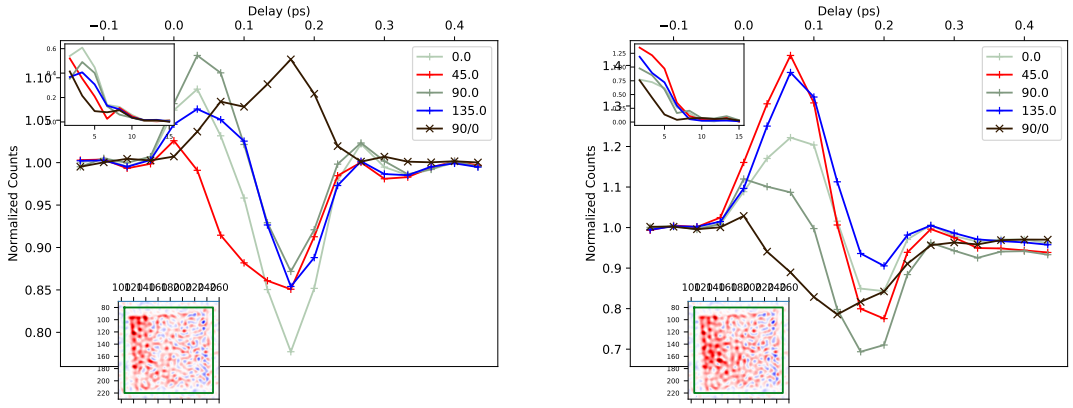

(a) Pump light polarization 0°

(b) Pump light polarization 90°

Figure 3.37: Time response of the SHG signal averaged over a $10\times10\mu m^2$ ferroelectric domain, for 0° and 90° light polarization angles of the pump. The 90° light polarization seems to be more efficient, especially for times below 0.1ps, when the SHG signal increases.

In an attempt to get a certain selectivity on the domains reactivity, we analyze the influence of the light polarization of the pump on the temporal variation of the SHG. The measurements are done for pump polarizations at angles 0° (vertical), ±30°, ±45°, ±60° and 90° (horizontal). The temporal evolution of the SHG at the main probe angles are displayed on Figures 3.37 and 3.38. We can confirm a visible change both in intensity and in symmetry.

Firstly, except from the horizontal pump (0°), the SHG at angles 45, 135 and 0° present a clear peak followed by a smaller dip, but with variable amplitudes, which can reach up to $(+40,-30)$% SHG variation. When the pump is horizontal (0°), the variation is attenuated, especially for the peak. In fact, 0° pump polarization is relatively inefficient: the decrease at later times is comparable, but the sub 0.1ps peak is of only 10%. Compared to the other SHG angles, the SHG at 90° has almost no peak, and a longer dip, except when the pump is polarized at 0° or 90°.

It always presents a secondary mode at 8THz. The ratio 90°/0° has always the same time variation as observed before, except for the pump at 0°, for which the evolution is positive.

Secondly, and it is maybe the most striking behavior, the relative amplitude for 45° and 135° SHG angles changes along with the orientation of the pump polarization. As Figure 3.37 illustrates, every time the pump polarization is mirrored with respect to the vertical plane in the laboratory frame (*i.e.* when the polarization angle changes sign), the probe responses at 45° and 135° are flipped too. The maximum contrast between red and blue seems to be achieved for a pump at ±45° angles, even though ±30° and ±60° give very similar results. At ±45°, the pump triggers an increase of SHG signal of 40%, and a decrease of 20%. The time evolution of the asymmetry maps is displayed on Figure 3.39. The alternation of symmetry is flipped when the pump polarization is flipped. As an illustration, let's consider a pump polarized at +45°. Most of the domains will experience a peak of their 45° (blue) signal, followed by a dip more pronounced at the center of the spot, which will let the red domains appear more intense, especially at the pump center.

In all cases, and for all the amplitudes, the variations stop at 0.3ps, similarly to the case at low fluence. If any multiferroic dynamics is present in our experiment, it happens within this time window, except for the low amplitude offset which remains over the nanosecond. Because of the simultaneity with the laser pulse within the first 0.3ps, it is difficult to separate all the effects and confirm that a change in the order parameters happens, but the differences observed between the different polarizations suggest that at least the internal electric field is temporary disturbed by the pump.

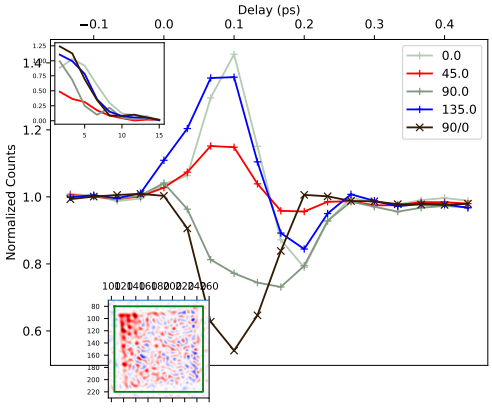

(a) Pump light polarization −30°

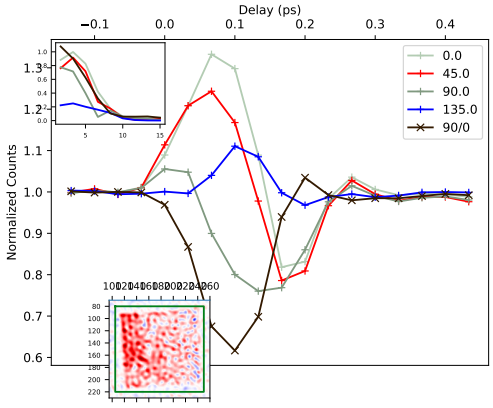

(b) Pump light polarization 30°

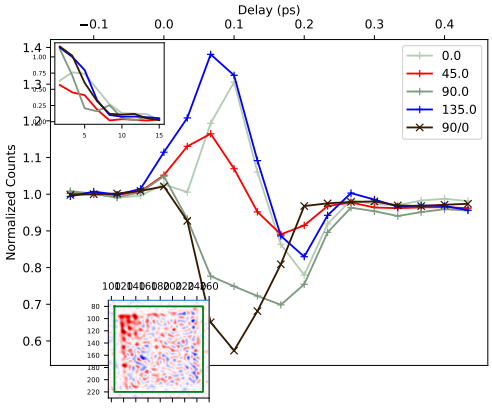

(c) Pump light polarization −45°

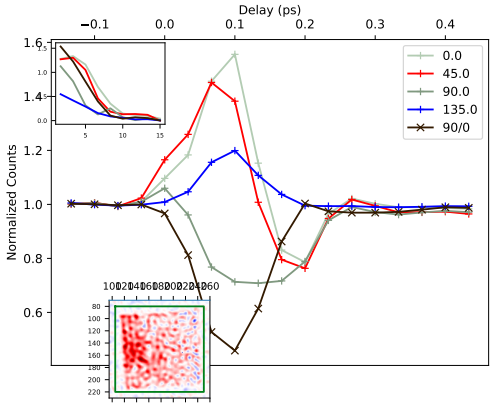

(d) Pump light polarization 45°

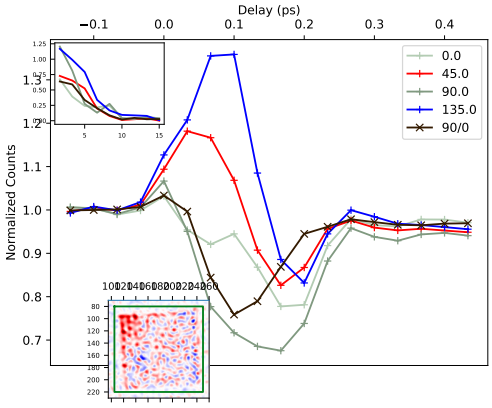

(e) Pump light polarization −60°

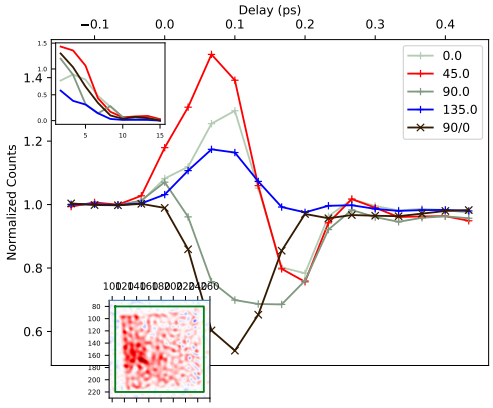

(f) Pump light polarization 60°

Figure 3.38: Time response of the SHG signal over a $10 \times 10 \mu m^2$ ferroelectric domain, for different polarization angles of the pump. The assymetry maps in insets are calculated for $t = -0.1$ps. The symmetry red/blue flips according to the angle of polarizations (left vs right). Angles $\pm 45°$ provide the largest contrast in SHG signal before 0.1ps.

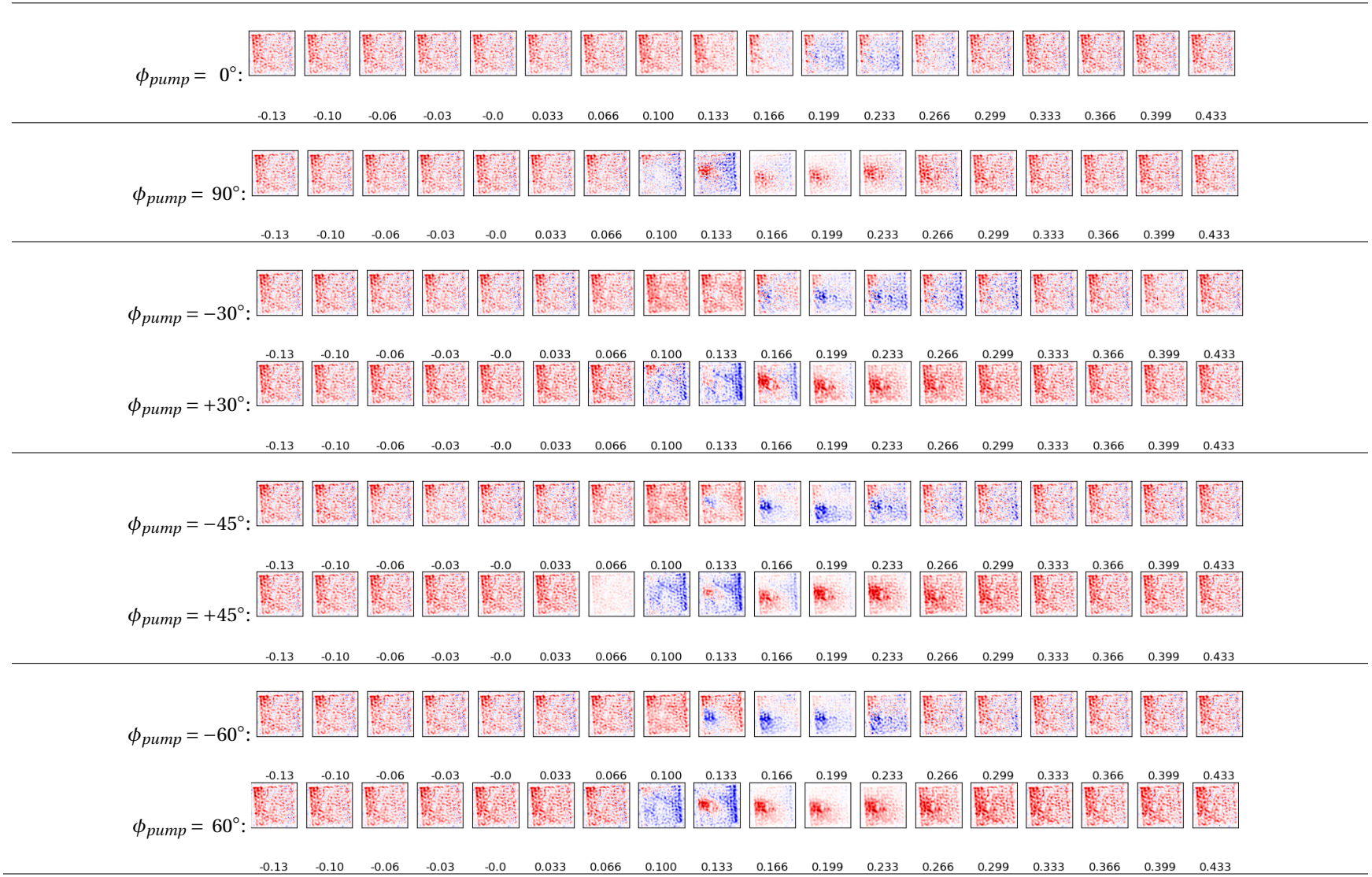

Figure 3.39: Time evolution of the asymmetric maps 45° − 135° for different polarization angles of the pump. An experimental offset on the angle estimated to −5° makes the maps appear more red than they should. White corresponds to mathematical 0, and the colorscale is constant over a row. The red/blue enhancement by the pump is inverted when the polarization angle is mirrored with respect to the vertical axis.

3.3.8 Conclusion on the Time-resolved SHG Imaging

We have shown some evidence of multiferroic dynamics induced by a laser pump at times below 0.3ps. The extraction of the antiferromagnetic contribution is difficult due to the short timescale. In this region, the overlap with the pump pulse induces other phenomena such as optical rectification, which are is difficult to discard given our time resolution, limited by the convolution of the two pulses.

Despite the fast dynamics, the time evolution of the SHG signal at 45° and 135° has shown a clear dependence both on the pump polarization and on the antiferromagnetic domain orientation. The detailed analysis of the dynamical changes of symmetry of the SHG polarization dependence is underway. Although it is difficult to understand our data at this stage, we can present here a few hypotheses on what could be happening. Indeed, the rapidity of the full dynamic response seems to indicate that electronic processes may be involved. Indeed the measured timescale is the same order of magnitude as that electrons would take to ballistically reach the surfaces. This could indicate that the first effect would be a screening of the electrical polarization. It is to be noted that other mechanisms relying on phonons or photostriction have been shown to happen at longer timescales [127].

Even for a fluence of 50mJ/cm^2, the antiferromagnetic texture was reset in 0.3ps, and no domain wall motion was clearly observed. This is rather surprising at first sight, but it could be due to the very fast speed at which electrical processes happen. Their coupling to a slower magnetic order parameter would thus not be very efficient to set the antiferromagnetic dynamics.

3.4 Conclusion on the SHG of $BiFeO_3$

In this chapter, we presented a method for observing antiferromagnetic domains in the multiferroic $BiFeO_3$ using second harmonic generation. With this method based on crystal symmetries, we could separate the ferroic orders with a spatial resolution below 1µm, and extract additional information on the electric charge repartition on the sample. This optical method is adapted to ultrafast measurements with a subpicosecond temporal resolution. We showed that a laser pump could induce an ultrafast variation of second harmonic generation, below 0.3ps, and that the polarization of the pump could change this variation. We suggest that the speed at which the entire process happens could be an indication for an electronic mechanism changing the internal field by providing screening charges.

No antiferromagnetic change in the picosecond timescale was clearly observed, perhaps because the induced perturbations are too fast to couple efficiently to the magnetic order parameter. In order to solve this problem, other sources of excitation should be considered. In particular, the use of a THz pulse would be more effective. Another possibility is to directly inject spin currents in the sample, using an adjacent layer. This approach is developed in the next chapter.

Chapter 4

Spin Current Injection

In this chapter, we will introduce new designs to manipulate the antiferromagnetic texture. The basic idea is to directly inject spin currents into the antiferromagnet. A badly designed injection could give disappointing results. The chances of affecting the antiferromagnetic texture are increased if the temporal shape of the excitation excites the resonances of the antiferromagnet. We have seen with our simulation in NiO that a spin transfer could result in a torque capable of switching an antiferromagnetic state. Based on this idea, this chapter is meant to present the first steps that could achieve experimentally the same mechanisms on $BiFeO_3$. We investigate an optical way to generate picosecond bursts of spin currents, which could match the $BiFeO_3$ antiferromagnetic resonance. For this, we take profit of the ultrafast demagnetization mechanism. The spin current can be measured by different methods which are presented in the course of this chapter.

Firstly, we will introduce briefly the spin↔charge conversion processes that could be sufficiently fast for responding in the picosecond timescale. Secondly we will present the optically-induced ultrafast demagnetization mechanism in ferromagnetic layers which can act as a source of picosecond spin current. Thirdly, we will present different experimental methods for characterizing the generated spin current, with the help of an adjacent layer. We will show that our measurements can discriminate conversions at different timescales and that different conversion mechanisms can lead to different dynamics. Finally, we will introduce our first attempts for switching the antiferromagnet $BiFeO_3$ by remote and local picosecond excitations based on the ultrafast demagnetization.

4.1 Spin ↔ Charge Conversion Processes

One convenient way to measure spin currents consists in converting them into charge currents which can be measured using conventional electronics. Several physical phenomena can convert a spin current into a charge current and vice versa. We focus here on two effects, namely the Inverse Spin Hall Effect (ISHE) and the Inverse Rashba-Edelstein Effect (IREE), and also mention the spin Seebeck effect.

4.1.1 Inverse spin Hall effect (ISHE)

Spin Hall Effect (SHE)

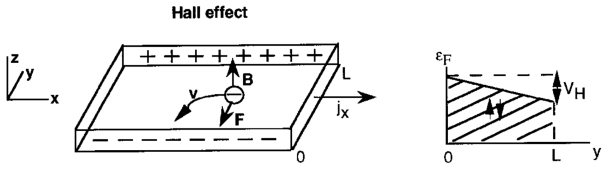

(a) In the Hall effect, electrons going along $-x$ are deviated by a $\boldsymbol{B}$ (parallel to z) to accumulate towards $-y$, creating a transverse charge accumulation.

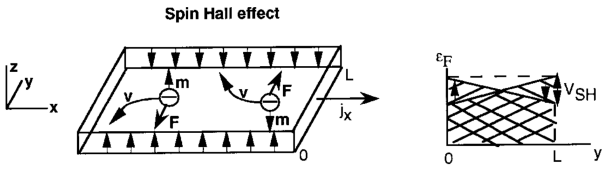

(b) In the spin-Hall effect, no magnetic field is applied. Electrons going along $-x$ are deviated separately according to their spin $\boldsymbol{m}$ (along $\pm z$) to accumulate towards $\pm y$ (or $\mp y$, depending on the material). As a consequence, a transverse spin accumulation is created.

Figure 4.1: Hall effect and Spin Hall Effect. From [128].

The Spin Hall Effect takes its name from the classical Hall effect where the charge carriers accumulate on the side of the conductor when an external magnetic field is applied, as a direct consequence of the Lorentz's force. In the case of the Spin Hall Effect, no external field is required. It is observed that in materials with strong spin-orbit coupling, spin up carriers accumulate on one side of the material, transverse to the current, while spin down carriers accumulate on the other side (Figure 4.1) [128]. A quantity called *Spin Hall Angle* quantifies the efficiency of this effect within materials. Platinum (Pt) and tungsten (W) have high spin Hall angles, and are commonly used for this conversion. Platinum has a positive spin Hall angle and tungsten a negative spin Hall angle, which makes them complementary materials for spintronic devices.

Inverse spin Hall effect (ISHE)

The opposite effect also exists and is called the *Inverse Spin Hall Effect* (ISHE). When a spin current is injected into a material with strong spin orbit coupling, the material will respond by generating a charge accumulation transverse to the spin current. This effect is commonly used for measuring a spin current with conventional electronic probes (voltmeters, oscilloscopes). A thin layer of high spin Hall angle material (a heavy metal) is deposited on the spintronic device: it acts as a sink for the spin current, which is converted into a charge accumulation measurable with a voltmeter. The conversion from spin current to charge current depends both on the spin Hall angle of the material, and on the spin-mixing conductance at the interface. For platinum, the intrinsic spin hall angle is estimated at 0.19 [129], but the interface with CoFeB and the spin mixing conductance $g^{\uparrow\downarrow} \simeq 0.1$ should degrade the conversion by at least a factor of ten. The total conversion is expected around $\sim 1-2\%$. Naturally, the presence of the heavy metal also changes the dynamics of the spin current [130], and can notably reduce the free spins lifetime.

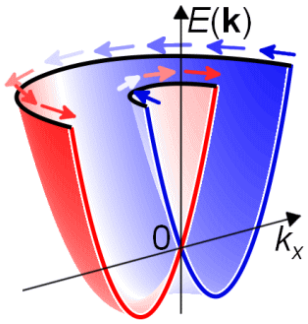

Figure 4.2: Spin-dependent Fermi surface in a Rashba system. The cross section shows the splitting of the potential well of the two spin populations caused by the Rashba effect. This system has a revolution symmetry around the axis of the local electric field, resulting in two opposite spin-dependent Fermi surfaces (black contours).

4.1.2 Inverse Rashba-Edelstein Effect (IREE)

Rashba Hamiltonian

The Rashba effect (also called the *inverse spin galvanic effect*) emerges from spin orbit coupling in materials lacking space-inversion symmetry. Because of this symmetry breaking requirement, it mostly appears at interfaces, or anywhere where there is a band bending. The space-inversion symmetry breaking can be seen as a local electric field. In virtue of the spin orbit interaction, in the reference frame of the orbiting electrons, this electric field is seen as a magnetic field, and favors a spin population over the other. For an electron of wavevector $\boldsymbol{k}$ and spin $\boldsymbol{s}$ (Pauli matrix $\boldsymbol{\sigma} = \frac{2}{\hbar}\boldsymbol{s}$), and an electric field along an axis $\hat{\boldsymbol{z}}$, the Rashba Hamiltonian is given by [131]:

$$\mathscr{H}_{\text{Rashba}} = \alpha_R \left(\boldsymbol{\sigma} \times \boldsymbol{k}\right) \cdot \hat{\boldsymbol{z}} \tag{4.1}$$

Where α_R is a scalar called the *Rashba coupling*, which is proportional to the spin orbit coupling (the electric field) and the hoping amplitude of the electrons from one site to another in reciprocal space. If we now add the kinetic contribution, with m the mass of the electron, we get:

$$\mathscr{H} = \frac{\hbar \boldsymbol{k}^2}{2\text{m}} + \alpha_R \left(\boldsymbol{\sigma} \times \boldsymbol{k}\right) \cdot \hat{\boldsymbol{z}} \tag{4.2}$$

Fundamentally, this asymmetric spin-flip scattering of the electrons results in a splitting of the Fermi surfaces for opposite spin populations, as pictured on Figure 4.2. This is commonly referred as a *Rashba splitting*.

Rashba-Edelstein effect

When a voltage is applied, the Fermi surfaces shift in the direction opposite to the current and favor a spin population over the other (Figure 4.3), resulting in the appearance of a spin current. This is the *Rashba-Edelstein effect*. First of all, the charge current gets spin polarized along $\boldsymbol{j}_c \times \hat{\boldsymbol{z}}$, and in addition, due to the asymmetric scattering, a transverse spin current appears.

Inverse Rashba-Edelstein effect

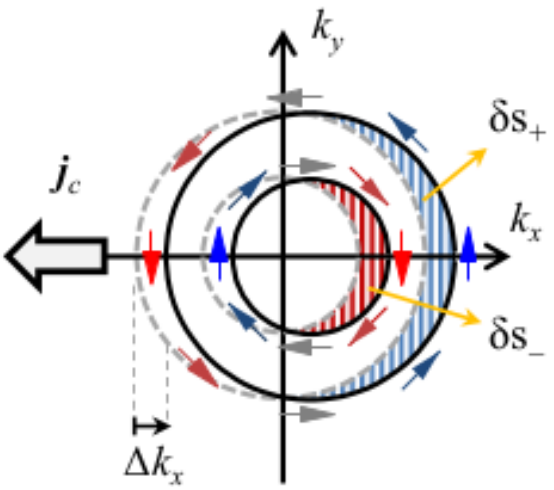

Figure 4.3: Rashba-Edelstein effect. From [132]. A charge current $\boldsymbol{j_c}$ shifts the Fermi surfaces along the direction of the electrons ($\Delta \boldsymbol{k}_x$). The difference in available states favors a spin population (δs_+) over the other (δs_-), resulting in the appearance of a spin current.

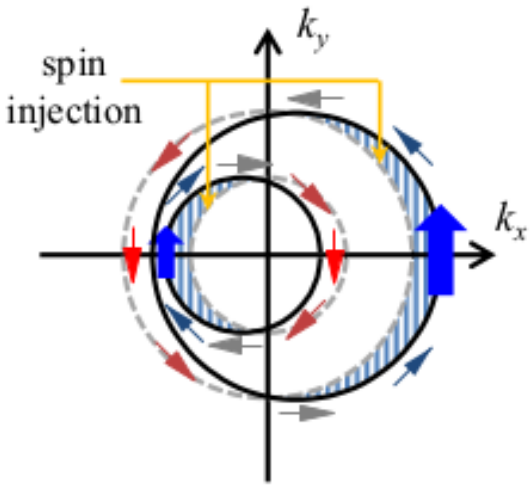

Figure 4.4: Inverse Rashba-Edelstein effect. From [132]. A spin current selectively fills (and empties) the states near the two Fermi surfaces, which consequently shift by an equal amount in opposite directions. The difference in size of the two Fermi surfaces results in a total nonzero $\boldsymbol{k}$, thus a net charge current.

Conversely, a spin current creates a charge current transverse to the direction of the spins in the $\hat{\boldsymbol{z}}$ plane $\boldsymbol{j_c} \propto -\left(\boldsymbol{y} \times \hat{\boldsymbol{z}}\right)$ (Figure 4.4). This is the *Inverse Rashba-Edelstein effect* (IREE).

4.1.3 Spin Seebeck

Just like a temperature gradient can generate a current via the Seebeck effect, it appears that a gradient of temperature on a ferromagnet generates a spin current [128, 133, 134]. A local elevation of temperature due to a laser pulse could trigger such an effect, and has to be considered when determining the origin of spin currents.

4.1.4 Spin ↔ charge conversion for THz emission

In the forthcoming sections, we show that a picosecond demagnetization can be achieved by an ultra-fast light pulse. Because of the conservation of the angular momentum, during this demagnetization process, the magnetic moment must be evacuated somehow. Several channels of evacuation are possible through the lattice, but one can also add an additional channel for the material to demagnetize thanks to an adjacent layer which can act as a spin sink. For example, a heavy metal with a strong spin Hall angle is a good candidate. Because ISHE and IREE originate form spin-orbit coupling, their response time is extremely fast, much faster than the picosecond. The spins will be converted into a charge current at the picosecond and achieve the generation of a THz pulse. Such THz emitters are reported to perform comparable outputs as more conventionnal sources based on ZnTe crystals [81, 135], and should be good resonant sources of excitation for antiferromagnets.

The spin sink could as well be directly an antiferromagnetic interface. A picosecond spin current injected in the proper direction at antiferromagnetic resonance could lead to a domain switch with very high efficiency. As a first step, we present a variety of methods for characterizing at various timescales the spin current we are capable of generating from the demagnetization of a magnetic layer, with the help of an adjacent heavy metal layer (sections 4.2 and 4.3) or with a Rashba interface (section 4.4). The injection of the picosecond spin currents directly into an antiferromagnet constitutes a second step (section 4.5).

4.2 Generation of Picosecond Spin Currents In Laser Excited Magnetic/Heavy Metal Bilayers

In this section we describe the way a femtosecond laser pulse can generate spin currents in a ferromagnet, taking into account all the effects at different timescales. We then consider the influence of a heavy metal adjacent layer on the demagnetization process.

4.2.1 Ultrafast demagnetization

When subject to an intense femtosecond optical excitation, an *ultrafast* demagnetization occurs in ferromagnets, much faster than their magnetic resonance. Such an effect was originaly demonstarted on ferromagnetic nickel [121] but has since been confirmed on many other ferromagnetic materials [136, 137, 138]. Although ferromagnetic dynamics usually lies in the GHz range, demagnetization can happen at picosecond time scale. The effect, still not fully understood, can be partially explaned by different successive models acting at different timescales [139]. There is an important distinction between the thermalization processes and the coherent processes (related to the laser pump). The thermalization processes can be explained with three baths of temperatures (electrons, spins and lattice), which thermalize at different timescales [121]. The demagnetization happens at the time of thermalization of the charge carriers ($\sim$ 50fs) without significant heat of the lattice. The two main phenomena at stake are the spin orbit interaction (confirmed by XMCD on CoPd [136]) and the reduction of the exchange splitting between majority and minority spins (confirmed by time-resolved photoemission on Gd [137] and permalloy [138]). As for the coherent processes, it has been shown that femtosecond pulses can change the magnetic ordering in a controlled fashion. At least three types of experiments illustrate this [139, 140, 141, 142, 143]. The main idea is that the electromagnetic pulse interacts with the valence cloud by adding an additionnal electric potential and can change the magnetic anisotropy or the magneto-optical response via the spin-orbit interaction [140]. In some cases, the polarization of the light can even determine the final magnetic state [143].

Looking into details of the sequence of excitation based on the different response times (Figure 4.5), we have [140]:

1. First, the dipolar transitions of the electrons which are selectively excited to higher energy bands, coupling to magnetism via the spin orbit interaction. This is a coherent and spectral-dependent phenomenon, which

decays with the dephasing time of the electronic levels (0.1fs to 1fs in metals).

2. Simultaneously, the quantum fluctuations related to the uncertainty in the spin density energy distribution have a breadth of ~ 1fs.
3. The recombination and redistribution of the electrons in the Fermi space, driven by the refilling of the low energy bands by Coulomb and exchange interactions occurs on the 100fs time scale. This results in inelastic scattering near the Fermi level, due to Pauli exclusion principle.
4. The heating of the lattice via coherent and non-coherent electron-spin-phonon interactions settles during ~ 1ps, depending on the specific heats of the baths, resulting in the final loss of magnetization.
5. Finally, spin transfers to the lattice and damped ferromagnetic precession rule the remagnetization dynamics on the nanosecond time scale.

Overall, 80% of the angular momentum from magnetization can be transfered to the lattice in 200fs [144].

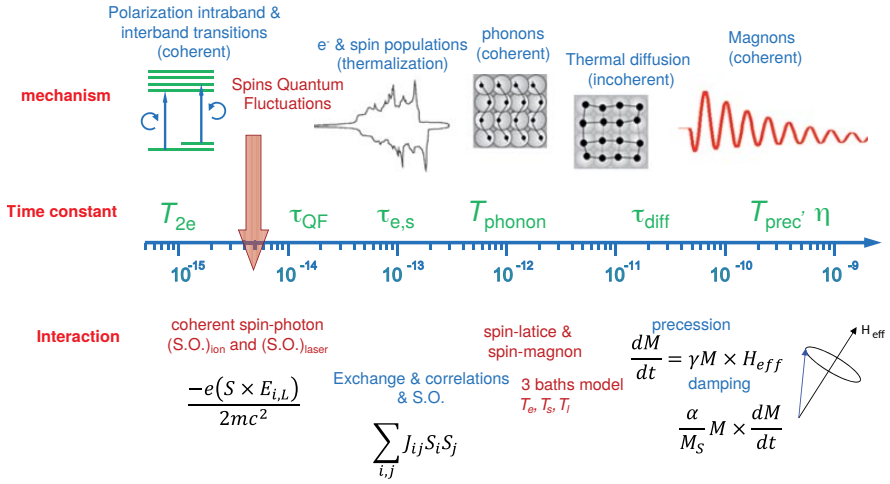

Figure 4.5: From [140]. Processes involved in the demagnetization and their response times.

4.2.2 Origins of the current in FM/HM bilayers

Because the ultrafast demagnetization creates hot spin polarized electrons in some femtoseconds, and can transfer angular momentum (coherently or not) to the lattice in less than 200fs, it is easy to imagine that an adjacent layer could partially collect the lost angular momentum. In particular, a heavy metal (platinum, in our case) adjacent layer can act as a spin sink by converting the spin polarized hot electrons into a charge current. On this system, we now need to consider the possible non-local phenomena that can happen in addition to the local ones discussed earlier (Figure 4.6). The spins can be transported via conduction or heat diffusion. In addition, hot electrons can fill spin polarized states above the Fermi level in the adjacent layer (state filling transport). As illustrated on Figure 4.6c, the thickness of the layers can impact the non-local effects.

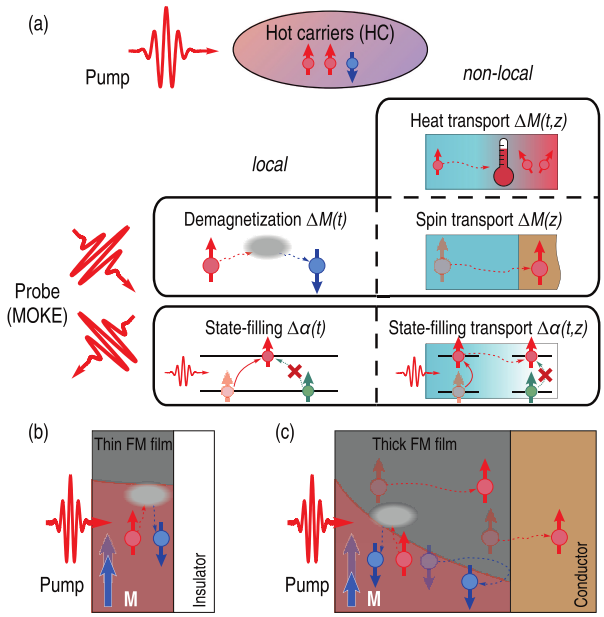

Figure 4.6: Ultrafast local and non-local electronic effects in magnetic bilayers. From [145]: "(a) Local and non-local electronic processes occurring upon femtosecond laser excitation of a ferromagnet leading to the emergence of hot non-equilibrium electrons. (b) and (c) Sketch of a femtosecond laser excitation of (b) a thin FM film on an insulating substrate, allowing for local processes only, and (c) a thick FM film on a conducting substrate, where both local and non-local processes are present. The red shaded areas represent the in-depth profiles of the laser excitation."

4.2.3 Choice of materials for the FM/HM bilayers

CoFeB is chosen because it presents almost no magneto-crystalline anisotropy and gives a good ferromagnetic resonance response. It is deposited in an amorphous state by sputtering on a glass substrate. On the heavy metal side, Pt is chosen because it has one of the largest spin Hall angle and is commonly available in growth facilities. Besides, CoFeB/Pt is reported to be the most efficient spin current emitter of the 'X/Pt' kind for generating THz [146]. The optimal thickness of the platinum layer for emitting THz radiation is 3nm and thicknesses between 3nm and 20nm for the CoFeB should give resonable results [146]. Later in this thesis, different thicknesses and other magnetic materials are tested, and the cap layer of platinum is compared to a cap layer of MgO.

4.3 Experimental Characterization Of The Spin Current

In this section, we present four ways of characterizing the laser-induced spin current in FM/HM bilayers, each giving access to informations at different timescales.

The first experimental method is an optical time-resolved measurement of the magnetization of the sample, for times between 0.1ps and 1ns. The second method is a time-resolved measurement of the terahertz radiation produced by the conversion of the spin current into a charge current. It probes times in the picosecond range. The third method is a measurement of the total charge current produced by the conversion, integrated over a millisecond. A fourth method combines the measurement of the ferromagnetic resonance of the bilayer by absorption of

a radio-frequency field, with the measurement of the spin pumping into the adjacent layer.

4.3.1 Time-Resolved ultrafast demagnetization measurement (by TR-MOKE)

In this section, we detail how the demagnetization of a magnetic material can be probed at a picosecond timescale with a measurement technique based on the the Magneto-Optic Kerr Effect (MOKE). This technique has been proven suitable for probing the ultrafast demagnetization phenomena even at femtosecond timescales[147, 148].

Magneto-optic Kerr effect (MOKE)

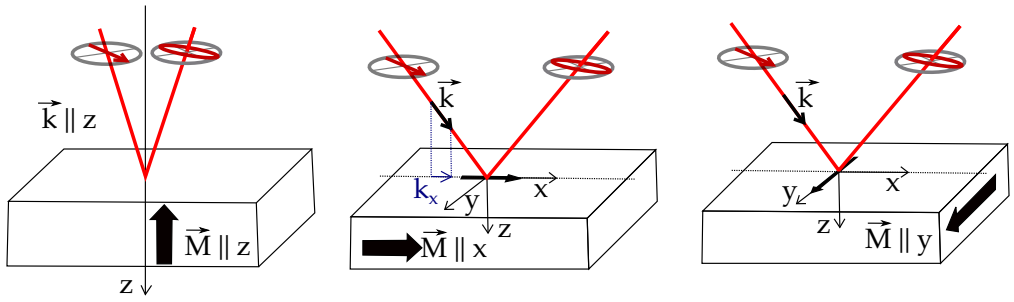

Figure 4.7: Magneto-optic Kerr effect (MOKE). Polar, longitudinal and transverse configurations, respective to the magnetization (thick arrows). The magnetization of the layer changes the polarization state of the reflected light.

To measure the magnetization at such timescales, the method has to be as fast as optics. We can use the *magneto-optic Kerr effect* (MOKE) to this aim, or the Faraday effect. Because a MOKE measurement has a configuration in *reflection*, we chose it over the Faraday effect which is a *transmission* experiment. Such measurement relies on the fact that the light changes polarization when reflecting on a magnetic surface (Figure 4.7). The effect is maximum when the magnetization is along the propagation vector of the light. The polarization can change both in orientation and in ellipticity. We can measure either one with similar setups, and both are necessary to fully reconstruct the demagnetization dynamics [145].

Experimental setup for MOKE magnetization measurements

Measuring the change of MOKE signal following a laser excitation can help quantify the magnetization. The MOKE signal is more sensitive when the beam is along the magnetization. In the case of films, shape anisotropy tends to favor an in-plane magnetization. Nonetheless, thin films can be very sensitive to the interface, specifically when they are a few nanometers thick. In particular, a platinum interface favors an out-of plane component [149]. For our concerns, and due to the setup environment, the MOKE beam reaches the sample with an incident angle close to 45°. As represented on Figure 4.8, the magnetic sample is placed in a magnetic field produced by a neodymium iron boron permanent magnet. The magnetic field intensity on the sample is measured by a gaussmeter to be 0.10T in-plane (and 0.04T out-of plane). A laser pulse of $\simeq$ 90fs, 400nm is produced by inserting a β-BBO in the Ti:sapphire laser beam. The polarization is corrected by a polarizer. The beam arrives at 45° incidence angle on the

sample with a power adjusted thanks to absorption attenuators to << 1mW on $20 \times 10 \mu m^2$, and the reflected beam is collected on a waveplate.

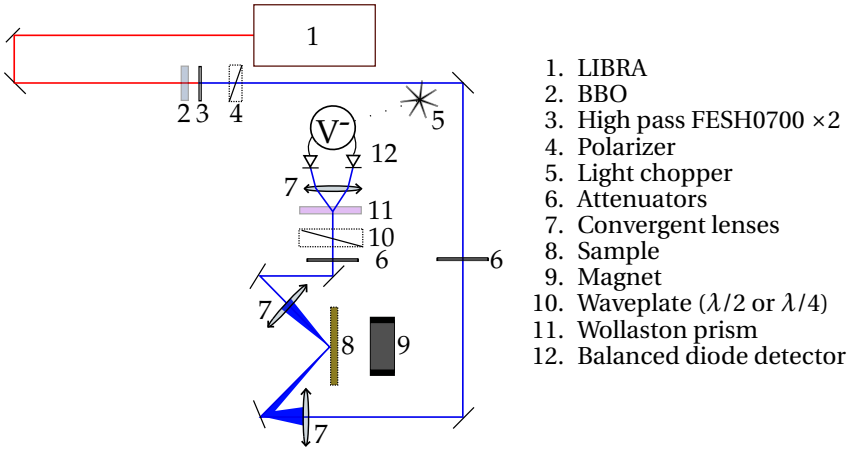

Figure 4.8: Experimental setup for MOKE magnetometry.

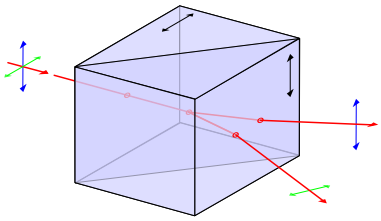

Figure 4.9: From [150]. A *Wollaston prism* projects an incoming light onto its two orthogonal axes of polarization, and let them come out as ordinary and extraordinary beams. When the incoming beam is linearly polarized along the diagonal of the Wollaston prism, or circularly polarized or elliptically polarized with a major axis along the diagonal of the prism, the two beams outgoing the Wollaston prism have equal intensities.

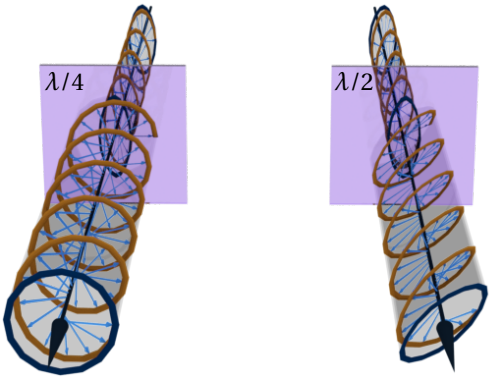

Figure 4.10: Quarter- and Half- waveplates. The *quarter waveplate* ($\lambda/4$) changes the ellipticity of the polarized light to circular (or, if the orientation of the Wollaston prism is favorable, to linear). The *half waveplate* ($\lambda/2$) changes the polarization angle and send it at 45° into the Wollaston prism. In both cases, the orientation of the waveplate must be so that the Wollaston prism projects the resulting polarization to two equally intense beams. Any change in the initial polarization state will change the correction of the waveplate and unbalance the intensity of the two beams exiting the Wollaston prism.

We use a half-waveplate to compensate for the change of light polarization orientation due to the MOKE on the sample at vertical magnetization and send it vertical on a Wollaston prism. When measuring the change of ellipticity, we replaced the half-waveplate by a quarter waveplate to compensate the change of ellipticity, and send circular polarized light on the Wollaston prism. When the corrected beam enters the Wollaston prism, it separates according to projections onto the crystal axis into ordinary and extraordinary beams, whose intensities can be compared in a balanced diode detector (Figure 4.9). The waveplate orientation is set so that the amount of light in both channels is equal when the magnetization is perpendicular to the beam (vertical). The balanced detector is composed of two photo-diodes on an amplifier circuit meant to amplify the difference between the two. It is connected to a lock-in amplifier synchronized to a chopper on the laser path. The chopper forces the laser to pulse at given harmonic of 1kHz (typically either 1kHz or 125Hz).

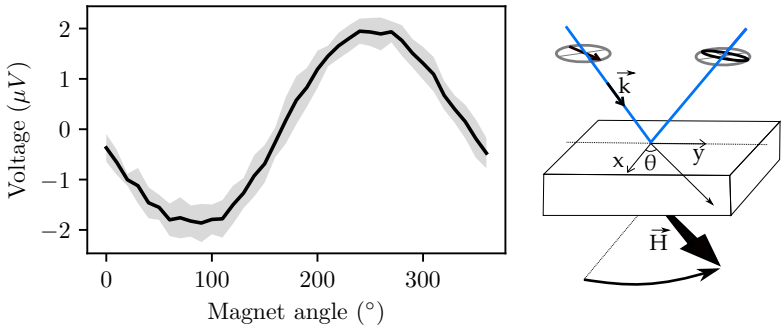

Figure 4.11: MOKE on CoFeB(7nm)/Pt(3nm). The voltage from the balanced detector measures the change of ellipticity of light after reflection on the sample. Changing the orientation of the magnetic field changes the ellipticity of light due to the MOKE.

At horizontal magnetization, the waveplate and the Wollaston prism are set so that the balance is achieved, and no voltage is measured in the detector. When the magnetic field of the sample is rotated, the orientation (ellipticity) of the light is changed and this unbalances the amount of light in the two channels coming out the Wollaston prism. The larger the signal, the bigger the longitudinal magnetization component in the sample. When rotating the magnetic field around the normal to the sample, we observe, as expected, a sine variation of the MOKE signal, as shown on Figure 4.11. This measurement of the MOKE amplitude at saturation magnetization will be our reference value for scaling the variations of the magnetization.

Experimental setup for TR-MOKE

The magnetization measurement has to be done optically to be sufficiently fast, while the demagnetization has to be induced by a blast shorter than the demagnetization timescales. In our case, the same laser generates both pulses, that we split in two thanks to a 97/3 beam splitter (Figure 4.12). The MOKE line presented earlier constitutes our probe. The pump is a 100fs, 800nm laser pulse attenuated to 100mW at normal incidence on the sample. When pumping, the lock-in amplifier of the balanced detector is locked on the chopper of the *pump* running at 125Hz. That way, we measure only the demagnetization occurring at the same frequency as the pump, and filter out any

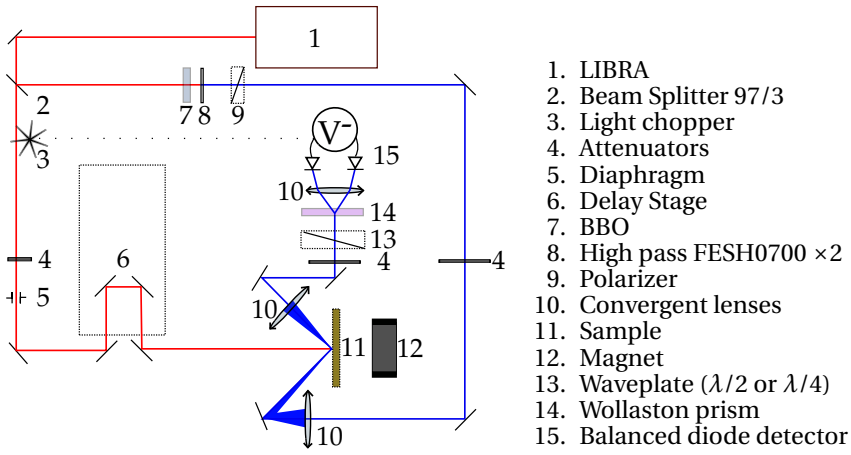

Figure 4.12: Experimental setup for TR-MOKE magnetometry. Chopper on pump.

possible parasitic signal induced by the probe (1kHz). As in the former chapter, the time resolution is achieved by adjusting the delay between the pump and probe pulses with the delay stage.

When hit by the laser, several physical phenomena occur (time-resolved reflectivity measurements have been made and are presented in Appendix E). To measure the demagnetization, we need to remove all the contributions of non-magnetic nature. For that, a time-resolved measurement at positive external magnetic field is subtracted from a time resolved measurement at negative external magnetic field. The permanent magnet is oriented at angles 90° and 180° to maximize the contrast of the MOKE (Figure 4.11).

Time resolution Because of the incidence angle of the probe close to 45°, the time resolution is degraded by the time the pulse takes to be reflected on the surface. The shape of the spot is elliptic and the major axis of the ellipse measures $\Delta l = 20\mu$m. The light needs $\Delta t = \frac{\Delta l}{\sqrt{2}c} = 47$fs for its reflection. Given the pulse duration of 90fs, our time-resolution is estimated to be $\simeq 140$fs for this experiment.

The time-resolved magnetic MOKE signal (in ellipticity and in rotation) of CoFeB(5nm)/Pt(3nm) for delays between 10fs and 800ps, obtained by subtracting the signals of the balanced detector for the two opposite magnet angles are displayed on Figure 4.13. The amplitude is expressed in percentage relative to the amplitude of the MOKE signal at maximum angle without pump (Figure 4.11).

Analysis of the TRMOKE curve

For both rotation and ellipticity, we observe two stages. First, an ultrafast demagnetization happening within 2ps after the pump. Second, a slower remagnetization, at a nanosecond time-scale (depending on damping), during which the magnetization precesses around the external magnetic field at ferromagnetic frequency. To extract the value of the maximum demagnetization, the ferromagnetic frequency and the characteristic remagnetization time, we fitted the data after demagnetization with the following model:

$$\frac{\Delta M(t)}{M_0} = -Ae^{-t/\tau} - S\cos\left(2\pi\nu t + \phi\right)e^{-t/\alpha} \tag{4.3}$$

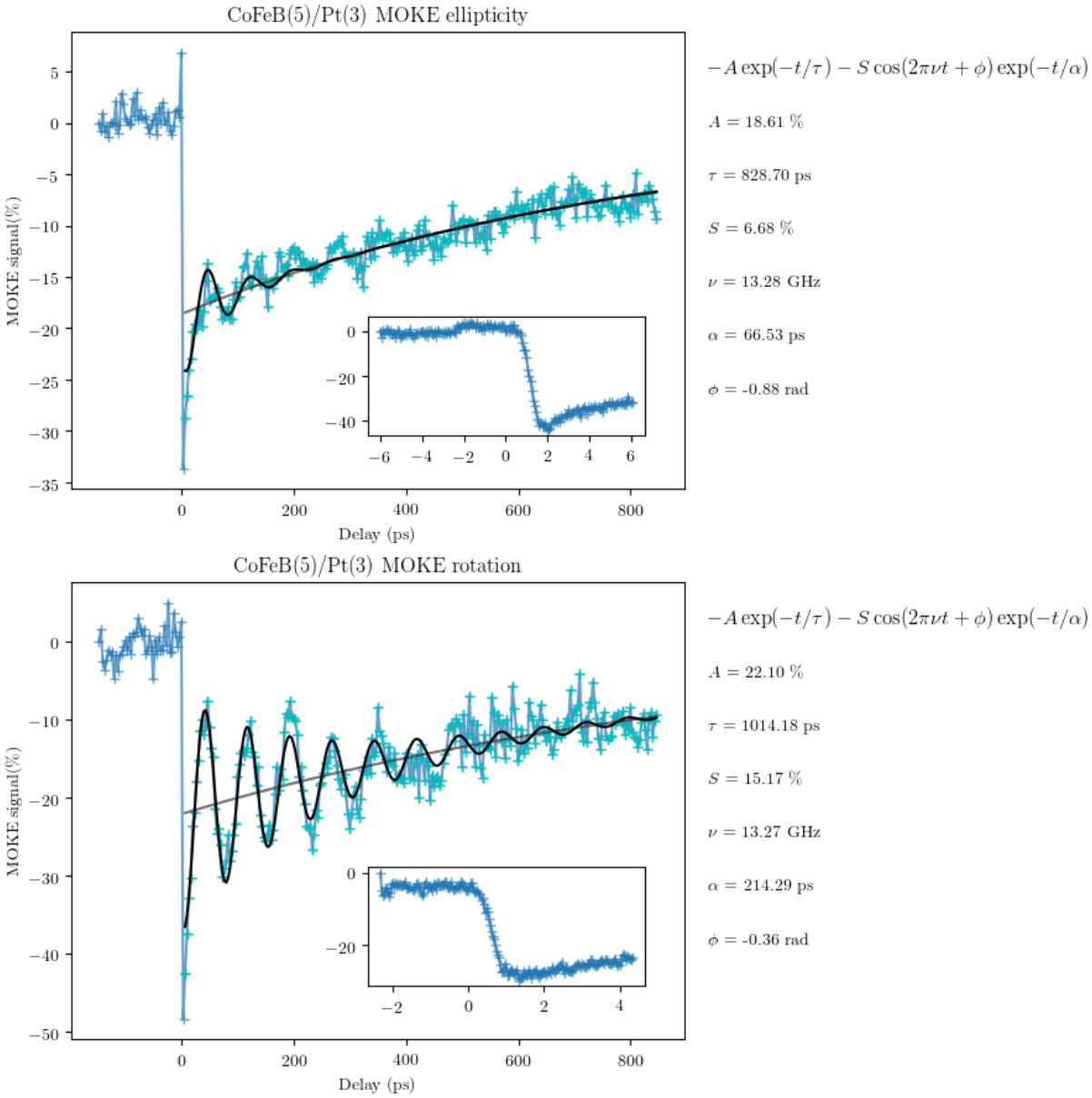

Figure 4.13: Ultrafast demagnetization of CoFeB(5)-Pt(3)

Where

- t is the time delay between the pump and the probe;
- $\frac{\Delta M(t)}{M_0}$ is the relative MOKE signal over time;
- A is the maximum demagnetization, free of precession;
- τ is a characteristic time of remagnetization;
- S is the amplitude of the precession on the MOKE signal;
- ν is the ferromagnetic precession frequency;
- ϕ is the phase at which the precession started;
- α is a characteristic damping time for the coherent precession to vanish.

This model separates the remagnetization into two phenomena: a global incoherent remagnetization of the sample at nanosecond timescale, and a precessional damped dynamics. In the precessional part, our model supposes the norm of the magnetization vector being constant, which is probably not very realistic. The model is nonetheless sufficient to separate the timescales of the different contributions.

The result of the fit is superimposed on our experimental data on Figure 4.11. Despite the fact that rotation and ellipticity do not show the same evolution due to the perturbation of the magneto-electrical coefficients [145], they show consistency with respect to the ferromagnetic precession frequency (Measurements on a thicker sample are presented in Appendix E.2). The percentage of MOKE signal loss at the beginning of the precession is also comparable, while almost doubled for the ellipticity. Both curves confirm that a change of magnetization happens in less than 2ps. The characteristic remagnetization time is in the order of nanoseconds. The magnetization precession is most likely due to an ultra-fast change of magnetic anisotropy accompanying the demagnetization process.

Conclusion from the TR-MOKE measurements

Thanks to the TR-MOKE technique, we observed ultrafast demagnetization below 2ps in our CoFeB/Pt samples. Our time-resolution of 140fs is not sufficient to resolve the exact duration.

4.3.2 THz radiation

THz radiation

The charge current created by ISHE has a temporal variation and therefore emits radiation. Since the demagnetization occurs in the picosecond regime, and the conversion process is extremely fast (spin orbit coupling is simply a relativistic effect), the emitted signal is expected to be in the terahertz. Several measurements of the THz emission on such bilayers have been done in the literature [81, 146].

Electro-optic sampling

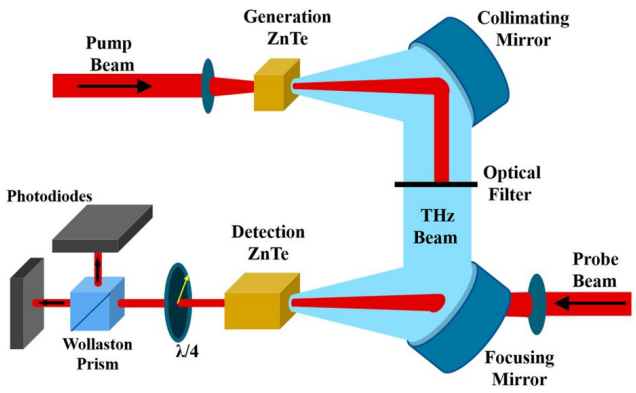

Figure 4.14: Electro-optic sampling. From [151]

The emitted radiation can be measured by electro-optic sampling. A piezoelectric crystal changes its optical

response time when hit by the teteraherz radiation. By measuring the electro-optical response at different delays, it is possible to reconstruct the terahertz emission and the original spin current [81] (Figure 4.14).

THz measurements on CoFeB/Pt

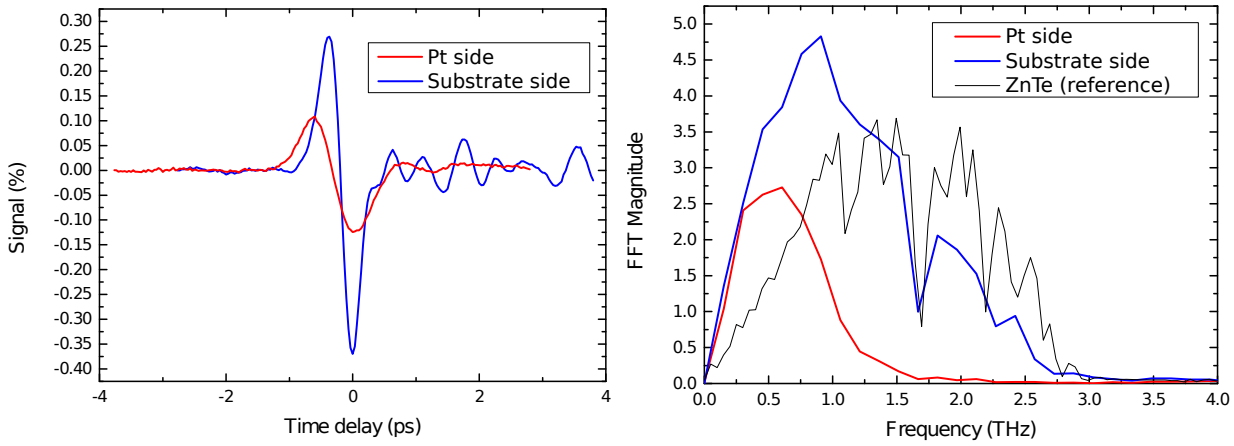

(a) (b)

Figure 4.15: Temporal and FFT responses of the electro-optical sampling signal. Courtesy NOVA IMMM Le Mans Université. Sample CoFeB(5)/Pt . The comparison between the two sides of the sample shows that the substrate absorbs THz radiations.

The measurements were done by Vincent Juvé from the NOVA group at Institut des Molécules et Matériaux du Mans (IMMM), with a Ti:sapphire laser similar to the one we use 100fs, repetition rate 1kHz, 1W on a spot of diameter 1cm). Figure 4.15 shows the electro-optical signal due to the THz radiation of our sample CoFeB(5)/Pt. The emission has a clear broad peak centered around 1THz, which covers the spectrum between 0 and 3THz. The comparison with conventional emission from ZnTe show that our devices are comparable, though slightly faster. An absorption band near 1.7THz is due to water molecules in the air between the emitter and the detector. Likewise, it is clear from the figure that the substrate can absorb some radiation.

The polarization of the THz emission can be turned simply by changing the orientation of the external magnetic field since it originates from the spin current from demagnetization (Figures 4.16 and 4.17). The amplitude of the THz emission can be increased by increasing the power of the laser pump (Figure 4.18), causing a stronger demagnetization of the ferromagnetic layer, until saturation.

4.3.3 Electrical DC measurements

In this section we present a technique meant to evaluate the spin current that we can extract from a laser-induced demagnetization, integrated over all timescales.

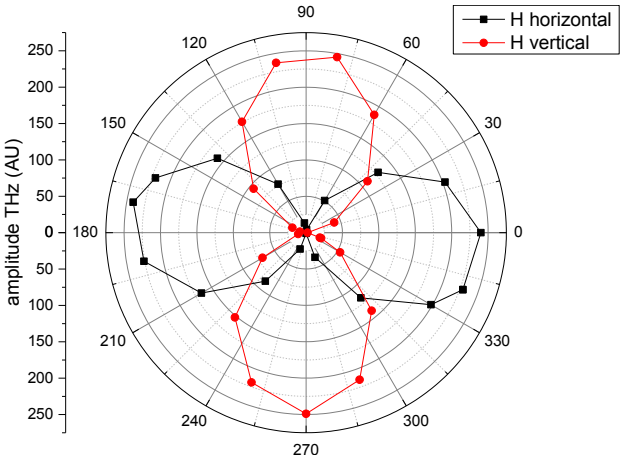

Figure 4.16: Polarization of the THz emitted field for two orthogonal orientations of the external magnetic field. Measured with a pyroelectric detector. Courtesy NOVA IMMM le Mans Univeristé.

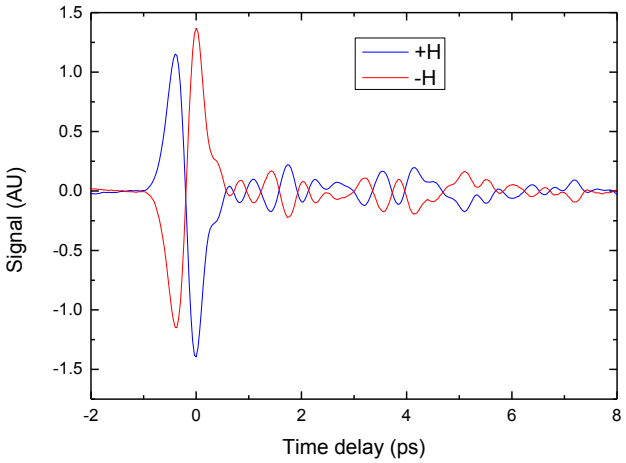

Figure 4.17: Electro-optical sampling for opposite orientations of the external magnetic field on CoFeB/Pt. Courtesy NOVA IMMM Le Mans université. The sign of the emission follows that of the magnetic field.

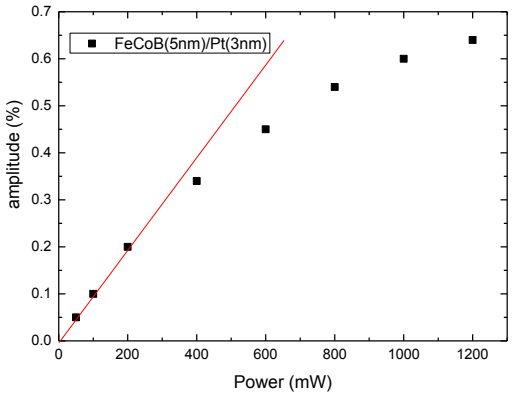

Figure 4.18: Amplutude of the THz emission with respect to the power of the laser pump. Courtesy NOVA IMMM le Mans Université. At low power the dependance is linear (red line), a saturation appears for power higher than 400mW. The beam spot diameter is slightly smaller than 1cm.

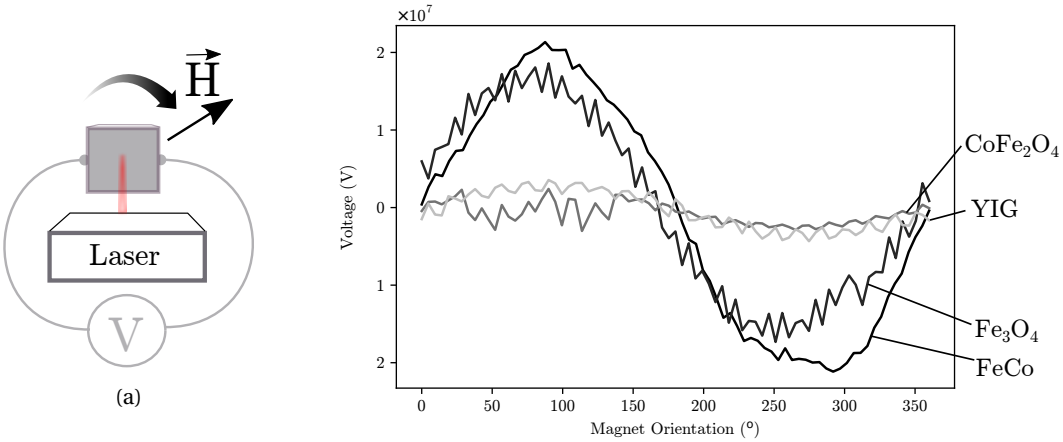

(a) (b)

Figure 4.19: Dependence of the measured voltage with respect to the in-plane magnetization angle. (a) Laser pulses are shone at normal incidence to a sample in an orientable magnetic field. The induced voltage is measured by a lock-in amplifier. (b) Voltage dependence on the magnet orientation for four different thin films of various thicknesses, capped with a few nanometers of platinum.

Electrical DC measurement of a spin current induced by a laser on a ferromagnetic layer

In this experiment, the laser beam is normal to the surface of the sample and a permanent magnet creates an external magnetic field which can be oriented in any angle in the plane of the sample. The spin current converted in the platinum into a charge accumulation can be measured by a lock-in amplifier synchronized on the laser frequency (chopped at 125Hz). The voltage we measure accounts for all the contributions to the charge accumulation, integrated over the duration between two laser pulses. The main contributions are: the ISHE during the ultrafast demagnetization and the remagnetization, the spin-Seebeck effect, and possibly the Seebeck effect. Figure 4.19b shows that the net charge accumulation is not null and that it strongly depends on the magnet orientation. As expected in a spin current induced scenario, the voltage varies like the sine of the angle. Different materials in thin film form were tested after deposition of 2nm of platinum. The effect could be reproduced on many ferrites, and even on yttrium iron garnet (YIG) which is a magnetic insulator. The thicknesses of the samples on Figure 4.19b are:

- $CoFe_2O_4$(12nm)/Pt(2nm)
- YIG(25nm)/Pt(7nm)
- Fe_3o_4(39nm)/Pt(2nm)
- FeCo(5nm)/Pt(3nm)

All the ferrites were elaborated by Jean-Baptiste Moussy in our group, by Molecular Beam Epitaxy (MBE) on α-Al_2O_3(001). The YIG (Yttrium Iron Garnet) sample was elaborated by Jamal Ben Youssef at LabSticc, Université de Bretagne Occidentale. The effect could be reproduced for laser wavelengths between 750 and 1000nm (Appendix E).

Conclusion on electrical DC measurement

The voltage measured in this electrical DC measurement is due to the spin currents converted in the platinum. The value gives information on the sum of all contributions to the spin current from the laser: demagnetization, remagnetization and the temperature gradient, regardless of their speed.

4.3.4 FMR and spin pumping

This section describes two additional methods, to enrich the exploration of the dynamic spintronic properties of our samples. I was not directly involved these measurements, but they will enrich significantly our analysis in the next section.

Ferromagnetic resonance (FMR)

The intrinsic dynamic response of the magnetic samples can be modeled by the Landau-Lifshitz equation of precession $\frac{d\boldsymbol{M}}{dt} = -\gamma\mu_0 \boldsymbol{M} \times \boldsymbol{H}$. A resonance emerges when driven by an external field oscillating at the proper frequency. It corresponds to the uniform mode, at which an oscillating external magnetic field makes all the magnetic moments precess in phase. In the first approximation, with H_0 the DC component of the external field $\boldsymbol{H}$, and M_S the magnetization at saturation, the angular frequency of the uniform mode of a flat magnetic sample (a thin film) is $\omega = \gamma\sqrt{H_0\,(H_0 + M_S)}$, for the case where $\boldsymbol{H}_0$ is in the plane of the thin film and the anisotropy is negligible [152][1]. This is the so-called FMR *Kittel formula*. In practice, the thin film is excited by a microwave external magnetic field at a given frequency, and an additional static field sweeps the values of H_0 until an increase of absorption of the microwave field by the sample is detected. The maximum of absorption corresponds to the resonance of the uniform mode. To reduce the noise of the measurement, the static field H_0 can be modulated, and the partial derivative of the absorption with respect to H_0 is measured instead, using a lock-in amplifier. In this case, the resonance corresponds to the inflexion point of the derivative, and the parity of the curve is expected to be odd relative to the external static field H_0. See Figure 4.24 for an illustration.

Spin pumping

A complementary measurement directly linked to our concerns of spin injection and conversion is the measurement of the voltage generated in the adjacent layer by *spin pumping* [130, 153]. In this measurement, the spin current that the precession generates can be absorbed and converted into a charge current in the adjacent layer via the inverse spin Hall effect, or the inverse Rashba-Edelstein effect. The continuous pumping via the microwave magnetic field maintains the electrical current generation in the adjacent layer, and electrical contacts on the sample can directly measure the voltage. Once again, the signal-to-noise ratio can be improved by a modulation of the microwave field via lock-in amplification, and by measuring the partial derivative of the voltage with respect to H_0. A drastic change of voltage is expected at the ferromagnetic resonance, as it is where the spin injection should be

[1] p380

maximum. Geometrical considerations tell us that the charge current should be odd with the external field H_0, so its derivative is expected to be even.

4.3.5 Conclusion on all different techniques

In this section 4.3, we presented four different experiments for generating and measuring spin currents in our thin films, each being specific to a different timescale. At ultrashort timescales 0.1 – 10ps, the demagnetization could be observed via the generation of a radiative terahertz pulse. For 0.3 – 800ps timescale, the ultrafast demagnetization and the slow remagnetization including ferromagnetic precession have been observed by time-resolved MOKE sensing. FMR and spin pumping probe the current generation at ferromagnetic resonance (~ 200ps), and direct current measurement probes at the millisecond timescale. This arsenal of techniques can give us good insights on the ultrafast demagnetization mechanism for the injection of spin currents.

4.4 Comparison Between Pt And MgO Cap Layers On CoFeB

In this section, we use the previous measurement techniques to compare the influence of a cap layer of MgO relative to the cap layer of platinum presented previously. MgO is a material widely used in magnetic tunnel junctions for its spintronic properties[154]. MgO is an insulator, no ISHE is present, so *a priori* we could expect no voltage from the demagnetization. In fact, we show that a conversion voltage appears for the CoFeB/MgO system in all our measurement techniques, that we can attribute to a spin charge conversion from inverse Rashba-Edelstein effect emerging from Rashba states at the interface between the two materials. For this study, we work on the following samples, grown at SPEC CEA by Amal Hamdache and Aurélie Solignac on glass substrates:

- //CoFeB(5nm)/Pt(3nm)
- //MgO(3nm)/CoFeB(5nm)/MgO(3nm)

4.4.1 TR-MOKE observations

The demagnetization of MgO/CoFeB(5 nm)/MgO has been measured by TRMOKE (Figure 4.20) and reveals a smaller drop of magnetization for a longer coherence time of the spins, compared to CoFeB(5nm)/Pt (Figure 4.13). This is explained by the fact that Pt is a very effective spin sink, being both conductor and an efficient spin-charge converter in the 10fs timescale. On the other hand, spin polarized electrons scatter more elastically on the CoFeB/MgO interface and can have a longer lifetime. Both systems globally re-magnetize at a similar rate in the nanosecond range.

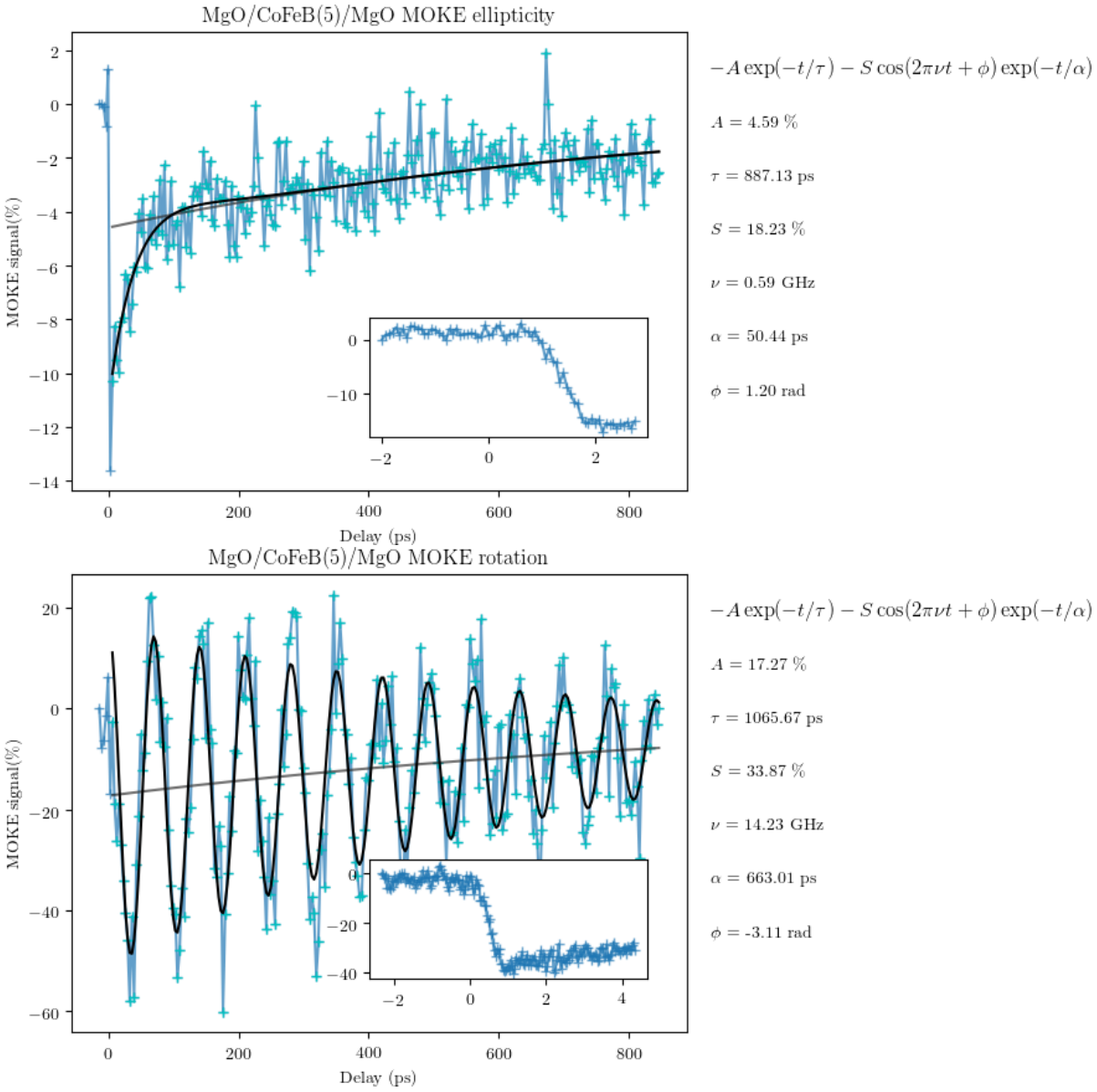

Figure 4.20: Utltrafast demagnetization of MgO-CoFeB(5)-MgO

4.4.2 Electrical DC observations

Observations

As shown on Figure 4.21, the laser excitation of the MgO(3nm)/CoFeB(5nm)/MgO(3nm) system can generate comparable DC currents as for the CoFeB(5nm)/Pt(3nm) case. With a 200mW laser pulse, the amplitude of the total electrical current induced by the laser is of approximately 3nA for MgO/CoFeB(5)/ MgO and 2nA for CoFeB(5)/ Pt. Such comparability was not originally expected as Pt is known to be a very efficient spin-to-charge converter in virtue of the large ISHE in this material. On the other hand, the conversion properties of the CoFeB/MgO interface are unknown but they turn out to be rather efficient. The relative signs between the two samples has been

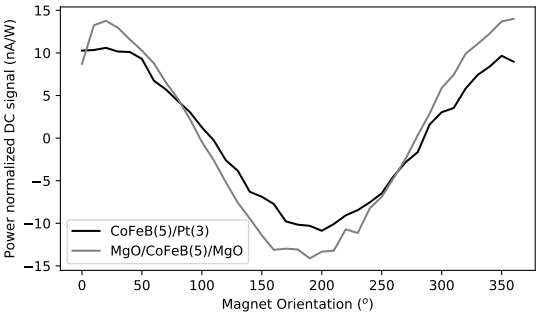

Figure 4.21: Electrical DC measurments on CoFeB/Pt and MgO/CoFeB/MgO systems. Electrical currents induced by a 200mW laser excitation at 800nm with respect to the external magnetic field orientation. For each sample, the current is obtained by dividing the measured voltage by the four-terminal sensing of the resistance ($R_{CoFeB(5)/Pt} = 205\Omega$, $R_{MgO(3)/CoFeB(5)/MgO(3)} = 233\Omega$). The current is then normalized by the power of the laser (200mW).

confirmed on the same experiment by Anas el Hamdi, PhD student in our group.

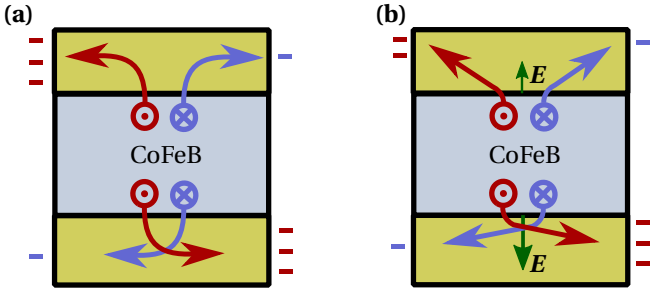

Figure 4.22: Spin transport with ISHE or IREE in sandwiched layers. **(a)** Spin transport in the case of ISHE. The Hall angle is intrinsic to the material. **(b)** Spin transport in the case of IREE. The spin deviation is relative to the electric field ***E*** at the interface. In case **(a)**, the transverse charge accumulations compete and depend on the heavy metal thicknesses, while in case **(b)**, they depend on the quality of the interfaces.

In spite of the supposedly large spin Hall angle of the platinum, the signal from MgO/CoFeB(5)/MgO appears to be larger. We must also mention the presence of two layers of the MgO, that we compare to a single layer of Pt. In the case of the the platinum cap, for which the inverse Spin Hall (bulk) effect is at stake, such a sandwich structure would be ineffective, because the voltages of each side would have canceled each other out (Figure 4.22). On the other hand, the signal from MgO/CoFeB(5)/MgO is suspected to arise from the inverse Rashba-Edelstein effect, which is an interface effect, much more sensitive to the quality of the growth. If both interfaces are not of equal quality, a voltage difference can arise. Depending on which side the IREE is the strongest, the single layer of Pt can give a positive or negative sign compared to MgO/CoFeB(5)/MgO.

Contribution of Seebeck and spin-Seebeck effects

For these measurements over long dynamic timescales, it must be considered whether the heat induced by the laser contributes to the charge migration because of the Seebeck and spin-Seebeck effects. The pure Seebeck effect is not spin-related and should absolutely be avoided. If the contacts are sufficiently far from the laser beam, the contribution from the Seebeck effect should annihilate since the same amount of charge migration should re-

sult on both contacts. Within this constrain, our circuit being open, moving the position of the contacts should not affect the result. For all our measurements, we ensured that they were outside the laser spot, and approximately equidistant. On the contrary, the spin-Seebeck effect can have a strong influence on the signal because the temperature gradient at stake is the one in the direction normal to the sample. To evaluate the influence of the spin-Seebeck effect on the signal, a series of measurements have been carried out on both sides of 20nm thick samples (//CoFeB(20nm)/Pt(3nm) and //CoFeB(20nm)/MgO(3nm), single capping) to emphasize the temperature gradient.

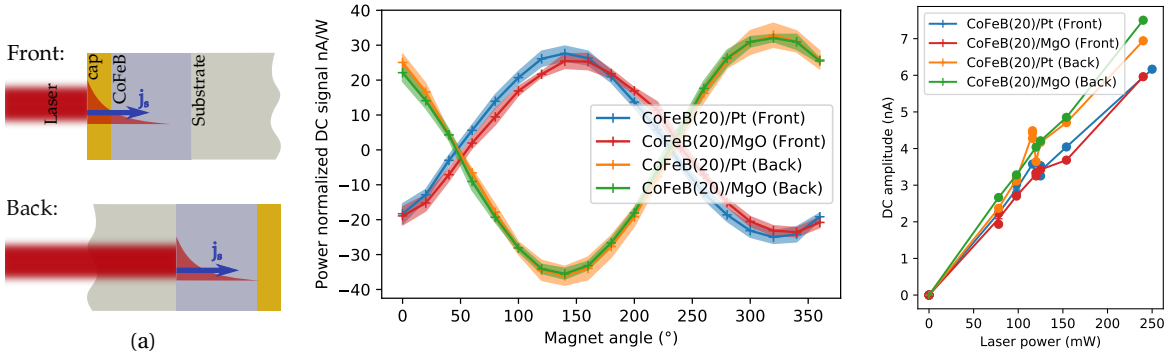

Figure 4.23: Electrical DC measurements on 20nm thick samples. **(a):** Sketch of the "Front" and "Back" configurations, crude representation of the temperature gradient and the spin-Seebeck current $\boldsymbol{j_s}$. **(b):** Electrical currents induced by a laser pulse on CoFeB(20nm)/Pt(3nm) or CoFeB(20nm)/MgO(3nm) with respect to the orientation of the external magnetic field, normalized by the power of the laser beam. The standard deviation between laser powers of 0, 78, 98, 120, 154 and 250mW is represented by the thickness of the curves. Flipping the sample with respect to the laser beam and the contacts reverses the sign of the spin current. **(c):** Linear dependence between 0 and 250mW of the spin current amplitude (absolute value) with respect to the laser pump power for each cap layer in both configuration.

When it has a demagnetization origin, the spin migration is always directed from the magnetic layer to the cap layer, but the orientation of the spins gives the direction (the sense) of the spin current. Two opposite spin currents will give opposite voltages after conversion in the cap layer. In the case of the Seebeck effect, the spin migration is always from the hot region to the cold region, with the orientation of the spin, again determining the conventional direction of the spin current. Let us consider a scenario without Spin-Seebeck. We assume that we get a positive voltage in the *front* configuration (Figure 4.23b), at a fixed external magnetic field. When we flip the sample, and the sample only (the probing contacts and the magnetic field are left unchanged), the spin current coming into the cap layer should be opposite to the one before flipping the sample. The voltage should be negative. Now, let us suppose that the laser heats up the side it hits, and that the spin-Seebeck effect directs the spin current from the hot surface to the cold bulk (Figure 4.23a). As in the previous scenario, let us suppose that the conversion gives a positive voltage in the 'front' configuration. Now, let's flip the sample in its back configuration. This time, and just like before, the temperature gradient directs the spin current from the hot surface to the cold bulk. From the cap layer's point of view, the direction of the spin current is unchanged and the conversion should also give a positive

voltage.

Our measurements displayed on Figure 4.23b show that a change of sign in the voltage is observed when the sample is flipped, confirming that the spin-Seebeck effect is not the main mechanism at stake. Nonetheless, the slight 20% change of amplitude from one side to the other on Figure 4.23b and the two different slopes on Figure 4.23c evidences a contribution from the spin-Seebeck effect. The laser penetration depth and the presence of the substrate can also affect the temperature gradient. An imperfect transparency of the substrate alone cannot explain this difference because the amplitude is larger in the 'back' configuration.

On Figure 4.23b, the voltage has been normalized by the resistance (four-terminal sensing) of the samples $R_{\mathrm{FeCoB(20)/Pt}} = 66.5\Omega$ and $R_{\mathrm{FeCoB(20)/MgO}} = 72.1\Omega$, and by the power of the laser. The measurements were carried out for laser powers between 0 and 250mW, and for this range of power, the measurements gave similar values once normalized, with less than 15% deviation, confirming that we operate in the linear regime (Figure 4.23c).

4.4.3 FMR, spin pumping observations

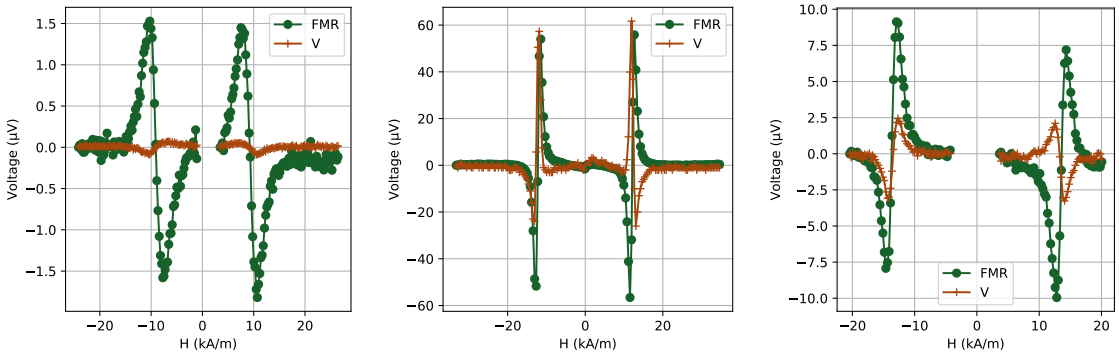

(a) CoFeB(5)/Pt (b) MgO/CoFeB/MgO (c) CoFeB/MgO/Ta

Figure 4.24: FMR and spin pumping experiments. FMR (green) and spin pumping (brown) voltages measured on different samples in a microwave magnetic field at 4GHz, with respect to the magnitude of an additional static magnetic field. The additional static magnetic field shifts the resonnance to the working frequency. It is modulated for a lock-in detection of the voltages, making appear the derivative of the microwave absorbance (green) and of the spin pumping conversion (brown).

The FMR and spin-pumping measurements have been made by Michel Viret and are displayed on Figure 4.21. The maximum of spin pumping is situated at the ferromagnetic resonance, as expected. The spin-charge conversion of the measured systems depend on the geometry and shapes of the samples. When scaled by these geometric factors, and by the four-sensing resistances, one finds that the MgO based layers generate comparable currents as the Pt ones. Interestingly, the sign of the spin pumping extracted from these measurements is the same for all three systems. The signal extracted from CoFeB/MgO and MgO/CoFeB/MgO are roughly the same, which indicates that the Rashba-Edelstein effect is likely to be the relevant one. We don't observe a clear cancellation as it would be the case for Pt/CoFeB/Pt. The remaining voltage might be due to an imperfect symmetry between the two interfaces, and also possibly because of the interface with the SiO_2 substrate.

4.4.4 THz radiation observations

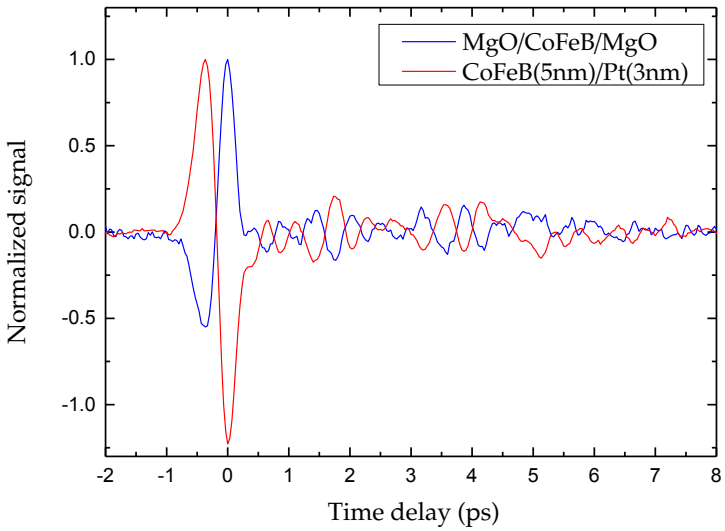

Figure 4.25: Comparison between CoFeB/Pt and MgO/CoFeB/MgO. (Courtesy NOVA IMMM Le Mans) Under the same condition (laser power: 1W and same magnetic field orientation), the shapes are identical but the signs are opposite. Before normalization, the signal from MgO/CoFeB/MgO is 25 times smaller than signal from CoFeB/Pt.

Finally, the THz measurements carried out by Vincent Juvé at NOVA group, IMMM Le Mans Université (Figure 4.25) reveal an extremely similar temporal shape for both MgO and Pt caps. It must be noted that the amplitude of the signal from MgO/CoFeB/MgO is 25 times smaller than for CoFeB/Pt, in contrast to what is measured with the techniques probing longer timescales. The similarities of the temporal shapes nevertheless proves that the ultrafast dynamics is governed by the CoFeB. This is rather surprising because the nature of the adjacent metallic layer has proven to modify the THz response in such heterostructures [81]. In our case, the platinum spin-flips so fast (below 10fs [81]) that the spin/charge conversion is instantaneous compared to the timescale of the spin current expelled from the magnetic layer. On the other hand, the interface state with MgO seems therefore to be inefficient at short timescales, but rather effective when signals are averaged at much longer times (~ 1ns). As a result, the main part of the signal is emitted at longer times and the THz signal is small.

4.4.5 Interpretation

To fully explain the origin of the conversion at the CoFeB/MgO interface, the spin-resolved band structures have been computed from ab initio calculations by colleagues at CEA Spintec, and are reproduced on Figure 4.26. They show three Rashba splittings near the Fermi level at the Γ point. Two strong splittings above the Fermi level are of opposite signs and can cancel each other, while another splitting at -40meV can be active for small fluctuations. Because of this configuration, hot electrons generated by the laser beam (up to 1.5eV) are subject to a very small Rashba splitting until they cool down near the Fermi level. Once thermalized, spin currents emitted in the re-magnetization processes can benefit from an efficient conversion into charge thanks to the Rashba split state near the Fermi level. This explains why the conversion into electrical current is not as efficient as for platinum on the

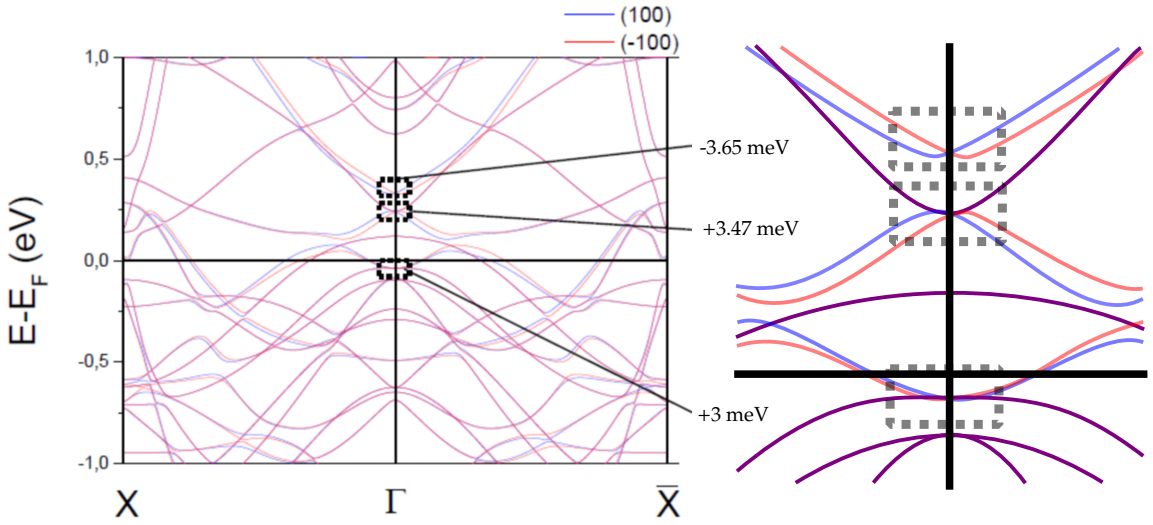

Figure 4.26: Ab initio calculations of the spin-resolved band diagram at the Fe/MgO interface. **Left:** Courtesy Mair Chshiev, Spintec Grenoble. Three Rashba splitting near Fermi level are visible at Γ point with energies −3.65meV, +3.47meV and +3meV from top to botom. **Right:** Bezier reproduction (not exact data), zoomed on the Rashba splittings.

THz measurements, whereas they reach equivalent yields on longer timescales as seen on spin pumping and DC measurements.

4.4.6 Conclusion

Our combined techniques have let us explore the dynamics of the laser-induced demagnetization of CoFeB for different timescales. We showed that the ultrafast demagnetization in the picosecond can generate THz pulses, that we predict well suited for our antiferromagnetic spintronics applications. The measurements were done with two different cap layers acting as spin-charge converters but having different conversion origins and different dynamics. Both gave the same THz pulse shape, therefore the picosecond characterization of CoFeB has an excellent fidelity. The cap layers we used do not seem to alter the intrinsic dynamics at such short timescales. Additionally, we have shown that the CoFeB/MgO interface presents a high spin-charge conversion efficiency which is due to a Rashba splitting near the Fermi level (−40meV). Although not entirely clear, the respective timescales of efficiency result in the CoFeB/Pt being the best THz emitter.

4.5 THz Excitation of $BiFeO_3$

Now that our THz emitters have proven their efficiency, we would like to use them on our $BiFeO_3$ experiment presented in the previous chapter. First using the THz far field from one of our FM/Pt emitter, then by direct local injection of spins from a deposited adjacent magnetic layer.

4.5.1 Far field THz excitation

The first test consists in evaluating the influence of a far field THz emitter on the second harmonic signal of $BiFeO_3$.

Experimental setup

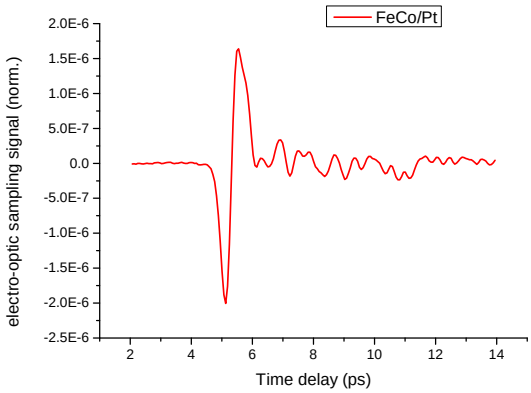

Figure 4.27: Electro-optic sampling signal associated to the THz emission of the FeCo/Pt sample.

This experiment has been done with a FeCo/Pt bilayer which had shown good results both on electrical DC measurements (Figure 4.19b) and in THz emission (Figure 4.27).

The setup of the experiment is the same as for Figure 3.6, except that the FeCo/Pt sample can be inserted between the half-waveplate and the low-pass filter FELH0750 (elements 7 and 8 on the sketch). The laser beam (100fs, 900nm, 1kHz) is collimated and the spot diameter is 1cm. A static magnetic field of 5mT aligned in the plane of the emitter is set by neodymium magnets on a rotating support, it controls the polarization of the radiated field.

Observations

The laser delivers 68mW at 900nm. When the FeCo/Pt bilayer is inserted, the power drops to 27mW. The FeCo/Pt can be replaced by a 50/50 beam splitter which can reproduce the same power drop (26mW), but without THz emission, *a priori*. A series of SHG measurements have been carried out on our $BiFeO_3$ sample, with each one of the two films, the results are displayed on Figure 4.28. It must be noted that the polarization of the THz emission can be changed at will thanks to an external magnetic field. We tried different polarization and alternated with the 50/50 beam splitter configuration (The order of the measurement is respected and indicated on Figure 4.28). We could see a clear difference of SHG signal between the FeCo/Pt and the 50/50 beam splitter cases. The THz emission generates more second harmonic than without. The change of polarization of the THz field did not seem to particularly affect the second harmonic generation signal, from this set of measurement. The THz polarization is perpendicular to the magnetic field. An orientation of 45° of the magnet corresponds to a polarization at −45°.

In all our measurements, the SHG images at 90° presents the same ferroelectric patterns. The full SHG analysis that we presented in chapter 3 does not work for these angular shapes, but the asymmetry around ±45° can still be

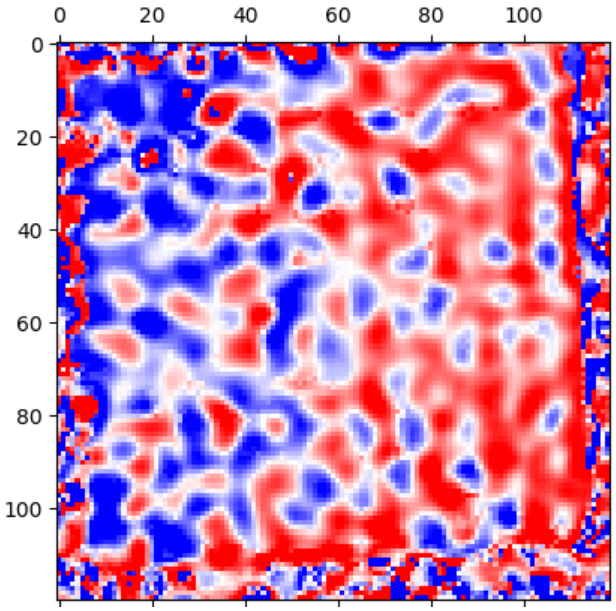

(a) Assymetry map on the $10 \times 10 \mu m^2$ domain.

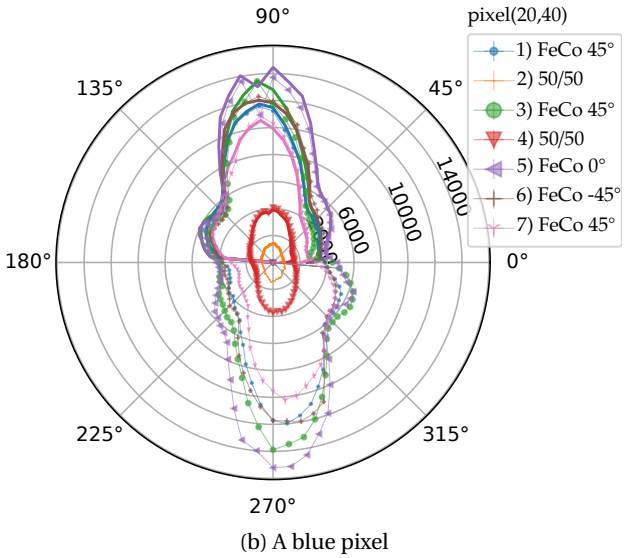

(b) A blue pixel

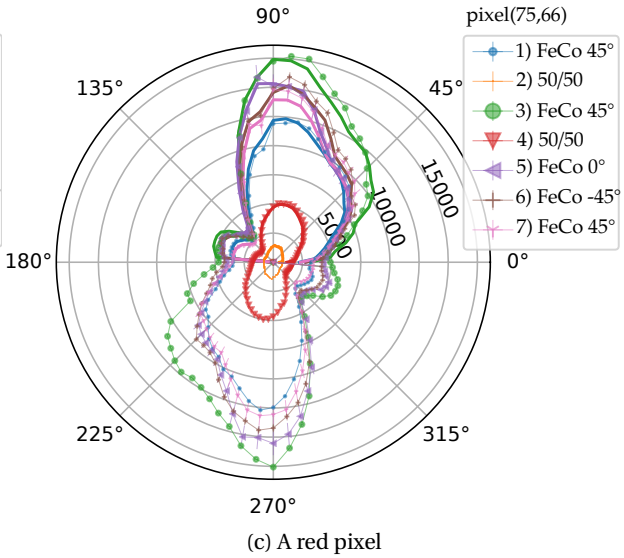

(c) A red pixel

Figure 4.28: Effect of a THz generation on the SHG signal of $BiFeO_3$. Angular dependence on a 'blue' and on a 'red' antiferromagnetic domain, during excitations by a FeCo/Pt THz emitter at different polarizations, controlled by an external magnetic field. The deformation associated to the THz is clear compared to a 50/50 beam splitter delivering the same laser power without THz field.

computed, and all delivered a similar asymmetry maps, that we reproduced on Figure 4.28a.

Before inserting the FeCo/Pt bilayer and the 50/50 beam splitter, a measurement had been done at high power (68mW). The angular profile is deformed in a similar way as when in the presence of the THz emitter (Figure 4.28). Let us stress once again that the 50/50 beam splitter and the THz emitter delivered both the same total power of 27mW on the sample. Because the power dependence of the SHG is quadratic, the SHG intensity becomes weaker by at least 75% (brown curve) compared to the high power. For this power, the angular profiles can be fitted to give the asymmetry map on the left of Figure 4.29.

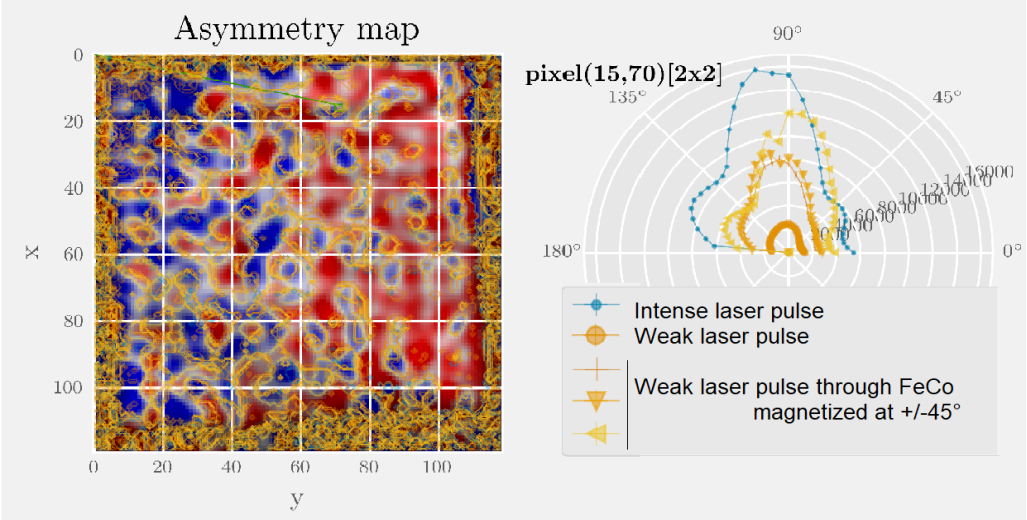

Figure 4.29: Comparison between intense femtosecond laser pulse and THz emisson on the SHG signal of $BiFeO_3$. The THz emitters modify the second harmonic generation angular dependance in a similar way as an intense laser pulse does.

On the same figure, the asymmetry maps associated to the SHG angular profiles when submitted to the THz radiation have been computed and their boundaries are superimposed in yellow contours onto the antiferromagnetic domain map on the left of Figure 4.28. Marginal differences can be noticed, close to domain walls.

Interpretations

It appears clearly that the THz radiation has an strong influence on the SHG signal. In that sense, the THz radiation seems more efficient than the light at 900nm, and delivers similar results compared to the laser at double the power. Nonetheless, as explained in section 3.1.6, the change of second harmonic generation does not necessarily means a change of the multiferroic order in the crystal. This effect can be due to the measurement of the THz field via $\underline{\underline{\chi}}^{\{3\}} \boldsymbol{E}^{[\omega]} \boldsymbol{E}^{[\omega]} \boldsymbol{E}^{[\mathrm{THz}]}$. In any case, the antiferromagnetic texture remained unchanged after the sample was illuminated by the THz pulses.

Since this experiment is not time resolved, it is not possible to tell exactly what is happening during the pulse, and if the deformations of the lobe are instantaneous. It can be inferred that phenomena like the ones we observed on Figure 3.36 occur. Our interpretation is that the THz radiation from the FeCo/Pt emitter triggers a slow perturbation on the internal electric field of the crystal[117] in a similar fashion to when we presented the optical rectification of the pump in $BiFeO_3$ (section 3.3.5), and that would happen at high power for the laser at 900nm

Perspectives

It would be possible to do time-resolved measurements with a setup similar to the one presented in section 3.3, with the THz as the source of excitation. For that, from Figure 3.27, the emitter should be inserted between the attenuator (element 10) and the parabolic mirror (element 11) so that the emission is focused on the sample. For a

better contrast and to get rid of the 800nmlaser pump, the beam splitter (element 12) can be replaced by an intrinsic silicon plate, which would reflect the laser beams (800nm of the pump and 900nm of the probe), but let the THz radiation go through.

4.5.2 Direct THz spin current injection

Preparation of the sample

To inject spin currents directly into our $BiFeO_3$ sample, a deposition of 3nm of permalloy plus a capping of 2nm of aluminum has been made by sputtering by Raphaël Weil at Laboratoire de Physique des Solides (Orsay), directly on the sample that we used in the study developed in Chapter 3. The metallic layers are in principle amorphous, to avoid an additional parasitic SHG.

The first thing we notice following this change, is that now the electric patterns are visible in first harmonic visible light imaging. Secondly, the second harmonic signal is lower than previously. This is simply explained by the fact that the added metallic layer between BFO and the objective lens is not transparent at the given wavelength ($450nm$). Thirdly, the metal deposition did not smooth the granularity on the ferroelectric textures that we observed in second harmonic imaging at angles 0° and 90°. If the visible textures in a ferroelectric monodomain were due to screening of dust at the surface, the metallic surface should have forced the homogenization of the electric potential at the surface. This is not the case, and textures remain.

SHG Experiment under magnetic field

The experimental setup for this experiment is very similar to the static SHG imaging experiment presented in section 3.1.7, except that an in-plane static magnetic field is added on the sample (Figure 4.30). In this transmission configuration, the magnetic field is generated by permanent magnets in a Halbach cylinder configuration mounted around the sample on a rotating support controlling its orientation. The in-plane magnetic field is of 0.1T.

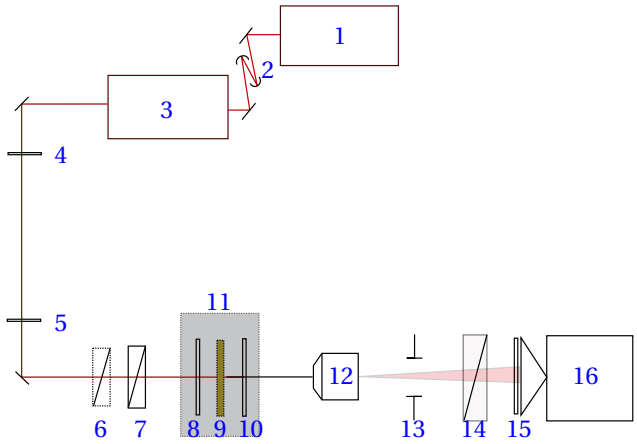

1. LIBRA
2. Telescope
3. OPA
4. Low-pass filter 800nm
5. High-pass filter 1600nm
6. Polarizer
7. Half-wave plate
8. Low-pass filter 750nm FELH0750
9. Sample
10. High-pass filter 750nm
11. Halbach magnet
12. Objective lens
13. Diaphragm
14. Analyser
15. Optical density filters BG39 & GG380
16. Camera

Figure 4.30: Experimental Setup for static SHG imagery of $BiFeO_3$/permalloy under magnetic field.

Results and perspectives

Unfortunately, the very first results of this study were negative: we did not see any change in the antiferromagnetic patterns, whatever the orientation of the static magnetic field. The permalloy did enhance the red asymmetry on the red domains, and the blue asymmetry in the blue domains, but independently of the external static magnetic field direction. Because of the lack of time [2], we could not carry on the experiments any further.

Nonetheless, hope is not lost since there is still a lot of room for improvement and that we saw promising results from the THz distant field. A pump line can easily be added and the power of the laser can still be increased by focusing the beam on the sample. The introduction of the time-resolution on this experiment would help finding ways to improve the temporal response of the magnetic layer.

In a near future, the full set of experiments will be redone. Those with the THz emitter with a beam more focused on the sample so that its fluence will be enhanced. The one with the magnetic layer directly deposited on the sample will necessitate more work for the interface optimization as well a a thinner BFO layer as the spin torque is mainly an interfacial effect. It is indeed a pity that the laboratory had to be entirely redone in the last few months of my PhD and these could not be carried out, but they are now the priority of the 'new' laboratory.

4.6 Conclusion On The Spin Current Injection

In this chapter, we have presented two important mechanisms of spin-charge conversion for the spintronics, taking their origins in the spin-orbit coupling: the inverse spin Hall effect and the inverse Rashba-Edelstein effect. These effects have been used complementarity in platinum and at the interface with manganese oxide to analyze the laser-induced ultrafast demagnetization of CoFeB thin layers, thanks to four distinct experimental techniques probing each a different timescale. Electrical direct current measurement could probe at the millisecond timescale, spin pumping could probe at the ferromagnetic resonance ($\sim$ 200ps), while 0.1ps – 800ns timescales could be probed using a time-resolved magneto-optical Kerr effect experiment, and terahertz radiation measurement could probe the 0.1 – 10ps regime. We showed that the ultrafast demagnetization of a magnetic layer could produce a terahertz generation of spin current suitable for antiferromagnetic spintronics. A terahertz radiation triggered visible signal in SHG imaging of our $BiFeO_3$ sample, but moderate effect on the antiferromagnetic patterns. A direct injection of picosecond spin currents using the demagnetization of a permalloy adjacent layer have so far given unsatisfactory results. Nonetheless, consequent steps forward have been achieved and we now have the tools for optimizing and developing a time-resolved analysis of spin injection in $BiFeO_3$, which should eventually lead to very rich spintronics physics and hopefully possible antiferromagnetic domain control.

[2] The experiments had to stop because of reconstruction work in the laboratory.

Chapter 5

Discussion and Perspectives for Further Work

5.1 Summary

In this thesis, we presented the concept of antiferromagnetic spintronics with the statement that antiferromagnets are good candidates for the next generation of memory devices because they are more stable and have a faster dynamic than ferromagnets, the current brick elements of hard disk drive memories.

To illustrate this, we simulated a spin transfer torque driven domain switch in NiO with a realistic anisotropy model, and predicted its feasibility within picoseconds with a spin current pulse available in the current state of the art. We then showed that antiferromagnetic structures in magnetoelectric multiferroic bismuth ferrite ($BiFeO_3$) can form, and are influenced by the ferroelectric state. A spin density wave in $BiFeO_3$ creates a stray field, which can be enhanced at multiferroic domain walls. An experimental work was done in parallel to image the antiferromagnetic domains in a thin layer of $BiFeO_3$, using second harmonic generation (SHG), with a spatial resolution of 0.5μm. The analysis revealed two types of antiferromagnetic domains, coexisting with a typical size of 0.5μm. Information about the ferroelectricity and the internal electric field could also be extracted from this analysis. We then excited the sample with a femtosecond laser pulse of 800nm and monitored the time-resolved SHG imaging signal. We observed an angular dependent SHG variation within 0.3ps, which could be related to an internal displacement of charges. The analysis could not claim anything on the antiferromagnetic dynamics, which would, if happening, be surprisingly fast within the given timescale. It was decided that the excitation source was not adapted to the antiferromagnetic dynamics, and that we should use resonant terahertz sources instead. For that, we studied the ultrafast laser-induced demagnetization of cobalt iron boron layers (CoFeB) capped with platinum (Pt) or magnesium oxide (MgO), with four different techniques, each measuring a different timescale. We showed that the ultrafast demagnetization produces a terahertz spin current, which can be converted efficiently into a terahertz radiation via the inverse spin-Hall effect. We also showed that comparable spin-charge conversion happens at the interface with

MgO, due to inverse Rashba-Edelstein effect, but with slower response time, resulting in an inefficient terahertz conversion. A bilayer of FeCo/Pt was then used as an emitter to excite the multiferroic textures in $BiFeO_3$. We saw a clear and encouraging impact on the asymmetry of the second harmonic signal, but no clear antiferromagnetic texture change has been measured. Finally, a permalloy layer has been deposited directly on the $BiFeO_3$ sample to directly inject terahertz spin currents into the antiferromagnets. The preliminary measurements showed again an enhanced SHG asymmetry, but no clear change in the antiferromagnetic patterns have been evidenced in the short period of measurement time we had.

5.2 Discussion and perspectives

The results we presented in this thesis are rather encouraging.

Our theoretical predictions on the picosecond switching of NiO, in accordance with the common knowledge on the antiferromagnets validate the realization of fast-writing memory states based on this material. So far, this study was based on a single atomic cell, assuming the whole bulk behaves in a collective way. The study could be developed by looking at the dynamical behavior at domain walls, or for exotic geometries.

The static simulations on $BiFeO_3$ have shown that a relatively large number of atoms could be simulated with our dynamical atomistic simulation code, which was able to reproduce a realistic behavior measured experimentally. Reproducing spin-flops and domain formation could give us more insight on the antiferromagnetic dynamics of $BiFeO_3$ in the future. Simulations offer the ability to tune parameters easily. We could for example investigate the parameters required to dynamically generate structures like antiferromagnetic skyrmions. Simulating a configuration similar to the one we measure experimentally in SHG would also help us understand the evolution of structural changes on the multiferroicity of $BiFeO_3$ under the optical excitation, or the spin injection.

In the course of the thesis, we have refined our SHG image analysis, and built up a time-resolved setup to observe the dynamical response of the multiferroic oder in $BiFeO_3$. Our spatial and temporal resolution, coupled with the angular analysis in polarization of the sample can help us extract a particular effect. Looking in particular locations, at a particular timescale will give more clues on the physical contributions in the SHG signal than a global average.

Exploring different timescales was illustrated on the laser-induced ultrafast demagnetization of the magnetic bilayers. The four measurement methods presented have proven their efficiency and their complementarity in extensively studying the generation and the conversion of terahertz spin currents. The spin current generation we obtained is rather satisfactory for picosecond operation using antiferromagnets. Some more work is required to quantitatively characterize the amount of demagnetization and the exact value of the spin current we generate.

The last experiment that we presented, where the spin current is directly injected into the $BiFeO_3$ sample thanks to the ultrafast demagnetization of a permalloy cap layer, is only at its beginning, and should be really promising, given the fact that the polarization of the spin current can be tuned at will. The observation of this system with our time-resolved SHG technique will help us track any dynamical evolution with a subpicosecond resolution. All the

elements are ready for measuring it in the coming months in the newly renovated laboratory.

Conclusion

Antiferromagnets are good candidates for the next generation of non-volatile memories and ultrafast computing devices, because their natural dynamical regime is in the terahertz. In addition, they are particularly robust to perturbations and generate no long-range magnetic stray field. Because of these advantages, they are also hard to observe and their controlled manipulation is still a challenge. In this thesis, the challenge is faced both from a simulation perspective and experimentally. A first simulation shows that available picosecond spin currents can be used to induce an efficient domain switch in antiferromagnetic NiO. A second simulation shows that the magnetoelectric coupling, naturally present in some multiferroic materials like $BiFeO_3$, can be used as a lever to control the antiferromagnetic textures. Experimentally, the femtosecond optical stimulation of $BiFeO_3$ has been imaged using second harmonic generation. No clear reproducible control of the antiferromagnetic patterns have been observed so far. To optimize the source of stimulation, the dynamical behavior following a laser-induced ultrafast demagnetization in Ferromagnet/Platinum bilayers have been studied for different timescales between 100fs and 1ms. It is shown that such systems are suitable for generating terahertz spin currents, close to the resonance of antiferromagnets like $BiFeO_3$. A first series of tests have been carried out on $BiFeO_3$ excited by such a terahertz source.

The whole study stresses the importance of the dynamics in the stimulation of antiferromagnets and shows that tools are available experimentally for working at their timescales.

Appendix A

Reproducibility of the Results on NiO From Reference [1]

The code we use (Spin-dynamics [61]) could reproduce the results of Reference [1], as shown in Figure A.1.

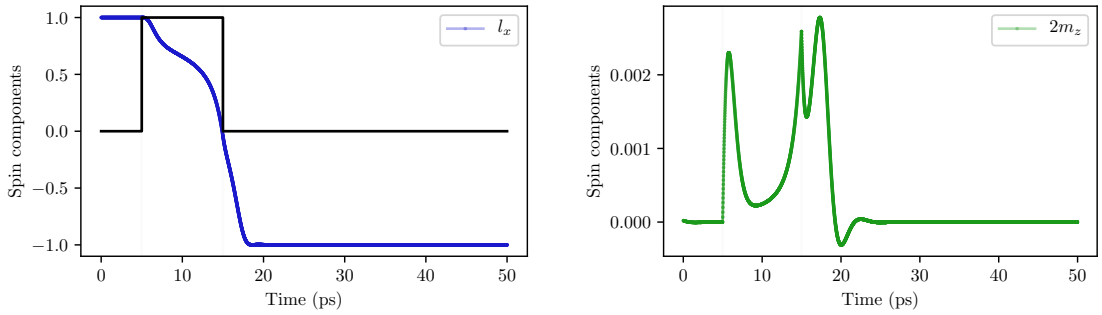

Figure A.1: Reproduction of the switch described by Reference [1]

Appendix B

Quantum Origin of the Landau-Lifshitz-Gilbert Equation

This appendix aims at linking the classical Landau-Lifshitz-Gilbert equation to the quantum nature of the spins, and analyze its validity for single atoms. In particular, we justify the value of the classical atomic magnetic momentum.

B.1 Atomic magnetic moment in solids

B.1.1 Spin Norm

For a given spin $s = \frac{n}{2}, n \in \mathbb{N}$, the norm of the spin is given by:

$$S = \hbar\sqrt{s(s+1)} \tag{B.1}$$

But its projection along an arbitrary z axis can only take the discrete values:

$$S_z = \{-s, (-s+1), ..., (s-1), s\}\,\hbar \tag{B.2}$$

In particular, for a single electron and for iron outer shell, we have:

	n	Hund	s	S	Sz
Single electron	1	$\uparrow$	$\frac{1}{2}$	$\frac{\sqrt{3}}{2}\hbar$	$\pm\frac{1}{2}\hbar$
Iron electrons	5	$\uparrow\uparrow\uparrow\uparrow\uparrow$	$\frac{5}{2}$	$\frac{\sqrt{35}}{2}\hbar$	$\pm\{\frac{5}{2}, \frac{3}{2}, \frac{1}{2}\}\hbar$

B.1.2 Spin Magnetic Moment

For spin 1/2 particles of mass m_s and charge q, the magnetic moment associated to the spin is:

$$\boldsymbol{\mu}_s = \mu_s \hat{\boldsymbol{s}} = \frac{g_S q}{2m_s} S\hat{\boldsymbol{s}} \tag{B.3}$$

But also, its projection on the z axis is:

$$\mu_{sz} = \frac{g_S q}{2m_s} S_z \tag{B.4}$$

Therefore:

☞ For the electron, $g_e = -g_S = -2.0023...$, $m_e = m_S$, $q = -e$ and $\mu_B = \frac{e\hbar}{2m_e}$. We get:

$$\mu_s \hat{\boldsymbol{s}} = g_e \frac{\mu_B}{\hbar} S\hat{\boldsymbol{S}} = g_e \mu_B \frac{\sqrt{3}}{2}\hat{\boldsymbol{S}} \tag{B.5}$$

$$\mu_{sz} = g_e \frac{\mu_B}{\hbar} S_z = \pm g_e \mu_B \frac{1}{2} \tag{B.6}$$

☞ For the 5 iron electrons, assuming the formula still holds, and Hund's rules keep the electrons aligned, we have $m_S = 5m_e$, $q = -5e$, $g_S = -g_e$. We get

$$\mu_s \hat{\boldsymbol{s}} = \frac{e\hbar g_e}{2m_e}\frac{\sqrt{35}}{2}\hat{\boldsymbol{S}} \tag{B.7a}$$

$$= g_e \mu_B \frac{\sqrt{35}}{2}\hat{\boldsymbol{S}} \tag{B.7b}$$

$$\mu_{sz} = \pm g_e \mu_B \left\{\frac{5}{2}, \frac{3}{2}, \frac{1}{2}\right\} \tag{B.7c}$$

So, which one to use for the norm of our classical magnetic moment? $S = \hbar\sqrt{s(s+1)}$ with equation B.3 or $S_z = \pm\{s, s-1, ...\}\hbar$ with equation B.4? To answer this question and for a better insight, let's see how a single spin precesses in quantum mechanics.

Quantum Larmor Precession

Classically, the magnetic energy is given by $\mathscr{E} = -\boldsymbol{\mu_s}\cdot\boldsymbol{B}$.

In quantum mechanics, we need to use the moment operator $\widehat{\boldsymbol{\mu_s}} = \frac{gq}{2m}\widehat{\hat{\boldsymbol{S}}}$ for the Hamiltonian: $\widehat{\mathscr{H}} = -\frac{gq}{2m}\widehat{\hat{\boldsymbol{S}}}\cdot\boldsymbol{B}$. Let's name $\hat{\boldsymbol{z}}$ the direction along the magnetic field, so that $\boldsymbol{B} = B\hat{\boldsymbol{z}}$. We get:

$$\widehat{\mathscr{H}} = -\frac{gq}{2m} B\widehat{S_z} \tag{B.8}$$

☞ For the electron, $\widehat{\mathscr{H}} = -\frac{g\mu_B}{\hbar} B\widehat{S_z}$. The eigenstates are

$$|+\rangle \qquad \text{with} \qquad \mathscr{E}_+ = +\frac{ge}{2\mathrm{m}} B\hbar \tag{B.9a}$$

$$|-\rangle \qquad \text{with} \qquad \mathscr{E}_- = -\frac{ge}{2\mathrm{m}} B\hbar \tag{B.9b}$$

The time dependent state is:

$$|\Phi(t)\rangle = c_+ e^{i\frac{ge}{2\mathrm{m}}Bt}|+\rangle + c_- e^{-i\frac{ge}{2\mathrm{m}}Bt}|-\rangle \tag{B.10}$$

Since $c_+^2 + c_-^2 = 1$, we can write

$$c_+ = \cos\frac{\theta}{2} \tag{B.11a}$$

$$c_+ = \sin\frac{\theta}{2} \tag{B.11b}$$

Using the expressions of the elctronic spin projection operators $\widehat{S_x} = \frac{\hbar}{2}\sigma_x$, $\widehat{S_y} = \frac{\hbar}{2}\sigma_y$, $\widehat{S_z} = \frac{\hbar}{2}\sigma_z$, $\widehat{S^2} = \frac{3\hbar}{4}\sigma_0$, where $\sigma_x, \sigma_y, \sigma_z, \sigma_0$ are the Pauli matrices. We can compute the expectation values $< S_x >$, $< S_y >$, $S_z >$ and $< S^2 >$:

$$< S_x > = \langle\Phi(t)|\widehat{S_x}|\Phi(t)\rangle \tag{B.12a}$$

$$= \frac{\hbar}{2} sin(\theta) cos\big(\gamma B t\big) \tag{B.12b}$$

$$< S_y > = \frac{\hbar}{2}\sin(\theta)\sin\big(\gamma B t\big) \tag{B.12c}$$

$$< S_z > = \frac{\hbar}{2}\cos(\theta) \tag{B.12d}$$

This set looks like Larmor precession with frequency γB, for a projection of magnitude $\frac{\hbar}{2}$, and with up state ($|+\rangle$) probability $\cos^2\theta$.

We also have $< S^2 >= \frac{1}{2}\left(\frac{1}{2}+1\right)\hbar^2$. This value nonetheless does not seem relevant in most classical context. When a magnetic moment is measured experimentally, it's always projected along an axis.

Conclusion for the spin magnetic moment: Since quantum Larmor precession for spin $\frac{1}{2}$ particles resemble classical Larmor precession with magnitude $\frac{\hbar}{2}$, we can assume that the norm of the classical spins used in LLG should be S_z, proportional to $\frac{\hbar}{2}$, (*not* $\frac{1}{2}\left(\frac{1}{2}+1\right)\hbar$). We generalize this assumption to spin $\frac{n}{2}$ particles and take $n\frac{\hbar}{2}$ for the classical norm. Practically, it means we will use equation (B.4) and $\boldsymbol{\mu}_{\boldsymbol{s}}^{classical} = \mu_{s_z}\hat{\boldsymbol{s}}$ to link spin with magnetic moment. μ_{s_z} is taken equal to its maximal value, because in crystals, the local field leaves the degeneracy between all the possible values.

B.1.3 Orbital Magnetic Moment

Generally, the fluctuation of the electronic cloud contributes to the magnetization via the orbital magnetic moment $\boldsymbol{L}$. Classically it corresponds to the magnetic field induced by the rotation of the electrons around the core. In quantum mechanics, it is quantized:

$$L = \sqrt{l(l+1)}\hbar \tag{B.13}$$

$$\boldsymbol{\mu_L} = -g_L \mu_B \frac{\boldsymbol{L}}{\hbar} \tag{B.14}$$

B.1.4 Total Magnetic Moment

For the total magnetization, we should take contributions of both spin $\boldsymbol{S}$ and orbital momentum $\boldsymbol{L}$.

$$\boldsymbol{J} = \boldsymbol{L} + \boldsymbol{S} \tag{B.15}$$

$$J = \sqrt{j(j+1)}\hbar \tag{B.16}$$

$$\boldsymbol{\mu_J} = -g_J \mu_B \frac{\boldsymbol{J}}{\hbar} \tag{B.17}$$

Summing relations are not as trivial as it seems, because the directions of $\boldsymbol{L}$ and $\boldsymbol{S}$ can be different. Moreover, g_J depends on g_L, g_S, S and L [155].

$$g_J = g_L \frac{J(J+1) - S(S+1) + L(L+1)}{2J(J+1)} + g_S \frac{J(J+1) + S(S+1) - L(L+1)}{2J(J+1)} \tag{B.18}$$

Fortunatelly for us, in solids, due to the asymmetric crystal field, the orbital moment $\boldsymbol{L}$ is quenched. We obtain $\boldsymbol{\mu_J} = \boldsymbol{\mu_s}$ for the total magnetic moment.

B.2 Quantum LLG equation

The quantum precession about an effective field was established by Larmor quantum precession, the only missing step to the LLG equation concerns the Gilbert damping. It can be shown that this term comes from the spin-orbit coupling [156]. The energy is eventually converted into phonon and heat to the crystal. fundamentally leading to a magnetic damping at the atomic scale, which finished to justifies the form of LLG equation in an atomic context.

It means that, even if each individual atom can have their magnetization measured either up or down, *in average, statistically,* they will have the probably given by the projection of LLG to be found in either one or the other state. In other words, the resolution of the equation will not accuratelly give the behaviour of each of the single spins, but will rather give the expected collective behaviour, in average.

The norm of the spin in LLG equation is taken to the maximal value of μ_z.

Appendix C

Susceptibility Tensors in the Laboratory Frame

$$\chi_0^{(i)} = \chi_+^{(i)} = \chi_-^{(i)} \tag{C.1}$$

$$= \begin{bmatrix} \frac{\sqrt{3}\chi_{111}^{(i)} - 3\sqrt{6}\chi_{113}^{(i)} - 2\sqrt{6}\chi_{333}^{(i)}}{9} & -\frac{\sqrt{3}\chi_{111}^{(i)} + \sqrt{6}\chi_{113}^{(i)}}{3} & \frac{2\sqrt{3}\chi_{111}^{(i)} - \sqrt{6}\chi_{333}^{(i)}}{9} & 0 & \frac{\sqrt{6}\chi_{111}^{(i)} - 3\sqrt{3}\chi_{113}^{(i)} + 2\sqrt{3}\chi_{333}^{(i)}}{9} & 0 \\ 0 & 0 & 0 & -\frac{\sqrt{6}\chi_{111}^{(i)} - \sqrt{3}\chi_{113}^{(i)}}{3} & 0 & -\frac{\sqrt{3}\chi_{111}^{(i)} + \sqrt{6}\chi_{113}^{(i)}}{3} \\ \frac{\sqrt{6}\chi_{111}^{(i)} - 3\sqrt{3}\chi_{113}^{(i)} + 2\sqrt{3}\chi_{333}^{(i)}}{9} & -\frac{\sqrt{6}\chi_{111}^{(i)} - \sqrt{3}\chi_{113}^{(i)}}{3} & \frac{2\sqrt{6}\chi_{111}^{(i)} + 6\sqrt{3}\chi_{113}^{(i)} + \sqrt{3}\chi_{333}^{(i)}}{9} & 0 & \frac{2\sqrt{3}\chi_{111}^{(i)} - \sqrt{6}\chi_{333}^{(i)}}{9} & 0 \end{bmatrix} \tag{C.2a}$$

$$\chi_0^{(c)} = \begin{bmatrix} \frac{\sqrt{3}\chi_{111}^{(c)} - 3\sqrt{6}\chi_{113}^{(c)} + 6\sqrt{3}\chi_{133}^{(c)} - 2\sqrt{6}\chi_{333}^{(c)}}{9} & \frac{\sqrt{3}\chi_{122}^{(c)} - \sqrt{6}\chi_{223}^{(c)}}{3} & \frac{2\sqrt{3}\chi_{111}^{(c)} - 3\sqrt{3}\chi_{133}^{(c)} - \sqrt{6}\chi_{333}^{(c)}}{9} & 0 & \frac{\sqrt{6}\chi_{111}^{(c)} - 3\sqrt{3}\chi_{113}^{(c)} + 2\sqrt{3}\chi_{333}^{(c)}}{9} & 0 \\ 0 & 0 & 0 & \frac{\sqrt{6}\chi_{122}^{(c)} + \sqrt{3}\chi_{223}^{(c)}}{3} & 0 & \frac{\sqrt{3}\chi_{122}^{(c)} - \sqrt{6}\chi_{223}^{(c)}}{3} \\ \frac{\sqrt{6}\chi_{111}^{(c)} - 3\sqrt{3}\chi_{113}^{(c)} + 2\sqrt{3}\chi_{333}^{(c)}}{9} & \frac{\sqrt{6}\chi_{122}^{(c)} + \sqrt{3}\chi_{223}^{(c)}}{3} & \frac{2\sqrt{6}\chi_{111}^{(c)} + 6\sqrt{3}\chi_{113}^{(c)} + 3\sqrt{6}\chi_{133}^{(c)} + \sqrt{3}\chi_{333}^{(c)}}{9} & 0 & \frac{2\sqrt{3}\chi_{111}^{(c)} - 3\sqrt{3}\chi_{133}^{(c)} - \sqrt{6}\chi_{333}^{(c)}}{9} & 0 \end{bmatrix} \tag{C.3a}$$

$$\chi_+^{(c)} = \begin{bmatrix} -\frac{\sqrt{3}\chi_{111}^{(c)} + 6\sqrt{6}\chi_{113}^{(c)} + 9\sqrt{3}\chi_{122}^{(c)} + 24\sqrt{3}\chi_{133}^{(c)} + 18\sqrt{6}\chi_{223}^{(c)} + 16\sqrt{6}\chi_{333}^{(c)}}{72} & -\frac{3\sqrt{3}\chi_{111}^{(c)} + 6\sqrt{6}\chi_{113}^{(c)} - 5\sqrt{3}\chi_{122}^{(c)} + 2\sqrt{6}\chi_{223}^{(c)}}{24} & -\frac{\sqrt{3}\chi_{111}^{(c)} + 9\sqrt{3}\chi_{122}^{(c)} - 6\sqrt{3}\chi_{133}^{(c)} + 4\sqrt{6}\chi_{333}^{(c)}}{36} \\ -\frac{\sqrt{3}\chi_{111}^{(c)} + 4\sqrt{6}\chi_{113}^{(c)} + \sqrt{3}\chi_{122}^{(c)} + 8\sqrt{3}\chi_{133}^{(c)} - 4\sqrt{6}\chi_{223}^{(c)}}{24} & -3\sqrt{3}\frac{\chi_{111}^{(c)} + \chi_{122}^{(c)}}{8} & -\frac{\sqrt{3}\chi_{111}^{(c)} - 2\sqrt{6}\chi_{113}^{(c)} + \sqrt{3}\chi_{122}^{(c)} + 2\sqrt{3}\chi_{133}^{(c)} + 2\sqrt{6}\chi_{223}^{(c)}}{12} \\ -\frac{\sqrt{6}\chi_{111}^{(c)} + 6\sqrt{3}\chi_{113}^{(c)} + 9\sqrt{6}\chi_{122}^{(c)} + 18\sqrt{3}\chi_{223}^{(c)} - 16\sqrt{3}\chi_{333}^{(c)}}{72} & -\frac{3\sqrt{6}\chi_{111}^{(c)} - 6\sqrt{3}\chi_{113}^{(c)} - 5\sqrt{6}\chi_{122}^{(c)} - 2\sqrt{3}\chi_{223}^{(c)}}{24} & -\frac{\sqrt{6}\chi_{111}^{(c)} - 6\sqrt{3}\chi_{113}^{(c)} + 9\sqrt{6}\chi_{122}^{(c)} + 6\sqrt{6}\chi_{133}^{(c)} - 18\sqrt{3}\chi_{223}^{(c)} - 4\sqrt{3}\chi_{333}^{(c)}}{36} \end{bmatrix} \tag{C.3b}$$

$$\begin{bmatrix} -\frac{\sqrt{6}\chi_{111}^{(c)} + 2\sqrt{3}\chi_{113}^{(c)} + \sqrt{6}\chi_{122}^{(c)} - 4\sqrt{6}\chi_{133}^{(c)} - 2\sqrt{3}\chi_{223}^{(c)}}{24} & -\frac{\sqrt{6}\chi_{111}^{(c)} + 6\sqrt{3}\chi_{113}^{(c)} + 9\sqrt{6}\chi_{122}^{(c)} + 18\sqrt{3}\chi_{223}^{(c)} - 16\sqrt{3}\chi_{333}^{(c)}}{72} & -\frac{\sqrt{3}\chi_{111}^{(c)} + 4\sqrt{6}\chi_{113}^{(c)} + \sqrt{3}\chi_{122}^{(c)} + 8\sqrt{3}\chi_{133}^{(c)} - 4\sqrt{6}\chi_{223}^{(c)}}{24} \\ -\frac{3\sqrt{6}\chi_{111}^{(c)} - 6\sqrt{3}\chi_{113}^{(c)} - 5\sqrt{6}\chi_{122}^{(c)} - 2\sqrt{3}\chi_{223}^{(c)}}{24} & -\frac{\sqrt{6}\chi_{111}^{(c)} + 2\sqrt{3}\chi_{113}^{(c)} + \sqrt{6}\chi_{122}^{(c)} - 4\sqrt{6}\chi_{133}^{(c)} - 2\sqrt{3}\chi_{223}^{(c)}}{24} & -\frac{3\sqrt{3}\chi_{111}^{(c)} + 6\sqrt{6}\chi_{113}^{(c)} - 5\sqrt{3}\chi_{122}^{(c)} + 2\sqrt{6}\chi_{223}^{(c)}}{24} \\ -\frac{\sqrt{3}\chi_{111}^{(c)} - 2\sqrt{6}\chi_{113}^{(c)} + \sqrt{3}\chi_{122}^{(c)} + 2\sqrt{3}\chi_{133}^{(c)} + 2\sqrt{6}\chi_{223}^{(c)}}{12} & -\frac{\sqrt{3}\chi_{111}^{(c)} + 9\sqrt{3}\chi_{122}^{(c)} - 6\sqrt{3}\chi_{133}^{(c)} + 4\sqrt{6}\chi_{333}^{(c)}}{36} & -\frac{\sqrt{6}\chi_{111}^{(c)} + 2\sqrt{3}\chi_{113}^{(c)} + \sqrt{6}\chi_{122}^{(c)} - 4\sqrt{6}\chi_{133}^{(c)} - 2\sqrt{3}\chi_{223}^{(c)}}{24} \end{bmatrix}$$

$$\chi_-^{(c)} = \begin{bmatrix} -\frac{\sqrt{3}\chi_{111}^{(c)} + 6\sqrt{6}\chi_{113}^{(c)} + 9\sqrt{3}\chi_{122}^{(c)} + 24\sqrt{3}\chi_{133}^{(c)} + 18\sqrt{6}\chi_{223}^{(c)} + 16\sqrt{6}\chi_{333}^{(c)}}{72} & -\frac{3\sqrt{3}\chi_{111}^{(c)} + 6\sqrt{6}\chi_{113}^{(c)} - 5\sqrt{3}\chi_{122}^{(c)} + 2\sqrt{6}\chi_{223}^{(c)}}{24} & -\frac{\sqrt{3}\chi_{111}^{(c)} + 9\sqrt{3}\chi_{122}^{(c)} - 6\sqrt{3}\chi_{133}^{(c)} + 4\sqrt{6}\chi_{333}^{(c)}}{36} \\ \frac{\sqrt{3}\chi_{111}^{(c)} + 4\sqrt{6}\chi_{113}^{(c)} + \sqrt{3}\chi_{122}^{(c)} + 8\sqrt{3}\chi_{133}^{(c)} - 4\sqrt{6}\chi_{223}^{(c)}}{24} & 3\sqrt{3}\frac{\chi_{111}^{(c)} + \chi_{122}^{(c)}}{8} & \frac{\sqrt{3}\chi_{111}^{(c)} - 2\sqrt{6}\chi_{113}^{(c)} + \sqrt{3}\chi_{122}^{(c)} + 2\sqrt{3}\chi_{133}^{(c)} + 2\sqrt{6}\chi_{223}^{(c)}}{12} \\ -\frac{\sqrt{6}\chi_{111}^{(c)} + 6\sqrt{3}\chi_{113}^{(c)} + 9\sqrt{6}\chi_{122}^{(c)} + 18\sqrt{3}\chi_{223}^{(c)} - 16\sqrt{3}\chi_{333}^{(c)}}{72} & -\frac{3\sqrt{6}\chi_{111}^{(c)} - 6\sqrt{3}\chi_{113}^{(c)} - 5\sqrt{6}\chi_{122}^{(c)} - 2\sqrt{3}\chi_{223}^{(c)}}{24} & -\frac{\sqrt{6}\chi_{111}^{(c)} - 6\sqrt{3}\chi_{113}^{(c)} + 9\sqrt{6}\chi_{122}^{(c)} + 6\sqrt{6}\chi_{133}^{(c)} - 18\sqrt{3}\chi_{223}^{(c)} - 4\sqrt{3}\chi_{333}^{(c)}}{36} \end{bmatrix} \tag{C.3c}$$

$$\begin{bmatrix} \frac{\sqrt{6}\chi_{111}^{(c)} + 2\sqrt{3}\chi_{113}^{(c)} + \sqrt{6}\chi_{122}^{(c)} - 4\sqrt{6}\chi_{133}^{(c)} - 2\sqrt{3}\chi_{223}^{(c)}}{24} & -\frac{\sqrt{6}\chi_{111}^{(c)} + 6\sqrt{3}\chi_{113}^{(c)} + 9\sqrt{6}\chi_{122}^{(c)} + 18\sqrt{3}\chi_{223}^{(c)} - 16\sqrt{3}\chi_{333}^{(c)}}{72} & \frac{\sqrt{3}\chi_{111}^{(c)} + 4\sqrt{6}\chi_{113}^{(c)} + \sqrt{3}\chi_{122}^{(c)} + 8\sqrt{3}\chi_{133}^{(c)} - 4\sqrt{6}\chi_{223}^{(c)}}{24} \\ -\frac{3\sqrt{6}\chi_{111}^{(c)} - 6\sqrt{3}\chi_{113}^{(c)} - 5\sqrt{6}\chi_{122}^{(c)} - 2\sqrt{3}\chi_{223}^{(c)}}{24} & \frac{\sqrt{6}\chi_{111}^{(c)} + 2\sqrt{3}\chi_{113}^{(c)} + \sqrt{6}\chi_{122}^{(c)} - 4\sqrt{6}\chi_{133}^{(c)} - 2\sqrt{3}\chi_{223}^{(c)}}{24} & -\frac{3\sqrt{3}\chi_{111}^{(c)} + 6\sqrt{6}\chi_{113}^{(c)} - 5\sqrt{3}\chi_{122}^{(c)} + 2\sqrt{6}\chi_{223}^{(c)}}{24} \\ \frac{\sqrt{3}\chi_{111}^{(c)} - 2\sqrt{6}\chi_{113}^{(c)} + \sqrt{3}\chi_{122}^{(c)} + 2\sqrt{3}\chi_{133}^{(c)} + 2\sqrt{6}\chi_{223}^{(c)}}{12} & -\frac{\sqrt{3}\chi_{111}^{(c)} + 9\sqrt{3}\chi_{122}^{(c)} - 6\sqrt{3}\chi_{133}^{(c)} + 4\sqrt{6}\chi_{333}^{(c)}}{36} & \frac{\sqrt{6}\chi_{111}^{(c)} + 2\sqrt{3}\chi_{113}^{(c)} + \sqrt{6}\chi_{122}^{(c)} - 4\sqrt{6}\chi_{133}^{(c)} - 2\sqrt{3}\chi_{223}^{(c)}}{24} \end{bmatrix}$$

Appendix D

Order Parameters and Suceptibility Tensors in BFO

D.1 Multiplications rules

$$(i) * (i) = (i) \tag{D.1a}$$

$$(i) * (c) = (c) \tag{D.1b}$$

$$(c) * (c) = (i) \tag{D.1c}$$

$$polar * polar = polar \tag{D.2a}$$

$$polar * axial = axial \tag{D.2b}$$

$$axial * axial = polar \tag{D.2c}$$

D.2 Tensors allowed by symmetry in $BiFeO_3$

$BiFeO_3$ has two ordering temperatures. The phases in $BiFeO_3$ have the following symmetries:

Temperature	(i)-order	(c)-order	Symmetry
	•	∅	m3m
T_C = 1100K			
	FE	∅	3m
T_N = 654K			
	FE	AFM	m

D.2.1 Paraelectric, paramagnetic phase

Above T_N and T_C, BFO has pseudocubic symmetry, that we consider being cubic $m3m$.

The cubic symmetry $m3m$ tells us that only (i/c)-type polar even rank tensors and (i/c)-type axial odd rank tensors are allowed.

No magnetism is at stake, so all the tensors allowed are of (i)-type.

The tensors above rank 3 allowed by symmetry are:

- 3rd rank (i) axial $\chi_{[3]}$
- 4rd rank (i) polar $\chi_{[4]}$
- 5rd rank (i) axial $\chi_{[5]}$
- ...

D.2.2 Ferroelectric, paramagnetic phase

Below T_C (but above T_N), $BiFeO_3$ enters its ferroelectric phase. The new group symmetry is $3m$.

From Ginzburg Landau thery, we can develop the free energy with the ordering parameter $\boldsymbol{P_e}$, and must ensure continuity at phase transition [125].

$\boldsymbol{P_e}$ is a 1rst rank (i)-type, polar tensor. At leading orders, we get:

1:

- 3rd rank (i) axial $\chi_{[3]}$
- 4th rank (i) polar $\chi_{[4]}$
- 5th rank (i) axial $\chi_{[5]}$

$\boldsymbol{P_e}$:

- 2nd rank (i) axial $\chi_{[3]}.\boldsymbol{P_e}$
- 3rd rank (i) polar $\chi_{[4]}.\boldsymbol{P_e}$
- 4th rank (i) axial $\chi_{[5]}.\boldsymbol{P_e}$

$\boldsymbol{P_e}^2$:

- ...

For our concerns, the developpement up till first order in $\boldsymbol{P_e}$ is sufficient.

D.2.3 Ferroelectric, antiferromagnetic phase

Below T_N, $BiFeO_3$ enters its antiferromagnetic (an ferroelectric) phase. The new point group symmetry is m. The new leading order parameter is $\mathbf{L}$ (+ possibly $\boldsymbol{\mu}$, but weaker). $\mathbf{L}$ is a 1rst rank (c)-type, axial tensor.

From the continuity at the phase transition, the leading tensors in this phase are:

1:

- 3rd rank (i) axial $\chi_{[3]}$
- 4th rank (i) polar $\chi_{[4]}$

- 5th rank (i) axial $\chi_{[5]}$
- 2nd rank (i) axial $\chi_{[3]}.\boldsymbol{P_e}$
- 3rd rank (i) polar $\chi_{[4]}.\boldsymbol{P_e}$
- 4th rank (i) axial $\chi_{[5]}.\boldsymbol{P_e}$

L:

- 2nd rank (c) polar $\chi_{[3]}.\mathbf{L}$
- 3rd rank (c) axial $\chi_{[4]}.\mathbf{L}$
- 4th rank (c) polar $\chi_{[5]}.\mathbf{L}$
- 1rst rank (c) polar $\chi_{[3]}.\boldsymbol{P_e}.\mathbf{L}$
- 2nd rank (c) axial $\chi_{[4]}.\boldsymbol{P_e}.\mathbf{L}$
- 3rd rank (c) polar $\chi_{[5]}.\boldsymbol{P_e}.\mathbf{L}$

$\mathbf{L}^2$

- ...

$\boldsymbol{\mu}$, $\boldsymbol{P_e\mu}$, $\mathbf{L}\boldsymbol{\mu}$, and higher terms are neglected.

D.3 Susceptibility Tensors for the SHG

For the second harmonic generation in $\boldsymbol{P} = \chi\boldsymbol{EE}$, because $\boldsymbol{P}$ and $\boldsymbol{E}$ are polar, we must consider the *3rd rank polar tensors* χ of leading order, in the ferroelectric-antiferromagnetic phase.

They are:

- (i) polar $\chi_{[4]}.\boldsymbol{P_e}$
- (c) polar $\chi_{[5]}.\boldsymbol{P_e}.\mathbf{L}$

$\chi_{[4]}$ and $\chi_{[5]}$ can be deduced from the symmetries ($m3m$ and $3m$) of the paramagnetic phases, and experimental measurements (e.g. Reference [112]).

Appendix E

Additional Measurements on FM/Pt

E.1 Reflectivity measurement

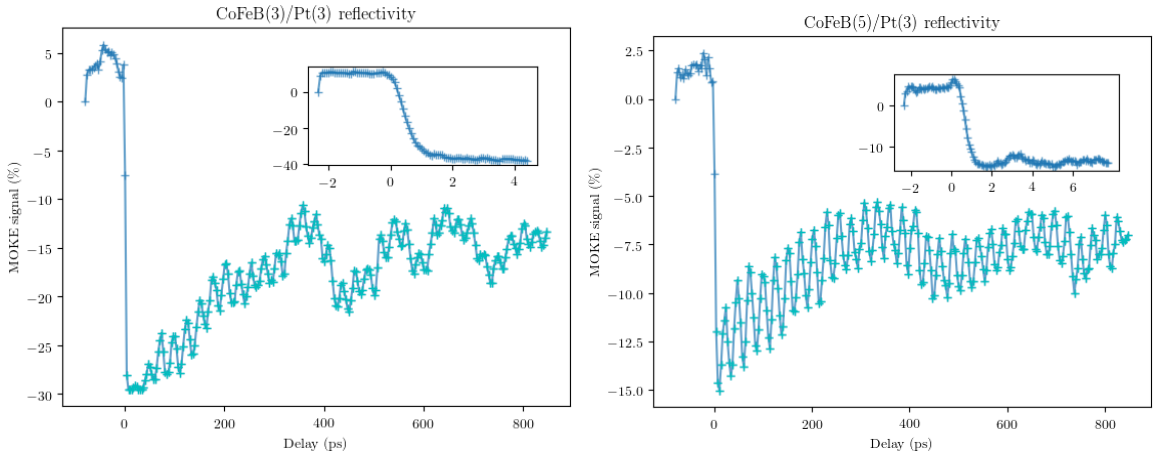

Figure E.1: Reflectivity measurement on CoFeB(3)/Pt(3) and on CoFeB(5)/Pt(3). Oscillations at 38.5GHz and 5GHz are of non-magnetic nature.

A set of reflectivity measurements has also been achieved, simply by replacing the waveplate, Wollaston prism and balanced detector by a photo-diode, to collect the sum (instead of the difference) of intensities on projected axes (Figure E.1). The reflectivity is affected by the demagnetization, but the return to equilibrium is different from the one seen on the previous remagnetization curves. Oscillations of different natures are visible, most probably related to phonons propagating in the substrate.

E.2 Thickness dependence of COFeB on the MOKE signal

When the thickness of the magnetic layer is changed from 5nm to 7nm, the contrast gets stronger (Figures 4.13 and E.2), but the frequency of the ferromagnetic precessional mode is almost unchanged.

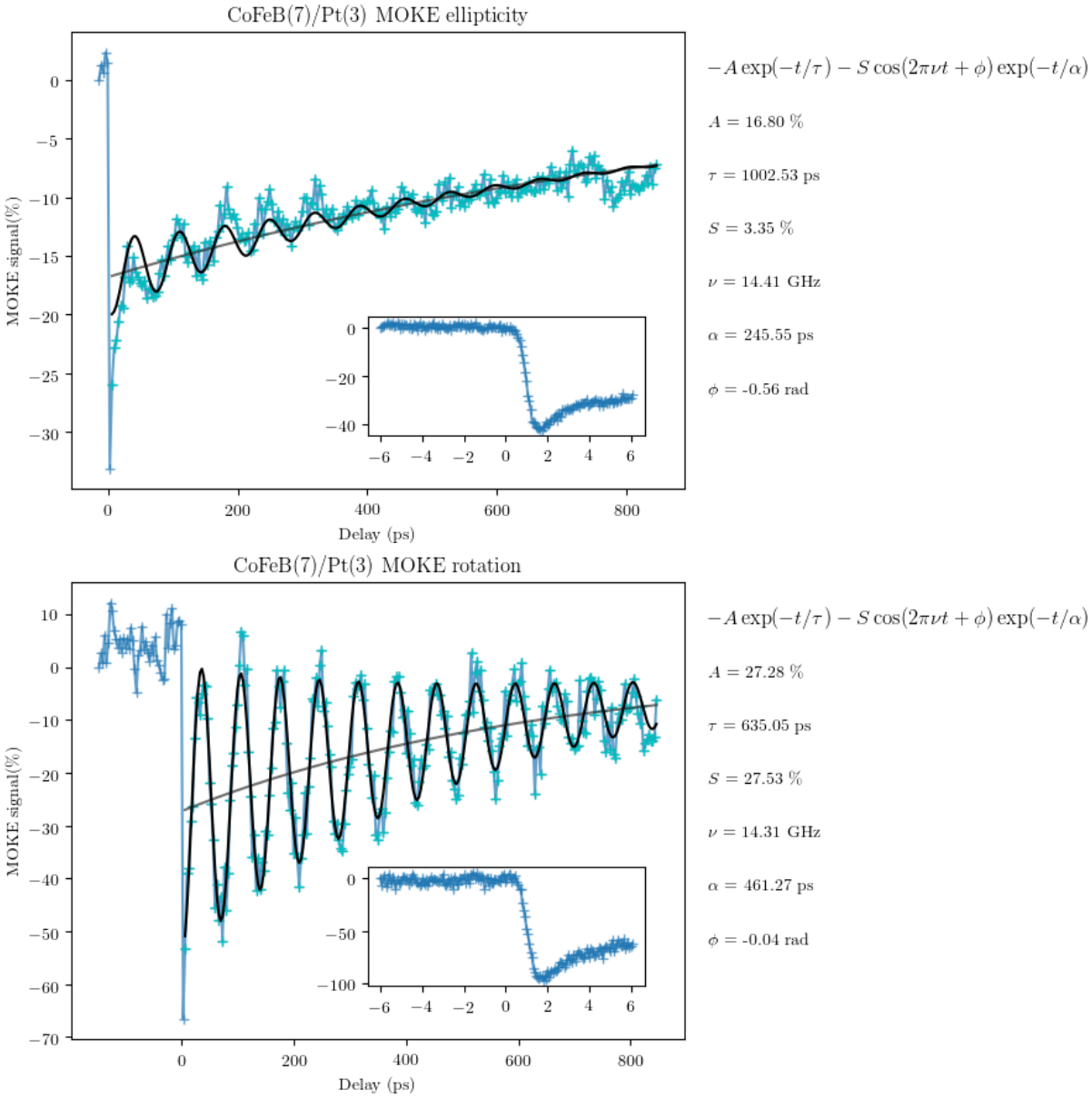

Figure E.2: Ultrafast demagnetization of CoFeB(7)-Pt(3). Blue crosses and lines are the raw data, grey and black curves are our fit after the ultrafast demagnetization. The insets show the zoom of the fast demagnetization.

E.3 Wavelength dependence

The DC voltage induced by the laser-induced demagnetization of Fe_3O_4(40nm)/Pt(2nm) is measured for different wavelengths (Figure E.3a). The wavelength is changed via an optical parametric amplifier (OPA), whose output power highly depends on the wavelength. For different ranges of wavelengths, changing of modules are required, which can bring discontinuities in the power (Figure E.3b). What is more, the mirrors we used on the setup to lead the laser beam to the sample do not have a flat spectral response, leading to a visible change of power, especially for wavelengths higher than 1300nm. Between 1300nm and 1600nm, the measurement should be interpreted with care, since the drop could be linked to flaws in the reflectivity of the mirrors.

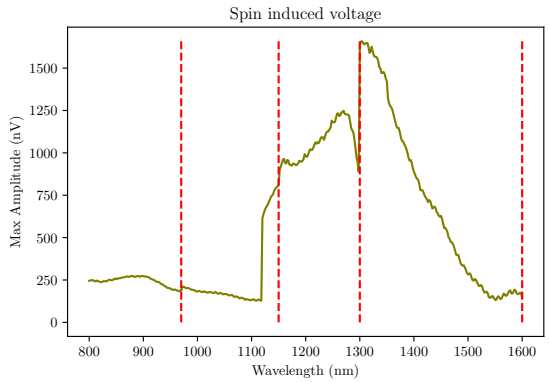

(a) Voltage

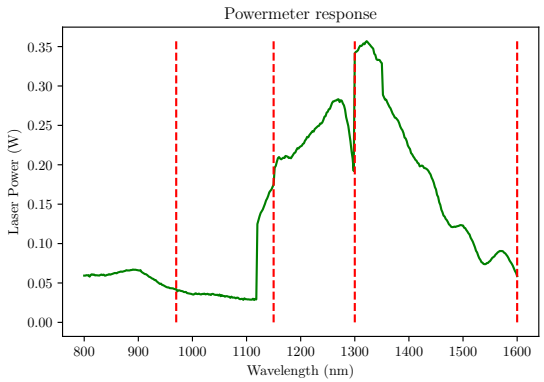

(b) Power

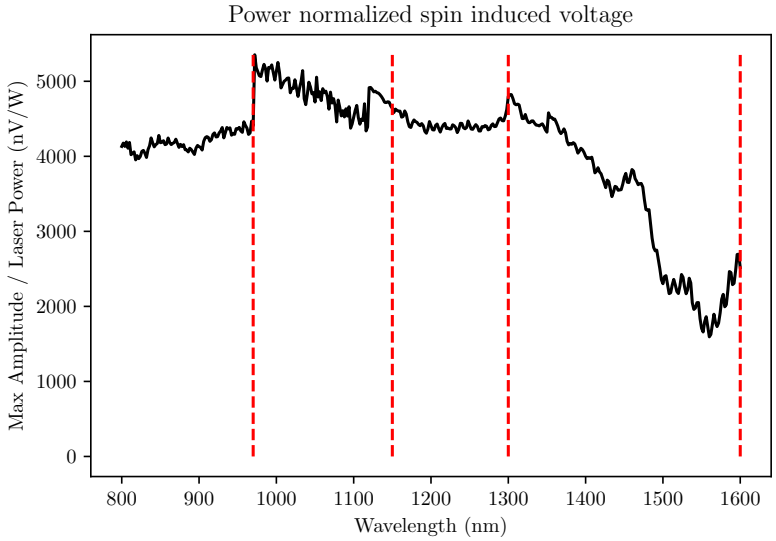

(c) Voltage/Power

Figure E.3: Wavelength dependence of the DC voltage on Fe_3O_4(40nm)/Pt(2nm) Vertical lines correspond to the change of mode of the optical parametric amplifier (OPA). (a) Measured DC voltage. (b) Power of the laser before hitting the sample. (c) Normalization of the DC voltage by the laser power.

The spectral variation of the voltage normalized by the power is displayed on Figure E.3c. Some variations are visible, and show an optimal working frequency of 980nm, but up till 1300nm, the values are comparable, and the mechanism responsible for the voltage do not seem to depend much on the wavelength.

Appendix F

References For Optical Filters

The terms *long-pass* and *short-pass* filters refer to the wavelength of the light, and are analogous to *low-pass* and *high-pass* filters, when refering to the frequency.

F.1 RG780

Long-pass cut-on Wavelength: 780nm.

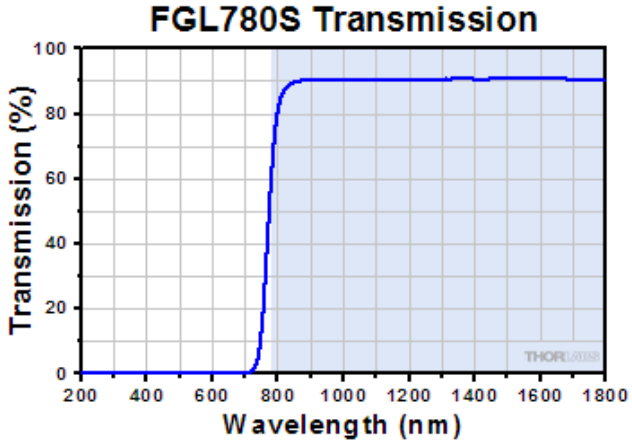

https://www.thorlabs.com/thorproduct.cfm?partnumber=FGL780S

F.2 FELH0750

Premium longpass filter, cut-on wavelength: 750 nm.

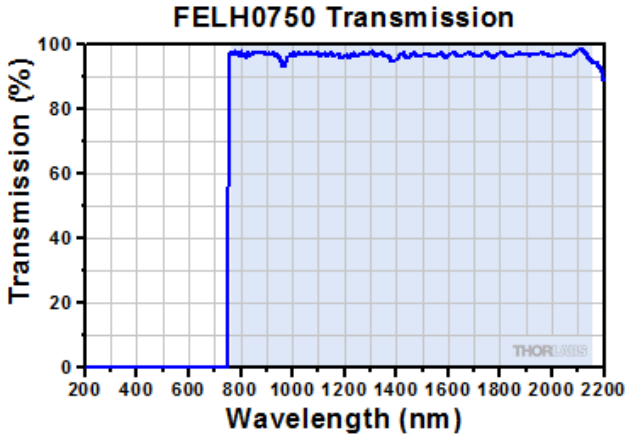

https://www.thorlabs.com/thorproduct.cfm?partnumber=FELH0750

F.3 FESH0750

Premium shortpass filter, cut-off wavelength: 750 nm.

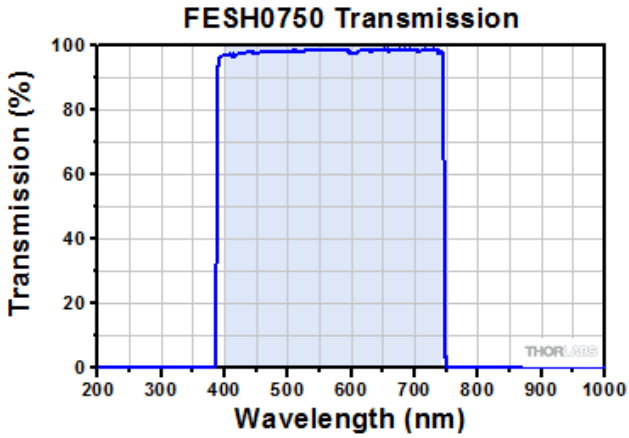

https://www.thorlabs.com/thorproduct.cfm?partnumber=FESH0750

F.4 FBH450-10

Premium bandpass filter, centering wavelength = 450 nm, full width at half maximum = 10 nm.

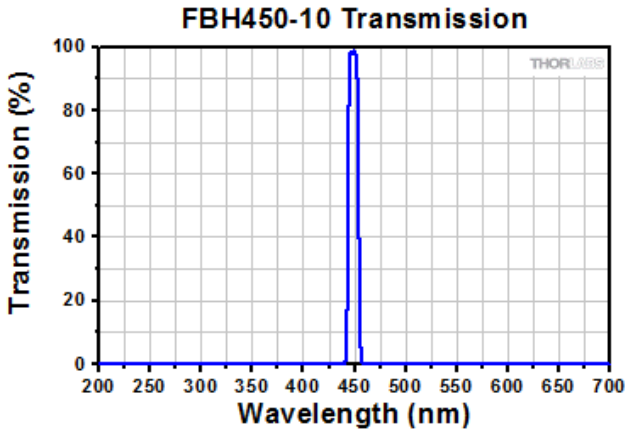

https://www.thorlabs.com/thorproduct.cfm?partnumber=FBH450-10

F.5 FGB37S

Colored glass bandpass Filter, 335 - 610 nm.

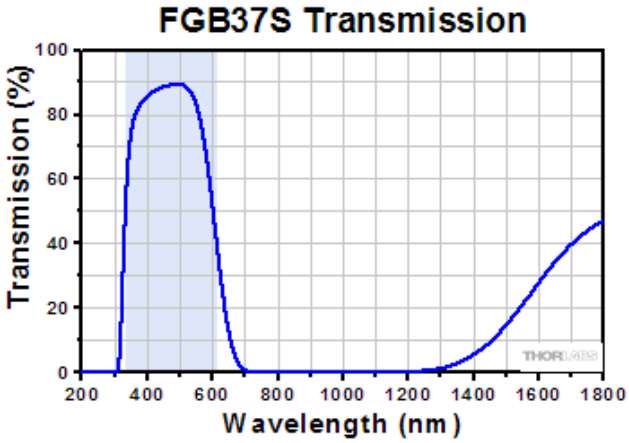

https://www.thorlabs.com/thorproduct.cfm?partnumber=FGB37S

Résumé en Français

G.1 Spintronique antiferromagnétique

La spintronique s'intéresse à la dynamique de l'aimantation et au transfert de spins dans les matériaux, avec des visées applicatives en forts liens avec les support de mémoires tels que les disques durs, ou encore les cartes magnétiques. La technologie actuelle basée sur les matériaux ferri- ou ferro-magnétiques, les aimants, voit ses limites mises à mal avec la course effrénée vers la miniaturisation. En particulier, quand les domaines magnétiques atteignent la dizaine de nanomètres, comme c'est le cas aujourd'hui, l'information stockée peut être altérée par le champ magnétique dipolaire environnant. par ailleurs, la dynamique de travail optimale pour les matériaux magnétiques est au gigahertz, fréquence à laquelle se trouvent les modes de précession. Une alternative au matériaux ferromagnétiques qui pallieraient ces limitations est offerte par les matériaux antiferromagnétiques. Naturellement, ces matériaux alignent leurs spins de façon antiparallèle, ce qui, en moyenne, ne crée aucun champ de fuite pouvant interférer avec l'extérieur. Par ailleurs, cet arrangement particulier ne les rend pas particulièrement sensible à l'application d'un champ magnétique statique extérieur, puisque quelques teslas à quelques dizaines de tesla sont nécessaires à l'apparition d'un spin-flop, configuration dans laquelle l'alignement antiparallèle se rend imparfait pour créer un petit moment magnétique perpendiculaire. Les matériaux antiferromagnétiques sont donc par nature, robustes. Le second avantage de ces matériaux est que leur mode de précession est au gigahertz, ce qui leur confère une rapidité 100 à 1000 fois plus élevée par rapport aux matériaux ferromagnétiques. Ensuite, les matériaux antiferromagnétiques sont relativement abondants, et en particulier parmis les oxides des métaux de transition, à cause d'un mécansme de super-échange (Figure 1.4) [28, 27]. Parmis eux, beaucoup sont isolants, contrairement aux ferromagnétiques, qui sont pour la plupart métalliques. Le caratère isolant constitue un autre avantage car l'ordre magnétique assure un transport possible de l'information via des ondes de spin, ondes ne nécessitant pas le transport d'électrons pouvant causer de fortes pertes par effet Joule [39]. Certains matériaux antiferromagnétiques peuvent propager les ondes de spins au delà du micromètre [40], ce qui est suffisant pour imaginer des composants de microélectroniques basés sur ces matériaux.

Le premier chapitre de cette thèse présente les outlis et concepts élémentaires de la spintronique et développe les avantages sus-cités des matérieux antiferromagnétiques dans ce cadre. En particulier, une preuve de concept de composant mémoire stable est citée (Figure 1.8) [32], ainsi qu'une prédiction de changement d'état magnétique en 15 picosecondes par l'application d'un *spin transfer torque* (STT) dans NiO (Figure 1.9) [1].

G.2 Simulation atomistique de systèmes antiferromagnétiques

G.2.1 NiO

Afin de développer l'étude sur le basculement du vecteur antiferromagnétique **L** d'un état à un autre dans NiO, nous avons analysé sa cristallographie de manière à modéliser au mieux son anisotropie dans un modèle dynamique.

Le modèle dynamique sur lequel la simulation est basée est l'équation de Landau-Lifshitz Gilbert (LLG) (Équation (2.2)), qui décrit le mouvement de précession d'un moment magnétique dans un champ, soumis à un amortissement. À cette équation est ajouté le terme de *spin transfert torque* (STT) [58] pouvant contrebalancer l'amortissement, et entretenir l'oscillation. Les interactions entrant en jeu dans la dynamique des spins sont donc (Équation (2.5)):

- un terme d'échange ;
- un terme d'intéraction de Dzyaloshinskii-Moriya ;
- un terme d'anisotropie ;
- un terme Zeeman ;
- un spin transfert torque.

Le modèle choisi pour l'anisotropie de NiO est un axe difficile selon [111], superposé à une anisotropie cubique d'axes naturels [100], [010], [001] (Équation (2.20)). En somme, et avec la valeur des coefficients ajustée sur les valeurs de résonance connues de NiO, l'anisotropie confère trois axes faciles à 120° les uns des autres et selon $\langle 11\bar{2} \rangle$ dans le plan (111). L'anisotropie hors plan confère la résonance à 1THz, tandis que celle autour de 0.2THz est due à l'anisotropie dans le plan (Figure 2.5).

Avec ce modèle, nous avons tâché de reproduire la démarche de [1], et de provoquer un basculement d'état d'équilibre en quelques picosecondes à l'aide d'une impulsion de STT. Il s'avère que notre modèle d'anisotropie confère en réalité une dynamique plus rapide que celui de [1]: un basculement est observé en moins de 5 picosecondes pour les mêmes valeurs de STT. Notre anisotropie confère en outre plus de positions d'équilibre, passant de 2 à 6 le nombre d'états possibles, laissant la possibilité d'un basculement à 60° seulement, en moins de 2 picosecondes (Figure 2.12). L'état final peut être choisi soit en augmentant le temps d'exposition au STT, soit en augmentant l'intensité du STT. Les valeurs requises sont globalement inversement proportionnelles l'une à l'autre pour un état donné (Figure 2.10). Cependant, nous avons noté des effets dynamique dus au coefficient d'amortissement de Gilbert α, qui rendent certaines durées d'exposition moins efficaces que d'autres (Figure 2.11). Nous avons également vu que la direction de STT optimale était la grande diagonale [111], et qu'à magnitude égale, les autres directions n'augmentaient pas la vitesse de basculement (Figure 2.15). Le temps de basculement minimal avec stabilisation sur une direction d'équilibre semble intimement lié à α. Enfin, nous avons simulé une impulsion de STT réalisable par les techniques optiques actuelles, et constaté que le basculement était envisageable, à condition que la somme des spins injectés dépasse la valeur seuil (aux effets dynamiques sus-mentionnés près).

G.2.2 $BiFeO_3$

La seconde simulation de ce travail de thèse a été menée sur $BiFeO_3$, qui est un multiferroïque (à la fois ferroélectrique et antiferromagnétique) à température ambiante, et présentant un couplage magnéto-électrique entre ses deux paramètres d'ordre. La structure cristalline et l'origine du couplage sont présentés (Figues 2.16, 2.17 et 2.19). Le couplage magnéto-électrique tend à former des cycloïdes antiferromagnétiques de 64nm dans le plan $(11\bar{2})$, légèrement voilées (Figures 2.20 et 2.21). Le voilage provient d'une intéraction Dzyaloshinskii-Moriya, et provoque une légère aimantation alternée dans la direction $\pm[11\bar{2}]$, avec la même période que la cycloïde (Figure 2.22). Un effondrement de la structure cycloïdale est observé en simulant un champ magnétique externe intense (*champ de flop*) (Figure 2.23). L'apparition de structures bidimentionnelles plus complexes est également simulé en jouant sur les paramètres magnéto-electriques et les conditions de bord (Figure 2.24).

Ce couplage magnétoélectrique a été utilisé pour forcer l'apparition de structures antiferromagnétiques aux parois de domaines ferroélectriques. Pour cela, des échantillons furent élaborés sur lesquels des bandes ferroélectriques forment des parois régulières avec un angle de 71° deux à deux (Figure 2.25). Il a été vu en rayon-X non élastiques résonnants que la polarisation électrique s'enroulait de façon chirale dans ces parois. Nous avons montré en simulation qu'un tel enroulement créait bien, via le couplage magnéto-électrique et l'intéraction de Dzyaloshinskii-Moriya, un champ de fuite semblable à celui observé en magnétométrie à centres NV (Figure 2.28).

G.2.3 Conclusion sur les simulations

Les simulations ont montré d'une part la dynamique très rapide dans un matériaux antiferromagnétique tel que NiO, et d'autre part la possibilité de simuler la formation de structures antiferromagnétiques, ainsi que la mise en évidence de l'importance du couplage magnéto-électrique, pouvant servir de levier pour contraindre les structures antiferromagnétiques. Ces deux aspects sont encourageants pour la formation et l'écriture très rapide de mémoires antiferromagnétiques.

G.3 Étude expérimentale de la dynamique ultrarapide dans un antiferromagnétique à couplage magnéto-électrique

G.3.1 Imagerie par génération de seconde harmonique (SHG)

Dans ce chapitre, nous réalisons l'observation expérimentale de domaines antiferromagnétiques dans une couche mince de $BiFeO_3$, par génération de seconde harmonique (SHG). Cette technique d'optique non linéaire repose sur le fait que les charges accélérées par une lumière incidente de fréquence ω émettent, en plus de la fréquence fondamentale, des harmoniques supérieures, dont une fréquence doublée à 2ω. Au premier ordre, cette génération de seconde harmonique est intimement liée aux brisures de centrosymétrie du cristal, qui déforme le potentiel d'intéraction des électrons. En conséquence, il est possible d'obtenir des informations sur le cristal en observant le signal de SHG. Une illustration du phénomène est faite sur un crystal de PZT sur lequel des éléctrodes

lithographiées permettent d'appliquer une tension et de changer la strucure crystalline par piezoéléctricité (Figures 3.7, 3.8, 3.9 et 3.10).

G.3.2 Imagerie du multiferroïque $BiFeO_3$

Cette technique d'imagerie SHG est appliquée à une couche mince de 100nm de $BiFeO_3$ (001), sur laquelle des domaines ferroélectriques de tailles micrométriques ont été écrits (Figure 3.14d). $BiFeO_3$ est épitaxié sur $SrTiO_3$, ce qui a pour effet d'empêcher la formation de la cycloïde antiferromagnétique (Figure 2.29), et de contraindre le nombre de domaines antiferromagnétiques possibles à trois, au sein d'un même domaine ferroélectrique. Une analyse tensorielle nous donne les dépendances angulaires du signal de SHG pour chacun de ces trois domaines. Compte tenu de nos données expérimentales, nous n'observons principalement que deux domaines, vraisemblablement dégénérés en énergie, alors que le troisième domaine pour lequel **L** devrait être totalement planaire, n'apparaît que peu ou pas (Figure 3.25). La dépendance angulaire en polarisation incidente du signal de seconde harmonique nous renseigne également sur le champ électrique interne local (Figures 3.23a et 3.23b).

G.3.3 Imagerie SHG résolue en temps dans $BiFeO_3$

On munit l'expérience d'imagerie d'un faisceau laser de pompe de longueur d'onde 800nm dont on peut ajuster le retard par rapport au faisceau de mesure, de longueur d'onde 900nm (Figures 3.26 et 3.27). Cette technique permet de mesurer l'évolution temporelle du signal de seconde harmonique après excitation par la pompe. Durant la superposition des deux impulsions laser, des phénomènes optiques peuvent avoir lieu dont il faut avoir conscience pour ne pas surinterpréter la dynamique interne au cristal de $BiFeO_3$ durant l'impulsion. Le premier est la génération de sommes de fréquences (Figure 3.29). Nous nous en servons pour trouver l'origine des retards, puis l'écartons en utilisant un filtre passe-bande étroite autour de la seconde harmonique de mesure (450nm). Un second phénomène, qui peut impacter le signal de seconde harmonique est le phénomène de rectification optique sur le faisceau de pompe. Par ce phénomène, un champ térahertz peut être créé au sein du cristal, qui peut impacter le signal de mesure SHG (Figures 3.31 et 3.30). Une mesure à basse fluence ($0.25 mJ/cm^2$) est faite afin d'observer ces phénomènes tout en perturbant le moins possible l'ordre multiferroïque de $BiFeO_3$ (Figure 3.32). Puis une mesure est faite à haute fluence ($50 mJ/cm^2$) dans le but de perturber l'ordre multiferroïque. Les évolutions temporelles des signaux pour les deux fluences donnent des résultats différents (Figures 3.32 et 3.34), ce qui semble indiquer que la haute fluence a une influence sur le cristal, et que le signal n'est pas simplement dû à la rectification optique de la pompe. À haute fluence, les images de seconde harmoniques perdent en intensité pendant l'impulsion (Figure 3.33). Dans les deux cas, le signal de seconde harmonique retrouve sa constance 300 femtosecondes après l'excitation, et les domaines antiferromagnétiques sont retrouvés inchangés. L'évolution temporelle du profil angulaire pour les deux populations de domaines antiferromagnétiques montre une variation dissymétrique claire, qui est propre à chaque domaine (Figure 3.36). Cependant, une variation de la ferroélectricité $\boldsymbol{P_e}$ pourrait suffire à expliquer ce changement.

Enfin, une étude montre que les évolutions de la SHG aux différents angles dépendent de la polarisation du

faisceau de pompe (Figure 3.38). En particulier, les asymétries entre les angles 45 et 135° peuvent être exacerbées, et dépendent de la distance au centre du faisceau (Figure 3.39).

G.3.4 Conclusion sur $BiFeO_3$ vu en SHG

Dans ce chapitre, nous avons pu observer la présence de domaines antiferromagnétiques dans $BiFeO_3$ par imagerie SHG, et avons mesuré la variation du signal avec l'ajout d'un laser de pompe à 800nm. Malheureusement, il n'a pas été possible de conclure sur l'éventuelle présence de perturbation d'origine antiferromagnétique. Afin de rendre la pompe plus efficace, nous nous tournons dans le dernier chapitre vers des sources d'émission au térahertz, susceptibles d'exciter la résonance antiferromagnétique de $BiFeO_3$.

G.4 Injection de courants de spin

G.4.1 Processus de conversion spin-charge

Deux processus tenant leur origine du couplage spin-orbite et permettant de convertir un courant de spin en courant de charge sont présentés: l'effet spin-Hall inverse et l'effet Rashba-Edelstein inverse. L'effet spin-Hall inverse est intrinsèque à un matériau et tient son origine du couplage spin-orbite au sein du matériau, tandis que l'effet Rashba-Edelstein inverse tient son origine d'un champ électrique local, qui peut être interfacial. L'effet Seebeck, permettant de convertir un gradient de température en courant de spin est également mentionné.

G.4.2 Génération laser de courants de spin picosecondes dans les bicouches Métal magnétique/Métal Lourd.

Dans cette section, nous détaillons le processus de désaimantation ultrarapide par excitation laser dans les matériaux magnétiques. La désaimantation peut se faire à l'échelle de la picoseconde [121, 139] (Figure 4.5). Durant cette désaimantation, un courant de spin est créé par les électrons chauds pour évaculer le moment angulaire, qui sera dissipé par différents processus dans le crystal [140]. Une couche adjacente d'un matériau avec un fort couplage spin-orbite peut recuillir le courant de spin et le convertir en courant de charge à la picoseconde, via les effets de spin-Hall inverse ou Rashba-Edelstein inverse (Figure 4.6). Ce type de bicouche peut ëtre utilisé pour générer des impulsions terahertz [81].

G.4.3 Caractérisation expérimentale du courant de spin.

De telles bicouches peuvent générer des courants de spin à différentes échelles temporelles, et doivent être caractérisées au moyen de différentes techniques. Quatre techniques sont présentées, chacune propre à une échelle de temps. La première est une technique de magnétométrie optique basée sur l'effet Kerr magnéto-optique, résolue en temps (MOKE) (Figures 4.8 et fig:MOKEmeasurement). Elle donne des informations d'aimantation entre 1ps et 800ps (Figure 4.13).s

La deuxième technique consiste à mesurer le champ térahertz émis par le mouvement des charges induit par la conversion spin-charge dans la couche adjacente. Cette technique met en jeu de l'échantillonnage électro-optique, et renseigne sur la dynamique picoseconde (Figure 4.15).

La troisième technique présentée est une mesure électrique DC qui mesure l'accumulation de charge moyennée sur une milliseconde (Figure 4.19b).

Enfin, la quatrième technique combine résonance magnétique (FMR) et mesure électrique par "spin-pumping". L'échelle de temps est aussi la milliseconde, avec une information sur la résonance, à la nanoseconde (Figure fig:FMRCoFeBMgOTa).

G.4.4 Comparaison entre les couches de Pt et de MgO sur CoFeB

Pour combiner l'ensemble de ces techniques, une couche adjacente est nécessaire afin de réaliser la conversion spin-charge. Dans cette section, nous comparons l'effet d'une couche de platine Pt (conversion par effet Hall de spin inverse) à celui d'une couche d'oxyde de manganèse MgO (conversion par effet Rashba-Edelstein inverse). Nous montrons qu'aux échelles de temps longues, la conversion est du même ordre de grandeur pour les deux couches (Figure 4.21), mais que la conversion à la picoseconde est plus efficace pour celle mettant en jeu l'effet Hall de spin inverse (Figure 4.25). En effet, le champ térahertz émis est d'intensité 25 fois moindre, bien que de même forme temporelle. Cette conversion plus lente est attribuée aux états Rashba proches du niveau de Fermi pour l'interface CoFeB/MgO, qui ne sont pas accessibles aux électrons trop chauds (Figure 4.26). La similitude spectrale suggère que la dynamique est imposée par la couche magnétique, et que l'excitation de CoFeB par une impulsion laser femtoseconde constitue un bon injecteur de spin au térahertz.

G.4.5 Excitation térahertz de $BiFeO_3$

Dans cette section, nous mettons à profit l'un de nos émetteur térahertz pour exciter l'échantillon de $BiFeO_3$ le plus proche possible de sa résonance antiferromagnétique. Nous montrons que l'émission THz change de façon significative le signal de SHG, tant en profil angulaire qu'en amplitude (Figures 4.28 et 4.29). Ce changement dépend du domaine antiferromagnétique dans lequel la mesure est faite. Ce résultat constitue un signe prometteur d'une sélectivité entre les domaines, mais ne semble en revanche pas indiquer la présence d'excitation de modes antiferromagnétiques.

Une seconde approche consiste à injecter directement un courant de spin térahertz au moyen d'une couche ferromagnétique adjacente à $BiFeO_3$. Pour cela, une couche de permalloy a été déposée sur l'échantillon et est excitée par le laser femtoseconde.

G.4.6 Conclusion sur l'injection de spin au terahertz

Les résultats préliminaires de ces deux approches n'ont pas donnée lieu à un changement visible des textures antiferromagnétiques. Cependant, il faut souligner que ces mesures ont été faites à basse fluence, et que plusieurs axes

d'amélioration sont possibles. En particulier, la fluence peut être largement augmentée, et la qualité de l'interface $BiFeO_3$/permalloy peut être optimisée.

G.5 Discussion et perspectives

Les résultats présentés sont encourageants. Nos prédictions théoriques sur la commutation de domaines dans NiO modélisé sur les connaissances dynamiques actuelles du matériau et les impulsions de spin réalisables en laboratoire valident la possibilité de réaliser une mémoire à écriture picoseconde dans ce matériau. L'étude n'a pour l'instant été menée qu'au sein du cristal, et pourrait être développée sans difficulté apparente à des géométries plus complexes, tel que des parois de domaines.

La simulation statique de $BiFeO_3$ a montré qu'il était possible de simuler un nombre relativement important d'atomes, et qu'il était possible de stabiliser des textures antiferromagnétiques influencées par le couplage magnéto-électrique, de sorte qu'il a été possible de reproduire et expliquer les observations expérimentales. La simulation offre la possibilité d'ajuster les paramètres facilement. Il devrait être possible de simuler la formation de skyrmions antiferromagnétiques, et de prévoir les valeurs expérimentales nécessaire pour leur apparition. Simuler une configuration similaire à celle de l'expérience de SHG devrait également nous permettre de mieux comprendre l'évolution de changement structuraux sous l'influence d'une impulsion laser, ou d'une injection de spin.

Au cours de cette thèse, nous avons raffiné notre technique d'analyse par SHG, et avons mis en place une expérience pompe-sonde permettant d'avoir accès à une bonne résolution temporelle pour le système multiferroïque $BiFeO_3$. Notre résolution temporelle de 0.3ps associée à notre résolution spatiale de 0.5µm et à la dépendance angulaire des signaux de SHG devraient à l'avenir permettre de découpler les effets et contributions des deux ordres ferroïques. Jusqu'ici l'analyse fut menée sur des moyennes spatiales, mais des effets locaux pourraient être isolés.

La mesure à différentes échelles de temps sur les courants de spin picoseconde induits par laser, et donnant lieu à une désaimantation ultrarapide nous a montré la complémentarité de nos quatre méthodes de mesure. Une caractérisation qualitative a pu être faite, mais un travail plus approfondi est nécessaire pour quantifier exactement les courants de spin générés.

La dernière mesure présentée, pour laquelle les courants de spin sont directement injectés dans l'échantillon de $BiFeO_3$ grâce à l'excitation laser d'une couche adjacente de permalloy, n'en est qu'à ses débuts et devrait être très prometteuse, étant donné que la polarisation du courant de spin peut être définie au simple moyen d'un champ magnétique extérieur. L'observation de ce système avec notre technique d'imagerie par SHG résolue en temps devrait nous aider à suivre les évolutions dynamiques avec une résolution subpicoseconde. Nous avons la possibilité d'augmenter l'intensité de l'excitation et toutes les clés en main pour poursuive cette étude.

Bibliography

[1] Cheng, R., Daniels, M. W., Zhu, J.-G. & Xiao, D. Ultrafast switching of antiferromagnets via spin-transfer torque. *Phys. Rev. B* **91**, 064423 (2015). URL https://link.aps.org/doi/10.1103/PhysRevB.91.064423.

[2] Cullity, B. D. & Graham, C. D. *Introduction to Magnetic Materials* (Wiley-IEEE Press, 2008), 2 edn.

[3] Stöhr, J. & Siegmann, H. C. *Magnetism: From Fundamentals to Nanoscale Dynamics*. 152 (Springer-Verlag Berlin Heidelberg, 2006), 1 edn.

[4] Åkerman, J. Toward a universal memory. *Science* **308**, 508–510 (2005). URL https://science.sciencemag.org/content/308/5721/508. https://science.sciencemag.org/content/308/5721/508.full.pdf.

[5] Hihinashvili, R. Derivation of the heisenberg hamiltonian. http://phycomp.technion.ac.il/~riki/Heisenberg.html. Accessed: 2019-10-27.

[6] A13ean. Stoner model for ferromagnetism. *CC BY-SA 3.0* (2011). URL https://commons.wikimedia.org/w/index.php?curid=16209709.

[7] Korenman, V. & Prange, R. E. Anomalous damping of spin waves in magnetic metals. *Phys. Rev. B* **6**, 2769–2777 (1972). URL https://link.aps.org/doi/10.1103/PhysRevB.6.2769.

[8] Evelt, M. *et al.* High-efficiency control of spin-wave propagation in ultra-thin yttrium iron garnet by the spin-orbit torque. *Applied Physics Letters* **108**, 172406 (2016). URL https://doi.org/10.1063/1.4948252. https://doi.org/10.1063/1.4948252.

[9] Collet, M. *et al.* Spin-wave propagation in ultra-thin yig based waveguides. *Applied Physics Letters* **110**, 092408 (2017). URL https://doi.org/10.1063/1.4976708. https://doi.org/10.1063/1.4976708.

[10] Baltz, V. *et al.* Antiferromagnetic spintronics. *Rev. Mod. Phys.* **90**, 015005 (2018). URL https://link.aps.org/doi/10.1103/RevModPhys.90.015005.

[11] Baibich, M. N. *et al.* Giant magnetoresistance of (001)Fe/(001)Cr magnetic superlattices. *Phys. Rev. Lett.* **61**, 2472–2475 (1988). URL https://link.aps.org/doi/10.1103/PhysRevLett.61.2472.

[12] Binasch, G., Grünberg, P., Saurenbach, F. & Zinn, W. Enhanced magnetoresistance in layered magnetic structures with antiferromagnetic interlayer exchange. *Phys. Rev. B* **39**, 4828–4830 (1989). URL https://link.aps.org/doi/10.1103/PhysRevB.39.4828.

[13] Bobeck, A. H., Bonyhard, P. I. & Geusic, J. E. Magnetic bubbles—an emerging new memory technology. *Proceedings of the IEEE* **63**, 1176–1195 (1975).

[14] Sampaio, J., Cros, V., Rohart, S., Thiaville, A. & Fert, A. Nucleation, stability and current-induced motion of isolated magnetic skyrmions in nanostructures. *Nature Nanotechnology* **8**, 839 (2013). URL https://doi.org/10.1038/nnano.2013.210.

[15] Iwasaki, J., Mochizuki, M. & Nagaosa, N. Current-induced skyrmion dynamics in constricted geometries. *Nature Nanotechnology* **8**, 742 (2013). URL https://doi.org/10.1038/nnano.2013.176.

[16] Mittal, S. A survey of techniques for architecting processor components using domain-wall memory. *J. Emerg. Technol. Comput. Syst.* **13**, 29:1–29:25 (2016). URL http://doi.acm.org/10.1145/2994550.

[17] Néel, Louis. Propriétés magnétiques de l'état métallique et énergie d'interaction entre atomes magnétiques. *Ann. Phys.* **11**, 232–279 (1936). URL https://doi.org/10.1051/anphys/193611050232.

[18] Néel, L. Propriétés magnétiques des ferrites ; ferrimagnétisme et antiferromagnétisme. *Ann. Phys.* **12**, 137–198 (1948). URL https://doi.org/10.1051/anphys/194812030137.

[19] Bizette, H., Squire, C. & Tsai, B. *C.R. Acad. Sci.* **207** (1938).

[20] Hutchings, M. T. & Samuelsen, E. J. Measurement of spin-wave dispersion in NiO by inelastic neutron scattering and its relation to magnetic properties. *Phys. Rev. B* **6**, 3447–3461 (1972). URL https://link.aps.org/doi/10.1103/PhysRevB.6.3447.

[21] Fishman, R. S. Field dependence of the spin state and spectroscopic modes of multiferroic $BiFeO_3$. *Phys. Rev. B* **87**, 224419 (2013). URL https://link.aps.org/doi/10.1103/PhysRevB.87.224419.

[22] Fishman, R. S. Orientation dependence of the critical magnetic field for multiferroic $BiFeO_3$. *Phys. Rev. B* **88**, 104419 (2013). URL https://link.aps.org/doi/10.1103/PhysRevB.88.104419.

[23] Machado, F. L. A. *et al.* Spin-flop transition in the easy-plane antiferromagnet nickel oxide. *Phys. Rev. B* **95**, 104418 (2017). URL https://link.aps.org/doi/10.1103/PhysRevB.95.104418.

[24] Jaccarino, V., King, A., Motokawa, M., Sakakibara, T. & Date, M. Temperature dependence of fef2 spin flop field. *Journal of Magnetism and Magnetic Materials* **31-34**, 1117 – 1118 (1983). URL http://www.sciencedirect.com/science/article/pii/0304885383908223.

[25] Beaujouan, D., Thibaudeau, P. & Barreteau, C. Anisotropic magnetic molecular dynamics of cobalt nanowires. *Phys. Rev. B* **86**, 174409 (2012). URL https://link.aps.org/doi/10.1103/PhysRevB.86.174409.

[26] Opel, M. Spintronic oxides grown by laser-MBE. *Journal of Physics D: Applied Physics* **45**, 033001 (2011). URL https://doi.org/10.1088%2F0022-3727%2F45%2F3%2F033001.

[27] Goodenough, J. B. Theory of the role of covalence in the perovskite-type manganites [La, m(II)]MnO_3. *Phys. Rev.* **100**, 564–573 (1955). URL https://link.aps.org/doi/10.1103/PhysRev.100.564.

[28] Anderson, P. W. Antiferromagnetism. theory of superexchange interaction. *Phys. Rev.* **79**, 350–356 (1950). URL https://link.aps.org/doi/10.1103/PhysRev.79.350.

[29] Wollan, E. O. & Koehler, W. C. Neutron diffraction study of the magnetic properties of the series of perovskite-type compounds [$(1-x)$La, xCa]Mno_3. *Phys. Rev.* **100**, 545–563 (1955). URL https://link.aps.org/doi/10.1103/PhysRev.100.545.

[30] Dagotto, E. *Nanoscale phase separation and colossal magnetoresistance (physics of manganites)*. Springer Series in Solid-State Sciences (Springer, 2003), 1st edition. edn.

[31] Néel, L. Magnetism and local molecular field. *Science* **174**, 985–992 (1971). URL https://science.sciencemag.org/content/174/4013/985. https://science.sciencemag.org/content/174/4013/985.full.pdf.

[32] Wadley, P. *et al.* Electrical switching of an antiferromagnet. *Science* **351**, 587–590 (2016). URL http://science.sciencemag.org/content/351/6273/587. http://science.sciencemag.org/content/351/6273/587.full.pdf.

[33] Cheng, R., Xiao, D. & Brataas, A. Terahertz antiferromagnetic spin hall nano-oscillator. *Phys. Rev. Lett.* **116**, 207603 (2016). URL https://link.aps.org/doi/10.1103/PhysRevLett.116.207603.

[34] Khymyn, R., Lisenkov, I., Tiberkevich, V., Ivanov, B. A. & Slavin, A. Antiferromagnetic thz-frequency josephson-like oscillator driven by spin current. *Scientific Reports* **7**, 43705 (2017). URL https://doi.org/10.1038/srep43705.

[35] Kampfrath, T. *et al.* Coherent terahertz control of antiferromagnetic spin waves. *Nature Photonics* **5**, 31 (2010). URL https://doi.org/10.1038/nphoton.2010.259.

[36] Talbayev, D., Lee, S., Cheong, S.-W. & Taylor, A. J. Terahertz wave generation via optical rectification from multiferroic $BiFeO_3$. *Applied Physics Letters* **93**, 212906 (2008). URL http://dx.doi.org/10.1063/1.3036526. http://dx.doi.org/10.1063/1.3036526.

[37] Cheng, R., Daniels, M. W., Zhu, J.-G. & Xiao, D. Antiferromagnetic spin wave field-effect transistor. *Scientific Reports* **6**, 24223 (2016). URL https://doi.org/10.1038/srep24223.

[38] Olejník, K. *et al.* Terahertz electrical writing speed in an antiferromagnetic memory. *Science Advances* **4** (2018). URL https://advances.sciencemag.org/content/4/3/eaar3566. https://advances.sciencemag.org/content/4/3/eaar3566.full.pdf.

[39] Hahn, C. *et al.* Conduction of spin currents through insulating antiferromagnetic oxides. *EPL (Europhysics Letters)* **108**, 57005 (2014). URL https://doi.org/10.1209%2F0295-5075%2F108%2F57005.

[40] Lebrun, R. *et al.* Tunable long-distance spin transport in a crystalline antiferromagnetic iron oxide. *Nature* **561**, 222–225 (2018). URL https://doi.org/10.1038/s41586-018-0490-7.

[41] Research, W. *ElementData* (Wolfram Research, 2007). URL https://periodictable.com/Properties/A/MagneticType.html.

[42] Nemec, P., Fiebig, M., Kampfrath, T. & Kimel, A. V. Antiferromagnetic opto-spintronics. *Nature Physics* **14**, 229–241 (2018). URL https://doi.org/10.1038/s41567-018-0051-x.

[43] Gomonay, H. V., Kunitsyn, R. V. & Loktev, V. M. Symmetry and the macroscopic dynamics of antiferromagnetic materials in the presence of spin-polarized current. *Phys. Rev. B* **85**, 134446 (2012). URL https://link.aps.org/doi/10.1103/PhysRevB.85.134446.

[44] Gomonay, H. V. & Loktev, V. M. Spin transfer and current-induced switching in antiferromagnets. *Phys. Rev. B* **81**, 144427 (2010). URL https://link.aps.org/doi/10.1103/PhysRevB.81.144427.

[45] Gomonay, E. V. & Loktev, V. M. Spintronics of antiferromagnetic systems (review article). *Low Temperature Physics* **40**, 17–35 (2014). URL https://doi.org/10.1063/1.4862467. https://doi.org/10.1063/1.4862467.

[46] Gomonay, O., Jungwirth, T. & Sinova, J. High antiferromagnetic domain wall velocity induced by néel spin-orbit torques. *Phys. Rev. Lett.* **117**, 017202 (2016). URL https://link.aps.org/doi/10.1103/PhysRevLett.117.017202.

[47] Gomonay, O., Kläui, M. & Sinova, J. Manipulating antiferromagnets with magnetic fields: Ratchet motion of multiple domain walls induced by asymmetric field pulses. *Applied Physics Letters* **109**, 142404 (2016). URL https://doi.org/10.1063/1.4964272. https://doi.org/10.1063/1.4964272.

[48] Gomonay, H. & Loktev, V. Spin-polarized current-induced instability in the spin-valve antiferromagnetic layer. *Journal of the Magnetics Society of Japan* **32**, 535–539 (2008).

[49] Gomonay, O., Baltz, V., Brataas, A. & Tserkovnyak, Y. Antiferromagnetic spin textures and dynamics. *Nature Physics* **14**, 213–216 (2018). URL https://doi.org/10.1038/s41567-018-0049-4.

[50] Reger, J. D., Riera, J. A. & Young, A. P. Monte carlo simulations of the spin-1/2heisenberg antiferromagnet in two dimensions. *Journal of Physics: Condensed Matter* **1**, 1855–1865 (1989). URL https://doi.org/10.1088%2F0953-8984%2F1%2F10%2F007.

[51] Vansteenkiste, A. *et al.* The design and verification of MuMax3. *AIP Advances* **4**, 107133 (2014). URL https://doi.org/10.1063/1.4899186. https://doi.org/10.1063/1.4899186.

[52] Donahue, M. & Porter, D. OOMMF user's guide, version 1.0. Interagency Report NISTIR 6376, National Institute of Standards and Technology, Gaithersburg, MD (Sept 1999).

[53] Kittel, C. Theory of antiferromagnetic resonance. *Phys. Rev.* **82**, 565–565 (1951). URL https://link.aps.org/doi/10.1103/PhysRev.82.565.

[54] Satoh, T. *et al.* Spin oscillations in antiferromagnetic NiO triggered by circularly polarized light. *Phys. Rev. Lett.* **105**, 077402 (2010). URL https://link.aps.org/doi/10.1103/PhysRevLett.105.077402.

[55] Sosnowska, I., Neumaier, T. P. & Steichele, E. Spiral magnetic ordering in bismuth ferrite. *Journal of Physics C: Solid State Physics* **15**, 4835–4846 (1982). URL https://doi.org/10.1088%2F0022-3719%2F15%2F23%2F020.

[56] Rahmedov, D., Wang, D., Íñiguez, J. & Bellaiche, L. Magnetic cycloid of $BiFeO_3$ from atomistic simulations. *Phys. Rev. Lett.* **109**, 037207 (2012). URL https://link.aps.org/doi/10.1103/PhysRevLett.109.037207.

[57] Makarov, A. M. Modeling of emerging resistive switching based memory cells. http://www.iue.tuwien.ac.at/phd/makarov/dissertationch5.html. Dissertation. Accessed: 2019-11-04.

[58] Slonczewski, J. Current-driven excitation of magnetic multilayers. *Journal of Magnetism and Magnetic Materials* **159**, L1 – L7 (1996). URL http://www.sciencedirect.com/science/article/pii/0304885396000625.

[59] Tranchida, J., Plimpton, S., Thibaudeau, P. & Thompson, A. Massively parallel symplectic algorithm for coupled magnetic spin dynamics and molecular dynamics. *Journal of Computational Physics* **372**, 406 – 425 (2018). URL http://www.sciencedirect.com/science/article/pii/S0021999118304200.

[60] Omelyan, I. P., Mryglod, I. M. & Folk, R. Algorithm for molecular dynamics simulations of spin liquids. *Phys. Rev. Lett.* **86**, 898–901 (2001). URL https://link.aps.org/doi/10.1103/PhysRevLett.86.898.

[61] Thibaudeau, P. *et al.* *Spindynamics* (GitHub repository, 2018). URL https://github.com/araven/spin-dynamics.

[62] Thibaudeau, P., Tranchida, J. & Nicols, S. Non-markovian magnetization dynamics for uniaxial nanomagnets. *IEEE Transactions on Magnetics* **52**, 1–4 (2016).

[63] Thibaudeau, P., Nussle, T. & Nicolis, S. Nambu mechanics for stochastic magnetization dynamics. *Journal of Magnetism and Magnetic Materials* **432**, 175 – 180 (2017). URL http://www.sciencedirect.com/science/article/pii/S0304885316325653.

[64] Moriyama, T., Oda, K., Ohkochi, T., Kimata, M. & Ono, T. Spin torque control of antiferromagnetic moments in NiO. *Scientific Reports* **8**, 14167 (2018). URL https://doi.org/10.1038/s41598-018-32508-w.

[65] Trzeciecki, M., Ney, O., Zhang, G. P. & Hübner, W. Laser-control of ferro- and antiferromagnetism. *B. Kramer (Ed.): Adv. in Solid State Phys.* **41, 547–555** (2001).

[66] Gómez-Abal, R., Ney, O., Satitkovitchai, K. & Hübner, W. All-optical subpicosecond magnetic switching in NiO(001). *Phys. Rev. Lett.* **92**, 227402 (2004). URL https://link.aps.org/doi/10.1103/PhysRevLett.92.227402.

[67] Lefkidis, G. & Hübner, W. First-principles study of ultrafast magneto-optical switching in NiO. *Phys. Rev. B* **76**, 014418 (2007). URL https://link.aps.org/doi/10.1103/PhysRevB.76.014418.

[68] Rinaldi-Montes, N. *et al.* Size effects on the néel temperature of antiferromagnetic nio nanoparticles. *AIP Advances* **6**, 056104 (2016). URL https://doi.org/10.1063/1.4943062. https://doi.org/10.1063/1.4943062.

[69] Roth, W. L. Magnetic structures of MnO, FeO, CoO, and NiO. *Phys. Rev.* **110**, 1333–1341 (1958). URL https://link.aps.org/doi/10.1103/PhysRev.110.1333.

[70] Yamada, T., Saito, S. & Shimomura, Y. Magnetic anisotropy, magnetostriction, and magnetic domain walls in NiO. ii. experiment. *Journal of the Physical Society of Japan* **21**, 672–680 (1966). URL https://doi.org/10.1143/JPSJ.21.672. https://doi.org/10.1143/JPSJ.21.672.

[71] Kondoh, H. & Takeda, T. Observation of antiferromagnetic domains in nickel oxide. *Journal of the Physical Society of Japan* **19**, 2041–2051 (1964). URL https://doi.org/10.1143/JPSJ.19.2041. https://doi.org/10.1143/JPSJ.19.2041.

[72] Duong, N. P., Satoh, T. & Fiebig, M. Ultrafast manipulation of antiferromagnetism of NiO. *Phys. Rev. Lett.* **93**, 117402 (2004). URL https://link.aps.org/doi/10.1103/PhysRevLett.93.117402.

[73] Rubano, A. *et al.* Influence of laser pulse shaping on the ultrafast dynamics in antiferromagnetic NiO. *Phys. Rev. B* **82**, 174431 (2010). URL https://link.aps.org/doi/10.1103/PhysRevB.82.174431.

[74] Sievers, A. J. & Tinkham, M. Far infrared antiferromagnetic resonance in MnO and NiO. *Phys. Rev.* **129**, 1566–1571 (1963). URL https://link.aps.org/doi/10.1103/PhysRev.129.1566.

[75] Milano, J., Steren, L. B. & Grimsditch, M. Effect of dipolar interaction on the antiferromagnetic resonance spectra of NiO. *Phys. Rev. Lett.* **93**, 077601 (2004). URL https://link.aps.org/doi/10.1103/PhysRevLett.93.077601.

[76] Kohmoto, T. & Moriyasu, T. Ultrafast magnon dynamics in antiferromagnetic nickel oxide observed by optical pump-probe and terahertz time-domain spectroscopies. In *2018 43rd International Conference on Infrared, Millimeter, and Terahertz Waves (IRMMW-THz)*, 1–2 (2018). URL https://ieeexplore.ieee.org/document/8510270.

[77] Kondoh, H. Antiferromagnetic resonance in NiO in far-infrared region. *Journal of the Physical Society of Japan* **15**, 1970–1975 (1960). URL https://doi.org/10.1143/JPSJ.15.1970. https://doi.org/10.1143/JPSJ.15.1970.

[78] Cheng, R., Xiao, J., Niu, Q. & Brataas, A. Spin pumping and spin-transfer torques in antiferromagnets. *Phys. Rev. Lett.* **113**, 057601 (2014). URL https://link.aps.org/doi/10.1103/PhysRevLett.113.057601.

[79] Cheng, R., Zhu, J.-G. & Xiao, D. Dynamic feedback in ferromagnet–spin hall metal heterostructures. *Phys. Rev. Lett.* **117**, 097202 (2016). URL https://link.aps.org/doi/10.1103/PhysRevLett.117.097202.

[80] Keffer, F. & Kittel, C. Theory of antiferromagnetic resonance. *Phys. Rev.* **85**, 329–337 (1952). URL https://link.aps.org/doi/10.1103/PhysRev.85.329.

[81] Kampfrath, T. *et al.* Terahertz spin current pulses controlled by magnetic heterostructures. *Nature Nanotechnology* **8**, 256 (2013). URL https://doi.org/10.1038/nnano.2013.43.

[82] Gross, I. *et al.* Real-space imaging of non-collinear antiferromagnetic order with a single-spin magnetometer. *Nature* **549**, 252 (2017). URL https://doi.org/10.1038/nature23656.

[83] Cohen, R. E. Origin of ferroelectricity in perovskite oxides. *Nature* **358**, 136–138 (1992). URL https://doi.org/10.1038/358136a0.

[84] Hill, N. A. Why are there so few magnetic ferroelectrics? *The Journal of Physical Chemistry B* **104**, 6694–6709 (2000). URL https://doi.org/10.1021/jp000114x.

[85] Maître, A., François, M. & Gachon, J. C. Experimental study of the Bi_2O_3-Fe_2O_3 pseudo-binary system. *Journal of Phase Equilibria and Diffusion* **25**, 59–67 (2004). URL https://doi.org/10.1007/s11669-004-0171-0.

[86] Zvezdin, A. K. & Pyatakov, A. P. On the problem of coexistence of the weak ferromagnetism and the spin flexoelectricity in multiferroic bismuth ferrite. *EPL (Europhysics Letters)* **99**, 57003 (2012). URL https://doi.org/10.1209%2F0295-5075%2F99%2F57003.

[87] Lebeugle, D., Colson, D., Forget, A. & Viret, M. Very large spontaneous electric polarization in $BiFeO_3$ single crystals at room temperature and its evolution under cycling fields. *Applied Physics Letters* **91**, 022907 (2007). URL https://doi.org/10.1063/1.2753390. https://doi.org/10.1063/1.2753390.

[88] Kiselev, S. V., Ozerov, R. P. & Zhdanov, G. S. Detection of Magnetic Order in Ferroelectric $BiFeO_3$ by Neutron Diffraction. *Soviet Physics Doklady* **7**, 742 (1963).

[89] Katsura, H., Nagaosa, N. & Balatsky, A. V. Spin current and magnetoelectric effect in noncollinear magnets. *Phys. Rev. Lett.* **95**, 057205 (2005). URL https://link.aps.org/doi/10.1103/PhysRevLett.95.057205.

[90] Sando, D. *et al.* Crafting the magnonic and spintronic response of $BiFeO_3$ films by epitaxial strain. *Nature Materials* **12**, 641 (2013). URL http://dx.doi.org/10.1038/nmat3629.

[91] Fishman, R. S., Haraldsen, J. T., Furukawa, N. & Miyahara, S. Spin state and spectroscopic modes of multiferroic $BiFeO_3$. *Phys. Rev. B* **87**, 134416 (2013). URL https://link.aps.org/doi/10.1103/PhysRevB.87.134416.

[92] Waterfield Price, N. *et al.* Coherent magnetoelastic domains in multiferroic $BiFeO_3$ films. *Phys. Rev. Lett.* **117**, 177601 (2016). URL https://link.aps.org/doi/10.1103/PhysRevLett.117.177601.

[93] Sosnowska, I. & Zvezdin, A. Origin of the long period magnetic ordering in $BiFeO_3$. *Journal of Magnetism and Magnetic Materials* **140-144**, 167 – 168 (1995). URL http://www.sciencedirect.com/science/article/pii/0304885394011206. International Conference on Magnetism.

[94] Jeong, J. *et al.* Temperature-dependent interplay of dzyaloshinskii-moriya interaction and single-ion anisotropy in multiferroic $BiFeO_3$. *Phys. Rev. Lett.* **113**, 107202 (2014). URL https://link.aps.org/doi/10.1103/PhysRevLett.113.107202.

[95] Ramazanoglu, M. *et al.* Local weak ferromagnetism in single-crystalline ferroelectric $BiFeO_3$. *Phys. Rev. Lett.* **107**, 207206 (2011). URL https://link.aps.org/doi/10.1103/PhysRevLett.107.207206.

[96] Seki, S., Yu, X. Z., Ishiwata, S. & Tokura, Y. Observation of skyrmions in a multiferroic material. *Science* **336**, 198–201 (2012). URL https://science.sciencemag.org/content/336/6078/198. https://science.sciencemag.org/content/336/6078/198.full.pdf.

[97] Nikiforov, A. & Sonin, E. Dynamics of magnetic vortices in a planar ferromagnet. *Sov. Phys. JETP* **58**, 110 (1983). URL http://www.jetp.ac.ru/cgi-bin/dn/e_058_02_0373.pdf. http://www.jetp.ac.ru/cgi-bin/dn/e_058_02_0373.pdf.

[98] Zhang, X., Zhou, Y. & Ezawa, M. Antiferromagnetic skyrmion: Stability, creation and manipulation. *Scientific Reports* **6**, 24795 (2016). URL https://doi.org/10.1038/srep24795.

[99] Park, B. G. *et al.* A spin-valve-like magnetoresistance of an antiferromagnet-based tunnel junction. *Nature Materials* **10**, 347–351 (2011). URL https://doi.org/10.1038/nmat2983.

[100] Andreev, A. F. & Marchenko, V. I. Symmetry and the macroscopic dynamics of magnetic materials. *Soviet Physics Uspekhi* **23**, 21–34 (1980). URL https://doi.org/10.1070%2Fpu1980v023n01abeh004859.

[101] Kirilyuk, A. & Rasing, T. Magnetization-induced-second-harmonic generation from surfaces and interfaces. *J. Opt. Soc. Am. B* **22**, 148–167 (2005). URL http://josab.osa.org/abstract.cfm?URI=josab-22-1-148.

[102] Kirilyuk, A., Kimel, A. V. & Rasing, T. Ultrafast optical manipulation of magnetic order. *Rev. Mod. Phys.* **82**, 2731–2784 (2010). URL https://link.aps.org/doi/10.1103/RevModPhys.82.2731.

[103] Fiebig, M. *et al.* Ultrafast magnetization dynamics of antiferromagnetic compounds. *Journal of Physics D: Applied Physics* **41**, 164005 (2008). URL https://doi.org/10.1088%2F0022-3727%2F41%2F16%2F164005.

[104] Ivanov, B. A. Spin dynamics of antiferromagnets under action of femtosecond laser pulses (review article). *Low Temperature Physics* **40**, 91–105 (2014). URL https://doi.org/10.1063/1.4865565. https://doi.org/10.1063/1.4865565.

[105] Denev, S. A., Lummen, T. T. A., Barnes, E., Kumar, A. & Gopalan, V. Probing ferroelectrics using optical second harmonic generation. *Journal of the American Ceramic Society* **94**, 2699–2727 (2011). URL http://dx.doi.org/10.1111/j.1551-2916.2011.04740.x.

[106] Fiebig, M., Pavlov, V. V. & Pisarev, R. V. Second-harmonic generation as a tool for studying electronic and magnetic structures of crystals: review. *J. Opt. Soc. Am. B* **22**, 96–118 (2005). URL http://josab.osa.org/abstract.cfm?URI=josab-22-1-96.

[107] Fiebig, M., Fröhlich, D., Sluyterman v. L., G. & Pisarev, R. V. Domain topography of antiferromagnetic Cr_2O_3 by second-harmonic generation. *Applied Physics Letters* **66**, 2906–2908 (1995). URL https://doi.org/10.1063/1.113699. https://doi.org/10.1063/1.113699.

[108] Fiebig, M., Fröhlich, D. & Thiele, H. J. Determination of spin direction in the spin-flop phase of Cr_2O_3. *Phys. Rev. B* **54**, R12681–R12684 (1996). URL https://link.aps.org/doi/10.1103/PhysRevB.54.R12681.

[109] Fiebig, M. *et al.* Second harmonic generation in the centrosymmetric antiferromagnet NiO. *Phys. Rev. Lett.* **87**, 137202 (2001). URL https://link.aps.org/doi/10.1103/PhysRevLett.87.137202.

[110] Fiebig, M., Lottermoser, T., Fröhlich, D., Goltsev, A. V. & Pisarev, R. V. Observation of coupled magnetic and electric domains. *Nature* **419**, 818–820 (2002). URL https://doi.org/10.1038/nature01077.

[111] Trassin, M., Luca, G. D., Manz, S. & Fiebig, M. Probing ferroelectric domain engineering in $BiFeO_3$ thin films by second harmonic generation. *Advanced Materials* **27**, 4871–4876 (2015). URL https://onlinelibrary.wiley.com/doi/abs/10.1002/adma.201501636. https://onlinelibrary.wiley.com/doi/pdf/10.1002/adma.201501636.

[112] Kumar, A. *et al.* Linear and nonlinear optical properties of $BiFeO_3$. *Applied Physics Letters* **92**, 121915 (2008). URL https://doi.org/10.1063/1.2901168. https://doi.org/10.1063/1.2901168.

[113] Chauleau, J.-Y., Haltz, E., Carrétéro, C., Fusil, S. & Viret, M. Multi-stimuli manipulation of antiferromagnetic domains assessed by second-harmonic imaging. *Nature Materials* **16**, 803 (2017). URL http://dx.doi.org/10.1038/nmat4899.

[114] Birss, R. *Symmetry and Magnetism* (North-Holland Publishing Co.-Amsterdam, 1966).

[115] Tinkham, M. & McKay, G. *Group Theory and Quantum Mechanics* (McGraw-Hill, 1964). P141.

[116] Trzeciecki, M. & Hübner, W. Time-reversal symmetry in nonlinear optics. *Phys. Rev. B* **62**, 13888–13891 (2000). URL https://link.aps.org/doi/10.1103/PhysRevB.62.13888.

[117] Nahata, A. & Heinz, T. F. Detection of freely propagating terahertz radiation by use of optical second-harmonic generation. *Opt. Lett.* **23**, 67–69 (1998). URL http://ol.osa.org/abstract.cfm?URI=ol-23-1-67.

[118] Gruverman, A. & Kalinin, S. V. Piezoresponse force microscopy and recent advances in nanoscale studies of ferroelectrics. *Journal of Materials Science* **41**, 107–116 (2006). URL https://doi.org/10.1007/s10853-005-5946-0.

[119] Ihlefeld, J. F. *et al.* Optical band gap of $BiFeO_3$ grown by molecular-beam epitaxy. *Applied Physics Letters* **92**, 142908 (2008). URL https://doi.org/10.1063/1.2901160. https://doi.org/10.1063/1.2901160.

[120] Basu, S. R. *et al.* Photoconductivity in $BiFeO_3$ thin films. *Applied Physics Letters* **92**, 091905 (2008). URL https://doi.org/10.1063/1.2887908. https://doi.org/10.1063/1.2887908.

[121] Beaurepaire, E., Merle, J.-C., Daunois, A. & Bigot, J.-Y. Ultrafast spin dynamics in ferromagnetic nickel. *Phys. Rev. Lett.* **76**, 4250–4253 (1996). URL https://link.aps.org/doi/10.1103/PhysRevLett.76.4250.

[122] Kimel, A. V. *et al.* Ultrafast non-thermal control of magnetization by instantaneous photomagnetic pulses. *Nature* **435**, 655–657 (2005). URL https://doi.org/10.1038/nature03564.

[123] Rana, D. S. *et al.* Understanding the nature of ultrafast polarization dynamics of ferroelectric memory in the multiferroic $BiFeO_3$. *Advanced Materials* **21**, 2881–2885 (2009). URL https://onlinelibrary.wiley.com/doi/abs/10.1002/adma.200802094. https://onlinelibrary.wiley.com/doi/pdf/10.1002/adma.200802094.

[124] Takahashi, K., Kida, N. & Tonouchi, M. Terahertz radiation by an ultrafast spontaneous polarization modulation of multiferroic $BiFeO_3$ thin films. *Phys. Rev. Lett.* **96**, 117402 (2006). URL https://link.aps.org/doi/10.1103/PhysRevLett.96.117402.

[125] Sa, D., Valentí, R. & Gros, C. A generalized ginzburg-landau approach to second harmonic generation. *The European Physical Journal B - Condensed Matter and Complex Systems* **14**, 301–305 (2000). URL https://doi.org/10.1007/s100510050133.

[126] Schick, D. *et al.* Localized excited charge carriers generate ultrafast inhomogeneous strain in the multiferroic $BiFeO_3$. *Phys. Rev. Lett.* **112**, 097602 (2014). URL https://link.aps.org/doi/10.1103/PhysRevLett.112.097602.

[127] Matzen, S. *et al.* Tuning ultrafast photoinduced strain in ferroelectric-based devices. *Advanced Electronic Materials* **5**, 1800709 (2019). URL https://onlinelibrary.wiley.com/doi/abs/10.1002/aelm.201800709. https://onlinelibrary.wiley.com/doi/pdf/10.1002/aelm.201800709.

[128] Hirsch, J. E. Spin hall effect. *Phys. Rev. Lett.* **83**, 1834–1837 (1999). URL https://link.aps.org/doi/10.1103/PhysRevLett.83.1834.

[129] Zhang, W., Han, W., Jiang, X., Yang, S.-H. & S. P. Parkin, S. Role of transparency of platinum-ferromagnet interfaces in determining the intrinsic magnitude of the spin hall effect. *Nature Physics* **11**, 496 (2015). URL https://doi.org/10.1038/nphys3304.

[130] Tserkovnyak, Y., Brataas, A. & Bauer, G. E. W. Enhanced gilbert damping in thin ferromagnetic films. *Phys. Rev. Lett.* **88**, 117601 (2002). URL https://link.aps.org/doi/10.1103/PhysRevLett.88.117601.

[131] Bychkov, Y. A. & Rashba, E. I. Properties of a 2d electron gas with lifted spectral degeneracy. *Pisma Zh. Eksp. Teor. Fiz.* **39** (1984). URL http://www.jetpletters.ac.ru/ps/1264/article_19121.pdf. [Sov. Phys. JETP Lett. 39, 78 (1984)].

[132] Lesne, E. *Non-Equilibrium Spin Accumulation Phenomena at the $LaAlO_3/SrTiO_3(001)$ Quasi-Two-Dimensional Electron System*. Ph.D. thesis, Paris 6 (2015). URL http://www.theses.fr/2015PA066417. 2015PA066417, http://www.theses.fr/2015PA066417/document.

[133] Adachi, H., ichi Uchida, K., Saitoh, E. & Maekawa, S. Theory of the spin seebeck effect. *Reports on Progress in Physics* **76**, 036501 (2013). URL https://doi.org/10.1088%2F0034-4885%2F76%2F3%2F036501.

[134] Uchida, K. *et al.* Observation of the spin seebeck effect. *Nature* **455**, 778 (2008). URL https://doi.org/10.1038/nature07321.

[135] Seifert, T. *et al.* Efficient metallic spintronic emitters of ultrabroadband terahertz radiation. *Nature Photonics* **10**, 483 (2016). URL https://doi.org/10.1038/nphoton.2016.91.

[136] Boeglin, C. *et al.* Distinguishing the ultrafast dynamics of spin and orbital moments in solids. *Nature* **465**, 458–461 (2010). URL https://doi.org/10.1038/nature09070.

[137] Carley, R. *et al.* Femtosecond laser excitation drives ferromagnetic gadolinium out of magnetic equilibrium. *Phys. Rev. Lett.* **109**, 057401 (2012). URL https://link.aps.org/doi/10.1103/PhysRevLett.109.057401.

[138] Mathias, S. *et al.* Probing the timescale of the exchange interaction in a ferromagnetic alloy. *Proceedings of the National Academy of Sciences* **109**, 4792–4797 (2012). URL https://www.pnas.org/content/109/13/4792. https://www.pnas.org/content/109/13/4792.full.pdf.

[139] Bigot, J.-Y., Vomir, M. & Beaurepaire, E. Coherent ultrafast magnetism induced by femtosecond laser pulses. *Nature Physics* **5**, 515 (2009). URL https://doi.org/10.1038/nphys1285.

[140] Bigot, J. & Vomir, M. Ultrafast magnetization dynamics of nanostructures. *Annalen der Physik* **525**, 2–30 (2013). URL https://doi.org/10.1002/andp.201200199.

[141] Guidoni, L., Beaurepaire, E. & Bigot, J.-Y. Magneto-optics in the ultrafast regime: Thermalization of spin populations in ferromagnetic films. *Phys. Rev. Lett.* **89**, 017401 (2002). URL https://link.aps.org/doi/10.1103/PhysRevLett.89.017401.

[142] Vonesch, H. & Bigot, J.-Y. Ultrafast spin-photon interaction investigated with coherent magneto-optics. *Phys. Rev. B* **85**, 180407 (2012). URL https://link.aps.org/doi/10.1103/PhysRevB.85.180407.

[143] Stanciu, C. D. *et al.* Ultrafast interaction of the angular momentum of photons with spins in the metallic amorphous alloy gdfeco. *Phys. Rev. Lett.* **98**, 207401 (2007). URL https://link.aps.org/doi/10.1103/PhysRevLett.98.207401.

[144] Dornes, C. *et al.* The ultrafast einstein-de haas effect. *Nature* **565**, 209–212 (2019). URL https://doi.org/10.1038/s41586-018-0822-7.

[145] Razdolski, I. *et al.* Analysis of the time-resolved magneto-optical kerr effect for ultrafast magnetization dynamics in ferromagnetic thin films. *Journal of Physics: Condensed Matter* **29**, 174002 (2017). URL https://doi.org/10.1088%2F1361-648x%2Faa63c6.

[146] Seifert, T. *et al.* Terahertz spin currents and inverse spin hall effect in thin-film heterostructures containing complex magnetic compounds. *SPIN* **07**, 1740010 (2017). URL https://doi.org/10.1142/S2010324717400100. https://doi.org/10.1142/S2010324717400100.

[147] Koopmans, B., van Kampen, M., Kohlhepp, J. T. & de Jonge, W. J. M. Ultrafast magneto-optics in nickel: Magnetism or optics? *Phys. Rev. Lett.* **85**, 844–847 (2000). URL https://link.aps.org/doi/10.1103/PhysRevLett.85.844.

[148] La-O-Vorakiat, C. *et al.* Ultrafast demagnetization measurements using extreme ultraviolet light: Comparison of electronic and magnetic contributions. *Phys. Rev. X* **2**, 011005 (2012). URL https://link.aps.org/doi/10.1103/PhysRevX.2.011005.

[149] Cui, B. *et al.* Perpendicular magnetic anisotropy in cofeb/x (x=mgo, ta, w, ti, and pt) multilayers. *Journal of Alloys and Compounds* **559**, 112 – 115 (2013). URL http://www.sciencedirect.com/science/article/pii/S0925838813001394.

[150] Fgalore. Wollaston-prism. *CC BY-SA 3.0* (2008). URL https://commons.wikimedia.org/wiki/File:Wollaston-prism.svg.

[151] Tomasino, A. *et al.* Wideband thz time domain spectroscopy based on optical rectification and electro-optic sampling. *Scientific Reports* **3**, 3116 (2013). URL https://doi.org/10.1038/srep03116.

[152] Kittel, C. *Introduction to Solid State Physics* (Wiley, 2004), 8 edn.

[153] Tserkovnyak, Y., Brataas, A. & Bauer, G. E. W. Spin pumping and magnetization dynamics in metallic multilayers. *Phys. Rev. B* **66**, 224403 (2002). URL https://link.aps.org/doi/10.1103/PhysRevB.66.224403.

[154] Ikeda, S. *et al.* A perpendicular-anisotropy cofeb-mgo magnetic tunnel junction. *Nature Materials* **9**, 721–724 (2010). URL https://doi.org/10.1038/nmat2804.

[155] Nave, C. R. *Magnetic interactions and the Lande' g-factor* (Georgia State University, 1999). URL hyperphysics.phy-astr.gsu.edu/hbase/quantum/Lande.html. Retrieved 14 October 2014.

[156] Hickey, M. C. & Moodera, J. S. Origin of intrinsic gilbert damping. *Phys. Rev. Lett.* **102**, 137601 (2009). URL https://link.aps.org/doi/10.1103/PhysRevLett.102.137601.

List of Figures

Titre : Nouveaux composants spintroniques à base de matériaux antiferromagnétiques

Mots clés : antiferromagnétiques, spintronique, génération de seconde harmonique, ultra-rapide, multiferroïques

Résumé : Les mémoires magnétiques actuelles commencent à atteindre leurs limites physiques en terme de stabilité, vitesse et consommation énergétique, alors que la course à la miniaturisation s'intensifie. Le champ émergeant de la spintronique étudie le comportement collectif des spins dans la matière ainsi que leurs interactions aux interfaces, afin de trouver une solution en termes de matériaux, architectures et sources excitatrices. En particulier, les matériaux antiferromagnétiques sont particulièrement prometteurs. Ces matériaux ordonnées sont abondants, naturellement stables, robustes, ultra rapides et compatibles avec l'électronique des isolants. En effet, la plupart des oxydes à base de métaux de transition sont des isolants antiferromagnétiques ayant leur fréquence de résonance dans le terahertz et un champ de flop de quelques dizaines de teslas. Ils peuvent aussi être semi-métalliques, métalliques, semiconducteurs, supraconducteurs ou multiferroïques. Cette thèse s'intéresse aux deux antiferromagnétiques: oxyde de nickel (NiO) et ferrite de bismuth ($BiFeO_3$). NiO est un antiferromagnétique type à température ambiante, avec une structure cristalline simple. Une étude basée sur des simulations dynamiques atomiques montre que des courants de spin atteignables peuvent réaliser une mémoire à trois états avec ce composé, avec un temps de réponse de l'ordre de la picoseconde. La simulation explique aussi la formation de structures chirales dans $BiFeO_3$, un antiferromagnétique également ferroélectrique, présentant un couplage magnétoélectrique entre ses deux ordres. Dans une deuxième partie, les domaines antiferromagnétiques dans $BiFeO_3$ sont observés expérimentalement par génération de seconde harmonique optique, avec une résolution spatiale de un micron. Les domaines antiferromagnétiques de $BiFeO_3$ sont ensuite excités par une impulsion laser intense, et la dynamique des deux ordres couplés (antiferromagnétisme et ferroélectricité) est étudiée dans le régime picoseconde. Enfin, l'injection d'impulsions de spins dans dans un antiferromagnétique, tel que $BiFeO_3$ ou NiO est envisagée en utilisant la génération de courant de spin induite par la désaimantation ultrarapide de couches adjacentes magnétiques par des impulsions laser.

Title : New spintronic components based on antiferromagnetic materials

Keywords : antiferromagnets, spintronics, second harmonic generation, ultrafast, multiferroics

Abstract : Current magnetic memory devices are reaching their physical limits in terms of stability, speed and power consumption as the race to miniaturization intensifies. The emergent research field of spintronics studies the collective behavior of spins in matter and their interplay at interfaces, to find new avenues in terms of materials, architectures and stimulation sources. A particularly promising group of materials are the antiferromagnets. These abundant magnetically ordered materials are naturally stable, robust, ultra-fast and compatible with insulator electronics. Indeed, most transition metal oxide compounds are antiferromagnetic insulators, have resonance in the terahertz range and flop fields of tens of teslas. They can also be semi-metals, metals, semiconductors, superconductors or multiferroics. This thesis focuses on two antiferromagnets: nickel oxide (NiO) and bismuth ferrite ($BiFeO_3$). NiO is the archetypical antiferromagnet at ambient temperature with a simple crystalline structure. Using dynamical atomistic simulations, I show that this compound can be the elemental brick of a three state memory device controlled by currently available pulses of spin currents, with a picosecond response time. The simulations also explain the formation of chiral structures in $BiFeO_3$, a ferroelectric antiferromagnet with magnetoelectric coupling between the two orders. In a second part, antiferromagnetic domains in $BiFeO_3$ are experimentally observed using second harmonic generation of light, with a sub-micron spatial resolution. Antiferromagnetic domains of $BiFeO_3$ are then excited by an intense femtosecond laser pulse, and the dynamics of the two coupled orders (antiferromagnetism and ferroelectricity) is studied with a sub-picosecond time resolution. Finally, the injection of spin current in an antiferromagnet such as $BiFeO_3$ or NiO is envisioned by characterizing the spin bursts generated by ultrafast laser-induced demagnetization of adjacent ferromagnetic layers.

Université Paris-Saclay
Espace Technologique / Immeuble Discovery
Route de l'Orme aux Merisiers RD 128 / 91190 Saint-Aubin, France